

# A generalised hybrid damage mechanics model for steel sheets and heavy plates

Von der Fakultät für Georessourcen und Materialtechnik  
der Rheinisch-Westfälischen Technischen Hochschule Aachen

zur Erlangung des akademischen Grades eines  
**Doktors der Ingenieurwissenschaften**  
genehmigte Dissertation

vorgelegt von Master of Science

**Junhe Lian**

aus Datong, China

**Berichter:** Univ.-Prof. Dr.-Ing. Wolfgang Bleck

Univ.-Prof. Dr.-Ing. Stefanie Reese

Tag der mündlichen Prüfung: 18. 09. 2015

Diese Dissertation ist auf den Internetseiten der Universitätsbibliothek online verfügbar.





**Berichte aus dem  
Institut für Eisenhüttenkunde**

**Junhe Lian**

---

**A generalised hybrid damage mechanics model  
for steel sheets and heavy plates**

---

Herausgeber:

Prof. Dr.-Ing. W. Bleck  
Prof. Dr.rer.nat. Dr.-Ing.e.h. W. Dahl  
Prof. Dr.-Ing. H.W. Gudenau  
Prof. Dr.-Ing. D. Senk

---

Band 9/2015

Shaker Verlag

**Bibliographic information published by the Deutsche Nationalbibliothek**

The Deutsche Nationalbibliothek lists this publication in the Deutsche Nationalbibliografie; detailed bibliographic data are available in the Internet at <http://dnb.d-nb.de>.

Zugl.: D 82 (Diss. RWTH Aachen University, 2015)

Copyright Shaker Verlag 2015

All rights reserved. No part of this publication may be reproduced, stored in a retrieval system, or transmitted, in any form or by any means, electronic, mechanical, photocopying, recording or otherwise, without the prior permission of the publishers.

Printed in Germany.

ISBN 978-3-8440-4063-0

ISSN 0943-4631

Shaker Verlag GmbH • P.O. BOX 101818 • D-52018 Aachen

Phone: 0049/2407/9596-0 • Telefax: 0049/2407/9596-9

Internet: [www.shaker.de](http://www.shaker.de) • e-mail: [info@shaker.de](mailto:info@shaker.de)

*To Ailin Liu & Kang Zhong*



# Acknowledgements

My sincere gratitude notably goes to Prof. Wolfgang Bleck, my primary advisor, who has given me the chance to work on this topic and inspired me to fall in love with research and development in general. The professional growth that I had in the past years benefiting from his experience, wisdom and visionary mindset is invaluable. The insightful advices and constructive comments from Prof. Stefanie Reese and Prof. Dieter Senk are also greatly appreciated.

I would like to particularly express my gratitude to Dr. Sebastian Muenstermann, the group leader of material mechanics group, who has supervised me for study-integrated thesis, master thesis, and finally the Ph.D. thesis. The continuous recognition and trust; the countless encouragements and discussions; and the permanent optimism and charms have leaped me over all the challenges and obstacle to reach this point.

I am very grateful to have had all the inspiring and directional discussions with Prof. Tomasz Wierzbicki from Massachusetts Institute of Technology and Prof. Yuanli Bai from University of Central Florida for our initiation to develop in the damage mechanics field. Many thanks to Dr. Peter Langenberg from IWT, Prof. Dirk Mohr from Ecole Polytechnique, Prof. Aida Nonn from OTH Regensburg, Dr. Holger Aretz from Hydro and Dr. Yanshan Lou from TU Dortmund for their consistent interests and pertinent suggestions related to my work.

It has been a pleasant and fruitful journey for me to work in the institute only owing to the tremendous help that I gained from all the greatest colleagues, technicians and students. I would like to thank Dr. Goetz Hessling, Ms. Nicole Olles, Ms. Christiane Beumers and Ms. Martina Sparrer for taking care of so many administrative issues for me. Special thanks to Thorsten Labbude, Maria Wildau, Ning Ma, Adrian Rueskamp, Tobias Ingendahl, Julia Daamen, Juergen Dartenne, Wilhelm Meier and Robert Gier for all the aspects concerning experiments, manufacturing specimens, conducting tests, evaluating and discussing results, providing valuable insights and supporting my various ideas and singular wishes. Generous gratitude is also dedicated to my lovely colleagues in the group for creating such a nice atmosphere for working and communication as well as to my excellent master students that provided numerous contributions in obtaining the results of my thesis.

My beloved colleagues, Mick and Moe. It is truly a fortune that we started together and finished together here. There have been too many memories in the past couple of years. It just from time to time occurs to me that we still work together in the office till late in the evening and have dinner together in restaurants during weekends. And Micky, we have even constantly made our girlfriends feel jealous about the companies that we afford to each other and do not even mention the beds that we have shared together. I could not imagine how less fun we would have had in this long run without each other. It is my treasure to have you as colleagues and as friends.

I reserve the deepest part of my heart for my family. My father Zhongru Lian, my mother Ailin Liu: It is your unconditional support, tolerance and love that foster me and push me to pursue higher goals. I will be forever in debt to you for the incredible dedication and sacrifice. The joys brought by my sister Min Lian and especially my two lovely daughters Sophie and Chloe are always the sunshine to start a day.

And the last, Kang, my wife – my biggest fan, my best friend and my forever Little MM... You are the magician that makes this routine, plain and challenging journey so colorful, so fun and so breathtaking. All the measures will after all fade away in this variable life, yet it is only your love to be the constant.

Junhe Lian

Aachen, September 2015.



# Abstract

The damage onset and evolution are of significant importance in the forming processes of high strength steels. These two features and their influence on fracture have challenged the predictive capability of the conventional damage mechanics models. The present thesis contributes to the accurate fracture prediction of both high strength steel sheets and heavy plates by proposing a new generalised hybrid damage mechanics model. A dual-phase steel sheet (DP600) and a high strength low alloy steel plate (S355J2+N), which show very different relation patterns between damage and fracture, are investigated. For both steels, an easy and systematic material parameter calibration procedure with different experiments is designed. Good prediction applying the model to Nakajima tests for the steel sheet and to bending tests for the heavy plate is achieved. This validates the generalised transferability and flexibility of the proposed model for high strength steels with complex damage-fracture relation under various stress states. As the model is formulated in a phenomenological sense, it also suffers from two drawbacks: having a large number of material parameters and a weak link to the material microstructure. Therefore, two approaches are provided to overcome these shortcomings: justified simplification of the model formulation for specific applications and linking the microstructure to the phenomenological material parameters by multiscale modelling.



# Kurzzusammenfassung

Die Schädigungsinitiierung und -entwicklung spielen eine signifikante Rolle in den duktilen Versagensmechanismen, die in den Umformprozessen moderner hochfester Stähle dominieren. Dies stellt eine Herausforderung für die konventionellen Schädigungsmodelle dar. In der aktuellen Arbeit wird ein neues hybrides Schädigungsmodell vorgestellt, mit dem eine genaue Beschreibung des Versagens von Stahlblechen verschiedener Dicken erzielt werden kann. Untersucht werden ein Feinblech aus Dualphasen-Stahl (DP600) und ein Grobblech aus einem mikrolegierten Stahl (S355J2+N), die sehr unterschiedliche Schädigungsabhängigkeiten des Versagens aufweisen. Für beide Stähle wird ein einfaches und zuverlässiges Verfahren zur Kalibrierung der Materialparameter anhand von verschiedenen Experimenten entwickelt. Bei Modellanwendungen zur Simulation von Nakajima- und Biegeversuchen konnten gute Übereinstimmungen erreicht werden. Dies bestätigt die allgemeine Übertragbarkeit und die Flexibilität des vorgestellten Modells bei Stahl-Anwendungen, gekennzeichnet durch den komplexen Zusammenhang zwischen Schädigung und Versagen bei unterschiedlichen Spannungszuständen. Da es sich um ein phänomenologisches Model handelt, leidet es unter zwei Nachteilen: Eine hohe Anzahl von Materialparametern und eine schwache Verbindung zum Gefüge. Zur Überwindung dieser Defizite werden zwei Ansätze präsentiert: zum einen wird die Modellformulierung bei bestimmten Anwendungen vereinfacht und zum anderen wird mithilfe der Multiskalenmodellierung eine Verbindung zwischen dem Gefüge und den phänomenologischen Materialparametern hergestellt.



# Table of contents

Acknowledgements .....	i
Abstract.....	iii
Kurzzusammenfassung .....	v
Table of contents .....	vii
Notations .....	xi
<b>Chapter 1 Introduction.....</b>	<b>1</b>
1.1 Background and problem definition .....	1
1.2 Aim and scope of the thesis .....	6
1.3 Outline of the thesis.....	7
<b>Chapter 2 Theoretical background .....</b>	<b>11</b>
2.1 Definitions.....	11
2.2 Damage mechanism for modern high strength steels.....	13
2.3 Experimental damage evaluation .....	16
2.3.1 Change of macroscopic physical properties.....	16
2.3.2 Changes in microscopic microstructural morphology .....	20
2.4 Numerical damage evaluation .....	21
2.4.1 Ductile damage modelling.....	22
2.4.2 Microstructure based modelling.....	27
<b>Chapter 3 A generalised hybrid damage mechanics model .....</b>	<b>31</b>
3.1 General introduction of the model .....	31
3.2 Formulation of the model.....	35
3.2.1 Characterization of stress state.....	35
3.2.2 Constitutive equations of the model .....	37
3.2.3 Numerical implementation algorithm .....	41
3.2.4 Extension of the model with an stress-state-dependent yield criterion.....	46
<b>Chapter 4 Materials.....</b>	<b>53</b>
4.1 Material selection.....	53
4.2 Chemical composition .....	54
4.3 Microstructure .....	54
<b>Chapter 5 Experimental techniques.....</b>	<b>57</b>
5.1 Tests for parameter calibration and validation .....	57

5.1.1	Selected tests for steel sheet DP600 .....	61
5.1.2	Selected tests for heavy plate S355J2+N .....	64
<b>5.2</b>	<b>Tests selected for model application.....</b>	<b>68</b>
5.2.1	Steel sheet: Nakajima test .....	68
5.2.2	Heavy plate: Bending test .....	70
<b>Chapter 6</b>	<b>Material parameter calibration and model validation .....</b>	<b>73</b>
6.1	Material parameter calibration strategy and methodology.....	73
6.2	Parameter calibration and validation for steel sheet DP600 .....	74
6.2.1	Parameter calibration .....	74
6.2.2	Validation and discussion .....	85
6.3	Parameter calibration and validation for heavy plate S355J2+N.....	88
6.3.1	Calibration programme and FE models .....	88
6.3.2	Parameter calibration .....	91
6.3.3	Validation and discussion .....	99
6.4	Summary of the calibrated material parameters .....	99
<b>Chapter 7</b>	<b>Model application .....</b>	<b>109</b>
7.1	Nakajima test of steel sheet DP600.....	109
7.1.1	Motivation of the prediction of forming limits .....	109
7.1.2	Experimental data and analysis .....	110
7.1.3	Prediction of the FLC at necking.....	111
7.1.4	Prediction of the FLC at ductile fracture .....	115
7.2	Bending test of heavy plate S355J2+N.....	122
7.2.1	Motivation of the simulation of the bending test.....	122
7.2.2	FE model .....	123
7.2.3	Results and discussion .....	126
7.3	Conclusions .....	128
<b>Chapter 8</b>	<b>Model improvement to reduce the number of material parameters ..</b>	<b>131</b>
8.1	Introduction .....	131
8.2	Constitutive equations .....	132
8.3	Experimental and numerical procedures .....	134
8.4	Results and discussion.....	136
8.4.1	Experimental investigation on the damage development during loading .....	136
8.4.2	Parameter calibration .....	138

---

8.4.3	Validation of the model and discussion .....	143
8.5	Conclusions .....	148
Chapter 9	Including a mechanism description by multiscale modelling .....	151
9.1	General ideas .....	151
9.2	Experimental study on the damage initiation .....	153
9.3	Numerical procedures for RVE simulation.....	154
9.3.1	RVE construction and data evaluation .....	154
9.3.2	Flow curve calibration.....	159
9.4	Results and discussion.....	161
9.4.1	RVE simulation under uniaxial tension loading condition .....	161
9.4.2	Prediction of damage initiation under different stress states .....	165
9.5	Conclusions .....	168
Chapter 10	Conclusions and future studies .....	171
10.1	Concluding remarks .....	171
10.2	Future studies .....	173
Appendix	.....	177
	Transformation between the space of $(\boldsymbol{\varepsilon}, \boldsymbol{\eta})$ and $(\boldsymbol{\varepsilon}_1, \boldsymbol{\varepsilon}_2)$ under the plane stress condition .....	177
Literature	.....	181





# Notations

## Abbreviations

AHSS	Advanced High Strength Steels
BCC	Body Centred Cubic
BW	Bai–Wierzbicki
C3D8R	Continuum 3D 8-node solid element with Reduced integration point
CDM	Continuum Damage Mechanics
CP	Complex Phase
CPS4R	Continuum 4-node Plane Stress element with Reduced integration point
CT	Compact Tension
CTOD	Crack Tip Opening Displacement
DCPD	Direct Current Potential Drop
DIC	Digital Image Correlation
DIL	Damage Initiation Locus
DP	Dual Phase
EBSD	Electron Back Scatter Diffraction
EPMA	Electron Probe Micro Analyser
FCC	Face Centred Cubic
FE	Finite Element
FEM	Finite Element Method
FLC	Forming Limit Curve
$FLC_f$	Forming Limit Curve to fracture
$FLC_n$	Forming Limit Curve to necking
FLD	Forming Limit Diagram
GLD	Gologanu–Leblond–Devaux
GTN	Gurson–Tvergaard–Needleman
HCP	Hexagonal Close Packed
HSLA	High Strength Low Alloy
ICME	Integrated Computational Materials Engineering
JC	Johnson–Cook
LOM	Light Optical Microscopy
MBW	Modified Bai–Wierzbicki
MFC	Maximum Force Criterion
MK	Marciniak–Kuczynski
MMC	Modified Mohr–Coulomb
MMFC	Modified Maximum Force Criterion
NDB	Notched Dog-Bone

NRB	Notched Round Bar
PE	PolyEthylene
PEEQ	EQuivalent Plastic strain
PLA	Phenomenologically Lode effect Added
PTFE	PolyTetraFluoroEthylene
PVC	PolyVinyl Chloride
RVE	Representative Volume Elements
SEM	Scanning Electron Microscopy
SENB	Single-Edge Notched Bending
SRB	Smooth Round Bar
TRIP	TTransformation Induced Plasticity
TWIP	TWinning Induced Plasticity
UTS	Ultimate Tensile Strength

## Symbols

$A_0$	Cross section area
$A_5$	Ultimate elongation with original gauge length $5.65 \sqrt{A_0}$
$A_{80}$	Ultimate elongation with original gauge length 80 mm
$A_u$	Uniform elongation
$b$	Burger's vector
$\mathbf{C}^e$	Elastic stiffness matrix
$C_1 - C_6$	Material parameter for damage initiation or fracture locus
$c_{\theta}^b, c_{\theta}^s, c_{\theta}^c, m$	Material parameters in Bai–Wierzbicki plasticity model
$D$	Scalar damage variable
$D_{cr}$	Critical damage parameter
$E$	Young's modulus
$E_0$	Original Young's modulus
$F$	Force
$f$	Void volume fraction
$f^*$	Modified void volume fraction
$f_c$	Critical void volume fraction
$G$	Shear modulus
$G_0$	Original shear modulus
$G_f$	Specific energy to open a unit area of crack
$\mathbf{I}$	Second-order identity tensor
$I_1$	First principal invariant of a stress tensor
$J_2, J_3$	Second and third invariants of stress deviator
$K$	Bulk modulus
$K_0$	Original bulk modulus

$k$	Shape parameter of the Lode parameter sensitivity function
$k_r$	Recovery rate
$L$	Characteristic element length
$L_d$	Dislocation mean free path
$l_0$	Initial length
$M$	Taylor factor
$\mathbf{N}$	Plastic flow direction tensor
$p$	Hydrostatic pressure
$q_1 - q_3$	GTN model material parameters
$R_m$	Tensile strength
$R_{p0.2}$	Yield strength
$r$	Radius
$\mathbf{s}$	Deviatoric stress tensor
$\tilde{\mathbf{s}}$	Effective deviatoric stress tensor
$t$	Thickness
$[t_n, t_{n+1}]$	A (pseudo-) time interval
$U$	Displacement
$Y$	Elastic damage energy release rate
$\alpha$	Stress ratio
$\beta$	Strain ratio
$\dot{\gamma}$	Plastic multiplier
$\boldsymbol{\varepsilon}$	Total strain tensor
$\boldsymbol{\varepsilon}^e$	Elastic strain tensor
$\boldsymbol{\varepsilon}_d^e$	Elastic strain deviatoric tensor
$\boldsymbol{\varepsilon}^p$	Plastic strain tensor
$\bar{\varepsilon}$	Equivalent strain
$\varepsilon_v^e$	Elastic volumetric strain
$\bar{\varepsilon}^p$	Equivalent plastic strain
$\bar{\varepsilon}_f^p$	Equivalent plastic strain to fracture
$\bar{\varepsilon}_i^p$	Equivalent plastic strain to damage initiation
$\varepsilon_{\text{eng}}$	Engineering strain
$\bar{\varepsilon}_f$	Fracture strain
$\eta$	Stress triaxiality
$\theta$	Lode angle
$\bar{\theta}$	Lode angle parameter
$\mu_\theta$	Lode parameter sensitivity function
$\nu$	Poisson's ratio.
$\xi$	Scaled version of $I_1$
$\rho$	Scaled version of $J_2$
$\boldsymbol{\sigma}$	Cauchy stress tensor
$\tilde{\boldsymbol{\sigma}}$	Effective Cauchy stress tensor
$\bar{\sigma}$	Mises equivalent stress

---

$\sigma_{\text{eng}}$	Engineering stress
$\sigma_{\text{H}}$	Invariant of the stress tensor
$\sigma_i$	Principal Cauchy stress
$\sigma_{\text{m}}$	Mean stress
$\sigma_{\text{p}}$	Peierl's stress
$\sigma_{\text{pc}}$	Strengthening due to precipitations and carbon in solution
$\sigma_y$	Yield stress of the matrix material
$\sigma_{\text{yi}}$	Yield stress when the damage initiation criterion is met
$\Phi$	Yield function
$\chi$	Non-negative material constant
$\Psi$	Dissipation potential
$\Psi_{\text{d}}$	Damage dissipation potential
$\Psi_{\text{p}}$	Plasticity dissipation potential
$\omega$	Lode angle related function

## Operators

$d(\cdot)$	Derivative of $(\cdot)$
$\exp(\cdot)$	Exponential of $(\cdot)$
$\ln(\cdot)$	Natural logarithm of $(\cdot)$
$\text{tr}(\cdot)$	Trace of $(\cdot)$
$\Delta(\cdot)$	Increment of $(\cdot)$
$\frac{\partial(\cdot)}{\partial a}$	Derivative of $(\cdot)$ with respect to $a$
$\ (\cdot)\ $	Euclidean norm of the tensor $(\cdot)$
$(\cdot)_n$	$(\cdot)$ at the time $t_n$
$(\cdot)_{n+1}$	$(\cdot)$ at the time $t_{n+1}$
$\dot{(\cdot)}$	Material time derivative of $(\cdot)$

# Chapter 1

## Introduction

### 1.1 Background and problem definition

Fracture happens every day and everywhere. It can be seen when tableware is accidentally knocked down. It also sometimes presents itself in a more dramatic and shocking way when engineering structures encounter it. Take the disaster on November 12, 2001 for instance, the American Airlines flight 587 crashed shortly after take-off due to the fracture on the vertical stabiliser of the plane. Such accidents, which are caused by fracture of materials, are not rare throughout the history of mankind. Therefore, the prevention of fracture, in particular in the engineering structures is the principal concern for both material and structure engineers.

For the application in the engineering structures, steels have been competitive due to their good strength, ductility and toughness properties. Since the development of the low carbon steels with excellent ductility in the middle of last century, steels have been the dominant element in various engineering applications, such as automotive industry, structure constructions, pressure vessels and pipelines, etc. In the recent development of the engineering structures starting from the end of last century, lightweight design principle has become one of the most efficient concepts to improve the ecological balance sheet as well as to realise economic benefits. For the steel industry, to be more competitive with other naturally lighter materials, such as aluminium alloys, magnesium alloys and composites, modern steels with high strength and good ductility have been developed based on the conventional high ductility steels. Focusing on two of the widest application fields of steel, steel sheets and heavy plates, different strategies are taken to generate the new steels with enhanced properties. For steel sheets, mostly driven by the demands from automotive and aerospace industry, the advanced high strength steels (AHSS), in particular the multiphase steels are intensively developed and

applied. The physical background of the development on the multiphase steels is mainly that their microstructure is designed to contain constituents with strongly distinctive mechanical properties of either extraordinary strength or excellent ductility in order to achieve an overall balanced combination. For hot rolled steels in the form of heavy plates, as a precise manipulation of the microstructure is not practically feasible due to the thick gauge, alternative methods, such as thermos-mechanical rolling and quench and temper process are applied to produce the attractive mechanical properties. With these methods, the alloying concept can retain easy and cheap, and therefore these steels are referred to as high strength low alloy (HSLA) steels. It can hence be expected that both multiphase steel sheets and hot rolled HSLA steels will be demanded for many high performance engineering structures in the future.

For the fracture prediction of these modern high strength steels, challenges are raised. As illustrated in Fig. 1.1, various failure patterns concerning the relation between localisation, damage and fracture are present for different steels. For the conventional highly ductile steels, e.g. the cold rolled low carbon single phase steels, the ductile failure event follows a clear pattern: plastic deformation, severe plastic localisation and fracture. Therefore, in the forming limit diagram (FLD) of these steels, substantial post-necking deformation is observed between the necking and fracture curves. However, this pattern is not valid for the recently developed high strength steels, such as the twinning induced plasticity (TWIP) steels, transformation induced plasticity (TRIP) and dual-phase (DP) or complex phase (CP) steels. For the TWIP/TRIP steels, it is often observed that fracture is prior to necking. As illustrated in the FLD in Fig. 1.1, the theoretical calculated necking curve is far beyond the realistic observed fracture curve due to the extraordinary strain hardening behaviour of these steels. More sophisticated failure patterns are present in the DP/CP steels consisting of different phases with distinctive mechanical properties. As shown in the FLD, the fracture curve could have intersection with the necking curve, which indicates that the failure patterns are dependent on the stress states. To compare the dominant failure mechanism between these steels, the thickness cross-section of the fractured specimens are illustrated in Fig. 1.1. For the highly ductile single phase steels, it is a typical localisation dominant failure pattern. Damage, in particular the decisive damage that is influencing the material strength property is a phase so close to the final fracture that the two terms damage and fracture are often not distinguished. For the TWIP/TRIP steels, it is clearly a fracture dominant failure pattern and no localisation is observed in the specimen. However, for the DP/CP steels, the failure patterns is a result of

the competition between localisation and damage. In these steels, damage is initiated in a much earlier phase than the highly ductile steels and its evolution is dependent on the stress states. Depending on the interaction between the damage-induced softening and strain hardening under different stress states, the failure pattern could be either localisation–damage dominant or fracture dominant.

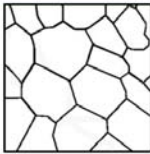
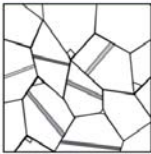
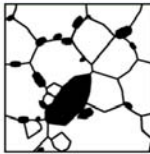
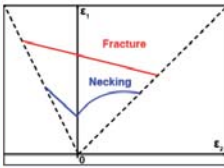
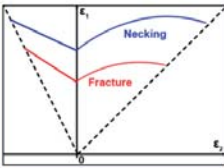
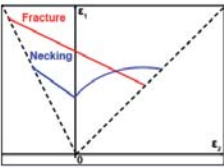


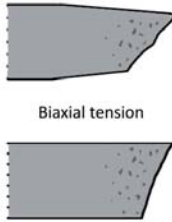
Material	Highly ductile single phase steels	TWIP/TRIP steels	Dual-phase/ Complex phase steels
Micro-structure			
FLD			
Thickness cross-section (Failure mechanism)	 <b>Localisation dominant</b>	 <b>Fracture dominant</b>	 Uniaxial tension Biaxial tension <b>Localisation &amp; damage competition</b>

Fig. 1.1: Schematic drawing of the microstructure, FLD and the thickness cross-section of fractured specimens representing the failure mechanism of three different classes of steels (the experimental observation is based on Chung et al. [1]).

The difference is naturally related to the underlying damage mechanisms of different steels. In the conventional highly ductile steels, microcracks or voids are generally triggered by the interaction between the matrix and inclusions or hard particles. As high cleanliness is reached in the steels, damage plays a negligible role during the plastic deformation until severe

localisation, as shown in Fig. 1.2 for a fractured tensile specimen of a single phase ferritic stainless steel (AISI439). Therefore, the fracture is decided by the extensive plastic localisation. On the contrary, for the modern high strength steels, due to the advanced microstructure-level design for enhanced strength properties, the damage mechanisms are more complex, as shown in Fig. 1.2 for a fractured tensile specimen of a DP steel (DP600). In the DP steel, microcracks or voids are mainly generated by the debonding at the phase boundaries and the inner brittle cracking of the hard phase, in addition to the conventional damage mechanism, debonding of inclusions and particles from the matrix. Consequently, the increased possibility of creating microcracks or voids by the new damage mechanisms considerably intensifies the importance of damage and its evolution. The local microstructure degradation caused by the accumulation of damage ultimately influences the material strength and ductility. It is also the reason for fracture prior to necking or very limited post-necking deformation.

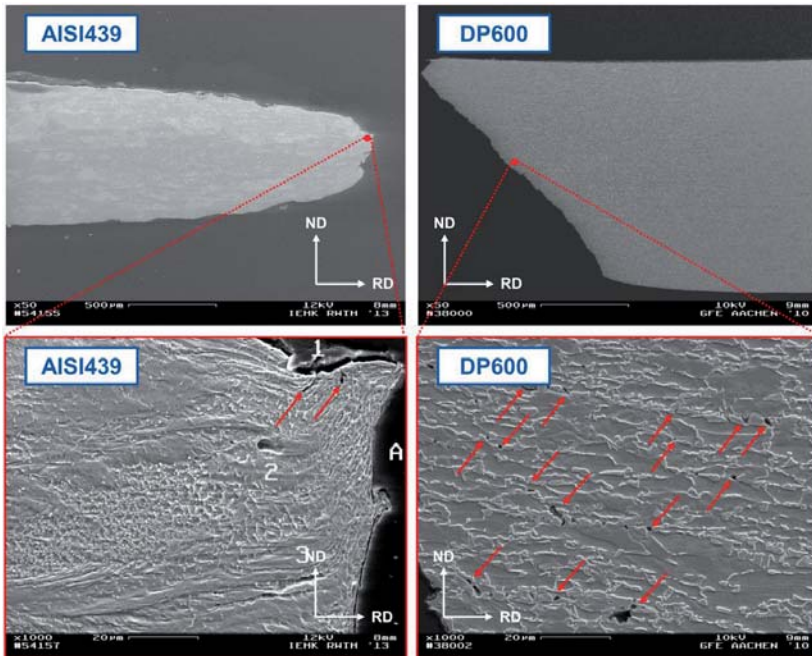


Fig. 1.2: Scanning electron microscopy (SEM) micrographs of the fractured samples under uniaxial loading in the thickness cross-section with various magnifications for a single-phase ferritic stainless steel (AISI 439) and a DP steel (DP600); the red arrows indicate the formation of microcracks and voids.



Therefore, for a precise prediction of fracture for these new steels, the following features shall be considered, i) damage and fracture shall be clearly distinguished but also correlated; ii) a microscopic threshold that corresponds to the onset of damage should be implemented in the damage mechanics models and, iii) a quantitative representation to express the extent of damage is also demanded to be integrated for the characterisation of overall material behaviour. Various types of models have been developed to predict fracture for decades, yet the aforementioned features for accurate fracture prediction for the modern high strength steels are not consistently defined in one model. On the contrary, different individual modelling approaches are developed for sheet metals and heavy plates (bulk materials) resulting from the conventional failure pattern (plastic deformation, severe strain localisation and fracture).

In the steel sheets community, for long time, strain localisation or necking is considered as the critical phase for forming processes due to the thin thickness. Different models based on the plane stress assumption, such as Hill and Swift necking criteria [2; 3], Marciniak–Kuczynski (MK) model [4], bifurcation theories [5], and the modified maximum force criterion (MMFC) [6], were proposed to predict necking. These models have been quite successful for the application of the conventional highly ductile steels, but their applicability is challenged by the modern high strength steels. As in these steels, necking is either a deformation phase that could be absent before fracture or a stage, at which a large amount of damage (in terms of microcracks or voids) is developed in the materials, as demonstrated in Fig. 1.1. Therefore, it is not valid to consider necking as the forming limit excluding the effect of damage. The onset of damage to indicate the defect-free forming limit and its evolution to interact with strain localisation and fracture are required for the characterisation of the formability of the new steels. In addition, as damage is a local phenomenon, the stress state at the local scale could cover a wider range than plane stress condition depending on the level of nonlinearity of materials and geometries. Therefore, a more general formulation in 3D stress and strain spaces covering a wide range of the stress/strain states is also desired.

For heavy plates (bulk materials), the prediction on the final fracture attracts more attentions as the strain localisation for them is less detrimental than sheet metals. Depending on the interaction between plasticity and damage, the existing models are basically classified into two categories, coupled and uncoupled models. In the uncoupled models, the flow behaviour is not influenced by the damage accumulation and normally a fracture strain criterion with a weighted function of the stress state is defined for the appearance of fracture. The coupled models, on

the contrast, incorporate the effect of the accumulated damage into the yield function. Two different approaches have been developed for last decades, the micromechanically motivated Gurson or Gurson-like model and the phenomenological continuum damage mechanics (CDM) model derived from a consistent thermodynamics framework. Both of the uncoupled and coupled approaches have their own advantages in application and response to individual requests of the fracture prediction of the high strength steels. However, the requests are not consistently defined in one of the existing individual models. The uncoupled models do not include the damage effect or implicitly include it into the matrix flow curve. They are not general to be used for the damage-sensitive steels. The coupled approaches always assume that the damage is a continuous process initiating from the onset of the plastic deformation and lacks the definition and characterisation of the damage initiation. Therefore, a general model that consistently delivers all the requests of the newly developed steels is desired.

In addition to the model formulation, the material parameter calibration is crucial for the transferability from theory to practical use. The model without a practical, reliable and systematic parameter calibration procedure loses its application appeal dramatically, despite its advance and comprehensiveness. For the parameter calibration, experiments over a wide stress states are required. Due to the difference between steel sheets and heavy plates, there are different types of experiments practically available accordingly. Therefore, a reliable parameter calibration procedure with designed experiments ideally for both steel sheets and heavy plates is required to attach to the model development.

## 1.2 Aim and scope of the thesis

The objective of the present thesis is to develop a *generalised* model for the fracture prediction of the modern high strength steel sheets and heavy plates. The *generalised* here has meaning in two folds: i) the model is developed in 3D stress/strain spaces that could be used for steel sheets and heavy plates in a wide range of stress states; ii) the model generally defines plastic deformation, damage initiation, damage evolution and fracture, and represents the various relation patters between them, which qualifies for the applications of different steels with different failure mechanisms, as shown in Fig. 1.1. Taking the advantages of individual approaches, the model is developed in a *hybrid* way by combining the uncoupled model to act as the damage threshold and coupled model to represent the damage evolution and its interaction with plastic flow and fracture. Due to its hybrid nature, the model is general to be

used as a complete uncoupled model for conventional highly ductile materials, or a coupled model for porous materials where damage is non-negligible since the beginning of plastic deformation, or a hybrid model for the modern high strength steels. Attached to the model, a practical, reliable and systematic material parameter calibration procedure with comprehensive experiments designed for both steel sheets and heavy plates is developed.

For both the model development and application examples in the present thesis, we restrict ourselves on the *isotropic* materials under the conditions of *room temperature*, *quasi-static* and *monotonic* loadings. Therefore, isotropic elasticity, plastic yielding and hardening are assumed for the material behaviour and rate-independent and temperature-insensitive formulation of the model is adopted. However, since the model framework is general, the constitutive equations accounting for rate-dependent and temperature-sensitive deformation can be simply added to the model for the corresponding applications.

The model developed in the present thesis is a phenomenological model. It can be generally used from material to material, but uses the material parameters to distinguish the intrinsic features of material microstructure. The advantage of it is the generalised transferability and good predictive capability, whereas it also suffers from two drawbacks: a large number of material parameters and a weak link to the material microstructure. These disadvantages also hinder its application, especially in the steel design field, where a quantitative, or at least a qualitative, link between the microstructure and the mechanical behaviour is required for the microstructure optimisation. In the present thesis, two approaches are provided to overcome these shortcomings. One approach is the simplification of the formulation of the model for specific applications in order to reduce the number of material parameters, ultimately the effort of the experiments for the material parameter calibration. The second one is to use the multiscale modelling approach to link the microstructure to the phenomenological material parameters. It results in a direct prediction of the material parameters of the macroscopic model for saving the effort on parameter calibration, and naturally the phenomenological model is also becoming microstructure-informed for the material design applications.

### 1.3 Outline of the thesis

The thesis consists of ten chapters, excluding the bibliography, and they are structured into mainly five parts. The first part, including Chapter 1 and 2 provides the motivation and aim of the thesis, the theoretical background and the state-of-the-art of the development of the

experimental and numerical investigations on damage and fracture. In the second part (Chapter 3), the formulation of the proposed model is presented. The third part, from Chapter 4 to 7, shows the use of the model for both steel sheets and heavy plates in terms of material parameter calibration strategy and procedure, model validation, and model application. The fourth part, Chapter 8 and 9, provides approaches to overcome the drawbacks of the model, a large number of material parameters and missing information of the material microstructural features. The last Chapter draws conclusions and give an outlook for future development. The content of each chapter is listed as follows.

- Chapter 1 introduces the background of the fracture prediction and the new developments of steels according to the lightweight design principle. The new challenges that motivate this study are pointed out for the fracture prediction of these new steels. The aim and the contents of the thesis are defined.
- Chapter 2 overviews the important experimental, theoretical and numerical developments of the failure analysis. The definition of damage and fracture are distinguished and the damage mechanisms for steels are reported. The experimental methods for study damage/fracture and various theoretical and numerical modes are briefly reviewed.
- Chapter 3 presents the development of the generalised hybrid damage mechanics model. The formulation consists of three main characteristics, a plasticity model, a damage initiation criterion and a damage evolution law.
- Chapter 4 provides the basic characteristics of the investigated material.
- Chapter 5 summarises the setups of all the employed experiments in the thesis and gives their corresponding stress states.
- Chapter 6 defines the material parameter calibration strategy of the model, and also gives the detailed calibration procedures for both steel sheet and heavy plates. The model and the selection of the parameters are further validated by experiments.
- Chapter 7 shows the predicative capability of the proposed model in two application cases, Nakajima test and bending test for steel sheet and heavy plate, respectively.
- Chapter 8 proposes an alternative formulation of the model to reduce the number of material parameters in the application of steel sheet and discusses its validity from local analysis.

- Chapter 9 describes an upscaling method from a microstructure-based model to the phenomenological macroscopic model for the determination of the material parameters and integration of the material character in the model for material design.
- Chapter 10 concludes the major results of the thesis and suggests the potential topics for the improvement and further investigation in the field.

The flow of the thesis contents and the interaction between parts and chapters are illustrated in the following figure. The readers are always referred to this figure before reading individual chapters for the connections in the overall context.

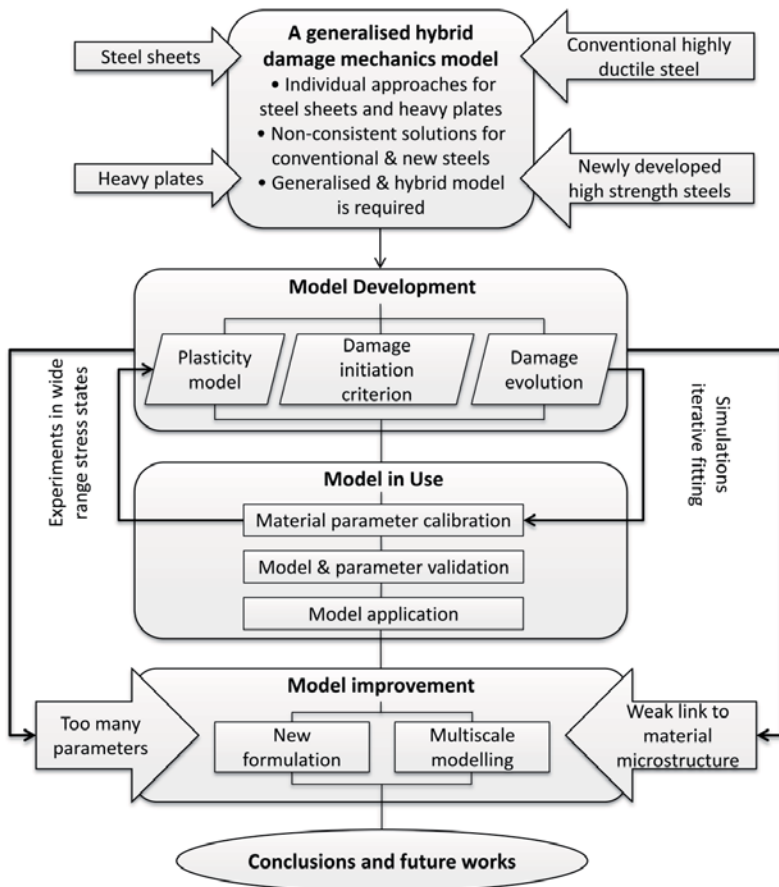


Fig. 1.3: Flow chart to illustrate the structure of the thesis and the interaction between the investigation modules.



# Chapter 2

## Theoretical background

### 2.1 Definitions

In order to avoid possible confusion, two terms are clearly differentiated in this thesis, damage and fracture. Fracture describes macroscopic behaviour that can be defined as occurring when a component or system stops complying with its service requirements. Damage corresponds to microscopic behaviour that can be defined as occurring when the microstructure develops an irreversible degradation on a given length scale. Depending on the material, microstructure and loading conditions, the length scale of it varies from a few microns to dozens of microns. Under various types of external loading, damage can also be divided into ductile damage, brittle damage, fatigue, creep, corrosion, etc. For ductile damage, it can be recognised normally as formation of microcracks, voids and shear bands. In this context, the initiation of damage does not refer to individual formation of voids or microcracks, but an aggregate accumulation of these defects in the material to a critical phase, so that the overall behaviour of the material cannot be represented by a flow curve from an almost defect-free material. The extensive accumulation of damage finally leads to the formation of macroscopic fracture and the complete loss of load carrying capacity of the component.

For the conventional highly ductile materials, the differentiation of these two terms makes minor impact on analysing the failure of materials or structural integrity, because the final fracture of these materials are mainly driven by extensive strain localisation rather than damage. Damage normally occurs in a quite late phase of deformation right prior to the final fracture. However, it is not the case for the newly developed steels, in particular the high-strength steels, where damage introduces non-negligible impacts on the strength and formability and finally triggers the final fracture.

As an example for illustration of the difference between damage and fracture, in Fig. 2.1, pressure and time response are demonstrated by the numerical simulation of a bulge test integrated with representative volume elements (RVE) to characterize the microstructure of a multiphase steel (TRIP700Z), in which elements in four different colours represent four different phases [7]. The effect of the three varied configurations of the microstructure (homogeneous, single banded, 2-banded) on damage occurrence has been investigated with a simulated bulge test. The first occurrence of microcracks is indicated in the pressure–time curve. It is clear that the microcrack or damage occurs prior to the final macro-failure or fracture, and the microstructure influences the actual occurrence of damage.

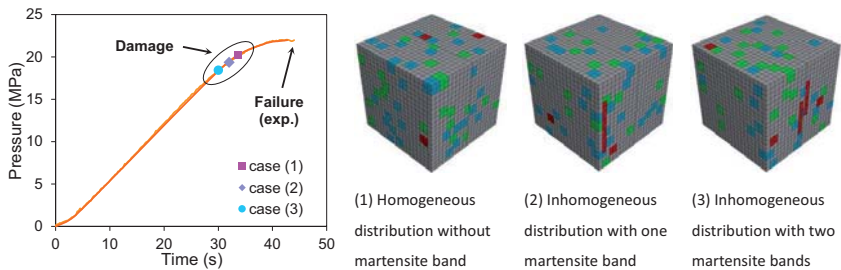


Fig. 2.1: Experimentally-determined material failure is compared to the numerically determined onset of damage with 3 RVE structures during a sheet bulge test; TRIP steel 700Z [7].

On a macro scale, depending on the magnitude of the inelastic deformation or the applied strain energy, fractures can be differentiated into ductile fracture and brittle fracture, as shown in Fig. 2.2. The physical background of ductile fracture in metals is known to be the initiation, growth and coalescence of voids [8]. Voids can initiate at inclusions, secondary phase particles or dislocation pile-ups. With increasing plastic deformation, these voids grow and then coalescence to form microcracks that eventually lead to macroscopic failure. At the void growth stage, depending on the stress state and strain history, two different mechanisms can be triggered: dimple fractures and shear fractures. In dimple fractures, the volume increase of the voids accounts for the degradation of the material stiffness. In shear fractures, the effect of the shape change overtakes the volume increase of voids, in which shear lips or bands are formed. These two mechanisms often coexist and interact during structural component failure.



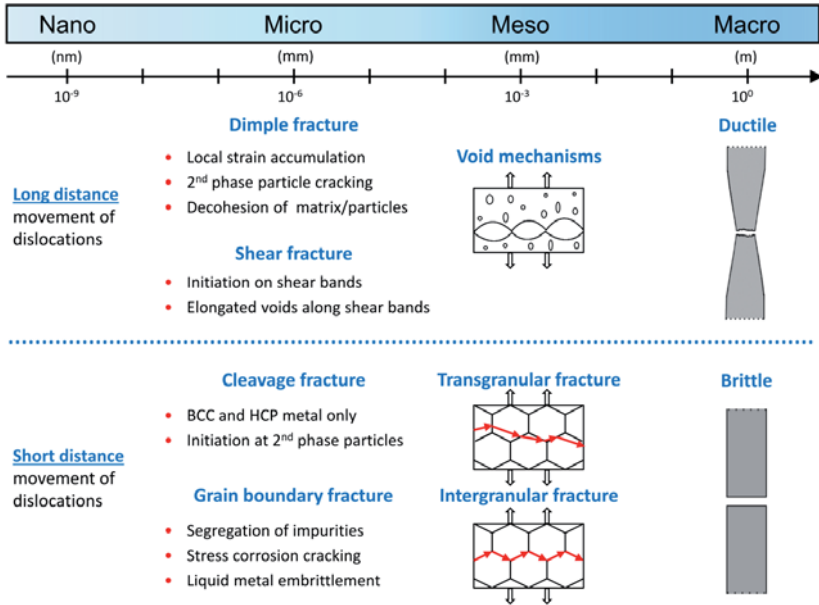


Fig. 2.2: Length scale of damage, description of fracture modes and specimen behaviours.

Regarding brittle fracture, there are two common mechanisms that account for it on the micro scale: cleavage fractures and grain boundary fractures. Cleavage fractures can be defined as the rapid propagation of a crack along a particular crystallographic plane, leading to transgranular fracture on the mesoscopic scale. If the maximum normal stress in body centred cubic (BCC) or hexagonal close packed (HCP) metals reaches a critical value, this lattice splitting will occur [9]. Regarding intergranular fractures, there are different conditions that can lead to cracking on grain boundaries, such as the precipitation of a brittle phase on the grain boundary, segregation, liquid metal embrittlement, environmental assisted cracking, intergranular corrosion and grain boundary cavitation [10].

## 2.2 Damage mechanism for modern high strength steels

For a long period of time, inclusions had been considered to be the main crack initiation points in cold, formable or high toughness structural steels. Therefore, the reduction of it in the content as well as the reduction in the size and the optimization of the shape of non-metallic inclusions, such as MnS, Al<sub>2</sub>O<sub>3</sub> and TiN, results in better toughness. In recently developed high-strength

pipeline steels for arctic environments, transition temperatures below  $-60$  °C and upper shelf Charpy toughness values as high as 350 Joule have been obtained [11]. In these steels, inclusions are no longer important to the mechanical behaviour, but small carbon-enriched zones in the bainitic matrix have been identified as damage-relevant areas for ductile failure. On the other hand, the transition between ductile and brittle failure is controlled by the bainite block size. In the modern multiphase steels, the damage mechanism is more complicated: both ductile and brittle fractures can occur simultaneously, and different mechanisms favourable in different phases also coexist and interact with each other, depending on the loading conditions and material microstructure. For a detailed look, we take the DP steels, recognized as the first generation of the AHSS, as an example.

The DP steels can be defined as low carbon steel that is thermo-mechanically processed to have a better formability than ferrite-pearlite steels of similar strength. They are widely used in industry, in particular automotive industry for light weight design due to their mechanical advantages, such as attractive combination of strength and formability. Dual-phase steels contain two phases, normally soft ferritic matrix and hard martensite islands dispersed in the matrix. Due to the strong distinctions in yielding of the two phases, the plastic deformation of DP steels is mainly dominated by ferrite.

Tasan et al. [12] compared the deformation of a DP steel at different strain stages of a uniaxial tension test by SEM micrographs, and it was observed that the hard martensite islands only constrain the plastic flow of the soft ferrite, while they remain primarily elastic deformation. Shen et al. [13] also studied the strain distribution pattern between ferrite and martensite of dual-phase steels with different volume fraction ratios by SEM micrographs at different stages under uniaxial tension loading. It is reported that for steel with low martensite volume fraction, the martensite phase remains elastic deformation while the ferrite deforms plastically, but for steel with high martensite volume fraction, the martensite phase can undergo plastic deformation due to the shearing of the ferrite–martensite phase boundary. Recent studies of the deformation mechanism of dual-phase steels often incorporate the digital image correlation (DIC) with the in situ test to quantitatively describe the strain partitioning in the ferrite and martensite phase at grain level [14-16]. The plastic deformation of martensite was detected and calculated. Different local strain partition ratios between the ferrite and martensite phase were found depending on the martensite phase fraction, carbon partition and the method used to characterise the strain partitioning [15; 16]. Despite the different behaviour of the martensite

phase in different DP steels, a common finding from these studies is that the localisation of the plastic deformation in the ferrite phase or at the ferrite–martensite interface due to the constrain of the adjacent martensite is the main source to trigger the subsequent damage, which can be in the ferrite phase, the martensite phase or at the interface.

Attributed to the deformation mechanism of the dual-phase steels, the damage or failure mechanism is often concluded to be three modes of void nucleation: martensite brittle cracking, ferrite–martensite interface decohesion and ferrite–ferrite grain boundary decohesion. All of these void nucleation modes were observed in different types of DP steels [16–21]. The factors that control the dominant damage mechanism or the inhomogeneity of the plastic deformation could be the chemical composition, the volume fraction of the martensite phase, the yield stress ratio of the ferrite over martensite phase, the morphology of the martensite phase, i.e. the size, shape and distribution of the martensite phase [22].

Maire et al. [18] carried out in-situ tensile tests on a DP600 steel sheet with 11% martensite phase and concluded that damage is never observed in the ferrite phase, but both the martensite cracking and ferrite–martensite decohesion were observed. Recently, Kadkhodapour et al. [19; 20] carried out a set of interrupted uniaxial tensile tests and subsequent SEM analysis of a DP800 steel sheet with about 23% martensite, and revealed that the main void initiation pattern should be the ferrite–ferrite grain boundary decohesion. The different behaviour of the damage mechanism shown above is approximately in line with the observation by Ahmad et al. [17], that for dual-phase steels with low or intermediate martensite volume fraction, the void initiation mode is mainly ferrite–martensite interface decohesion, while with high volume fraction of the martensite phase, the ferrite–ferrite interface decohesion and martensite cracking are more dominant.

Other researchers have also confirmed that the ferrite–martensite decohesion is the main damage mechanism of DP steels [23–25]. However, the volume fraction of martensite is not the only factor that decides the preferred damage mechanism of DP steels. Erdogan [26] concluded that the morphology of the coarse and interconnected martensite along the ferrite grain boundaries can facilitate the martensite cracking. Avramovic-Cingara et al. [21] compared the damage mechanisms of two types of DP600 steels, and concluded that the void nucleation for the DP600 with the martensite bands at the centre line of the sheet thickness is caused by martensite cracking, ferrite–martensite interface decohesion and separation of the adjacent martensite grains, while the major void nucleation of the DP600 with uniformly distributed

martensite phase is ferrite–martensite interface decohesion. Calcagnotto et al. [27] showed that in dual-phase steels with coarse grains, the main damage mechanism is martensite cracking and the ferrite–martensite interface decohesion is the primary damage mechanism with ultra-fine grains.

## 2.3 Experimental damage evaluation

### 2.3.1 Change of macroscopic physical properties

#### 2.3.1.1 Direct current potential drop (DCPD) method

Fracture or macroscopic crack initiation is a local phenomenon, which is considered to be caused by the accumulation of damage within the material at the mesoscopic and microscopic level [28]. In the literature, there are generally two approaches for the identification of damage and/or fracture. The first one is observation by eye or DIC to detect the macro crack formation [29-35]. This method focuses on the local and macro crack formation, and gives a characteristic length of crack with an order of 0.1 mm. It is also limited on the surface of the specimens.

An alternative approach focuses on the detection of the critical amount of damage accumulation in terms of formation of voids and microcracks within the material. One often used strategy is to conduct interrupted tests combined with subsequent metallographic investigations [36; 37], which will be discussed in the following section. Despite the exact capture of the instant and location of the critical damage initiation, extensive effort is involved for testing and metallography. For this reason, another method, direct current potential drop (DCPD) method is developed. Muenstermann et al. [38] performed a comparison study on two methods for the detection of damage initiation, interrupted tests combined with metallography and DCPD method, by analysing the fracture mechanics characteristics of single-edge notched bending (SENB) tests. The result showed a good agreement between the interrupted tests method and DCPD method.

A schematic setup of experiments is demonstrated in Fig. 2.3. At the points (I, I'), a constant direct current is conducted to the specimen. The amperage is selected according to the material and the dimension of the specimen to avoid critical heating on the specimen. Plastic insulators are mounted on two sides of the specimen clamping systems to prevent current leakage. Two metal pins are welded onto two sides of the gauge section (V, V') and connected to a voltmeter to record the potential drop during the test.

As shown in Fig. 2.4 (a), the potential slightly increases at the beginning of the test due to the progressive reduction of the area of the cross section caused by the incremental loading. At a particular phase of the experiment, due to the appearance of severe discontinuity induced by the coalescence of voids or the formation of microcrack or shear bands, the electrical resistance/potential increases suddenly. This time instant is assumed as the onset of damage and the corresponding force as the critical load.

To correlate the response of current potential to the underlying damage mechanisms and identify the characteristic length of the damage identified by the method, a program involving interrupted tests in conjunction with subsequent metallographic investigations was performed [39]. Identical notched specimens were loaded to different forces in the vicinity of the critical force obtained from the DCPD method. The specimens were subsequently prepared for the metallographic investigation from the interrupted tests. The voids coalescence was not successfully observed from the light optical microscopy (LOM) until the specimen was loaded to the critical force. The micrograph at the damage initiation point is shown in Fig. 2.4 (b). As seen from the LOM graph, this method provides a detection of damage with the length scale of dozens of microns.

The main advantage of the method is its easy installation and proceeding to couple with the laboratorial experiment facility, though the quantitative correlation between the microscopic material behaviour and the macroscopic parameter that determines the damage still needs to be explicitly defined.

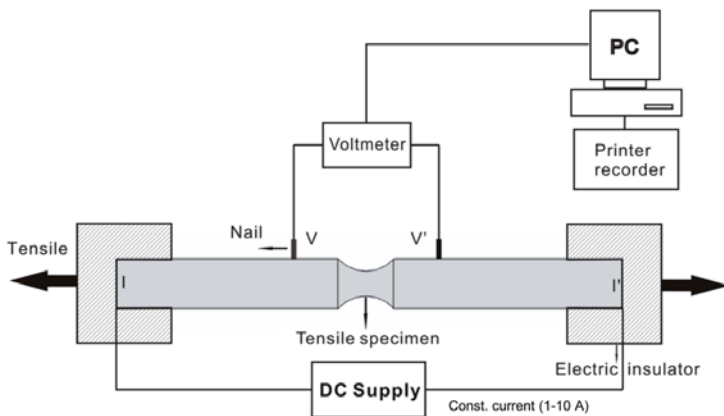


Fig. 2.3: Direct current potential drop method for the determination of damage initiation during tensile test.

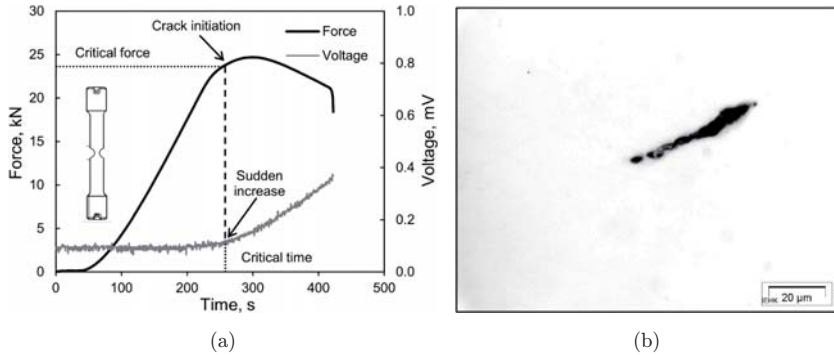


Fig. 2.4: (a) A plot of force and electric potential vs. time curves [39], (b) Micrograph of the occurrence of void coalescence at the damage initiation point [39].

### 2.3.1.2 Local temperature measurement

Local temperature measurement is widely used in fatigue tests to identify the onset of damage or crack initiation [40].

In the setup of the tensile test experiments, an isothermal chamber is used to prevent heat exchange between the specimen and the atmosphere. As shown in Fig. 2.5, three thermocouples are installed on the specimen to record the temperature history at the most deformed section. A temperature change is accordingly obtained according to the formula in Fig. 2.5. A schematic plot in Fig. 2.6 shows the temperature change and stress amplitude history in the test.

In this loading increasing test, as the number of cycles loaded on the specimen increases, the stress amplitude also increases incrementally. A sudden temperature increase after remaining zero for a period time is identified to correspond to the damage or crack initiation. Therefore, the corresponding number of cycles is also defined as the critical cycles at the given stress amplitude. The increase in temperature is caused by the heat produced at the beginning of the plastic deformation within the specimen.

The further development of the method in order to determine the onset of damage with monotonic loading is also an undergoing study. With the observation, especially in high-manganese steels, that a sudden temperature change is triggered at a certain point of increased monotonic loading, the correlation of damage and temperature is evident.

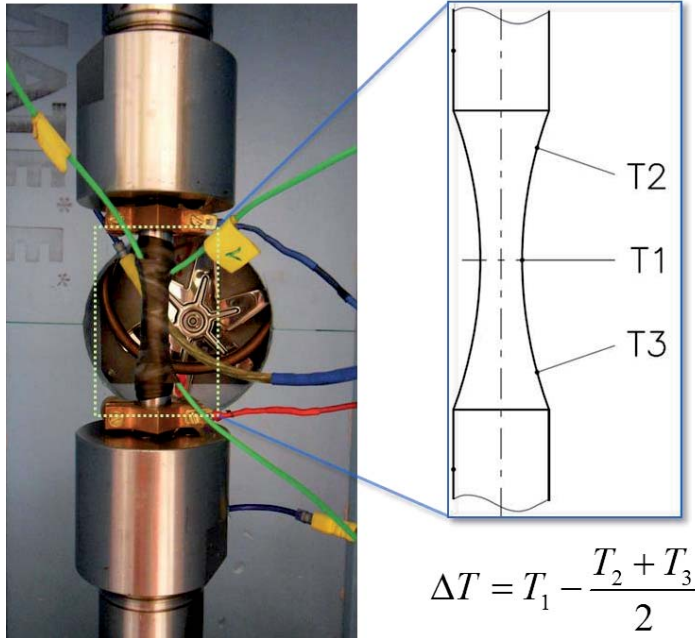


Fig. 2.5: Setup of the local temperature measurement for an uniaxial tensile test, modified from Kucharczyk et al. [41].

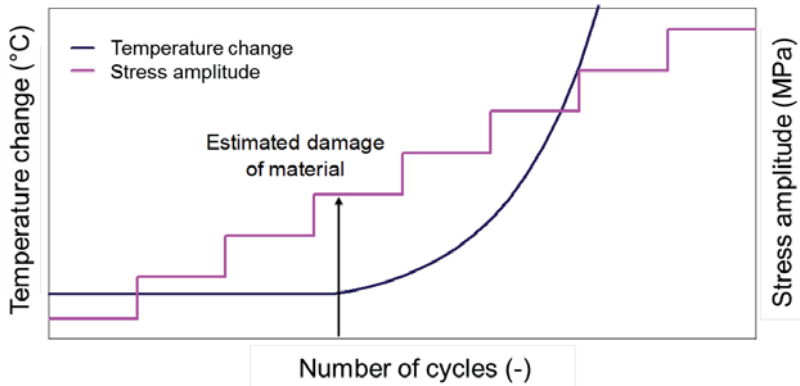


Fig. 2.6: Schematic drawing for temperature change and stress amplitude history with respect to the number of cycles, adapted from Kucharczyk et al. [41].

## 2.3.2 Changes in microscopic microstructural morphology

### 2.3.2.1 2D metallography

2D metallography is the most often used method to correlate macroscopic fracture to microscopic damage mechanisms. Generally there are two types of investigations according to the observation time and locations. The first one is the metallography after the fracture of specimens and on the fracture surface. It is also often referred to as fractography. The second one is to observe damage during the deformation, and it is often conducted by either interrupted tests or in situ tests. For the interrupted tests, initially, the test is run until fracture, and the fracture displacement and force are recorded. Subsequently, specimens with the same geometry are tested and interrupted at a stage earlier than the fracture. The relevant part of the specimen is cut off and analysed using relevant microscopies. The test is repeated with varying interrupted displacements or forces until the critical fracture phenomena are captured in the metallographs. This approach is easy to perform, but highly time and specimen consuming. On the contrary, for the in situ tests, the microstructural information and damage can be directly obtained during the deformation for one specimen. The often used instruments for observation are LOM, SEM and electron backscatter diffraction (EBSD). The formation of voids in observations via both SEM and EBSD is shown in Fig. 2.7. In Fig. 2.7 (a), the martensite island brittle cracking in a DP steel is captured by SEM [42]. In Fig. 2.7 (b), voids generated by the debonding of the martensite islands from the ferrite matrix in a DP steels is observed by EBSD in an in situ bending test [43].

### 2.3.2.2 X-ray tomography

Recently, using X-ray tomography with synchrotron radiation to measure ductile damage in metals has received significant interest [18; 44]. With its high resolution and well-established tomography software, different damage mechanisms and behaviour can be recognised and even quantified. This method was used by Maire et al. [18] with an in-situ tensile tests on a DP600 steel sheet with 11% martensite phase. The void initiation and evolution are successfully followed and quantified by the method in 3D.

In Fig. 2.8, the 3D representation of the population of voids inside the tensile test specimen is illustrated for the initial state before the deformation and the last stage just before final fracture. One can clearly observe that for this steel, there are significant amount of voids generated during the deformation.



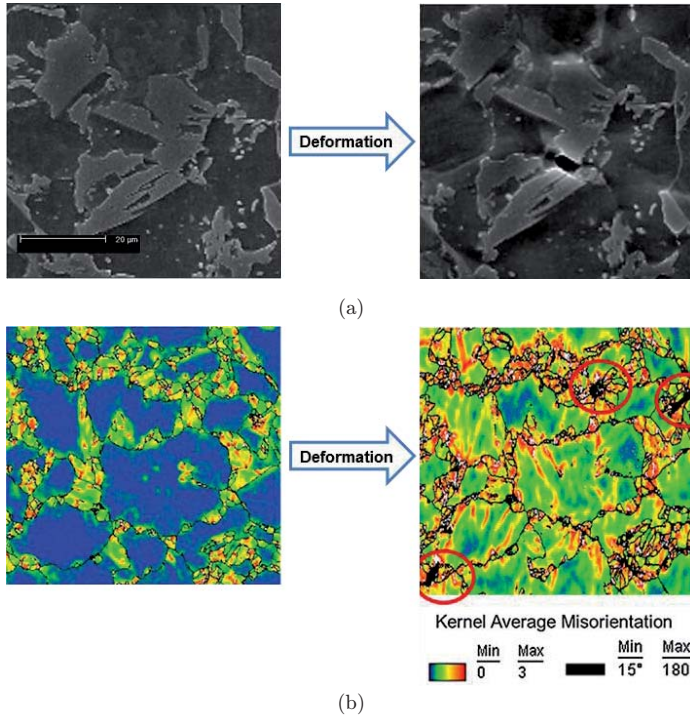


Fig. 2.7: Metallographs of void formation under the observation of (a) SEM for a DP steel, in which voids are generated by martensite cracking [42] and (b) EBSD for a DP steel, red circles indicating the initiated voids [43].

The measurements can also be analysed in terms of density, size, aspect ratio of the voids and these characteristic values are further correlated to the local deformation and the stress state. In the end, these findings can support to get more insights of the damage initiation and evolution and validate or improved the damage mechanics models.

## 2.4 Numerical damage evaluation

As shown in Fig. 2.9, damage models are generally classified into two branches based on the type of damage representation: surface or volume [45]. In the application of metals, the second group of damage models have been intensively developed and widely applied to the solution of practical problems in recent decades. They are normally used individually to perform macroscopic damage and fracture prediction for various applications, but recently they are also

used in parallel for, in particular, the microstructure based simulations. However, it is not the intention of the present thesis to give a comprehensive literature review on the different models and their various extensions. Instead, it attempts to summarise the main trends regarding these models and compare their capabilities in terms of their ease of formulation and parameter calibration, their major limitations and finally their correlation to the material microstructural features.

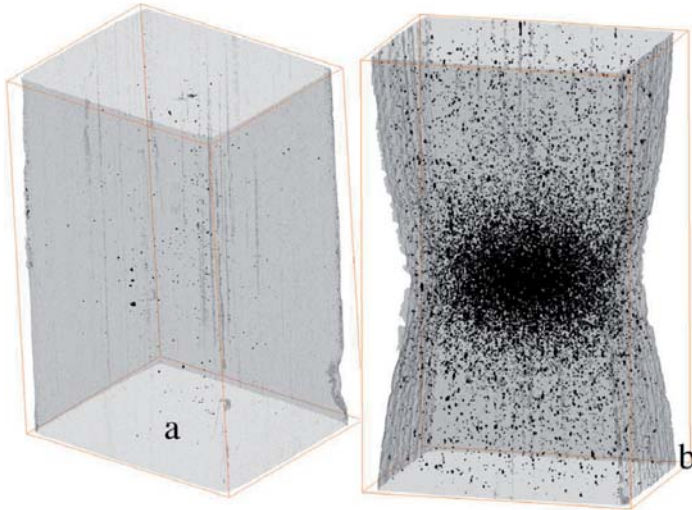


Fig. 2.8: 3-D representation of the population of cavities (indicated by black area) inside a deformed tensile test specimen of a DP steel investigated by 3D x-ray tomography at its initial state before straining (a) and the state just before fracture (b). The perspective view makes the insertion of a scale bar inappropriate. The dimension of the reconstructed block (indicated by the orange lines) is  $1 \text{ mm} \times 1 \text{ mm} \times 1.5 \text{ mm}$  [18].

### 2.4.1 Ductile damage modelling

In view of the interaction between damage and plasticity behaviour, the ductile damage mechanics models are classified into two groups: uncoupled and coupled [45; 46]. Uncoupled models usually define the critical loading conditions responsible for the appearance of either damage or failure. These include empirical models and void growth models. Coupled models take into account the effects of damage on the yield surface. These include porous plasticity models and continuum damage mechanics (CDM) models.

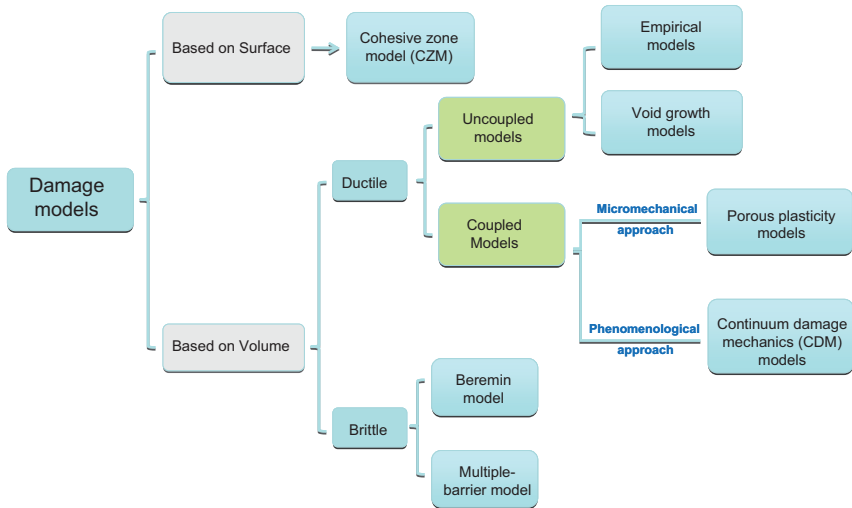


Fig. 2.9: Classification of damage models, inspired by Besson [45].

#### 2.4.1.1 Uncoupled damage mechanics models

##### Void growth models

Regarding the uncoupled models, the void growth model is the most direct approach to investigate void behaviour. As the process of ductile fracture is mainly void-controlled, to explicitly implement the voids into the FE model can physically reflect the process of damage. With the assumption of periodic boundary conditions, a unit cell model containing one void constructed in 2D or 3D is frequently used to calibrate the parameters for micromechanical models [47-50]. However, its application to the structural failure assessment is limited due to its explicit implementation of voids into the FE mesh and the subsequent size-dependence.

##### Empirical models

In empirical models, the critical loading condition responsible for the appearance of fracture is defined. The loading condition is normally characterised by a weighted function of equivalent plastic strain. The accumulation of damage or the equivalent plastic strain to fracture is independent on the plasticity behaviour. No damage-induced softening effect is taken into account in the material strength expression. Experimental evidence has shown that the equivalent plastic strain to fracture is strongly dependent on stress triaxiality, defined as the ratio of the mean stress over the equivalent stress [51-58]. It was also observed in the theoretical study of the growth of long cylindrical and spherical voids [59; 60]. There are various types of

empirical models developed based on this concept in the recent decades [57; 60-63]. In a commonly used empirical model, the Johnson–Cook (JC) model [57], the fracture strain  $\bar{\epsilon}_f$  takes the form with respect to stress triaxiality  $\eta$  that is shown in Eq. 2.1, in which  $C_1$ – $C_3$  are material parameters, when the influence of temperature and strain rate on ductility is excluded from consideration. It is also referred to as a ductile failure curve [36], as shown in Fig. 2.10 (a). Recently, it was realised that another variable, the Lode angle parameter, which is related to the third invariant of the deviatoric stress tensor, has an impact on ductile fracture [64-68]. A phenomenological formulation of the fracture strain with respect to stress triaxiality  $\eta$  and Lode angle parameter  $\bar{\theta}$  is presented in Eq. 2.2, where  $C_1$ – $C_6$  are material parameters, and it is also visualised for an application of an aluminium alloy in Fig. 2.10 (b) [64].

$$\bar{\epsilon}_f = C_1 e^{-C_2 \eta} + C_3 \quad \text{Eq. 2.1}$$

$$\bar{\epsilon}_f = \left[ \frac{1}{2} (C_1 e^{-C_2 \eta} + C_5 e^{-C_6 \eta}) - C_3 e^{-C_4 \eta} \right] \bar{\theta}^2 + \frac{1}{2} (C_1 e^{-C_2 \eta} - C_5 e^{-C_6 \eta}) + C_3 e^{-C_4 \eta} \quad \text{Eq. 2.2}$$

The parameter calibration of empirical models is straightforward due to the uncoupled fracture and plasticity, though an extensive experimental program must be carried out when stress triaxiality and the Lode angle parameter are both considered [62; 69-73].

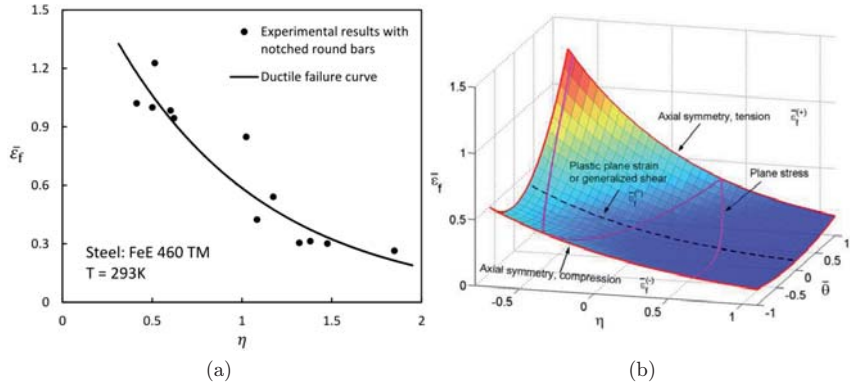


Fig. 2.10: (a) Ductile failure curve [36], (b) Ductile failure locus [64].

The empirical models are widely adopted in many applications due to their simple formulation and ease of calibration [74]. For example, the recent modified Mohr–Coulomb (MMC) criterion [68] has been also extended to account for anisotropic fracture [32; 75] and the post-initiation softening and crack propagation [76; 77]. On the other hand, the empirical models could lead

to inaccurate predictions of fractures in modern steels, such as the modern multiphase steels, in which damage evolution plays a significant role in the plastic deformation history [12]. In contrast to conventional ductile steels, the onset of damage and its evolution have received more critical attention than the occurrence of fracture in these steels. Consequently, the prediction of the onset of damage with empirical models should replace fracture prediction, and damage-induced softening must be introduced into material plasticity behaviour.

#### 2.4.1.2 Coupled damage mechanics models

##### CDM-based models (phenomenological approach)

CDM-based models take damage into account in material stress–strain response and treat damage evolution in a macroscopic and phenomenological way. The realistic material response is separated into two parts, a part based on perfect matrix behaviour and a part based on the softening of the matrix induced by damage. An internal variable  $D$  is introduced to phenomenologically quantify the extent of damage or material degradation. The fundamental theory was proposed by Kachanov [78] in the application of ductile creep. For ductile fracture, Lemaitre [28; 79] further developed the CDM model and defined the damage variable under the definition of the damage process as an irreversible process in a consistent thermodynamic framework. By introducing the dissipation potential  $\Psi$ , which consists of two components, the plasticity dissipation potential  $\Psi_p$  and damage dissipation potential  $\Psi_d$ , the evolution of the internal damage variable is defined in Eq. 2.3:

$$\dot{D} = -\dot{\gamma} \frac{\partial \Psi}{\partial Y} \quad \text{Eq. 2.3}$$

$Y$  is the elastic damage energy release rate, which is similarly defined as the stress intensity factor or J–integral in fracture mechanics [28], and  $\dot{\gamma}$  is the plastic multiplier. Once the accumulated damage variable  $D$  reaches a certain value,  $D_{cr}$ , fracture is predicted to occur.

CDM based models have been continuously developed and used in the metal society for damage and fracture prediction [28; 79–85]. Benefitting from the formation of the constitutive equations in the CDM models, the implementation of damage combined with kinematic hardening, anisotropy and the crack closure effect is relatively easy [86–92]. In the simplified Lemaitre model, considering only isotropic hardening and damage, only three damage parameters must be calibrated from the experiments, besides the true stress–strain curve. In CDM based models, the damage is naturally integrated into the material strength. The damage-induced softening takes place along with the plastic deformation. As a result, to determine the true stress–strain

curve from a uniaxial tensile test is not an easy task in uncoupled models [29]. Very often, it is obtained, together with the damage material parameters, by using an inverse method to calibrate the numerical result, e.g. the force–displacement response, in order to be as close as possible to the experimental results [83]. As an alternative, the unloading–reloading tensile test is also adapted to measure the damage variable via the resulting effective Young’s modulus [28; 79; 93]. However, the calibrated parameters at uniaxial tension fail to give a consistent prediction of failure in a broad stress state, due to the formation of the model [28; 83].

In addition, the macroscopic consideration of damage eases the formulation of the constitutive equations and the subsequent parameter calibration as compared to the micromechanical approach, but it neglects the microscopic damage mechanisms, such as the void nucleation, growth and coalescence as well as the formation of shear bands. With the different damage phenomena being dominated by different damage mechanisms in conventional ductile materials and AHSS, a sole macroscopic damage representation could lead to inaccuracy.

#### Porous plasticity models (micromechanical approach)

The micromechanical approach is addressed in the studies of McClintock [59] and Rice and Tracey [60] on the analytical derivation of the growth of cylindrical and spherical voids in a rigid plastic matrix. Gurson [94] developed the widely accepted porous plasticity model. The void volume fraction  $f$  was introduced as the damage indicator, and the damage-induced softening was taken into account in the yield potential in addition to the first and second stress invariants. To account for the void coalescence and nucleation, modifications were later introduced by Tvergaard [95; 96] and Tvergaard and Needleman [97] to form the complete Gurson–Tvergaard–Needleman (GTN) model. In this model, a modified void volume fraction  $f^*$  was used to characterise the accelerated damage process after the void volume fraction reaches the critical value,  $f_c$ . The yield function of the GTN is defined by

$$\Phi = \left( \frac{\bar{\sigma}}{\sigma_y} \right)^2 + 2q_1 f^* \cosh \left( \frac{3}{2} q_2 \frac{\sigma_H}{\sigma_y} \right) - (1 + q_3 f^{*2}) \quad \text{Eq. 2.4}$$

where:

- $\Phi$ : yield function,
- $\bar{\sigma}$ : Mises equivalent stress,
- $\sigma_H$ : invariant of the stress tensor,
- $\sigma_y$ : yield stress of the matrix material,

$q_1, q_2, q_3$ : fit parameter by Tvergaard and Needleman,  
 $f^*$ : modified damage parameter.

As the derivation of GTN model is based on the spherical voids in an axisymmetric stress state, it is limited in its application under low stress triaxiality and non-axisymmetric stress conditions, such as a plane strain or shear stress state. The Gologanu–Leblond–Devaux (GLD) model [98-100] was developed to account for the void shape changes and their effects on the yield potential. Other extensions [101; 102] were also proposed to characterize the void rotation effect. Recently, Xue [103] and Nahshon and Hutchinson [104] introduced the shearing effect into the void growth and coalescence expression to account for the Lode angle dependence. Further modifications of the GTN model on the shear effect were also introduced by Nielsen and Tvergaard [105; 106].

Numerous modifications and extensions give rise to the capabilities of the porous plasticity model. However, it also burdens the process of calibrating the parameters. Despite the increased number of materials parameters from the original nine in the GTN model, calibrating those mainly microscopic parameters is challenging to the micromechanical characterisation methods. Additionally, the identification of the large number of parameters is not direct; an iterative calibration procedure is normally employed to evaluate the mutual influence of the parameters [107]. The prediction of the calibrated parameters on the geometries that were not involved in the calibration procedure has not been proved to be satisfactory [108; 109]. Nevertheless, the correlation between some of the parameters and the material's microstructural features can provide a perspective that can help in designing the microstructure for damage tolerance [110; 111].

#### 2.4.2 Microstructure based modelling

In understanding the relation of the microstructural features and the mechanical properties of materials, in particular the relation between the plastic deformation and damage mechanisms in microstructural level and the macroscopic behaviour of plasticity and ductility, micromechanics based finite element models using the representative volume element (RVE) technique is typically employed. Based on the early studies by McClintock [59] and Rice and Tracey [60] on the analytical derivation of the growth of cylindrical and spherical voids in a rigid plastic matrix, a unit cell model incorporating a regular array of circular, cylindrical, spherical or elliptical inclusions representing voids or hard phase particles was developed [66; 107; 112-115]. In addition to the unit cell modelling, another approach of the RVE modelling

is based on the explicit description of material microstructure, generated either by real microstructure [7; 116-127] or statistically characterised synthetic microstructure [128-130]. The later approach received numerous attentions in the recent decade, in particular in the application of multiphase steels, where several failure mechanisms occur in parallel because of the different microstructure constituents.

According to the damage mechanisms addressed above, a straightforward implementation in the RVE is that different damage mechanisms, such as brittle fractures of the martensite phase as described by cleavage fracture stress criterion, brittle or ductile fractures due to the debonding of interfaces as described by the cohesive zone model or ductile fracture as described by the empirical or porous plasticity ductile damage models, are assigned and interacting with each other [7; 116-120; 131]. For the RVE modelling based on real material microstructure, the global and sub-modelling techniques is normally employed for the sake of numerical cost and upscaling of the microstructural features to macroscopic mechanical behaviour. As demonstrated in Fig. 2.11, in the simulation of, for example, notched tensile bar tests, hole expansion tests or Nakajima tests, the RVE can be attached locally in order to investigate the microscopic response under a macroscopic loading condition.

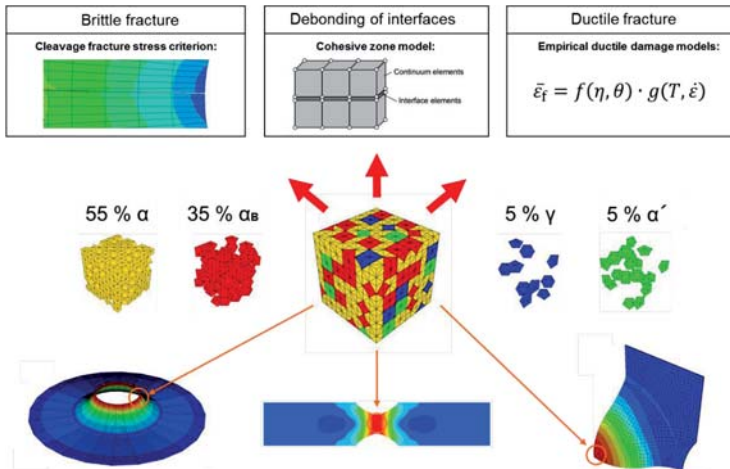


Fig. 2.11: Microstructure-based modelling by different damage models in a multiphase RVE model, enhanced from the dissertation of Uthaisangsuk [131].

Alternatively, Sun et al. [123; 124] developed a plastic deformation localisation theory for the prediction of failure modes and ultimate ductility of DP steels. The theory emphasised that



---

the microstructural-level inhomogeneity of deformation serves the sole source of the initial imperfection and triggers the instability of DP steels. In the RVE, no prescribed failure or damage models and imperfections are assigned, and the ductile failure and failure models are the nature outcome of the plastic strain localisation. Different from the previous one, this theory neglects the specific damage mechanisms possibly visible in the DP steels and addresses the significance of the plastic strain localisation due to the deformation incompatibility which is the ultimate source of different damage mechanisms. This approach has been applied in many different grades of DP steels [125-127; 132], and also extended to TRIP steels [133; 134].



# Chapter 3

## A generalised hybrid damage mechanics model

### 3.1 General introduction of the model

The goal of the generalised hybrid damage plasticity model is to form a *general* and *consistent approach* of ductile damage modelling that properly represents the new damage features of modern high strength steels. In this context, by taking the advantages of both uncoupled models (high accuracy and ease of formulation and material parameter calibration) and coupled models (integration of damage to material behaviour), the model is formulated in a *hybrid* way with three main constituents:

- A plasticity model to characterise the material behaviour before damage initiation.
- A phenomenological criterion to indicate the initiation of damage.
- A damage evolution law to characterise the macroscopic post-damage material behaviour to final fracture.

The whole damage process generally is not linear. The intention of introducing a damage initiation value followed by a linear damage evolution law is to approximate the nonlinear damage process. This concept can be visualized and proven by analysing Fig. 3.1 (a) and (b). They are both damage evolution measurements for a copper 99.9% [135] and a DP steel [136] by using the elastic degradation method and X-ray tomography, respectively. It can be seen from the comparison between the experimental measurement and the added red and blue lines consisting of a damage initiation and linear evolution law that the proposed concept gives a very good approximation of the damage process in reality for both materials. In literature, it is also assumed by several researchers that there exists a threshold value of the plastic strain, under

which damage is not accumulated [137; 138]. This value is normally a scalar constant calibrated based on the experiments. However, it is clearly shown in Fig. 3.1 (b) that the damage initiation strains are dependent on the stress states, as the two DP specimens with different geometries (indicating different stress triaxialities) show very different initiation strains of damage. Therefore, a general form of the damage initiation strain depending on stress triaxiality and Lode angle parameter is used in the proposed model.

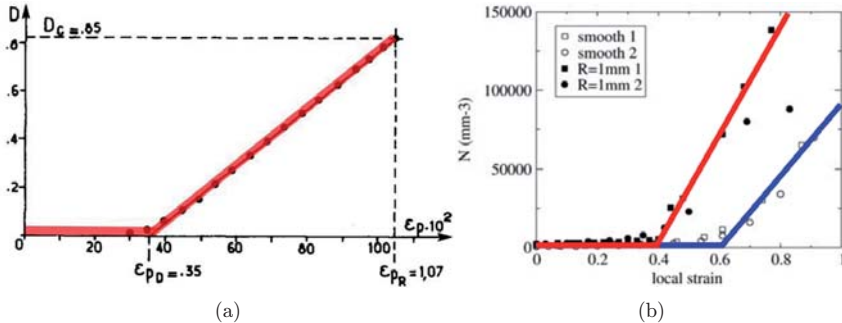


Fig. 3.1: (a) Ductile plastic damage of copper 99.9% (original Fig. 2 in Ref. [135] and the red line is added by the current author); (b) Measurement of the number density of cavities  $N$  as a function of the local strain for a DP steel by X-ray tomography (original Fig. 2 in Ref. [136] and the red and blue lines are added by the current author).

With the introduction of the damage initiation strain and a subsequent linear damage evolution law, the different relation patterns between plastic localisation, damage and fracture shown in Chapter 1 can be flexibly and accurately captured. In addition to reaching better fitting for the global force–displacement curve, the significance of the proposed concept is to enable a quantitative description of a critical phase of deformation which is closely related to the materials' microstructure. This critical phase has its relevance in practice. For the application of the model in component testing or production in industry, the damage initiation phase has more guiding significance than fracture, as it gives an indication of the forming limit. Beyond the damage initiation phase, although there is still room for further deformation, damage is large enough to influence the strength and toughness behaviour of the material. In this context, to predict the damage initiation is more beneficial than fracture to guide the manufacturing process for steel components. Furthermore, the damage initiation criterion has even more application potential in the material and/or structure design fields. Plastic yielding is conventionally taken as the loading limit to prevent failure in these fields. However, it

significantly underestimates the strength of the excellent strain hardening behaviour of the recent developed steels. By adopting the damage initiation criterion as a limit phase to present failure, it is on the one hand still within the safe margin, in particular for high strength steels and on the other hand could explore the potential of the mechanical properties of these steels and ultimately enable the light-weight design principle. The whole concept is also user-friendly for material parameter calibration, because the damage initiation strains can be experimentally measured and no iterative fitting is required. In addition, there is also only one parameter required to control the slope in the linear damage evolution law.

Rather than developing new highly non-linear equations for the description of the failure process, the current study focuses on providing a solution to predicting the failure process for different kinds of steels featuring different failure patterns with the following distinctions:

- **Simplicity and flexibility:** By simplifying the non-linear failure process to a piecewise linear configurations and emphasising the significance of damage initiation, the model enables a flexible description of various failure process patterns and a straightforward material parameter calibration strategy.
- **Practicability:** The introduction of the damage initiation criterion followed by a linear damage evolution promotes the application of the model in the fields of manufacturing and forming processes for components as well as the material and structure design processes with more guidance significance and potential to further explore the excellent mechanical properties of steels, respectively.
- **Microstructure-relativity:** Correlating the damage initiation with the material microstructure (details in Chapter 9) provides a physical understanding on the damage dependency on stress states and also allows the quantitative microstructure optimisation for more damage-tolerant steels.

The concept of the model formulation is schematically depicted in Fig. 3.2. A proper plasticity model is initially employed to characterise the stress–strain behaviour before the damage initiation. In this stage, the damage accumulation also remains zero. To indicate the moment when damage starts to play a role in the process, an empirical damage model is introduced. With a customised experimental method to measure the instant of damage initiation, the criterion here is not to indicate the final fracture ( $\bar{\epsilon}_f^p$ ) as it is normally adopted in the literature [29; 30; 64], but to characterise the initiation of damage ( $\bar{\epsilon}_i^p$ ). In the void-controlled ductile damage mechanism, it physically corresponds to the critical phase of the void coalescence that

leads to an accelerated damage accumulation rate, as is also emphasised in the GTN model as the critical void volume fracture,  $f_c$ .

Once the  $\bar{\epsilon}_1^p$  is triggered at the corresponding stress state, the deformation-induced damage becomes critical until the final fracture. To represent the damage-induced softening, a damage evolution law based on the energy dissipated during the damage progress is introduced. An internal parameter  $D$  characterises the accumulated damage, and a critical value of  $D$ ,  $D_{cr}$ , represents the final separation of the continuum material, i.e. fracture. From a local viewpoint, once the critical damage accumulation is reached of a material point/element, it also corresponds to the complete loss of the load carrying capacity. With this modelling approach, the multiscale characterisation of both damage and fracture can be realised and a quantitative representation of damage evolution can be obtained for the corresponding modelling processes. Owing to its hybrid character, the proposed model can be used in a hybrid way but also in individual way for necessary cases. For instance, the model can be used as a complete uncoupled model for the characterisation of fracture, if damage is not pronounced in the deformation of materials. On the other hand, the model can also be used as a completely coupled model for a continuous damage evolution from the beginning of the plastic deformation, which fits the application of porous materials.

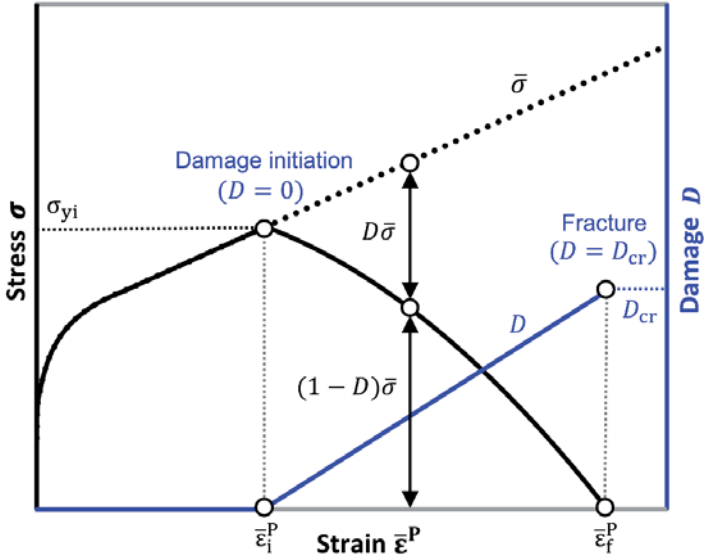


Fig. 3.2: Schematic illustration of the formulation of the proposed model.

The model framework is broad, and there are various choices for the three constituents, plasticity model, damage initiation criterion, and damage evolution law. In this thesis, we restrict ourselves on only *isotropic* material under *monotonic* loading, so only isotropic plasticity models, conventional J2 plasticity model and a non-quadratic plasticity model taking the third invariant of the deviatoric stress tensor into account are employed and incorporated to the isotropic hardening law. All the investigations also focus only on the *quasi-static* process, so the plasticity model formulation is rate-independent and temperature-insensitive. Furthermore, the influence of temperature and strain rate on the damage initiation and evolution is also not included in this study. For the damage initiation criterion, there are also various models existing, and the formulation proposed by Bai and Wierzbicki [64] for the failure strains is scaled down and embedded into a CDM based damage mechanics model theme for this study. Therefore, the current configuration of the model is also referred to as modified Bai-Wierzbicki (MBW) damage model.

In the following sections, the formulation and the numerical implementation of the model is introduced in detail. Before the introduction of the model, the characterisation of stress state by stress triaxiality and Lode angle is presented in section 3.2.1. The constitutive equations of the model with the J2/Mises plasticity are introduced in section 3.2.2, followed by its numerical implementation in Abaqus/Explicit. The model is further extended to cope with a more advanced plasticity mode that account for the Lode angle effect on yielding and hardening in section 3.2.4. The flow rule and the convexity condition of the plasticity model are also given in detail.

## 3.2 Formulation of the model

### 3.2.1 Characterization of stress state

For a certain stress state, the stress tensor  $\boldsymbol{\sigma}$  can be expressed by spherical and deviatoric parts:

$$\boldsymbol{\sigma} = \mathbf{s} + p\mathbf{I} \tag{Eq. 3.1}$$

where  $\mathbf{s}$  is the deviatoric stress tensor,  $\mathbf{I}$  is the identity tensor,  $p$  is hydrostatic pressure related to the mean stress  $\sigma_m$

$$p = \sigma_m = \frac{1}{3}\text{tr}[\boldsymbol{\sigma}] \tag{Eq. 3.2}$$

The three main invariants of the stress tensor and its deviatoric part are defined as follows:

$$I_1 = \text{tr}[\boldsymbol{\sigma}] \quad \text{Eq. 3.3}$$

$$J_2 = \frac{1}{2} \mathbf{s} : \mathbf{s} \quad \text{Eq. 3.4}$$

$$J_3 = \det(\mathbf{s}) = \frac{1}{3} (\mathbf{s} \cdot \mathbf{s}) : \mathbf{s} \quad \text{Eq. 3.5}$$

The Mises equivalent stress is also defined with respect to  $J_2$ :

$$\bar{\sigma} = \sqrt{3J_2} = \sqrt{\frac{3}{2} \mathbf{s} : \mathbf{s}} = \sqrt{\frac{3}{2}} \|\mathbf{s}\| \quad \text{Eq. 3.6}$$

A stress state can be presented in the space of three principal stresses by a point of P  $(\sigma_1, \sigma_2, \sigma_3)$  as shown in Fig. 3.3. In the same figure, it can also be expressed in the Haigh-Westergaard space by  $(\xi, \rho, \theta)$ , where  $\xi$  corresponds to the distance of the origin and the deviatoric plane that stress state P is located,  $\rho$  is the projection of OP in the deviatoric plane and  $\theta$  represents the angle between the projection of OP and the  $\sigma_1$  axis in the deviatoric plane. This angle is also referred to as the Lode angle. All the components are expressed by the three invariants as following:

$$\xi = \sqrt{3}I_1 \quad \text{Eq. 3.7}$$

$$\rho = \sqrt{2J_2} \quad \text{Eq. 3.8}$$

$$\cos 3\theta = \frac{3\sqrt{3}}{2} \frac{J_3}{J_2^{3/2}} \quad \text{Eq. 3.9}$$

where the Lode angle  $\theta$  is in the range of  $0 \leq \theta \leq \pi/3$ . Consequently, two dimensionless parameters, stress triaxiality and Lode angle parameter are defined:

$$\eta = \frac{\sigma_m}{\bar{\sigma}} = \frac{I_1}{3\sqrt{3}J_2} \quad \text{Eq. 3.10}$$

$$\bar{\theta} = 1 - \frac{2}{\pi} \cos^{-1} \left( \frac{3\sqrt{3}}{2} \frac{J_3}{J_2^{3/2}} \right) \quad \text{Eq. 3.11}$$

where stress triaxiality  $\eta$  is defined by the ratio of the mean stress over the Mises equivalent stress, while the Lode angle parameter  $\bar{\theta}$  is the normalised Lode angle, which has a range of  $-1 \leq \bar{\theta} \leq 1$ . Therefore, any stress state can be represented by the combination of these two dimensionless parameters.



Under the condition of plane stress, the Lode angle parameters can be related to stress triaxiality by the following equation [64]:

$$\bar{\theta} = 1 - \frac{2}{\pi} \arccos \left[ \frac{27}{2} \eta \left( \eta^2 - \frac{1}{3} \right) \right] \quad \text{Eq. 3.12}$$

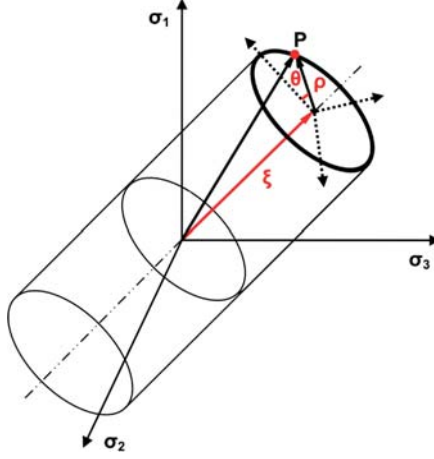


Fig. 3.3: Geometric representation of a stress state in the space of principal stresses and Haigh-Westergaard space.

### 3.2.2 Constitutive equations of the model

The model is formulated in the range of small strains, where the additive strain decomposition is used. The total strain rate of the solid materials is decomposed into elastic and plastic parts:

$$\dot{\boldsymbol{\epsilon}} = \dot{\boldsymbol{\epsilon}}^e + \dot{\boldsymbol{\epsilon}}^p \quad \text{Eq. 3.13}$$

Based on the definition of damage and strain equivalence hypothesis [28], damage causes both the stiffness degradation, and the flow curve softening. Progressive degradation of material stiffness can be represented by the weakening of Young' s modulus

$$E = (1 - D)E_0 \quad \text{Eq. 3.14}$$

where  $E_0$  is the original Young' s modulus for undamaged material and  $E$  is its degraded result. Consequently, stress deviator,  $\mathbf{s}$ , and the hydrostatic stress,  $p$ , are defined as below:

$$\mathbf{s} = (1 - D)2G_0\boldsymbol{\epsilon}_d^e; \quad p = (1 - D)K_0\epsilon_v^e \quad \text{Eq. 3.15}$$

where  $\boldsymbol{\varepsilon}_d^e$  is the elastic strain deviator and  $\varepsilon_v^e \equiv \text{tr}[\boldsymbol{\varepsilon}^e]$  is the elastic volumetric strain;  $G_0$  and  $K_0$  are, respectively, the original shear modulus and bulk modulus of the undamaged material, defined by:

$$G_0 = \frac{E_0}{2(1 + \nu)}; K_0 = \frac{E_0}{3(1 - 2\nu)} \quad \text{Eq. 3.16}$$

where  $\nu$  is the Poisson's ratio.

### Plasticity model

The hypothesis of strain equivalence by Lemaitre [28; 79; 135] is the foundation of the model formulation. Taking the Mises plasticity model, the yield function coupled with damage is expressed as:

$$\Phi = \bar{\sigma} - (1 - D)\sigma_y(\bar{\varepsilon}^p) \leq 0 \quad \text{Eq. 3.17}$$

where  $\sigma_y(\bar{\varepsilon}^p)$  is the yield stress, i.e. the actual size of the yield surface curve for undamaged material function of the equivalent plastic strain, and  $\bar{\sigma}$  is the Mises equivalent stress. It is noted that the damage induced softening part is only valid once the damage initiation criterion is met. Accordingly the conventional associated flow rule is applied to the present plasticity model.

$$\dot{\boldsymbol{\varepsilon}}^p = \dot{\gamma} \frac{\partial \Phi}{\partial \boldsymbol{\sigma}} = \dot{\gamma} \frac{3}{2} \frac{\boldsymbol{s}}{\|\boldsymbol{s}\|} \quad \text{Eq. 3.18}$$

where  $\dot{\boldsymbol{\varepsilon}}^p$  represents the plastic strain rate components and  $\dot{\gamma}$  is the plastic multiplier, which is subjected to for the loading and unloading conditions:

$$\dot{\gamma} \geq 0; \Phi \leq 0; \dot{\gamma}\Phi = 0 \quad \text{Eq. 3.19}$$

Based on the definition of the equivalent plastic strain rate,  $\dot{\bar{\varepsilon}}^p = \sqrt{2/3} \|\dot{\boldsymbol{\varepsilon}}^p\|$ , and  $\dot{\gamma}$  is therefore the same as  $\dot{\bar{\varepsilon}}^p$ .

### Damage initiation criterion

As shown in Fig. 3.2, it is assumed that a critical equivalent plastic strain,  $\bar{\varepsilon}_1^p$ , has to be applied to provoke damage initiation. Inspired by the fracture strain of the original BW model, the damage initiation strain of the MBW model is defined as a function of stress triaxiality and Lode angle parameter. Furthermore, the damage initiation strain is assumed to be symmetric with respect to the Lode angle parameter showing the lowest values for  $\bar{\theta} = 0$ . Likewise, only

four material parameters,  $C_1 - C_4$ , need to be calibrated to define the damage initiation locus (DIL) according to the following equation:

$$\bar{\varepsilon}_1^{\text{P}} = [C_1 e^{-C_2 \eta} - C_3 e^{-C_4 \eta}] \bar{\theta}^2 + C_3 e^{-C_4 \eta} \quad \text{Eq. 3.20}$$

### Damage evolution law

After the initiation of damage, isotropic damage evolution is assumed and the effect of damage in materials is shown in terms of stiffness degradation and stress–strain curve softening, as shown in Fig. 3.2. A dissipation-energy-based damage evolution law applied in finite element (FE) code [139] is adopted. This concept has already been used by Hillerborg as fracture energy model for brittle fracture [140]. As strain softening occurs, a strong mesh dependency can be caused due to the strain localisation. By defining a specific energy to open a unit area of crack,  $G_{\text{f}}$ , as a material parameter, the mesh dependency is therefore reduced by creating a stress–displacement response after the damage is initiated. Defining  $L$  as the characteristic length associated with an integration point to reduce the mesh dependency in the finite element model, the fracture energy is given as:

$$G_{\text{f}} = \int_{\bar{\varepsilon}_1^{\text{P}}}^{\bar{\varepsilon}_{\text{f}}^{\text{P}}} L \sigma_{\text{y}_i} d\bar{\varepsilon}^{\text{P}} \quad \text{Eq. 3.21}$$

where  $\bar{\varepsilon}_{\text{f}}^{\text{P}}$  is the equivalent plastic strain to fracture, and  $\sigma_{\text{y}_i}$  is the yield stress when the damage initiation criterion is met, as shown in Fig. 3.2. It is noted that the presented approach is a more engineering solution, which can be easily implemented and effectively reduces the mesh dependency in terms of force–displacement response. A more generalised and fundamental approach to reduce the mesh dependency is based on the non-local formulation of damage models [141–143].

Assuming a linear damage evolution with respect to the equivalent plastic strain, the damage evolution rate is defined by:

$$\dot{D} = \frac{\sigma_{\text{y}_i} L}{2G_{\text{f}}} \dot{\bar{\varepsilon}}^{\text{P}} \quad \text{Eq. 3.22}$$

As shown in Fig. 3.2, the final fracture is reached when the damage  $D$  is accumulated to a critical value  $D_{\text{cr}}$ .

$$D_{\text{cr}} = \int_{\bar{\varepsilon}_1^{\text{P}}}^{\bar{\varepsilon}_{\text{f}}^{\text{P}}} \frac{\sigma_{\text{y}_i} L}{2G_{\text{f}}} d\bar{\varepsilon}^{\text{P}} \quad \text{Eq. 3.23}$$

The easiest criterion for the determination of  $D_{cr}$  would be to let  $D$  reach one, so that the stress is automatically zero. However, there is also the case that one is not reached and the material has already lost its complete load carrying capacity. In that case,  $D_{cr}$  is a material parameter to be calibrated.

Depending on the loading process,  $D$  is consequently distributed in the following range:

$$D = \begin{cases} 0; & \bar{\varepsilon}^p \leq \bar{\varepsilon}_1^p \\ \int_{\bar{\varepsilon}_1^p}^{\bar{\varepsilon}^p} \frac{\sigma_{yi}L}{2G_f} d\bar{\varepsilon}^p; & \bar{\varepsilon}_1^p < \bar{\varepsilon}^p < \bar{\varepsilon}_f^p \\ D_{cr}; & \bar{\varepsilon}_f^p \leq \bar{\varepsilon}^p \end{cases} \quad \text{Eq. 3.24}$$

The key constitutive equations of the model are summarised in Box. 1 and the corresponding material parameters are listed in Tab. 3.1

**a. Elastoplastic split of total strain.**

$$\boldsymbol{\varepsilon} = \boldsymbol{\varepsilon}^e + \boldsymbol{\varepsilon}^p$$

**b. Coupled elastic-damage law.**

$$\boldsymbol{\sigma} = (1 - D)\mathbf{C}^e : \boldsymbol{\varepsilon}^e$$

**c. Yield criterion.**

$$\Phi = \bar{\sigma} - (1 - D)\sigma_y(\bar{\varepsilon}^p)$$

**d. Damage initiation criterion.**

$$\bar{\varepsilon}_1^p = [C_1 e^{-C_2 \eta} - C_3 e^{-C_4 \eta}] \bar{\theta}^2 + C_3 e^{-C_4 \eta}$$

**e. Plastic flow and damage evolution.**

$$\dot{\boldsymbol{\varepsilon}}^p = \dot{\gamma} \frac{\partial \Phi}{\partial \boldsymbol{\sigma}} = \dot{\gamma} \sqrt{\frac{3}{2} \frac{\mathbf{s}}{\|\mathbf{s}\|}}$$

$$\dot{D} = \frac{\sigma_{yi}L}{2G_f} \dot{\gamma}$$

**f. Damage accumulation.**

$$D = \begin{cases} 0; & \bar{\varepsilon}^p \leq \bar{\varepsilon}_1^p \\ \int_{\bar{\varepsilon}_1^p}^{\bar{\varepsilon}^p} \frac{\sigma_{yi}L}{2G_f} d\bar{\varepsilon}^p; & \bar{\varepsilon}_1^p < \bar{\varepsilon}^p < \bar{\varepsilon}_f^p \\ D_{cr}; & \bar{\varepsilon}_f^p \leq \bar{\varepsilon}^p \end{cases}$$

**g. Loading/Unloading condition.**

$$\dot{\gamma} \geq 0; \Phi \leq 0; \dot{\gamma}\Phi = 0$$

Box 1: Summary of the key constitutive equations for the MBW damage model.

Tab. 3.1: Summary of all the material parameters in the MBW model with J2 plasticity model.

Material parameter	Description
$\sigma_y(\bar{\epsilon}^p)$	Flow curve
$C_1$ - $C_4$	Damage initiation locus parameters
$G_f$	Specific energy to open a unit area of crack
$D_{cr}$	Critical damage parameter

### 3.2.3 Numerical implementation algorithm

The MBW model in cooperation with Mises plasticity model presented in this study is implemented into Abaqus/Explicit as a VUMAT using a fully implicit backward Euler integration scheme. The classical elastic predictor/plastic corrector (return mapping) scheme is adopted to numerically integrate the constitutive equations of the MBW damage model. For the detailed introduction of such methodology, the readers are referred to de Souza Neto et al. [144].

In the finite element context, for a typical Gauss point during a (pseudo-) time interval  $[t_n, t_{n+1}]$ , the values of  $\boldsymbol{\sigma}_n$ ,  $\boldsymbol{\epsilon}_n^p$  and  $D_n$  at  $t_n$  are known and a strain increment  $\Delta \boldsymbol{\epsilon}$  is given to be loaded within the time interval. The variables at  $t_{n+1}$ ,  $\boldsymbol{\sigma}_{n+1}$ ,  $\boldsymbol{\epsilon}_{n+1}^p$  and  $D_{n+1}$ , are required to be updated by the numerical integration algorithm.

#### 3.2.3.1 The elastic prediction

Considering the total strain increment  $\Delta \boldsymbol{\epsilon}$  given at the beginning of each step fully elastic, the elastic trial strain, trial equivalent plastic strain and the trial damage variable are given by

$$\begin{aligned}
 \boldsymbol{\epsilon}_{n+1}^{e \text{ trial}} &= \boldsymbol{\epsilon}_n^e + \Delta \boldsymbol{\epsilon} \\
 \bar{\epsilon}_{n+1}^{p, \text{ trial}} &= \bar{\epsilon}_n^p \\
 D_{n+1}^{\text{trial}} &= D_n.
 \end{aligned}
 \tag{Eq. 3.25}$$

Therefore the trial deviatoric/hydrostatic part of stress tensor is computed as

$$\begin{aligned}
 \mathbf{s}_{n+1}^{\text{trial}} &= (1 - D_n) 2G_0 \boldsymbol{\epsilon}_{d \ n+1}^{e \text{ trial}} \\
 p_{n+1}^{\text{trial}} &= (1 - D_n) K_0 \boldsymbol{\epsilon}_{d \ n+1}^{e \text{ trial}},
 \end{aligned}
 \tag{Eq. 3.26}$$

where the trial deviatoric and volumetric elastic strain are calculated by

$$\begin{aligned}\boldsymbol{\varepsilon}_{d\,n+1}^e \text{ trial} &= \boldsymbol{\varepsilon}_{n+1}^e \text{ trial} - \frac{1}{3} \varepsilon_{v\,n+1}^e \text{ trial} \mathbf{I} \\ \varepsilon_{v\,n+1}^e \text{ trial} &= \text{tr}(\boldsymbol{\varepsilon}_{n+1}^e \text{ trial}).\end{aligned}\tag{Eq. 3.27}$$

Thus, the corresponding trial yield function is obtained as

$$\Phi^{\text{trial}} = \bar{\sigma}_{n+1}^{\text{trial}} - (1 - D_n) \sigma_y(\bar{\varepsilon}_n^{\text{p}})\tag{Eq. 3.28}$$

where the trial equivalent stress is defined as

$$\bar{\sigma}_{n+1}^{\text{trial}} = \sqrt{3J_2(\mathbf{s}_{n+1}^{\text{trial}})} = \sqrt{\frac{3}{2} \|\mathbf{s}_{n+1}^{\text{trial}}\|}\tag{Eq. 3.29}$$

If  $\Phi^{\text{trial}} \leq 0$ , it means there is no plastic deformation and thus the corresponding stress and state variables are updated as their trial values:

$$\begin{aligned}\boldsymbol{\sigma}_{n+1} &= \mathbf{s}_{n+1}^{\text{trial}} + p^{\text{trial}} \mathbf{I} \\ \bar{\varepsilon}_{n+1}^{\text{p}} &= \bar{\varepsilon}_{n+1}^{\text{p trial}} \\ D_{n+1} &= D_{n+1}^{\text{trial}}.\end{aligned}\tag{Eq. 3.30}$$

Otherwise, the process is elastoplastic and the plastic corrector/return mapping step should be applied to compute the plastic strain part, the correct stress and state variables.

### 3.2.3.2 The plastic correction

The elastic strain tensor  $\boldsymbol{\varepsilon}_{n+1}^e$ , equivalent plastic strain  $\bar{\varepsilon}_{n+1}^{\text{p}}$  and damage variable  $D_{n+1}$  must be integrated numerically by using a standard backward Euler approximation. Therefore, the three key values become

$$\begin{aligned}\boldsymbol{\varepsilon}_{n+1}^e &= \boldsymbol{\varepsilon}_{n+1}^e \text{ trial} - \boldsymbol{\varepsilon}_{n+1}^{\text{p}} = \boldsymbol{\varepsilon}_{n+1}^e \text{ trial} - \Delta\gamma \sqrt{\frac{3}{2} \frac{\mathbf{s}_{n+1}}{\|\mathbf{s}_{n+1}\|}} \\ \bar{\varepsilon}_{n+1}^{\text{p}} &= \bar{\varepsilon}_n^{\text{p}} + \Delta\gamma \\ D_{n+1} &= D_n + \frac{\sigma_{y0} L}{2G_f} \Delta\gamma\end{aligned}\tag{Eq. 3.31}$$

The above equations must be complemented by the consistency condition which guarantees that the stress state at the end of plastic step lies on the updated yield surface. It is mathematically expressed as

$$\Phi_{n+1} = \bar{\sigma}_{n+1} - (1 - D_{n+1}) \sigma_y(\bar{\varepsilon}_{n+1}^{\text{p}}) = 0\tag{Eq. 3.32}$$

To solve all the unknowns, the system of equations are simplified. Considering the deviatoric/volumetric split in step  $n+1$ , because of the plastic incompressibility, the volumetric strain can be updated as its trial value and thus the corresponding deviatoric split can be also obtained from Eq. 3.27,

$$\begin{aligned}\varepsilon_{v\ n+1}^e &= \varepsilon_{v\ n+1}^{e\ \text{trial}} \\ \boldsymbol{\varepsilon}_{d\ n+1}^e &= \boldsymbol{\varepsilon}_{d\ n+1}^{e\ \text{trial}} - \Delta\gamma \sqrt{\frac{3}{2}} \frac{\mathbf{s}_{n+1}}{\|\mathbf{s}_{n+1}\|}.\end{aligned}\quad \text{Eq. 3.33}$$

With the update of the volumetric strain in step  $n+1$ , the hydrostatic pressure is also obtained as

$$p_{n+1} = (1 - D_{n+1})K_0\varepsilon_{v\ n+1}^e \quad \text{Eq. 3.34}$$

In terms of the deviatoric stress, it is obtained as

$$\mathbf{s}_{n+1} = (1 - D_{n+1})2G_0\boldsymbol{\varepsilon}_{d\ n+1}^{e\ \text{trial}} - (1 - D_{n+1})2G_0\Delta\gamma \sqrt{\frac{3}{2}} \frac{\mathbf{s}_{n+1}}{\|\mathbf{s}_{n+1}\|}.\quad \text{Eq. 3.35}$$

By further simplification, the updating equation for the stress deviator is given by

$$\mathbf{s}_{n+1} = \frac{1 - D_{n+1}}{1 - D_n} \mathbf{s}_{n+1}^{\text{trial}} - (1 - D_{n+1})2G_0\Delta\gamma \sqrt{\frac{3}{2}} \frac{\mathbf{s}_{n+1}}{\|\mathbf{s}_{n+1}\|}.\quad \text{Eq. 3.36}$$

From Eq. 3.36, it is clear that  $\mathbf{s}_{n+1}^{\text{trial}}$  is proportional to  $\mathbf{s}_{n+1}$ , so that it may be equivalently written as

$$\mathbf{s}_{n+1} = (1 - D_{n+1}) \left( \frac{1}{1 - D_n} - \frac{3G_0\Delta\gamma}{\bar{\sigma}_{n+1}^{\text{trial}}} \right) \mathbf{s}_{n+1}^{\text{trial}}.\quad \text{Eq. 3.37}$$

From the last expression and the definition of the Mises equivalent stress, we obtain

$$\bar{\sigma}_{n+1} = (1 - D_{n+1}) \left( \frac{1}{1 - D_n} \bar{\sigma}_{n+1}^{\text{trial}} - 3G_0\Delta\gamma \right).\quad \text{Eq. 3.38}$$

Thus, taking Eq. 3.31<sub>(2)</sub> and Eq. 3.38 to the consistency equation in step  $n+1$ , it is converted to

$$\Phi_{n+1} = \frac{1}{1 - D_n} \bar{\sigma}_{n+1}^{\text{trial}} - 3G_0\Delta\gamma - \sigma_y(\bar{\varepsilon}_n^p + \Delta\gamma) = 0.\quad \text{Eq. 3.39}$$

It is clear that the system of equations of the return mapping algorithm of the MBW damage model is now reduced to one nonlinear equation with the only unknown  $\Delta\gamma$ . With  $\Delta\gamma$  at hand,

all the stresses and the state variables are updated. From the above equation, the damage effect only exists in the  $\bar{\sigma}_{n+1}^{\text{trial}}$  part. Inserting Eq. 3.26<sub>(1)</sub> and Eq. 3.29, it is replaced by

$$\Phi_{n+1} = \sqrt{6}G_0 \|\boldsymbol{\varepsilon}_{d\,n+1}^{\text{trial}}\| - 3G_0\Delta\gamma - \sigma_y(\bar{\boldsymbol{\varepsilon}}_n^{\text{p}} + \Delta\gamma) = 0. \quad \text{Eq. 3.40}$$

It is noted that there is no effect of damage in the above equation, and the solution of the unknown  $\Delta\gamma$  is the same as the classical Mises plasticity. The reason for this lies in the fact that in the current configuration of the MBW model, it is not only the stress–strain curve is softened by the damage effect, but also the elastic modulus is reduced by the same amount. To solve the above nonlinear equation, an iterative scheme using Newton–Raphson method is applied. It is also noted that the only nonlinearity of the equation is from the nonlinear nature of the stress–strain curve. However, in the process of the application of the stress–strain curve, it is often assumed to be piecewise linear with sufficiently large number of pairs of stress and strain values, because the direct measured stress–strain curve from experiments is formatted in a discrete way. With the linear approximation, the stress–strain curve can be correspondingly converted to

$$\sigma_y(\bar{\boldsymbol{\varepsilon}}_n^{\text{p}} + \Delta\gamma) = \sigma_y(\bar{\boldsymbol{\varepsilon}}_n^{\text{p}}) + H\Delta\gamma, \quad \text{Eq. 3.41}$$

where  $H$  is the hardening modulus calculated by interpolation of two adjacent data points in the measured stress–strain curve. Therefore, the unknown  $\Delta\gamma$  can be simply solved in a closed form.

$$\Delta\gamma = \frac{\sqrt{6}G_0 \|\boldsymbol{\varepsilon}_{d\,n+1}^{\text{trial}}\| - \sigma_y(\bar{\boldsymbol{\varepsilon}}_n^{\text{p}})}{3G_0 + H} \quad \text{Eq. 3.42}$$

The closed form solution of the plastic multiplier would be adequately approximate the solution in the required tolerance and absolutely improve the computational efficiency, especially when a large amount of elements are discretized in the FE model. Correspondingly, all the stresses and the state variables are updated

$$\boldsymbol{\sigma}_{n+1} = \boldsymbol{s}_{n+1} + p_{n+1}\mathbf{I}. \quad \text{Eq. 3.43}$$

### 3.2.3.3 Summary of numerical implementation algorithm

The implicit elastic predictor/return mapping algorithm for the MBW damage model is summarised in the following box.



- a. **Elastic predictor.** Calculate the *trial stress and state variables* using the given incremental strain  $\Delta \boldsymbol{\varepsilon}$  and the state variables of step  $n$  at the beginning of the step:

$$\boldsymbol{\varepsilon}_{n+1}^{\text{e trial}} = \boldsymbol{\varepsilon}_n^{\text{e}} + \Delta \boldsymbol{\varepsilon}$$

$$\bar{\varepsilon}_{n+1}^{\text{p,trial}} = \bar{\varepsilon}_n^{\text{p}}, \quad D_{n+1}^{\text{trial}} = D_n$$

$$\mathbf{s}_{n+1}^{\text{trial}} = (1 - D_n) 2G_0 \boldsymbol{\varepsilon}_{n+1}^{\text{e trial}}$$

$$p_{n+1}^{\text{trial}} = (1 - D_n) K_0 \varepsilon_{d,n+1}^{\text{e trial}}$$

$$\bar{\sigma}_{n+1}^{\text{trial}} = \sqrt{\frac{3}{2}} \|\mathbf{s}_{n+1}^{\text{trial}}\|$$

- b. **Check yielding.**

$$\text{IF } \Phi^{\text{trial}} = \bar{\sigma}_{n+1}^{\text{trial}} - (1 - D_n) \sigma_y(\bar{\varepsilon}_{n+1}^{\text{p trial}}) \leq 0$$

$$\text{THEN set } (\cdot)_{n+1} = (\cdot)_{n+1}^{\text{trial}} \text{ and EXIT}$$

- c. **Return mapping.** Solve the following equation for  $\Delta \gamma$  using the *Newton-Raphson method* or the *closed-form* equation:

$$\Phi_{n+1} = \frac{1}{1 - D_n} \bar{\sigma}_{n+1}^{\text{trial}} - 3G_0 \Delta \gamma - \sigma_y(\bar{\varepsilon}_n^{\text{p}} + \Delta \gamma) = 0$$

- d. **Update the stress and the state variables**

$$\bar{\varepsilon}_{n+1}^{\text{p}} = \bar{\varepsilon}_n^{\text{p}} + \Delta \gamma$$

$$D_{n+1} = D_n + \frac{\sigma_{y0} L}{2G_f} \Delta \gamma$$

$$\mathbf{s}_{n+1} = (1 - D_{n+1}) \left( \frac{1}{1 - D_n} - \frac{3G_0 \Delta \gamma}{\bar{\sigma}_{n+1}^{\text{trial}}} \right) \mathbf{s}_{n+1}^{\text{trial}}$$

$$p_{n+1} = (1 - D_{n+1}) K_0 \varepsilon_{v,n+1}^{\text{e}}$$

$$\boldsymbol{\sigma}_{n+1} = \mathbf{s}_{n+1} + p_{n+1} \mathbf{I}$$

$$\boldsymbol{\varepsilon}_{n+1}^{\text{e}} = \frac{1}{2G_0(1 - D_{n+1})} \mathbf{s}_{n+1} + \frac{1}{3} \varepsilon_{v,n+1}^{\text{e}} \mathbf{I}$$

- e. **Exit.**

Box 2: Fully implicit elastic predictor/return-mapping algorithm for the MBW damage model.

### 3.2.4 Extension of the model with an stress-state-dependent yield criterion

Damage or fracture is seen as a phenomenon involving large stress or strain gradients at the local potential fracture locations. To give a reliable and precise prediction of the failure in mechanical components, the accuracy of the plasticity model that delivers the local stress and strain variables is essential. In the characterization of isotropic pressure-insensitive materials, the conventional J2 plasticity model is frequently employed, in which yielding is only dependent on the second invariant of the deviatoric stress tensor. In BCC metals, however, the plastic flow shows the dependences on temperature, strain-rate and stress state (including a tension-compression asymmetry) due to the non-planar dislocation core structures in non-close-packed crystal lattices [145]. To account for the stress-state effect on the plastic deformation, non-quadratic yield functions are formulated [64; 68; 146-149]. Here we employ the more generalised non-quadratic plasticity model postulated by Bai and Wierzbicki [64], with the associated flow rule and the isotropic hardening law to characterise the stress-strain behaviour of the high-strength steels before the damage initiation.

By using the yield potential of Bai-Wierzbicki plasticity model for pressure-independent materials in the conjunction with an isotropic power hardening law, the yield criterion is defined as follows:

$$\Phi = \bar{\sigma} - (1 - D)\sigma_y(\bar{\varepsilon}^p, \theta) \leq 0 \quad \text{Eq. 3.44}$$

Note that the dependency of yielding on stress state is incorporated to the yield stress by introducing the effect of Lode angle, which is related to the third invariant of the stress deviator. Due to the general acknowledgement of the assumption of incompressibility, the effect of stress triaxiality on yielding is not included.

$$\sigma_y(\bar{\varepsilon}^p, \theta) = \sigma_y(\bar{\varepsilon}^p) \left[ c_\theta^s + (c_\theta^{\text{ax}} - c_\theta^s) \cdot \left( \omega - \frac{\omega^{m+1}}{m+1} \right) \right] \leq 0 \quad \text{Eq. 3.45}$$

where  $\sigma_y(\bar{\varepsilon}^p)$ , in this context, is representing the flow curve of the perfect materials without damage from the reference test, e.g. uniaxial tensile test, compression test or shear test;  $\omega$  and  $c_\theta^{\text{ax}}$  are defined as follows:

$$\omega = \frac{\sqrt{3}}{2 - \sqrt{3}} \left[ \sec\left(\theta - \frac{\pi}{6}\right) - 1 \right] = \frac{\sqrt{3}}{2 - \sqrt{3}} \left[ \sec\left(\frac{\bar{\theta}\pi}{6}\right) - 1 \right] \quad \text{Eq. 3.46}$$

$$c_\theta^{\text{ax}} = \begin{cases} c_\theta^t, & \bar{\theta} \geq 0 \\ c_\theta^c, & \bar{\theta} < 0 \end{cases} \quad \text{Eq. 3.47}$$

where  $c_\theta^t$ ,  $c_\theta^s$ ,  $c_\theta^c$  and  $m$  are material constants. As shown in Fig. 3.4, the yield function is formulated by comparing the Mises and Tresca yield criteria, and  $c_\theta^t$ ,  $c_\theta^s$ ,  $c_\theta^c$  are the parameters corresponding to tension, shear and compression stress state respectively, whereas  $m$  is a non-negative integer in the higher order power term of  $\gamma$  to ensure the smoothness of the yield locus. The values of the three key material parameters corresponding to three different stress states are relative, i.e. the parameter is set to be unity if the test of its corresponding stress state is chosen as the reference test used for the calibration of the flow curve,  $\sigma_y(\bar{\epsilon}^p)$ . For example, if a uniaxial tensile test is used for the calibration of the reference flow curve, the parameter  $c_\theta^t$  is automatically set to be one. Consequently, the other parameters as well as the higher order non-negative integer are calibrated using different experimental data. The same rule is applied to shear test and compression test.

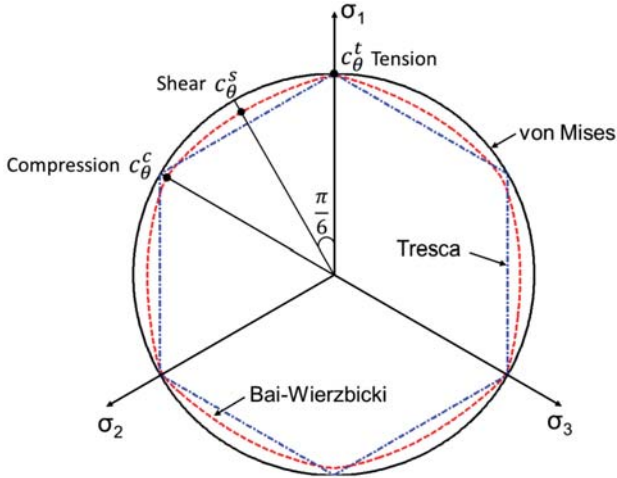


Fig. 3.4: Different yield loci on the deviatoric plane, Mises, Tresca and Bai-Wierzbicki yield criteria ( $c_\theta^t = 1$ ,  $c_\theta^s = 0.93$ ,  $c_\theta^c = 0.97$  and  $m = 5$ ).

The plasticity model presented here is taking a general form with the Lode angle correction; by choosing different parameters, it can be reduced into simpler quadratic or non-quadratic yield functions. For example, the Mises yield function can be obtained by assuming  $c_\theta^t = c_\theta^c = c_\theta^s = 1$  or  $m = 0$ , and the Tresca yield function is given by taking  $c_\theta^t = c_\theta^c = 1$ ,  $c_\theta^s = \sqrt{3}/2$ , and  $m = +\infty$ . By fixing  $c_\theta^t = c_\theta^c = 1$  and  $m = +\infty$ , the yield function with variation of  $c_\theta^s$  in terms of  $\bar{\sigma}$  and  $\bar{\theta}$  can be one-to-one related to the non-quadratic Hosford yield function with respect to the exponent  $k$ . The reader is referred to Ref. [64] for more detailed discussion. As

shown in Fig. 3.4, the Bai–Wierzbicki plasticity model features a more general range which could freely vary between Mises and Tresca criteria by changing the ratio of parameters. In addition, it also differentiates the tension and compression yield stress, which enables a more general application of the plasticity model for precise prediction of the stress–strain behaviour of steels or more complex materials.

Accordingly the conventional associated flow rule is applied to the present plasticity model.

$$\dot{\boldsymbol{\epsilon}}^p = \dot{\gamma} \frac{\partial \Phi}{\partial \boldsymbol{\sigma}} \quad \text{Eq. 3.48}$$

The detailed derivation of the normal direction with respect to yield locus,  $\frac{\partial \Phi}{\partial \boldsymbol{\sigma}}$ , can be found in Ref. [64]. Note that without the consideration of the pressure dependency of the yield function, the fully associated flow rule satisfies the assumption of plastic incompressibility.

It can be readily proved that the yield function (Eq. 3.45) satisfies the requirement of differentiability and smoothness. When the associated flow rule is applied, another feature of the yield function, convexity, is a necessary condition to ensure the uniqueness of the solution in numerical simulation [150; 151]. For isotropic materials, to prove the convexity of the adapted yield function without the effect of pressure in this study, only the convexity of the yield locus on the deviatoric plane needs to be proved.

To represent the yield locus in the deviatoric plane, the yield function from Eq. 3.45 is transformed to a function in the polar coordinate system by converting  $\bar{\sigma}$  into  $\rho$ . Since the yield stress is a positive constant factor, the yield function is simplified to the Eq. 3.49 in the deviatoric plane.

$$\rho(\theta) = c_{\theta}^s + (c_{\theta}^{\text{ax}} - c_{\theta}^s) \cdot \left( \omega - \frac{\omega^{m+1}}{m+1} \right) \quad \text{Eq. 3.49}$$

The convexity of the function  $\rho = \rho(\theta)$  is preserved if the condition

$$\rho^2 + 2\rho'^2 - \rho\rho'' \geq 0 \quad \text{Eq. 3.50}$$

is satisfied [150; 151], in which  $\rho' = \partial\rho/\partial\theta$  and  $\rho'' = \partial^2\rho/\partial\theta^2$ . With the function of  $\rho = \rho(\theta)$  in Eq. 3.49, the inequality required for the sufficient and necessary condition for convexity becomes as follows:

$$\begin{aligned} & \left[ c_{\theta}^s + (c_{\theta}^{\text{ax}} - c_{\theta}^s) \cdot \left( \omega - \frac{\omega^{m+1}}{m+1} \right) \right]^2 + 2(c_{\theta}^{\text{ax}} - c_{\theta}^s)^2 \cdot \omega'^2 \cdot (1 - \omega^m)^2 - \left[ c_{\theta}^s + \right. \\ & \left. (c_{\theta}^{\text{ax}} - c_{\theta}^s) \cdot \left( \omega - \frac{\omega^{m+1}}{m+1} \right) \right] \cdot (c_{\theta}^{\text{ax}} - c_{\theta}^s) \cdot [\omega'' - m\omega^{m-1}\omega'^2 - \omega^m\omega''] \geq 0 \end{aligned} \quad \text{Eq. 3.51}$$

where:

$$\omega = \frac{\sqrt{3}}{2 - \sqrt{3}} \left[ \sec\left(\theta - \frac{\pi}{6}\right) - 1 \right] \quad \text{Eq. 3.52}$$

$$\omega' = \frac{\sqrt{3}}{2 - \sqrt{3}} \frac{\sin(\theta - \pi/6)}{\cos^2(\theta - \pi/6)} \quad \text{Eq. 3.53}$$

$$\omega'' = \frac{\sqrt{3}}{2 - \sqrt{3}} \frac{1 + \sin^2(\theta - \pi/6)}{\cos^3(\theta - \pi/6)} \quad \text{Eq. 3.54}$$

By evaluating the inequality numerically for various values of parameters,  $c_{\theta}^t$ ,  $c_{\theta}^s$ ,  $c_{\theta}^c$  and  $m$ , the convexity of the yield locus is controlled by  $c_{\theta}^s/c_{\theta}^{\text{ax}}$  and  $m$ . The numerically calculated valid range for the convexity of the yield locus is demonstrated in Fig. 3.5. Generally the range for the convexity is bounded by an upper and lower limit. When  $m = 0$ , the range for  $c_{\theta}^s/c_{\theta}^{\text{ax}}$  to satisfy a convex yield locus is  $[0, +\infty]$ . The change of the valid range of  $c_{\theta}^s/c_{\theta}^{\text{ax}}$  is extensive when  $m$  is between zero and one. After  $m$  increases from one, the lower and upper limits are approaching to two constant values,  $\sqrt{3}/2$  and 1, respectively. As generally recommended,  $m$  is selected as a non-negative integer. However, when  $m = 0$ , the effect of the Lode angle is not present in the yield function, as seen from Eq. 3.45 or Eq. 3.49. For practical applications,  $m$  as a positive integer is recommended. Therefore a simple and conservative condition for the convexity of the yield locus is given as independent on  $m$ :

$$\frac{\sqrt{3}}{2} \leq \frac{c_{\theta}^s}{c_{\theta}^{\text{ax}}} \leq 1 \Leftrightarrow \begin{cases} \frac{\sqrt{3}}{2} \leq \frac{c_{\theta}^s}{c_{\theta}^t} \leq 1 \\ \frac{\sqrt{3}}{2} \leq \frac{c_{\theta}^s}{c_{\theta}^c} \leq 1 \end{cases} \quad \text{Eq. 3.55}$$

In Fig. 3.6 (a), the yield loci with various values of  $c_{\theta}^s/c_{\theta}^{\text{ax}}$ , 0.7, 0.8, 0.887, 0.9, 1.0 and 1.1 are demonstrated at  $m = 5$ . Only the values of the ratio within the valid range (Eq. 3.55) give convex shapes. The reason that  $m$  is not playing a major role in the controlling of the convexity of the yield locus is that it is introduced to satisfy the smoothness of the yield locus only at the Lode angle in the vicinity of 0 or  $\pi/3$  and the effect of the higher power order term of  $\gamma$  on the main part of the yield locus is negligible. In Fig. 3.6 (b), the yield loci with different values of  $m$ , 0, 1 and 5 are presented at  $c_{\theta}^s/c_{\theta}^{\text{ax}} = 0.9$ . The yield locus becomes a circle with the radius of  $c_{\theta}^s$  as von Mises yield criterion at  $m = 0$ . After  $m$  increases from zero, the distances of  $\rho(\theta = 0)$  and  $\rho(\theta = \pi/3)$  are approaching to  $c_{\theta}^t$  and  $c_{\theta}^c$  respectively, whereas the shape of the yield locus remains nearly unchanged when Lode angle is around  $\pi/6$ . It is noted that the condition for the convexity can be also interpreted by the geometrical

representation. As shown in Fig. 3.4, when  $c_{\theta}^s/c_{\theta}^{ax} = \sqrt{3}/2$ , the yield stress of the present yield locus at  $\theta = \pi/6$  is identical to the one of Tresca criterion. In this case, the Tresca criterion (a straight line from  $\theta = 0$  to  $\theta = \pi/3$ ) represents the limit for a convex shape. Therefore the lower limit of Eq. 3.55 is obtained. The upper limit can be similarly observed when considering the convexity of the symmetry of yield locus at three axes. The values of  $\rho(\theta)$  at the axes need to be the maximum to satisfy the convexity of the yield locus, which results in the upper limit of  $c_{\theta}^s/c_{\theta}^{ax} = 1$ .

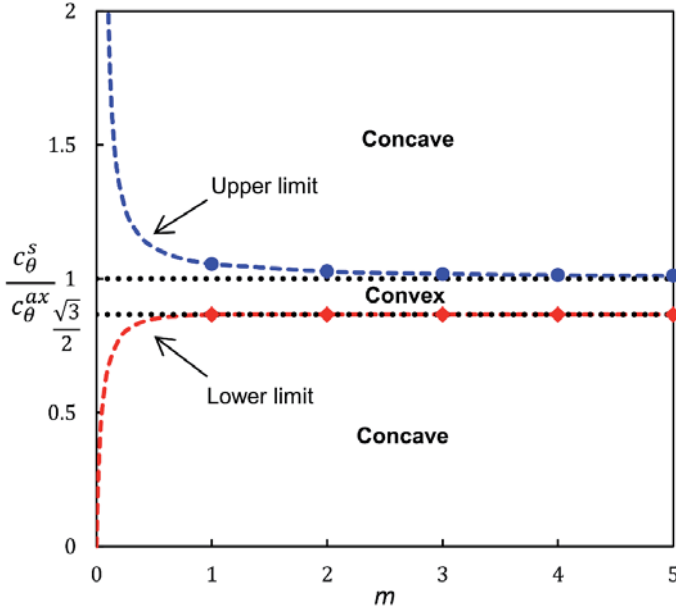


Fig. 3.5: Valid range for the convexity of the presented yield locus in the space of  $c_{\theta}^s/c_{\theta}^{ax}$  and  $m$ .

The Bai-Wierzbicki plasticity model is embedded into the framework of the hybrid damage plasticity model incorporating with the damage initiation criterion and the subsequent damage evolution. The formulated model is numerically implemented into ABAQUS/Explicit as a VUMAT subroutine on the basis of the implementation in the previous section. Accordingly, for the application of the J2-J3 plasticity model in conjunction with the damage model, more material parameters are required to be calibrated and the complete material parameters set is summarised in Tab. 3.2.

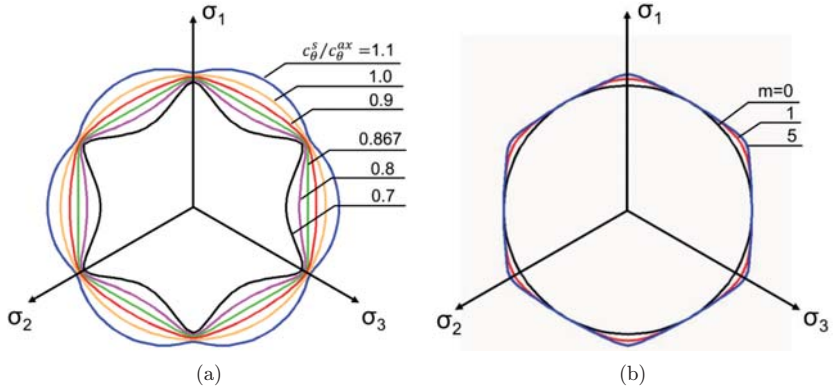


Fig. 3.6: (a) The present yield loci with different ratios of  $c_{\theta}^s/c_{\theta}^{ax}$  when  $m = 5$ ; (b) The present yield loci with different values of  $m$  when  $c_{\theta}^s/c_{\theta}^{ax} = 0.9$ .

Tab. 3.2: Summary of all the material parameters in the MBW model with Lode-dependent plasticity model.

Material parameter	Description
$\sigma_y(\bar{\epsilon}^P)$	Flow curve
$c_{\theta}^t$	Tension coefficient in BW yield locus
$c_{\theta}^c$	Compression coefficient in BW yield locus
$c_{\theta}^s$	Shear coefficient in BW yield locus
$m$	non-negative integer to ensure the smoothness of the BW yield locus
$C_1-C_4$	Damage initiation locus parameters
$G_f$	Specific energy to open a unit area of crack
$D_{cr}$	Critical damage parameter





# Chapter 4

## Materials

### 4.1 Material selection

In this study, two types of steels, a dual-phase steel (DP600) in the form of thin sheets and a structural steel (S355J2+N) in the form of heavy plates are chosen for the investigation of the mechanical properties in particular the cold formability by the proposed model in the last chapter. These two steels are widely used in various industrial applications and the characterisation of their cold formability is of importance for the forming process. As they also represent two major types of steels production, sheet and heavy plate, the study of them shows the general applicability of the proposed model to characterise the plasticity and fracture behaviour for various types of steels.

The dual-phase steel, recognised as the first generation of the AHSS, can be defined as low carbon steel that is thermo-mechanically processed to have a better formability than ferrite-pearlite steels of similar strength. Dual-phase steels contain two phases, normally soft ferritic matrix and hard martensite islands dispersed in the matrix. They are widely used in industry, in particular automotive industry for light weight design due to their mechanical advantages, such as attractive combination of strength and formability.

The steel S355J2+N is an HSLA steel. The name is according to the European standard EN 10025 [152] and “S” stands for structural steel; the number “355” is the minimum yield strength in MPa; “J2” means the minimal impact energy is equal to 27 J at -20 °C and “N” means the supply condition of the steel is normalised or normalised rolled. This steel has a high strength and a good ductility, but the price is comparatively cheap. Benefiting from this, it is popular for civil construction. It is mainly applied in the offshore structure, shipbuilding, freight cars, transmission towers, cranes, trailers, bull dozers and so on.

## 4.2 Chemical composition

The DP600 steel used in this study is a cold-rolled 1.5 mm thick steel sheet. The chemical composition of it is listed in Tab. 4.1. It has rather low carbon content and the main alloying elements are Mn, Cr and Mo. The high content of Mn improves the tensile strength and wear resistance of the DP steel. Similar functions are also provided by Cr and Mo. They are also used to delay the formation of perlite and reduce the martensite transformation starting temperature so that the critical cooling rate of the production process is reduced.

Tab. 4.1: Chemical composition of the DP600 steel, mass contents in %.

C	Si	Mn	P	S	Cr	Mo	Ni	Al	Ti	Nb
0.11	0.39	1.38	0.017	<0.001	0.18	0.05	0.02	0.029	0.01	0.01

The S355J2+N steel was delivered as a hot rolled material in a plate thickness of 15 mm by ThyssenKrupp. The chemical composition of it is summarised Tab. 4.2. Obviously, the alloying concept is rather slim to achieve good weld ability properties and an economic production cost level. The alloy shows low contents of S and P. It is Al-killed and microalloyed with Ti and Nb.

Tab. 4.2: Chemical composition of steel S355J2+N, mass content in %.

C	Si	Mn	P	S	Cr	Mo	Ni	Al	Ti	Nb
0.16	0.20	1.40	0.016	0.004	0.04	0.01	0.02	0.027	0.02	0.01

## 4.3 Microstructure

EBSM is used to characterise the microstructure of the DP600 and the micrograph is shown in Fig. 4.1. Compared to the LOM or SEM, different phases can be distinguished clearly and the phase fraction can be estimated precisely by EBSM measurement. This is essential for the microscopic study in Chapter 9. The measurement shown in Fig. 4.1 is based on the in-plane view of the sheet and the ferrite phase is indexed by the colour map indicating the orientation of each grain, while the black areas are regarded as martensite phase. According to the EBSM measurements on several spots of the sample, the average martensite volume fraction of the DP600 sheet is about 10%. The average grain sizes for ferrite and martensite islands are 9.5  $\mu\text{m}$  and 1.4  $\mu\text{m}$ , respectively.

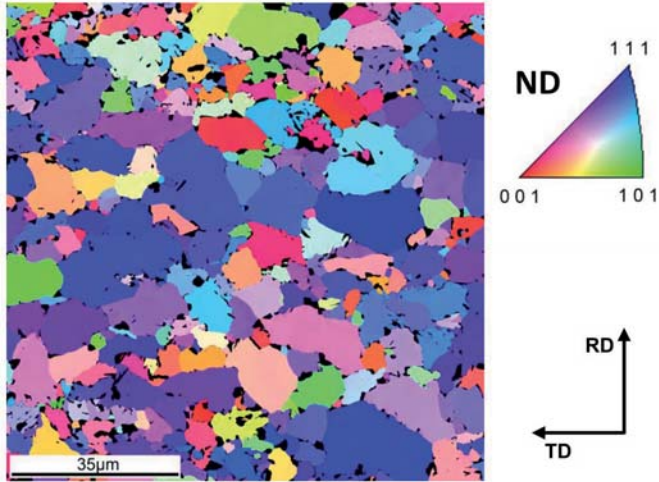


Fig. 4.1: Electron Back-Scattered Diffraction (EBSD) micrograph (normal direction inverse pole figure) of DP600 steel microstructure; the colour map corresponds to the grain orientation of ferrite grains and the martensite phase is represented by black colour.

The microstructure of the steel S355J2+N is analysed by means of LOM. In order to study the internal cleanliness, a sample was polished and investigated by LOM at a magnification of 200:1. As indicated in Fig. 4.2, globular oxides and cementites are revealed. These inclusions play an important role in the ductile failure process as they are favourable nucleation sites for voids. Consequently, they would be detrimental for the toughness properties, but to sum up, the internal cleanliness of steel S355J2+N is on a high level since the number of large inclusions is relatively small. After these investigations, the sample was etched with  $\text{HNO}_3$  for microstructure analysis. As shown in Fig. 4.3, the steel consists of two phases, ferrite (light colour) and pearlite (dark colour), with a relatively fine grain size. By means of quantitative image analysis, the phase volume contents were determined to be 73% and 27% for ferrite and pearlite, respectively. The average grain size of ferrite is 8.8  $\mu\text{m}$ . The pearlite prefers to distribute along the rolling direction. The lamellar spacing of pearlite is relatively small, which enhances the yield strength and toughness property of the steel.

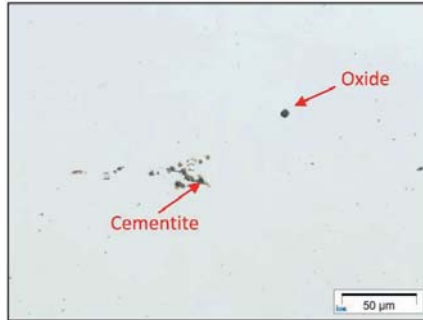


Fig. 4.2: Light optical microscopy investigation of a polished surface of steel S355J2+N.

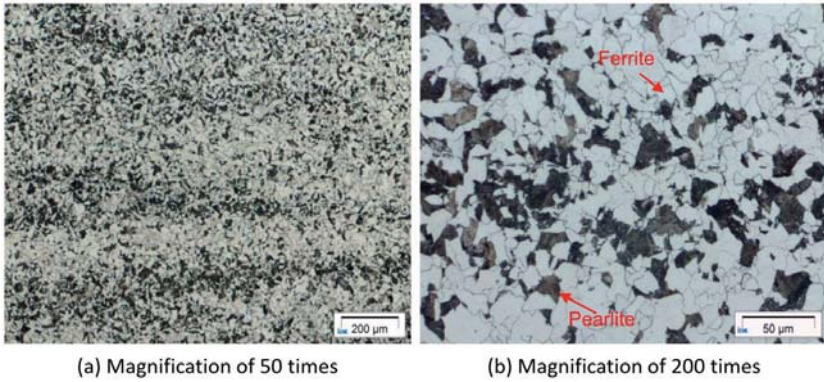


Fig. 4.3: Microstructure of steel S355J2+N after HNO<sub>3</sub>-etching. Two magnifications are given.

# Chapter 5

## Experimental techniques

### 5.1 Tests for parameter calibration and validation

With the previously defined hybrid damage plasticity model, both the plasticity and damage behaviour of materials under different stress states are required to calibrate the material parameters and validate the model. In this chapter, all the experiments involved in this thesis are introduced. These experiments are used for three purposes, material parameter calibration, model validation, and model application. In this section, a brief introduction of all the experiments and their corresponding stress states is given.

Before detailing the specific stress states with respect to stress triaxiality and Lode angle parameter, several assumptions are defined: i) isotropy behaviour of the material, in terms of elasticity, plasticity, damage and fracture, is assumed; ii) the material is assumed to be elasto-plastic; iii) Mises plasticity is assumed for the plastic deformation; iv) plastic incompressibility is also assumed; v) cleavage fracture is not considered.

The following analysis in this paragraph is based on the description in Ref. [67]. The parameter stress triaxiality  $\eta$  ranges in  $[-\infty, +\infty]$ , and its characteristic values are  $1/3$  for uniaxial tension stress state  $(\sigma, 0, 0)$  with  $\sigma > 0$ , zero for pure shear  $(\sigma, -\sigma, 0)$ , and  $-1/3$  for uniaxial compression  $(\sigma, 0, 0)$  with  $\sigma < 0$ . Pure hydrostatic stress state  $(\sigma, \sigma, \sigma)$  results in the limiting cases of  $\eta = \pm\infty$  depending on its tension stress ( $\sigma > 0$ ) or compression stress ( $\sigma < 0$ ). The range of Lode angle parameter  $\bar{\theta}$  is  $[-1, 1]$  and it is equal to 1 for principal stress states of like  $(\sigma_A, \sigma_B, \sigma_B)$  with  $\sigma_A > \sigma_B$ , to zero for  $(\sigma_A, \sigma_B, (\sigma_A + \sigma_B)/2)$ , and to  $-1$  for  $(\sigma_A, \sigma_B, \sigma_B)$  with  $\sigma_A < \sigma_B$ . A typical example for  $\bar{\theta} = -1$  for is the stress state at the centre of axisymmetric structures in axisymmetric tension loading and it also includes the uniaxial

tension when  $\sigma_B = 0$  or pure hydrostatic tension when  $\sigma_A = \sigma_B$ . For  $\bar{\theta} = 0$ , it is a generalised plastic plane strain state and includes the pure shear when  $\sigma_A = -\sigma_B$ . The stress state of  $\bar{\theta} = -1$  is usually present in the centre of axisymmetric structures under axisymmetric compression including uniaxial compression when  $\sigma_B = 0$  or pure hydrostatic compression when  $\sigma_A = \sigma_B$ . For more details, readers are referred to Ref. [67]. These relations are summarised in Tab. 5.1.

Tab. 5.1: The correlation of three typical Lode angle parameter values with the principle stresses representation and stress states, summarised based on Ref. [67].

Lode angle parameter	$\bar{\theta} = 1$	$\bar{\theta} = 0$	$\bar{\theta} = -1$
Principle stresses	$(\sigma_A, \sigma_B, \sigma_B)$ $\sigma_A > \sigma_B$	$(\sigma_A, \sigma_B, (\sigma_A + \sigma_B)/2)$	$(\sigma_A, \sigma_B, \sigma_B)$ $\sigma_A < \sigma_B$
General stress state	Axisymmetric tension	Generalised plastic plane strain	Axisymmetric compression
Special cases	<ul style="list-style-type: none"> <li>• Uniaxial tension</li> <li>• <math>\sigma_B = 0</math></li> <li>• hydrostatic tension</li> <li>• <math>\sigma_A = \sigma_B</math></li> </ul>	<ul style="list-style-type: none"> <li>• Pure shear or torsion</li> <li>• <math>\sigma_A = -\sigma_B</math></li> </ul>	<ul style="list-style-type: none"> <li>• Uniaxial compression</li> <li>• <math>\sigma_B = 0</math></li> <li>• hydrostatic compression</li> <li>• <math>\sigma_A = \sigma_B</math></li> </ul>

In Fig. 5.1, seven typical stress states are presented in the space of stress triaxiality and Lode angle parameter. The seven typical stress states all feature plane stress condition, under which stress triaxiality and Lode angle parameter are dependent on each other, presented as the red dashed line in Fig. 5.1. The principle stresses representation of these stress states and their corresponding values for  $\eta$  and  $\bar{\theta}$  are listed in Tab. 5.2.

In addition to the seven typical stress states, the typical experiments for characterisation of sheet metals and heavy plates are also presented with their featured stress triaxiality and Lode angle parameter in Fig. 5.1.

For uniaxial tension, there are several possibilities to choose for both sheet metals and heavy plates. The smooth dog-bone flat specimen and round bar specimen both feature uniaxial tension through the plastic deformation zone before necking. After necking, the history of stress triaxiality becomes non-linear, but the centre of the specimen still features axisymmetric tension ( $\bar{\theta} = 1$ ). For fracture study of materials, the central-hole specimen can also be used for this purpose, as the critical deformation point of this type of specimen also features uniaxial tension stress state, as it is described in detail in section 5.1.1 and 6.2.1.

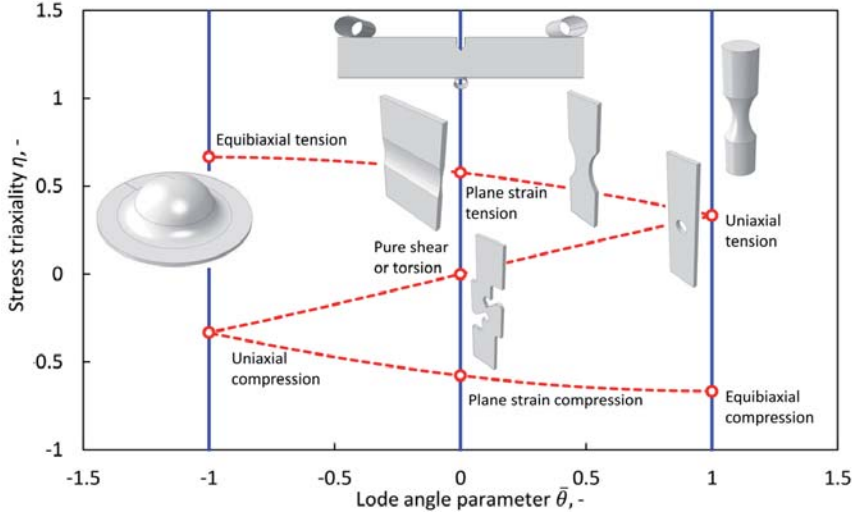


Fig. 5.1: Geometric illustration of the stress states of typical specimens for sheet metal and heavy plates testing.

Tab. 5.2: The seven specific stress states under plane-stress condition and their corresponding principle stresses representation, stress triaxiality  $\eta$  and Lode angle parameter  $\bar{\theta}$ . (Note in the principle stress representation  $(\sigma_1, \sigma_2, \sigma_3)$ , by convention,  $\sigma_1 > \sigma_2 > \sigma_3$  is defined.)

Specific stress state	Principle stresses	$\eta$	$\bar{\theta}$
Uniaxial tension	$(\sigma_1, 0, 0)$	$\eta = 1/3$	$\bar{\theta} = 1$
Equibiaxial compression	$(0, \sigma_3, \sigma_3)$	$\eta = -2/3$	$\bar{\theta} = 1$
Plane strain tension	$(\sigma_1, \sigma_1/2, 0)$	$\eta = \sqrt{3}/2$	$\bar{\theta} = 0$
Pure shear	$(\sigma_1, 0, -\sigma_1)$	$\eta = 0$	$\bar{\theta} = 0$
Plane strain compression	$(0, \sigma_3/2, \sigma_3)$	$\eta = -\sqrt{3}/2$	$\bar{\theta} = 0$
Equibiaxial tension	$(\sigma_1, \sigma_1, 0)$	$\eta = 2/3$	$\bar{\theta} = -1$
Uniaxial compression	$(0, 0, \sigma_3)$	$\eta = -1/3$	$\bar{\theta} = -1$

The notched round bars are commonly employed for various studies, and the centre of this type specimen is under axisymmetric tension, so they feature  $\bar{\theta} = 1$  but increased stress triaxiality with decreasing notch radius, as discussed in section 5.1.2 and 6.3.2.

The stress state of notched dog-bone flat specimens is located between the uniaxial tension and plane-strain tension. With smaller notch radius, the stress state transfers towards plane-strain tension.

The flat-grooved specimens are an alternative to characterise the plane-strain tension stress state, and in addition, it can also produce more generalised plane-strain tension with increased stress triaxiality under  $\bar{\theta} = 0$  by decreasing the notch radius, as shown in section 5.1.1 and 6.2.1. The stress triaxiality can be increased considerably (to 1.5 or even 2) under the generalised plane-strain tension by the fracture mechanics tests, such as compact tension (CT) test or SENB tests, where very high hydrostatic pressure is introduced by the sharp fatigue pre-crack. The details of the SENB test are discussed in section 5.1.2 and 6.3.2.

To realise pure shear stress state, a special designed specimen that works on a universal tensile machine is adopted for simplicity. The geometry of it and its realised stress state is given in section 5.1.1 and 6.2.1. For equibiaxial tension stress state, the hydraulic bulge test is used as described in section 5.1.1 and 6.2.1 as well.

For the rest three compression stress states, they can be also realised by corresponding tests, but they are not included in the thesis, as compression is less destructive than tension for the application of the investigated materials.

One shall note that all the featured stress states of the discussed experiments are only valid for a specific deformation zone of the specimen, not all the plastic deformation region. For example, only the centre of the notch round bar is under the axisymmetric tension condition, whereas the material point away from the centre features a Lode angle parameter lower than one. In addition, the direct measurement of the stress state and even the local strain, in particular when the critical point is not on the surface of the specimen, is not easy to access for most of the tests.

Due to these reasons, normally a hybrid experimental-numerical approach is adopted to calibrate the material parameter of the model. There are various combinations of the tests for both sheet metals and heavy plates to cover a wide stress states. In this thesis, we use central-hole specimen, notched dog-bone specimens, flat-grooved specimens, pure-shear specimens and bulge test to calibrate and validate the material parameters in the hybrid damage plasticity model for the sheet metal DP600, while the notched round bars and the SENB tests are employed for the heavy plates S355J2+N. After the material parameter calibration and validation, Nakajima test and bending test are used as application examples for DP600 and S355J2+N, respectively.



## 5.1.1 Selected tests for steel sheet DP600

### 5.1.1.1 Tensile tests

The tensile tests include the smooth dog-bone tensile test and tensile tests with central-hole, notched dog-bone, flat-grooved, and pure-shear specimens. All the specimens used in this study are extracted from one large DP600 steel sheet. They are cut such that the loading direction of the specimen is orientated along the rolling direction, except for the smooth tensile tests in which the anisotropy of material is considered.

The smooth dog-bone tensile tests are performed to obtain the basic mechanical properties of DP600, as it will be detailed in Section 6.2.1, as well as to provide the experimental basis of the flow curve which is required in the following simulations. The tests are performed at room temperature on a universal testing machine Zwick Z100/TL3. The standard specimens with a gauge length of 120 mm are employed in this investigation according to EN 10002-1 [153]. The geometry of the specimen is shown in Fig. 5.2 and the corresponding dimensions are listed in Tab. 5.3. To achieve a quasi-static test condition, the crosshead speed is chosen as 2 mm/min, which results in a strain rate of the order of  $10^{-4} \text{ s}^{-1}$ .

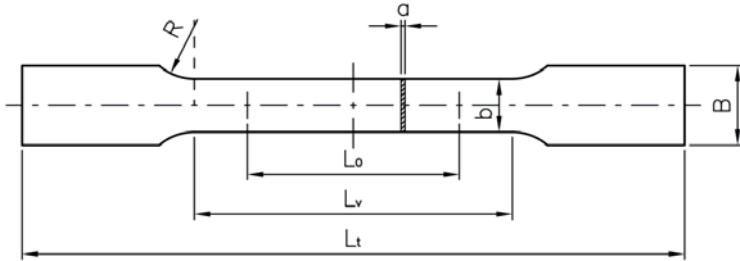


Fig. 5.2: Geometric illustration of the smooth dog-bone specimen in tensile tests.

Tab. 5.3: Dimensions of the smooth dog-bone tensile specimen, all units in mm.

Standard	Sample Description	a	b	$L_0$	$L_v$	$L_t$	B	R
EN 10002-1	flat specimen 20 x 80	1.5	20	80	120	250	30	20

For the other tensile test specimens, a constant strain rate is not possible, and the local strain rate is not homogeneously distributed due to the geometry nonlinearity. The deformation rate locally at the edge of the hole for the central-hole specimen, for example, is much higher than the rest part of the specimen, so a very slow crosshead speed, 0.2 mm/s, is chosen for a quasi-static loading condition, even locally. In addition, the special customised clamping system to

measure the electric potential during the test is also employed for all the rest tests, as they are mainly used to characterise the onset of damage.

Two types of geometry configurations are designed, differing in the cutting shape at the centre of specimens (Fig. 5.3). The first type is a circular cut with a radius of 3 mm. The other configurations feature an elliptical cut at the centre with a constant minor radius of 2 mm and varied major radii of 3 mm, 5 mm and 7 mm.

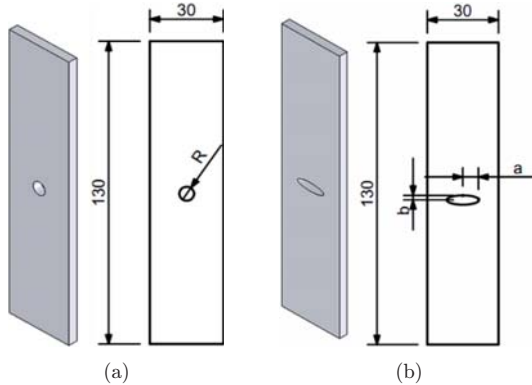


Fig. 5.3: Geometry of central-hole specimens with (a) circular cut-out, (b) elliptical cut-out.

Three different geometry configurations of dog-bone specimens are designed as shown in Fig. 5.4. Notches with circular cuts, “U” and “V” shapes are used to generate various stress states. The first configuration produces the closest stress state to uniaxial tension. The decreased notches provide a stress state between uniaxial tension and plane strain condition.

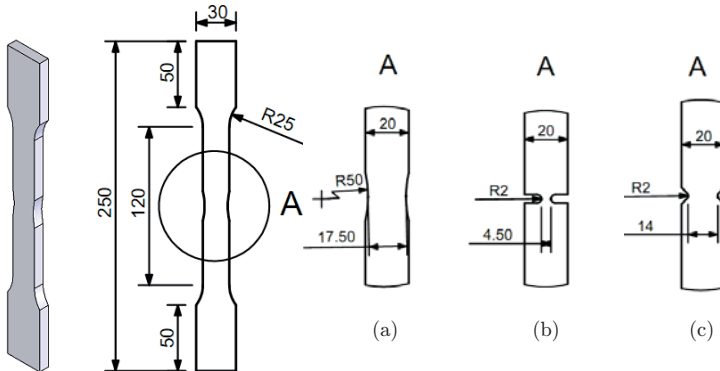


Fig. 5.4: Geometry of dog-bone specimens with (a) circular cut-out, (b) “U” notch, (c) “V” notch.

The design of flat-grooved specimens is illustrated in Fig. 5.5. The width of all the specimens is 50 mm and the height is 130 mm. Five different radii of the grooves, 15 mm, 12.5 mm, 7.5 mm, 4 mm and 1.5 mm, are manufactured.

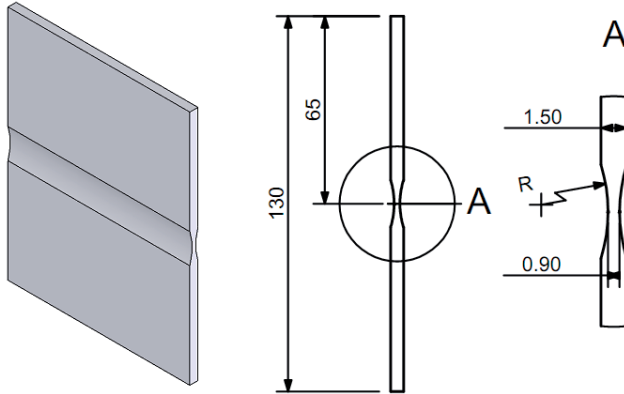


Fig. 5.5: Geometry of flat-grooved specimens with transverse notches of different radii.

A pure-shear specimen is designed to achieve lower stress triaxiality in the region of zero Lode angle parameter at a uniaxial tensile test machine. The design is adopted from the work in Ref. [154] and [54]. Fig. 5.6 shows the design of the pure-shear specimen. An out-of-plane notch between the two holes in the middle of the specimen is manufactured on both sides to achieve an explicit damage initiation spot.

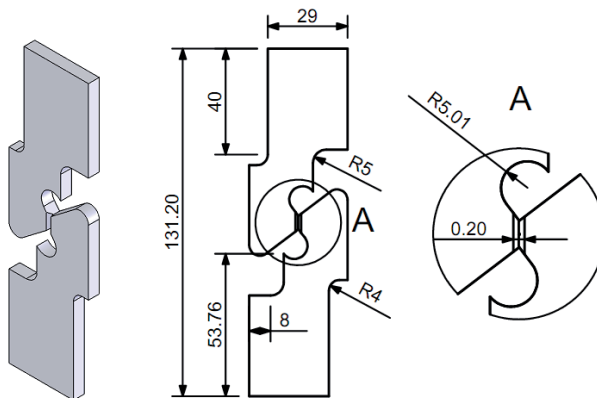


Fig. 5.6: Geometry of pure-shear specimen for a universal tensile test machine.

### 5.1.1.2 Bulge test

The bulge test is characterised by a biaxial stress and/or strain state. In the test, a circular blank with a diameter of 160 mm is clamped along its perimeter between the sheet holder and the forming die with the inner diameter of 100mm on an Erichsen<sup>®</sup> 145/60 universal sheet testing machine. The hydraulic pressure is applied to the lower surface of the blank through the oil under the compression of the displacement-controlled punch.

The velocity of the punch is pre-assigned at 15 mm/min. During the loading, a bulge occurs and costs thinning of the material, as schematically shown in Fig. 5.7. The punch force is measured during the process continuously and accordingly the pressure is calculated. The top surface of the specimen is patterned with circular grids with a diameter of 2mm and neighbour spacing of 5mm. A measuring method with a laser light section for geometry analysis and a camera device for local strain determination are attached to measure the local strain and further calculate the effective strain. For details of the measuring method and the calculation procedure, readers are referred to Ref. [131; 155; 156]. In the present thesis, an inverse method with hybrid experimental-numerical approach is used for the determination of the flow hardening under equibiaxial tension loading. Therefore, only the pressure and the bulge height of the specimen are of interest.

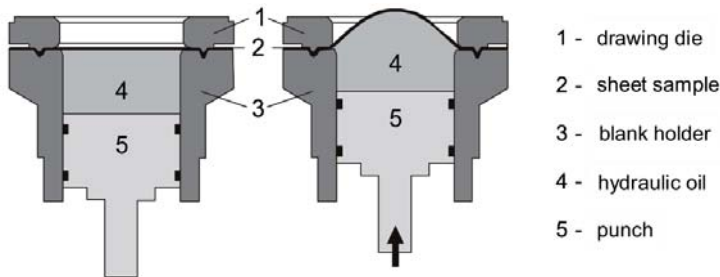


Fig. 5.7: Schematic representation of the setup of a hydraulic bulge test [155].

## 5.1.2 Selected tests for heavy plate S355J2+N

### 5.1.2.1 Tensile tests

For the bulk material, steel S355J2+N, two types of the tensile tests listed in Fig. 5.1 are employed, smooth round bar (SRB) tensile test and notched round bar (NRB) tensile test. For the consideration of anisotropy, the SRBs are cut along two directions, rolling direction and

transverse direction. However, for the description of the damage and fracture, only loading along rolling direction is considered, i.e. the NRBs are all cut along the rolling direction.

The SRB tests are performed at room temperature on the Zwick Z100/TL3 machine. According to the European standard EN 10002-1 [153], specimens with geometry illustrated in Fig. 5.8 are prepared. The detailed dimensions are listed in Tab. 5.4. To achieve quasi-static loading condition, the crosshead speed of 0.8 mm/min is set, and the resulted strain rate for the uniaxial loading is about  $3 \times 10^{-4} \text{ s}^{-1}$ .

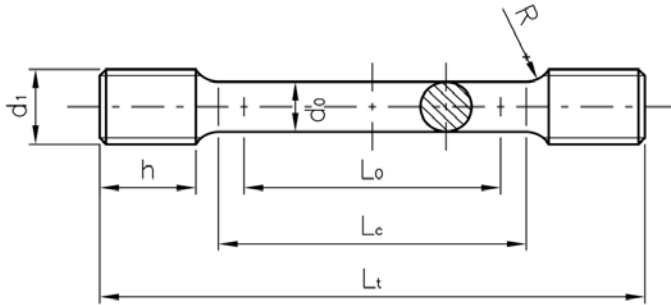


Fig. 5.8: Geometric illustration of the SRB specimens in tensile tests.

Tab. 5.4: Dimension of the SRB tensile specimens of steel S355J2+N, in mm.

European standard	Sample description	$d_0$	$L_0$	$d_1$	$h$	$L_c$	$L_t$	$R$
EN 10002-1	B8 x 40	8	40	12	10	48	75	4

The NRB specimens were produced based on the SNB specimens according to the standard DIN EN 10025. A circular notch was applied to the centre of the cylindrical bars as shown in Fig. 5.9. Four different notch radii, 2mm, 6mm, 12mm and 42mm were designed. In all cases, the remaining diameter in the notch ground should be 4 mm, so that the notch depth is 2 mm. The exact notch geometries were measured again after the mechanical manufacture of the samples, as given in Tab. 5.5.

The NRB tests were also performed on the same testing machine at ambient temperature and a constant crosshead velocity of 0.2 mm/min. The specimens were stretched until they were broken and the corresponding global force and displacement were recorded. At the same time, the DCPD technique was applied in order to identify damage initiation by the increase of the electric resistance.

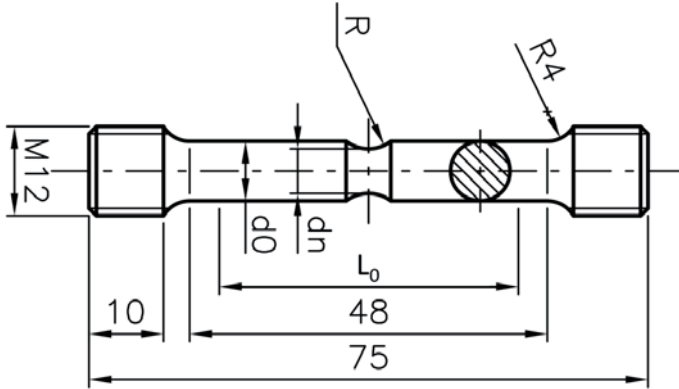


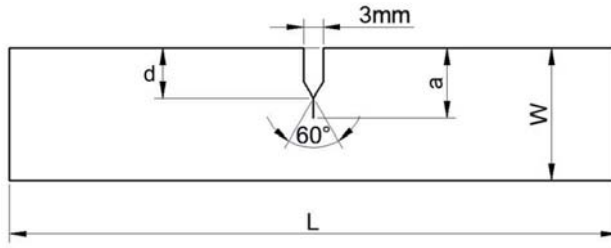
Fig. 5.9: Geometric illustration of NRB specimens. The dimensions of the different designs of the notch radius are measured in Tab. 5.5.

Tab. 5.5: Geometry dimensions of NRB specimens.

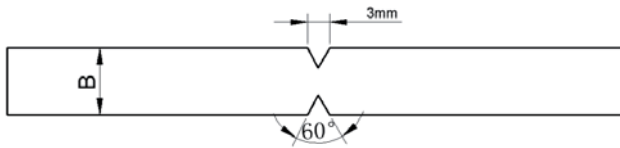
Specimen name	R, mm	$L_0$ , mm	$d_0$ , mm	$d_n$ , mm
R2	2	30.00	7.95	4.01
R6	6	30.00	7.97	4.05
R12	12	29.89	8.00	4.08
R42	42	30.96	8.01	4.08

#### 5.1.2.2 Single edge notched bending (SENB) test

The geometrical features of the SENB specimens are illustrated in Fig. 5.10. All specimens have got a length of 92 mm, a width of 10 mm and a height of 20 mm. There are two characteristics in the design of SENB specimens: pre-crack and side-groove. As aforementioned, the target for the design is to cover a broad range of stress states. The first crack that appears in SENB specimens is located beneath the pre-crack or notch (when no pre-crack is assigned) in the mid-plane of the thickness direction. The stress state at this location features a Lode angle parameter in the vicinity of zero and its value is influenced by the implementation of side-grooves. The stress triaxiality of the same location is varied by the existence of pre-cracks. Therefore, there are four different types of specimens investigated, according to the possible combination of these two characteristics. The corresponding measured dimensions after the manufacture of these samples are listed in Tab. 5.6.



(a) Front view of a specimen without side grooves



(b) Bottom view of a specimen with side grooves

Fig. 5.10: Geometric illustration of SENB specimens.

Tab. 5.6: Geometry dimensions of SENB specimens.

Sample name	L, mm	B, mm	W, mm	d, mm	a, mm	Side groove
a	92	10	20	10.4	10.4	no
b	92	10	20	10.4	10.4	yes
c	92	10	20	6.6	12.5	no
d	92	10	20	6.6	12.8	yes

The SENB tests were performed in a Schenck servo hydraulic testing machine with a maximum force of 400 kN at room temperature at a constant piston velocity of 0.4 mm/min. During the tests, the applied force was measured with a load cell. Furthermore, the crack tip opening displacement (CTOD) was determined with clip gages. The experimental device for carrying out the SENB test consists of two rollers at a distance of 80 mm, serving as supports on the top side of the specimen. The third roller embedded in a piston presses the specimen in the middle from the bottom side. The two support bearings have the same diameter of 10 mm, while the third roller fixed to the piston has a diameter of 5 mm. All tests were performed until the specimens were totally fractured. The instant of damage initiation was again identified according to the DCPD method.

## 5.2 Tests selected for model application

### 5.2.1 Steel sheet: Nakajima test

The FLD is a standard criterion to characterise the formability of sheet metals. Either in the laboratory or industry Nakajima stretch-forming test is often conducted to determine the FLD. In the Nakajima test for DP600, the sheet material is clamped between a fixed drawing die and a blank holder with a clamping force of 200 kN. Subsequently a semi-spherical punch with a diameter of 100 mm moves vertically from below to deform the blank until the formation of fracture at a constant speed rate of 90 mm/min, as shown in Fig. 5.11. Following the standard (DIN EN ISO 12004-2), ten blanks with a length of 190 mm but different width of 20, 40, 80, 90, 100, 130, 140, 150, 160, 190 mm in waisted region were used to describe a range of stress state from uniaxial to biaxial tension. Between the blank and the punch during the test, a stack of lubricant, composed of one layer of soft polyvinyl chloride (PVC), e.g. Mipolamff, between two polyethylene (PE) or polytetrafluoroethylene (PTFE), e.g. Teflonff, layers and oil or grease on both sides of each layer, is conducted to dispel the friction.

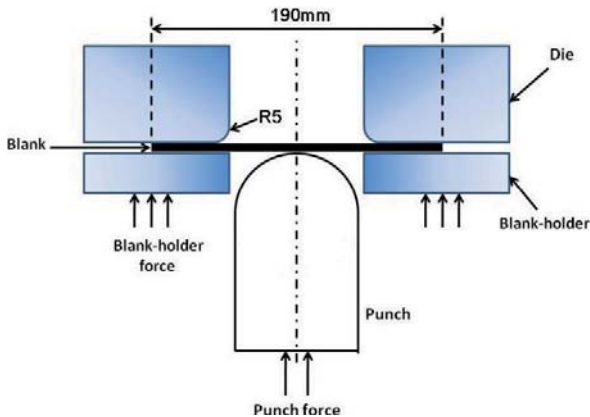


Fig. 5.11: (a) Schematic drawing of the setup of Nakajima test.

On the blank deterministic grids with a size of 2 mm are etched electrochemically. An optical measuring system, Autogrid Vialux 4, is also attached to measure the out-of-plane deformation of the specimen by a sample rate of 10 Hertz. The strain distribution on the surface of the specimen is computed during the test.

There are several methods to analyse the result, namely, visual method, position-dependent method and time-dependent method. In this thesis, the first two are both used. For the visual



method, the last seconds in the video before necking and/or cracking are investigated with regard to formation of necking and/or fracture on the surface. The picture 0.1 second before these incidences is used for finding the maximum strain pair  $\varepsilon_1/\varepsilon_2$  in the centre of the blank. One example on the analysis of the forming limit on specimen with web width of 190 mm is illustrated in Fig. 5.12. The forming limit curve was determined using method of DIN EN ISO 12004-2 by measuring the strain distribution and the maximum pair major and minor strain of the cracked blank in unloaded condition. Subsequently the in-plane major and minor strains at either necking or fracture, depending on the incidence chosen in the video, can be drawn on the forming limit diagram.

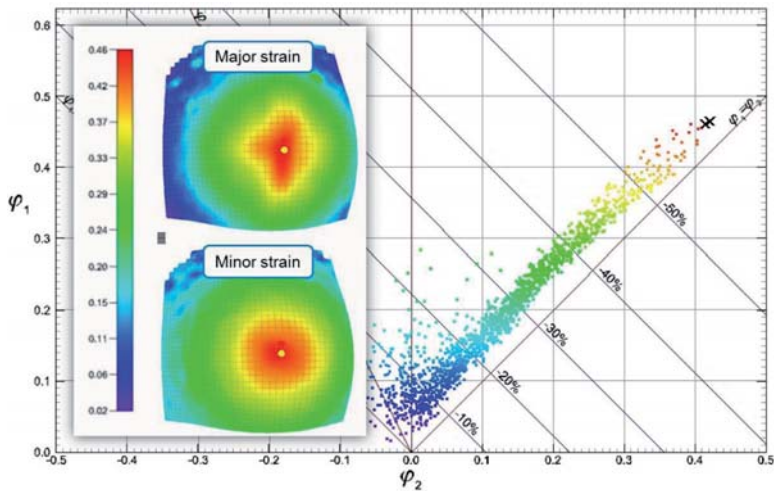


Fig. 5.12: The analysis of the forming limit at necking of the specimen with web width of 190 mm by visual method.

The position-dependent method is recommended by the standard DIN EN ISO 12004-2. The key steps of the analysis of forming limit by position-dependent method are shown in Fig. 5.13. The analysis starts with the location of the crack path from the last picture of the test when the crack is visible. The fit window for the later step consisted of the cross section points (10 strain points on each side of the crack path) perpendicular to the crack on the image is defined. These points are then transferred to one picture before the crack occurrence for sorting the in-plane major and minor strain values without crack opening. By removing the strain points in the necked area, the strain distribution just before the onset of necking is reconstructed in this

region by curve fitting (inverse parabola) of the remaining part of the strain distribution on both sides of the neck. Instead of the directly read values in the necked area, the fitted ones are defined as the forming limit strains according to the position-dependent method. Due to this reason, the position-dependent method is more conservative, compared to the visual method.

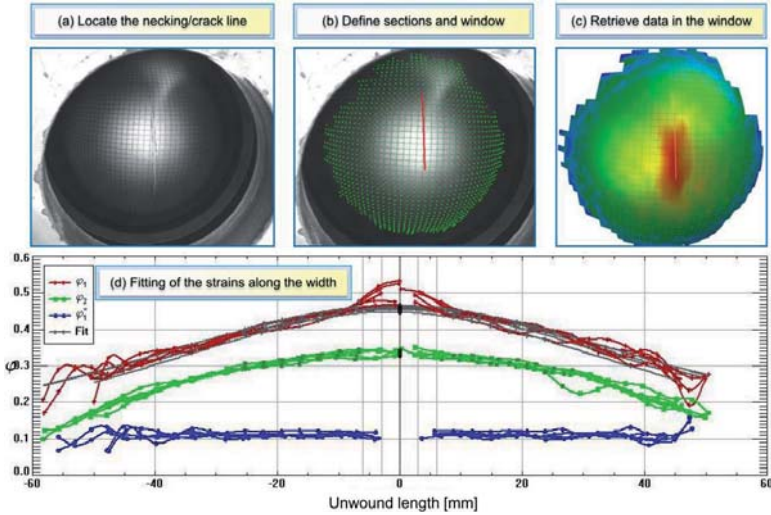


Fig. 5.13. The key steps of the analysis of the forming limit at necking by position-dependent method according to standard DIN EN ISO 12004-2: (a) location of the crack path from the last picture of the test when the crack is visible; (b) Definition of the fit window consisting of the cross section points perpendicular to the crack, highlighted by green grids; (c) Retrieving the in-plane major and minor strain values on one picture before the crack occurrence; (d) Inverse parabola curve fitting of the strain distribution on both sides of the neck after removing the strain points in the necked area.

### 5.2.2 Heavy plate: Bending test

Three-point bending test is a standard test for characterisation of bendability [157]. For the heavy plate application, it is also often used as an experimental technique to assess the cold formability of steels for manufacture of components with the extensive cold forming involved. In the experimental set-up of bending test, a steel plate of defined size is subjected to a symmetric three point bending treatment. As indicated in Fig. 5.14, the distance between the two support bearings is a function of the plate thickness and of the radius of the cylindrical

punch which applies the load, so that the whole geometrical set-up of the test is defined by the punch radius  $r$  and the sample thickness  $t$ .

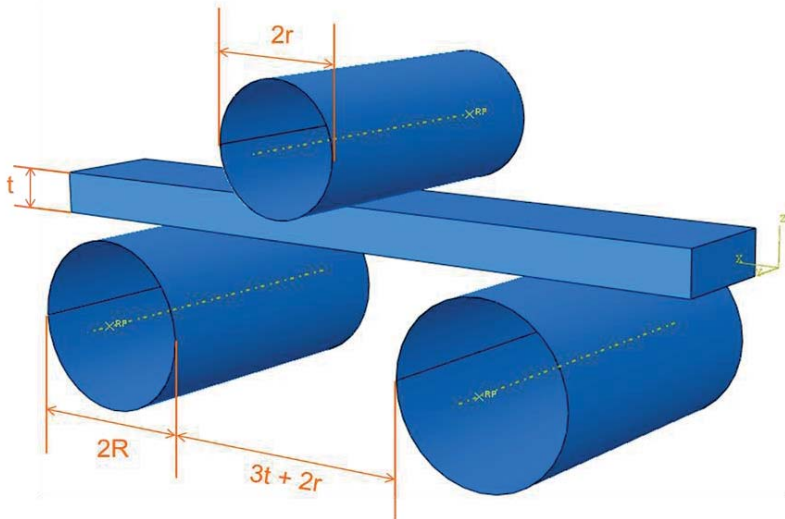


Fig. 5.14: Experimental set-up of bending tests.

The working cycle of bending test is illustrated in Fig. 5.15: (a) the plate is placed according to a given  $r/t$  ratio; (b) the punch moves from top to the bottom to deform the plate into a certain extent when the plate is bended at approximately  $90^\circ$  in the middle; (c) the punch goes backwards to the initial place and allows the plate to release its elastic deformation. After one cycle, the plate is removed and the system starts with another working cycle. In this way, a series of test are performed, in which the dimension of the plate is constant, but the  $r/t$  ratio is defined as a variable by varying the punch radius. Accordingly the distance between two barriers,  $3t+2r$  is changed for each test. The investigation is aiming to find the critical  $r/t$  ratio to trigger crack/damage initiation on the plate.

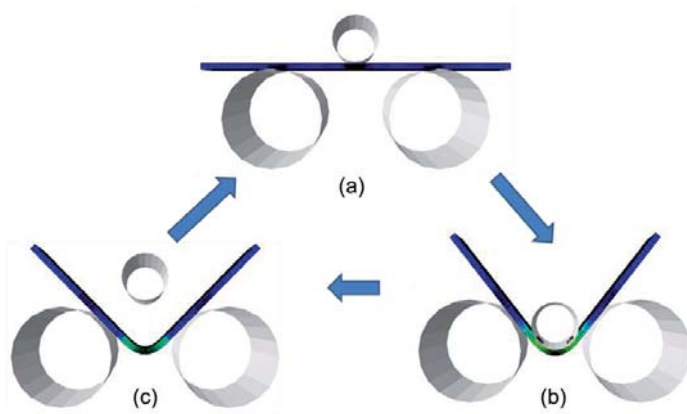


Fig. 5.15: Operating cycle of the cold forming test: (a) Setup of the test with a given  $r/t$  ratio; (b) Bending deformation of the plate to approximately  $90^\circ$  by the movement of the punch; (c) Unloading by moving the punch to its initial place to allow the plate to release the elastic deformation .

# Chapter 6

## Material parameter calibration and model validation

### 6.1 Material parameter calibration strategy and methodology

Based on the formulation of the hybrid damage plasticity model, there are mainly three sections of material parameter involved, plasticity characterisation, damage initiation characterisation, and damage evolution characterisation. The prerequisite for the calibration of these parameters is the reference flow curve of the material. For the study, the tensile flow curve is always employed. A hybrid experimental and numerical calibration strategy is proposed in the following, which could serve as a general instruction for any other type of materials:

- Carry out a standard tensile test and calibrate the reference flow curve from it;
- Carry out a series of fracture tests that covers a broad range of stress states associated with DCPD method and record the force and potential response during the whole deformation until fracture;
- Determine the instant and location of damage initiation by experimental data and metallography methods;
- Perform the numerical simulations for the fracture tests with the chosen plasticity model and calibrate the parameters of the plasticity model based on the comparison of global force–displacement responses between experiments and simulations until the onset of damage;
- Retrieve the local variables, equivalent plastic strain, stress triaxiality, and Lode angle parameters, from the simulation with calibrated parameters of the plasticity model at the

experimentally determined damage instant and location and calibrate the parameters for the damage initiation locus;

- Perform simulations for selected fracture test with the damage initiation locus and damage-induced softening and calibrate the parameters for damage-induced softening based on the comparison of global force–displacement responses between experiments and simulations until the final fracture.

For the studied materials, the DCPD method is employed to detect the damage initiation instant due to its applicability and simplicity. For the determination of the location damage initiation, it has been widely accepted in the literature that the location of the onset of damage/fracture coincides with the location of the highest equivalent plastic strain within the specimen at the instant of damage/fracture. This assumption works well when the analysis is focused on a macroscopic failure such as the final fracture. However, when a microscopic damage initiation instant is adopted, a more sophisticated procedure needs to be carried out. Firstly, a microscopic digital camera is attached to monitor the specimen surface at the gauge section during the history of testing. The crack initiation location that occurs on the surface of the specimen is therefore captured by the camera. Secondly, a fractography study is carried out. To detect the accurate damage initiation location, the fracture mode and the underlying damage mechanisms that control the whole process are investigated. SEM fractography is therefore employed to identify the dominating damage mechanism, dimple or shearing.

## 6.2 Parameter calibration and validation for steel sheet DP600

### 6.2.1 Parameter calibration

#### 6.2.1.1 Calibration of flow curve

The detailed specimen geometry and the test condition of the smooth dog-bone tensile tests are described in section 5.1.1. To study the anisotropy of the material, specimens cut along the rolling direction ( $0^\circ$ ) and the transverse direction ( $90^\circ$ ) were tested and the results are shown in Fig. 6.1. Three parallel tests were performed for each direction, and one can note that the material behaves isotropically in general but it shows quite large uncertainty band close to failure. The average basic characteristics of the mechanical properties of DP600 are summarised in Tab. 6.1.

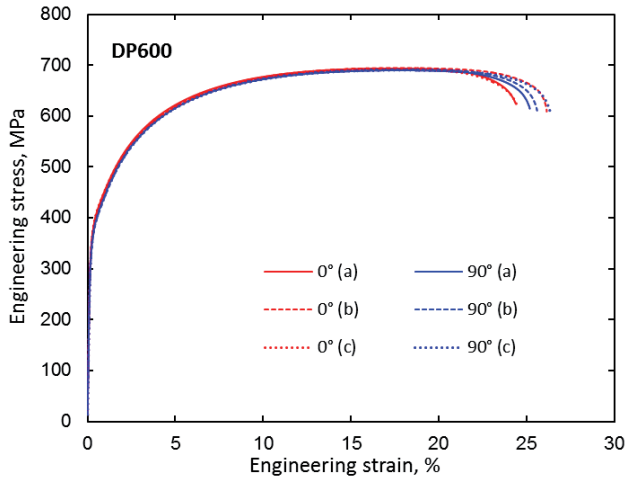


Fig. 6.1: Engineering stress–strain curves of six samples of DP600 steel, three loading along the rolling direction (indicated as  $0^\circ$ ) and three loading perpendicular to the rolling direction (indicated as  $90^\circ$ ).

Tab. 6.1: Mechanical properties of DP600 steel sheet.

Young's modulus	Yield strength	Ultimate tensile strength	Uniform elongation	Fracture elongation
$E$	$R_{p0.2}$	$R_m$	$A_u$	$A_{80}$
214 GPa	390 MPa	704 MPa	16.5 %	25.4 %

For the purpose of simulation, a flow curve is necessary to describe the plastic flow behaviour of the material during large plastic deformation. The engineering stress strain curve of DP600 steel is converted to the true stress–strain curve before the appearance of necking, which is corresponding to the ultimate tensile strength (UTS) point, and it is then fitted and extrapolated by the Hollomon equation as shown below.

$$\bar{\sigma}(\bar{\varepsilon}^p) = A(\bar{\varepsilon}^p)^n \quad \text{Eq. 6.1}$$

The fitted parameters are  $A = 1201 \text{ MPa}$  and  $n = 0.198$ . As the Hollomon flow curve estimates very low stress at the beginning of the plastic deformation, the experimental part is used for the beginning part and then combined with the extrapolation. The comparison of the experimental true stress–strain curve and the extrapolated flow curve is shown in Fig. 6.2.

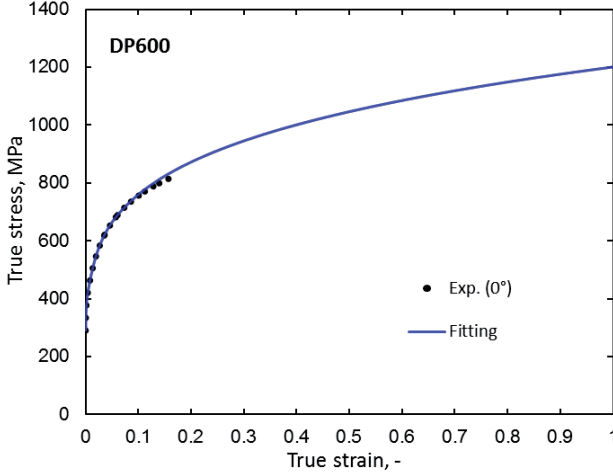


Fig. 6.2: Comparison of the experimental true stress–strain curve and the extrapolated flow curve by Hollomon equation.

#### 6.2.1.2 Calibration of the stress-state effect on plastic behaviour

For the DP600 steel sheet, the stress-state dependency of the plasticity behaviour is observed as shown in the following study. The advanced stress-state-dependent yield function is therefore used for accurate local deformation description. As the stress–strain description is obtained from a smooth dog-bone tensile test,  $c_0^t$  is equal to one. Only  $c_0^s$ ,  $c_0^c$  and  $m$  remain unknown. In this study both notched dog-bone and flat-grooved specimens with varied geometries under tension are used to calibrate  $c_0^s$  and  $m$ . Because the stress states at different deformed locations are not the same, more stress states are considered than in the conventional calibration strategy [64] to achieve better fitting results. Due to the difficulty in performing upsetting tests for sheet materials, a hydraulic bulge test is conducted to calibrate  $c_0^c$ .

##### Notched dog-bone and flat-grooved tensile tests

The specimen geometry and the experimental procedure are described in section 5.1.1. The FE code ABAQUS/Explicit is employed to carry out the numerical analysis. All the specimens are modelled in three dimensions. Considering the symmetry of the specimen geometry and load condition, only 1/8 of the specimen is modelled. 3D 8-node solid elements with reduced integration (C3D8R) are used for all cases. The mesh is designed in a way that, in the plastically deformed area, the element size is small and gradually increases towards the only elastically deformed area. Before the calibration of parameters, the mesh dependency is studied. Three



different mesh sizes, 0.2 mm, 0.1 mm and 50  $\mu\text{m}$  are employed. Based on the comparisons of force and equivalent plastic strain versus displacement responses, the influence of the mesh size is negligible. Therefore the medium mesh size, 0.1 mm, is chosen for all the FE models in the study. Moreover, this mesh size is also of importance under the consideration for the element removal. The configuration of mesh conducted for dog-bone specimens is also applied for the rest of specimens.

All the FE models for notched dog-bone and flat-grooved tensile test are run with the user material subroutine (VUMAT). Only the plasticity model is active and the functions of damage initiation and the damage evolution is switched off in the calculation. To calibrate  $c_0^s$  and  $m$ , an iterative programme is defined as follows:

- Perform the simulations of corresponding tests with initially-guessed parameters;
- Compare the force–displacement curve obtained from the simulation to the experimental record prior to the damage initiation;
- Modify the value of parameters based on the deviation exhibited from the comparison;
- Repeat previous three steps till the difference between experimental and numerical force–displacement curves for all the tests is minimised.

The calibrated  $c_0^s$  and  $m$  are 0.93 and 5.0, respectively. The comparison of the force–displacement curves between experiments and simulations with different yield criteria for notched dog-bone and flat-grooved tensile tests is shown in Fig. 6.3. For both specimens, Mises criterion overestimate the force with an error about 2.3% and 2.2% respectively, while with the Lode correction in the advanced stress-state-dependent yield function the relative errors of the force prediction for both cases are reduced to less than 1%. Note that the error is only calculated until the point of damage initiation, and the subsequent mechanical behaviour will be subjected to the damage-induced softening correction. Here, only the comparison of the dog-bone specimen ( $R=50$  mm) and the plane-strain specimen ( $R=7.5$  mm) is demonstrated for the respective group. The other geometries behave likewise.

#### Bulge test

The experimental procedure and the data processing of the bulge test are described in section 5.1.1.1. In the FE simulation, a quarter of the whole test assembly is modelled because of the geometrical symmetry. Although an axisymmetric condition exists in the bulge test, a quarter of the specimen is still adopted to guarantee the exclusion of the numerical influence on the material parameter calibration by using the same type and size of the element as other

simulations. In the model, the drawing die and blank holder are modelled as rigid bodies. A surface-to-surface contact is applied between the specimen and the drawing die as well as between the specimen and the blank holder with a friction coefficient of 0.3. The same iterative procedure is performed with the previously calibrated  $c_0^s$  and  $m$  to determine  $c_0^c$ . As shown in Fig. 6.4, the pressure predicted by Mises plasticity is beyond the experimental data. With a fitted value of  $c_0^c$  as 0.97, a good agreement with the experimental curve is achieved.

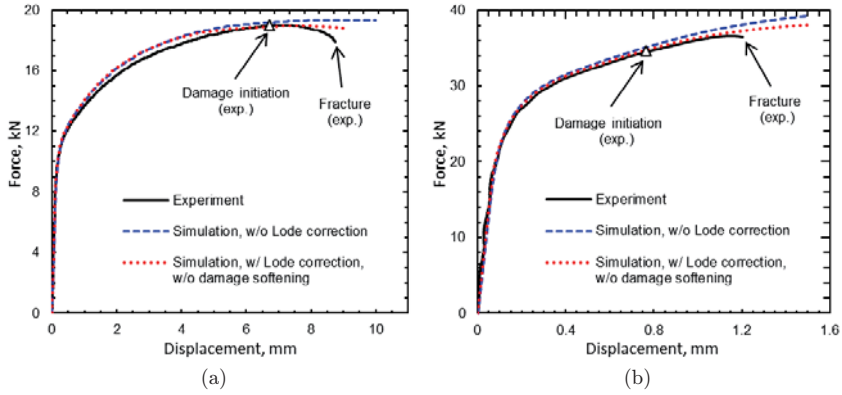


Fig. 6.3: Comparison of the experimental and numerical load vs. displacement curves for (a) the notched dog-bone specimen ( $R=50$  mm), (b) the flat-grooved specimen ( $R=7.5$  mm).

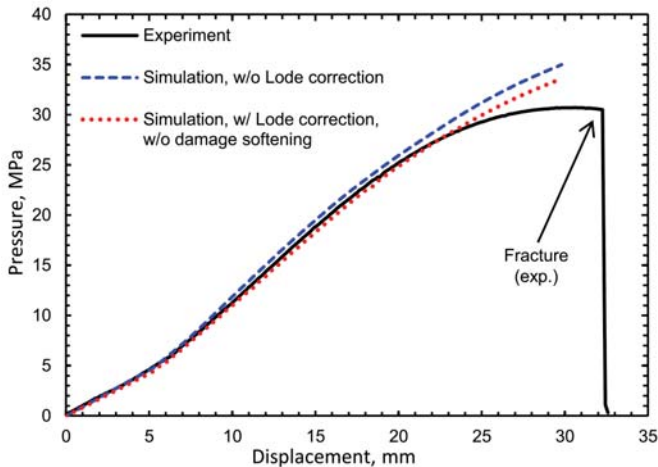


Fig. 6.4: Comparison of the experimental and numerical load vs. displacement curves for the bulge test.

### 6.2.1.3 Calibration of the damage initiation locus

In this section, three different types of tensile test are adopted to calibrate the corresponding parameters, central-hole, pure-shear and flat-grooved tensile tests. To obtain the data points in the space of  $\eta$ ,  $\bar{\theta}$ , and  $\bar{\epsilon}_1^p$ , the damage initiation instant and location need to be determined from experiments by the DCPD method and fractography analysis. Note that only the fractured surfaces of the specimens are subjected to the investigation. The local data history of these variables at the critical spot is obtained from the subsequent numerical simulations.

#### Central-hole tensile test

The specimen geometry and the experimental procedure are described in section 5.1.1. The fractured surface of the central-hole specimen is shown in Fig. 6.5. A “V” shape fracture mode is observed at the inner edge of the hole and extended along the transverse axis. It is similar to the “cup-cone” fracture model often observed in the round specimens. The crack/damage is initiated at the intersection of the circular cut and the transverse axis in the middle plane of the specimen. The SEM fractographs are investigated at the crack initiation spot to analyse the corresponding damage mechanisms. As shown in Fig. 6.5, a mass of voids can be observed. They are mostly presented in spherical shapes, except for some linked or enlarged voids. Most voids are relatively large and at the similar size. This type of void is often referred to as the primary void, while the other type of void with smaller size is referred to as the secondary void which is assumed to be nucleated during the primary voids coalescence at smaller microstructural constituents [110]. A limited number of secondary voids is observed.

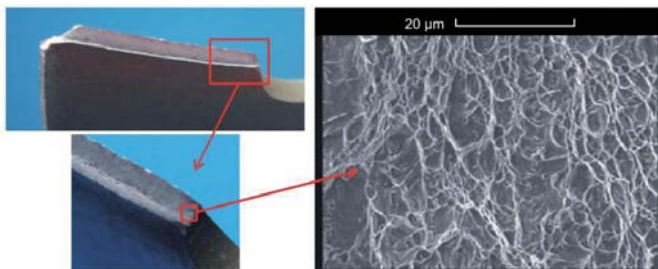


Fig. 6.5: Fractographs of central-hole specimen.

After the numerical simulation, as it can be seen in Fig. 6.6, the strain is concentrated at the region where the crack/damage initiation was observed in the experiment. The corresponding local data for all geometry configurations are extracted at the same spot and plotted in Fig. 6.6. For each configuration, the stress triaxiality and Lode angle parameter are almost constant

during the deformation history. This behaviour facilitates the minimisation of the error which resulted from the experimental damage initiation determination in the comparison of the dog-bone specimens, of which the stress triaxiality and Lode angle parameter both exhibit an increasing trend as the load increases. Bao et al. [154] studied the influence of the circular cut radius on the stress triaxiality and showed that there was no obvious change of the stress state (uniaxial) with only varied circular cut radii. However, in the present study by change of the a/b ratio of the elliptical cut, more stress states in addition to uniaxial tension are generated with increased stress triaxiality and decrease of Lode angle parameter, as shown in Fig. 6.6.

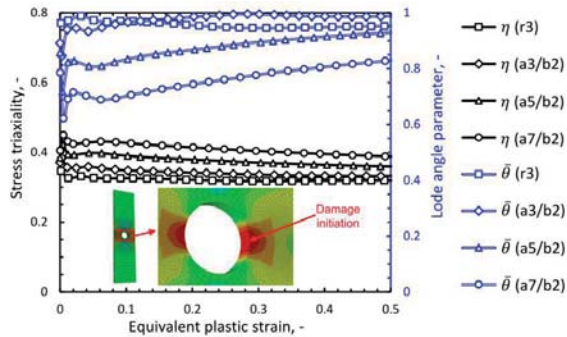


Fig. 6.6: History of stress triaxiality and Lode angle parameter for central-hole specimens.

### Pure-shear tensile test

The specimen geometry and the experimental procedure of the pure-shear tensile test are described in section 5.1.1. As shown in Fig. 6.7, a flat shearing fracture mode is observed. It can be determined that the damage initiation spot is on the edge of the thinnest part of the specimen close to the holes. In contrast to the void-dominant mechanism, the cause of damage in the pure-shear specimens is the formation of shear bands.

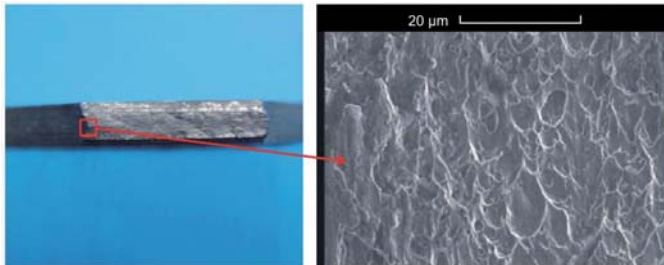


Fig. 6.7: Fractographs of pure-shear specimen.

Due to the symmetry in the thickness direction, 1/2 of the specimen is modelled. In Fig. 6.8, one can see that the strain is concentrated at the same place as observed in fractographs. The local variables, stress triaxiality, Lode angle parameter and equivalent plastic strain, are extracted at that element and plotted. The Lode angle parameter keeps constant at 0 during the whole deformation, and the stress triaxiality deviates from 0 with a small number between 0.05 and 0.08. It is proved that with the current design of the specimen, shear stress state is achieved by the uniaxial tension loading.

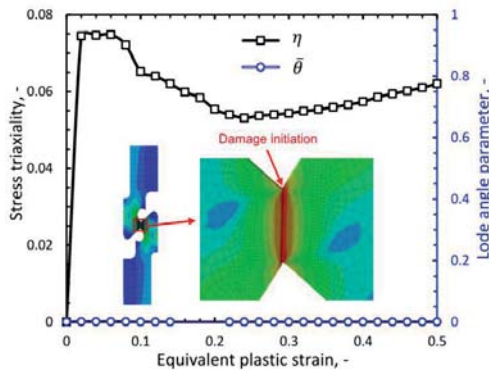


Fig. 6.8: History of stress triaxiality and Lode angle parameter for pure-shear specimen.

#### Flat-grooved tensile test

The global force and displacement history and the critical load to damage initiation for flat-grooved specimens were obtained in section 6.2.1.2. Only the critical location, at which the local variables are extracted, needs to be identified. The studies on fracture surface morphology and subsequent SEM fractographs are performed. As shown in Fig. 6.9, the fracture mode is a mixture of “V” shape fracture and slant fracture. At the centre of the specimen, the “V” shape fracture mode is present. It extends along the transverse axis in both directions. At a certain point, the fracture mode becomes unstable and transmits into a slant fracture. At the end of the specimen in the transverse direction, a diffused neck is also formed. On the other hand the crack initiation is not found at the surface of the specimen from the camera attached on the tensile machine. It can be determined that the damage initiation takes place at the centre of the specimen and propagates through the transverse and thickness directions. As observed in the subsequent SEM fractographs, the void-controlled damage mechanism is dominant. In

contrast to the central-hole specimen, the secondary voids in this case account for the major fraction.

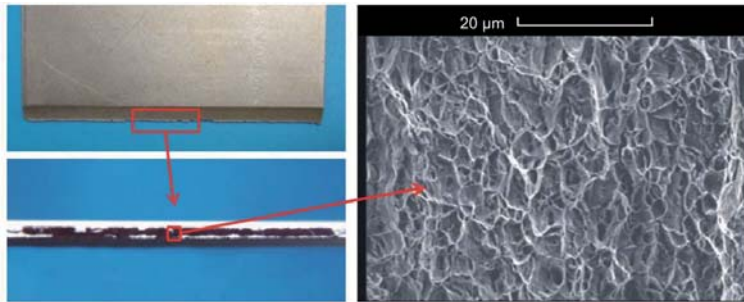


Fig. 6.9: Fractographs of plane-strain specimen.

As shown in Fig. 6.10, the stress triaxiality of specimen R=15 mm starts with 0.57 (the initial stress triaxiality of the plane-strain tension stress state), and increases gradually with the deformation. The Lode angle parameter starts, by contrast, with a slight deviation from zero, but reaches zero with further loading. With the decreased radius of the notch, the stress triaxiality increases accordingly, but the Lode angle parameter continues to follow the similar trend. This guarantees that various stress states are achieved at the crack initiation at the region of the low Lode angle parameter.

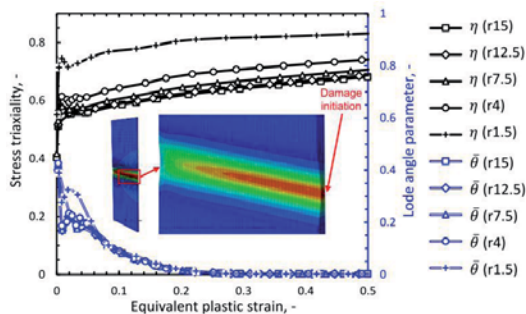


Fig. 6.10: History of stress triaxiality and Lode angle parameter for plane-strain specimens.

#### Damage initiation locus (DIL) fitting

With the histories of  $\eta$ ,  $\bar{\theta}$ , and  $\bar{\epsilon}_1^p$  obtained from the simulation and the critical instant of damage initiation from experiments, the experimental data points are determined. These data points are subsequently used to calibrate the DIL. One should note that neither compression nor the biaxial tension test is introduced due the technical difficulties in conducting the tests

or the damage initiation measurement system. No data in the negative Lode angle region is therefore accessible from the experiments. A symmetric damage initiation locus with only material parameters  $C_1 - C_4$  is employed, as shown in Eq. 3.20.

The conventional calibration procedure, in which  $C_1$  and  $C_2$  are fitted by the central-hole specimen, and  $C_3$  and  $C_4$  are fitted by the plane-strain specimens and pure-shear specimen, is not used here. Based on the quantitative study of the history of the local variables, the values of  $\eta$  and  $\bar{\theta}$  are not constant in the entire deformation process. More importantly,  $\bar{\theta}$  also deviates from 1 and 0 for central-hole and flat-grooved specimens, respectively, when the geometry is varied, as demonstrated in Fig. 6.6 and Fig. 6.10.

Consequently, four parameters are calibrated based on all the data points obtained from the three types of experiments using the nonlinear least square surface fitting in Matlab. The calibrated symmetric DIL and the experimental data used to calibrate the parameters are shown in Fig. 6.11. The corresponding equation with the calibrated parameters is as follows:

$$\bar{\epsilon}_1^p = [0.43e^{-1.14\eta} - 0.12e^{-0.98\eta}]\bar{\theta}^2 + 0.12e^{-0.98\eta} \quad \text{Eq. 6.2}$$

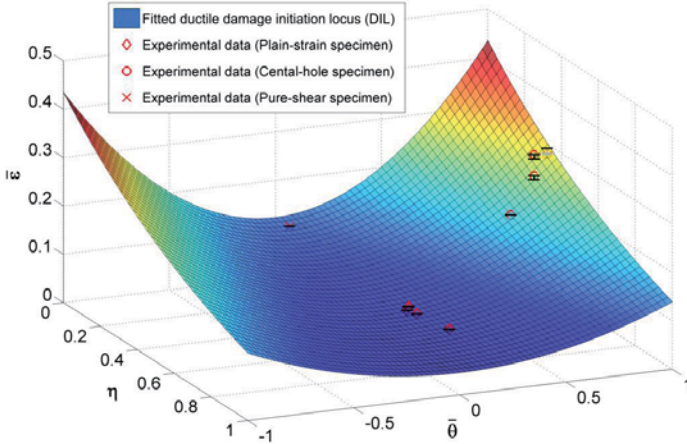


Fig. 6.11: Damage initiation locus (DIL) and experimental data points of DP600 in the space of stress triaxiality  $\eta$ , Lode angle parameter  $\bar{\theta}$  and equivalent plastic strain  $\bar{\epsilon}_1^p$ .

#### 6.2.1.4 Calibration of the damage evolution law

With the previously calibrated parameters, the material behaviour is characterised till the moment of damage initiation. Once this stage is reached, the damage-induced softening plays

a significant role during the post-crack-initiation deformation. In this section, the parameters,  $G_f$  and  $D_{cr}$ , need to be determined from the experiments.

By comparing the experimental and numerical material responses, an iterative procedure is employed to identify  $G_f$ . Depending on the data chosen for the comparison, there are two approaches to carry out the iterative procedure:

- An approach based on the true stress–strain curve.
- An approach based on the force–displacement of certain geometry configuration of tests.

One should note that both of these two sets of data need to contain the material response information from the beginning of the deformation to the final fracture. Considering the numerical cost and time effort, this first approach is easier to achieve. To obtain the numerical stress–strain curve, only a unit cell element tensile or compression test needs to be conducted. On the other hand, the experimental true stress–strain curve till the final fracture is difficult to obtain. Mirone et al. [158] proposed a phenomenological formula for true stress and strain curve after necking for a round bar tensile test. However, the procedure to validate the formula is rather complex, and its application to the sheet tensile test has not been verified. Therefore, in this study, the second approach is adopted. The experimental data for this approach, in contrast to the first one, is easy to access, while the numerical cost is rather high.

The notched dog-bone specimen with circular cut ( $R=50$  mm) is chosen to be the reference experimental result. The corresponding numerical simulation results with different  $G_f$  values are compared with the experimental one, as shown in Fig. 6.12 (a). It can be determined that the force–displacement curve with  $G_f$  of 300 fits the experimental result best before the occurrence of the final fracture. To predict the macro fracture,  $D_{cr}$  is therefore calibrated based on the same specimen. As shown in Fig. 6.12 (b), a good agreement is achieved when  $D_{cr}$  is considered as 0.1. Once  $D_{cr}$  is reached for all the integration points in an element, it is considered that the load carrying capability of this element is totally lost, and the element is removed from the model for the following computation by the element deletion technique. The mesh size is therefore sensitive to the solution. In this study, a mesh size of  $0.1$  mm  $\times$   $0.1$  mm  $\times$   $0.1$  mm is employed. It is small enough that the mesh dependency of local variables is not pronounced. More importantly, it also corresponds to the characteristic size of the macro crack formation observed by eye. On the other hand, the characteristic length  $L$  associated with an integration point is introduced to the formulation of  $D$ . The mesh dependency in the finite element model is therefore reduced during the damage softening part by this intrinsic length.



However, the calibrated parameters are consequently related to the mesh size. Thus, a consistent mesh size is conducted in the calibration models as well as the following verification simulations.

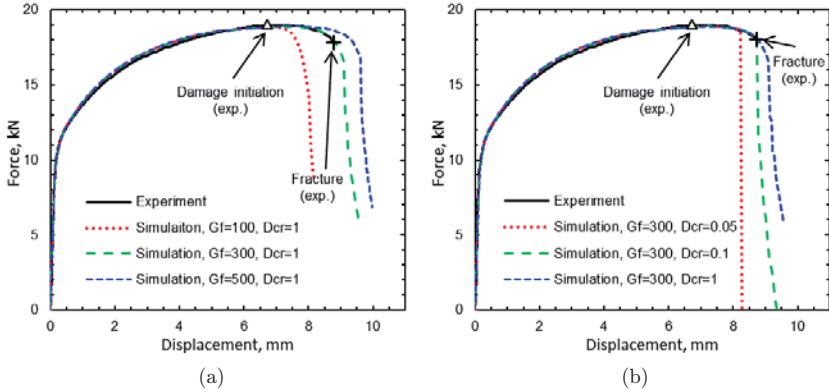


Fig. 6.12: Comparison of the experimental and numerical load vs. displacement curves for the notched dog-bone specimen ( $R=50$  mm) (a) to determine the value of material parameter  $G_f$ , (b) to determine the value of material parameter  $D_{cr}$ .

## 6.2.2 Validation and discussion

### 6.2.2.1 Failure prediction of flat-grooved tensile test

A flat-grooved tensile test was used in the calibration of both plasticity and damage initiation locus parameters, except for the determination of  $G_f$  and  $D_{cr}$ . The complete set of parameters is first applied to this specimen to predict the materials behaviour from the plastic deformation to the final fracture. The experimental and numerical force–displacement responses are compared in Fig. 6.13. During the first phase, a good agreement is achieved till the damage initiation. Secondly, the damage initiation point is compared to validate the parameters for the crack initiation locus. In the simulation, this point is obtained at the moment when the first element in the model reaches the damage threshold. Compared with the experimental result, almost the same displacement to the damage initiation is predicted by the numerical salutation. However, the displacement to the final failure is estimated by the simulation at about 10% more than the experimental result. The reason for the over-prediction lies in the description of the damage evolution. The current model assumes that the onset of damage is dependent on the stress state, whereas the internal damage variable  $D$  relies only on the accumulated plastic

strain, not yet depending on the stress state, i.e. the stress triaxiality and Lode angle parameter. Nevertheless, due to the implementation of the damage initiation threshold which depends on the stress states, the prediction is improved from the modelling based on the conventional CDM model [83; 158].

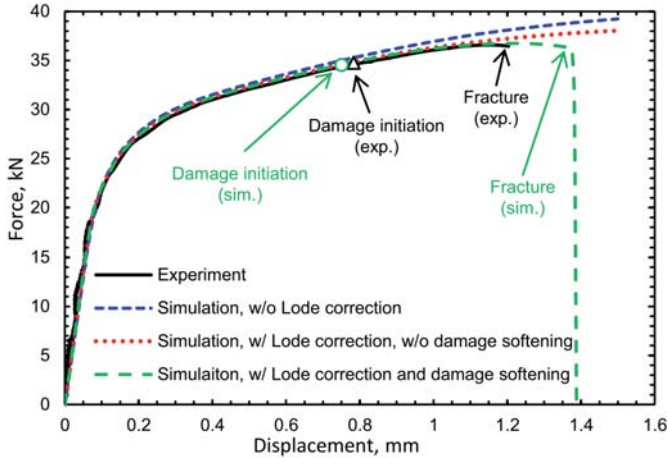


Fig. 6.13: Validation of the model by comparison of the experimental and numerical load vs. displacement curves for the plane strain specimen ( $R=7.5$  mm).

#### 6.2.2.2 Failure prediction of bulge test

The bulge test was used only to calibrate the parameters in the plasticity model. With the further-calibrated parameters from other tests, the numerical prediction of the pressure–displacement response is compared to the experimental one in Fig. 6.14. Due to the difficulty in attaching the measurement instruments, the comparison between experimental and numerical results on the damage initiation points is not conducted. Before the damage initiation point detected by simulation, the Mises plasticity model gives a relative error about 5%, while with the Lode correction the error reduces to less than 2%. In the whole process of the deformation, the numerically predicted pressure–displacement response coincides with the experimental one including the prediction of the final fracture.

#### 6.2.2.3 Failure prediction of newly designed notched dog-bone tensile test

A newly designed dog-bone tensile specimen, which was not involved in any calibration procedures, is employed to validate the model and the calibrated parameters. The design is based on the dog-bone specimens. A different configuration of a circular cut with a notch radius

of 30 mm is introduced at the centre of the gauge section. The minimum width of the specimen is accordingly 16.6 mm. The tensile experiment, coupled with the DCPD method, is carried out. The comparison of force–displacement responses is shown in Fig. 6.15. An overall good agreement is achieved between the experimental and numerical results.

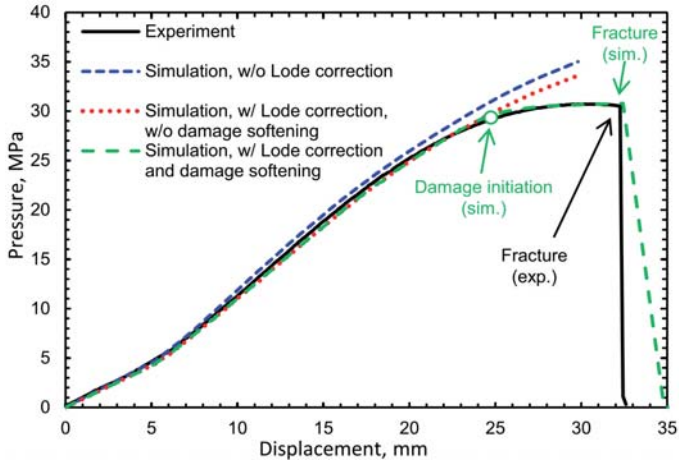


Fig. 6.14: Validation of the model by comparison of the experimental and numerical load vs. displacement curves for the bulge test.

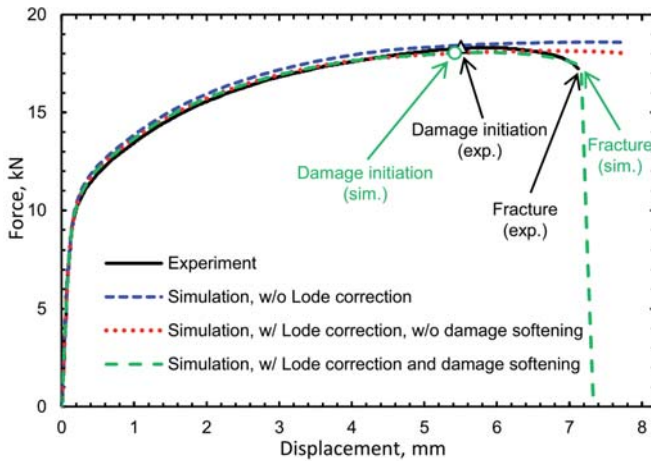


Fig. 6.15: Validation of the model by comparison of the experimental and numerical load vs. displacement curves for the newly designed dog-bone specimen ( $R=30$  mm).

## 6.3 Parameter calibration and validation for heavy plate S355J2+N

### 6.3.1 Calibration programme and FE models

For the heavy plate material, three types of tests are involved for the material parameter calibration and validation, SRB tensile tests, NRB tensile tests and SENB tests. The SRB tensile test is performed for the based strength properties and flow curve calibration. The NRB tensile test and SENB test are performed to characterise the cold formability under different stress states and calibrate the parameters for the model. This selection is due to the fact that there are distinctive differences in the states of stress typically present in these specimens:

- In NRB specimens, the Lode angle parameter in the elements on the rotation axis is one because of the axial symmetry of the specimen, and the stress triaxiality can be adjusted by the notch geometry.
- In SENB specimens, the plane strain state at the mid-plane in the thickness direction results in the Lode angle parameter in the vicinity of zero. Furthermore, the stress triaxiality can be adjusted by applying additional side grooves and by adding a fatigue pre-crack.

For the selected material, the influence of the stress state on the plasticity behaviour is not considered for simplicity. Mises plasticity model is used for the material flow behaviour before damage initiation. Therefore, only the material parameters in the damage initiation locus and damage evolution description are calibrated and further validated.

The specimen geometry and the experimental procedure of the NRB tensile test are described in section 5.1.2. After the tests were performed, the corresponding FE models are constructed in the commercial FE code Abaqus. The NRB tensile test is axisymmetric and a 2D model can be naturally constructed. However, for keeping the consistency of element type and size across all the models, including the following SENB tests, a 3D model corresponding to one eighth of the specimen is built, as shown in Fig. 6.16.

One can also notice that only the part of the sample within the measurement of the extensometer is modelled, as the displacement is measured within this height and force is only concentrated around the notch region. During the deformation, the nodes on three symmetrical planes are basically restricted on moving in the corresponding normal direction, while a constant velocity is applied to the nodes on the top of the model.

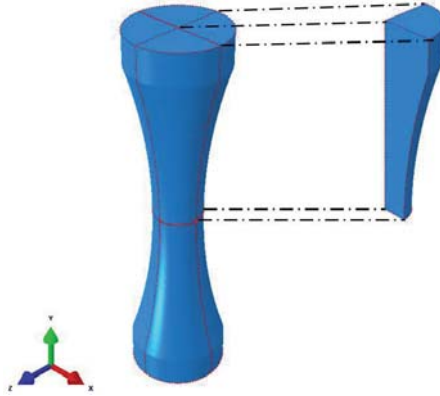


Fig. 6.16: The symmetry of NRB tensile test in the FE model.

As mesh is a key factor influencing the FE simulation, especially damage mechanics simulations, in this study, we are using always the consistent element type and size at the critical plastic deformation zone across all the models to avoid the severe impact of mesh size. As shown in Fig. 6.17, the bottom of the NRB model is meshed with fine and regular 3D brick elements with reduced integration (C3D8R), while the rest part of the model features a coarser mesh. This concept of meshing contributes to save time for calculations, at the same time, keeps the fine mesh as consistent as necessary. As the setting of the simulation for the sheet steel DP600, the element size of the fine mesh here is also  $0.1 \text{ mm} \times 0.1 \text{ mm} \times 0.1 \text{ mm}$  for the same reason.

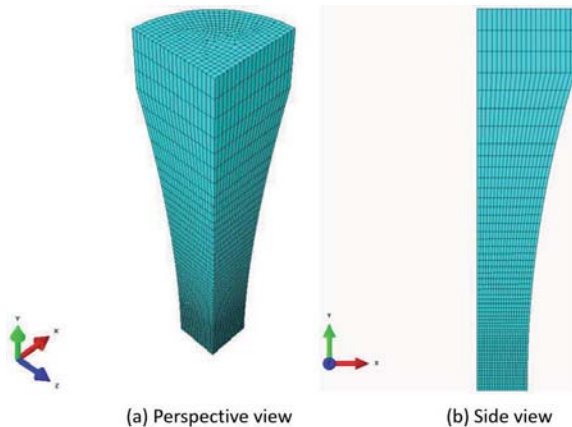


Fig. 6.17: The enmeshment of the study part in NRB tensile test model.

For the simulation of SENB tests, the assembly of the FE model of a SENB test is illustrated in Fig. 6.18. For these simulations, only half a sample is modelled for reasons of symmetry. The elements are again of the type C3D8R, and also the enmeshment is similar to the NRB specimen since the elements in and around the ligament had a size of  $0.1 \text{ mm} \times 0.1 \text{ mm} \times 0.1 \text{ mm}$ . As presented in Fig. 6.19, the remaining part of the specimen has a significantly coarser enmeshment to improve the computational efficiency. The support bearings and the punch are modelled as rigid solids, and a Coulomb friction value of 0.1 is assumed to consider the contact phenomena between sample and rollers. According to the experiment, two supporting rollers on the top are fixed in all degree of freedoms, while the bottom roller is lifted up with a constant velocity to bend the specimen till it is fractured.

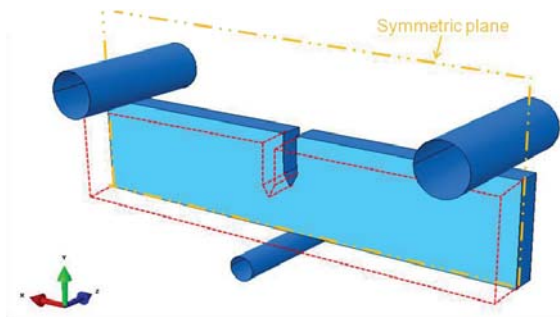


Fig. 6.18: The configuration of SENB test in the model.

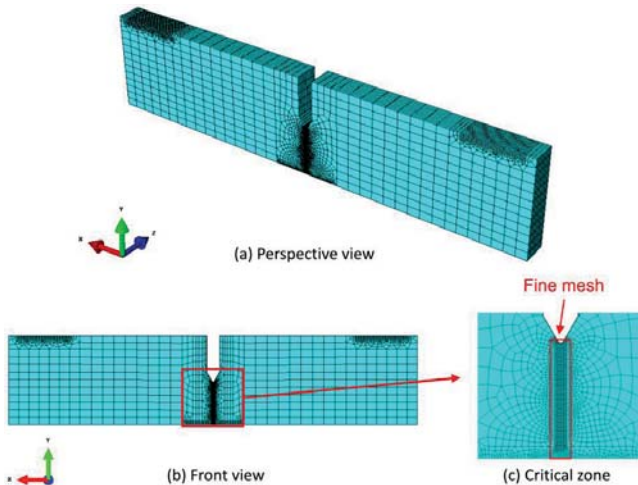


Fig. 6.19: The enmeshment of the study part in SENB test model.

### 6.3.2 Parameter calibration

#### 6.3.2.1 Calibration of flow curve

The experimental setup and specimen geometry of the SRB tensile tests are described in section 5.1.2. Due to the observed alignment of pearlite, these tensile tests were performed on specimen that were cut longitudinal (“L”) and transverse (“T”) to the rolling direction. While Tab. 6.2 summarises the characteristic values determined in these tests, the engineering stress–strain curves for both directions are shown in Fig. 6.20. Obviously, there is no pronounced anisotropy in the strain hardening behaviour since the curves for L- and T-specimens nearly coincide with each other from the flow stress to the ultimate tensile strength.

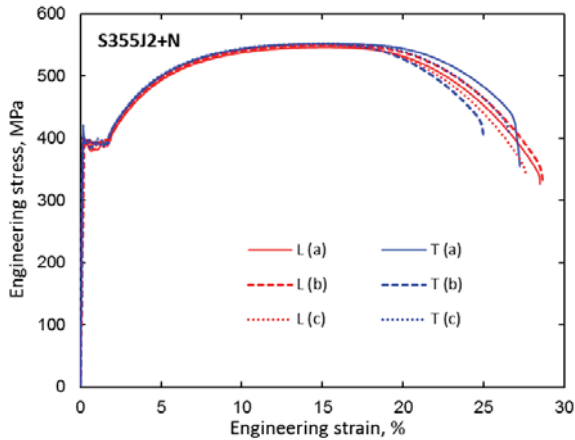


Fig. 6.20: Engineering stress–strain curves of steel S355J2+N taken longitudinal and transverse to the rolling direction.

Tab. 6.2: Mechanical properties of steel S355J2+N.

Loading direction	Young’s modulus, $E$	Yield strength, $R_{p0.2}$	Tensile strength, $R_m$	Uniform elongation, $A_u$	Fracture elongation, $A_5$
L	216 GPa	398 MPa	549 MPa	14.4%	27.6%
T	198 GPa	405 MPa	551 MPa	14.8%	26.4%

Since there is no significant anisotropy in the strain hardening behaviour, only one flow curve was determined out of the experimental results. This flow curve was mathematically fitted according to Hollomon equation and extrapolated after the experimentally determined part. For steel S355J2+N,  $A = 866.1 \text{ MPa}$  and  $n = 0.157$  were calibrated by least square fitting.

The experimental true stress–strain curve and the extrapolated one are both shown in Fig. 6.21.

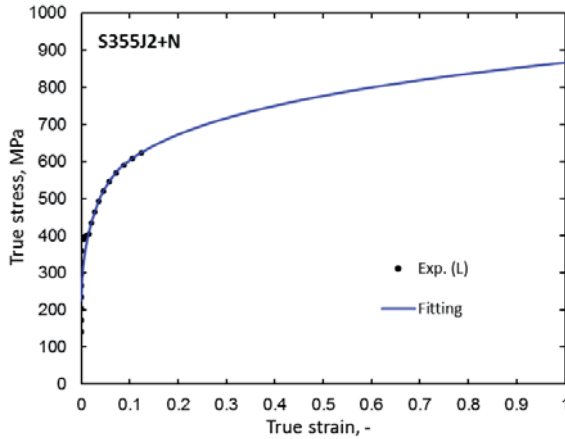


Fig. 6.21: Experimental true stress–strain curve and the extrapolate flow curve according to Hollomon equation.

### 6.3.2.2 Calibration of the damage initiation locus

In the left column of Fig. 6.22, the global experimental and numerical force–displacement curves are given together with the development of the electric potential for all NRB tests. In addition, the dotted line highlights the instant of damage initiation as determined by the moment, at which a nonlinear sudden increase of the potential appears, as indicated by the red line. From the curves it can be concluded that the classical Mises plasticity model provides a sufficient description of the plastic deformation behaviour as long as damage initiation has not yet taken place.

For all investigated samples, damage initiation happens after the maximum force has been reached. The critical zone of damage initiation is to be the place subjected to the largest deformation. In the case of NRB tests, it is corresponding to the centre of the specimen. Taking an example of NRB specimen with notch radius of 42 mm (R42), the centre zone also features the maximum equivalent plastic strain (PEEQ), as shown in Fig. 6.23. Therefore the centre element is considered as the critical element, and the local variables, such as equivalent plastic strain, stress triaxiality and Lode angle parameter, are evaluated from the critical element for the determination of DIL.



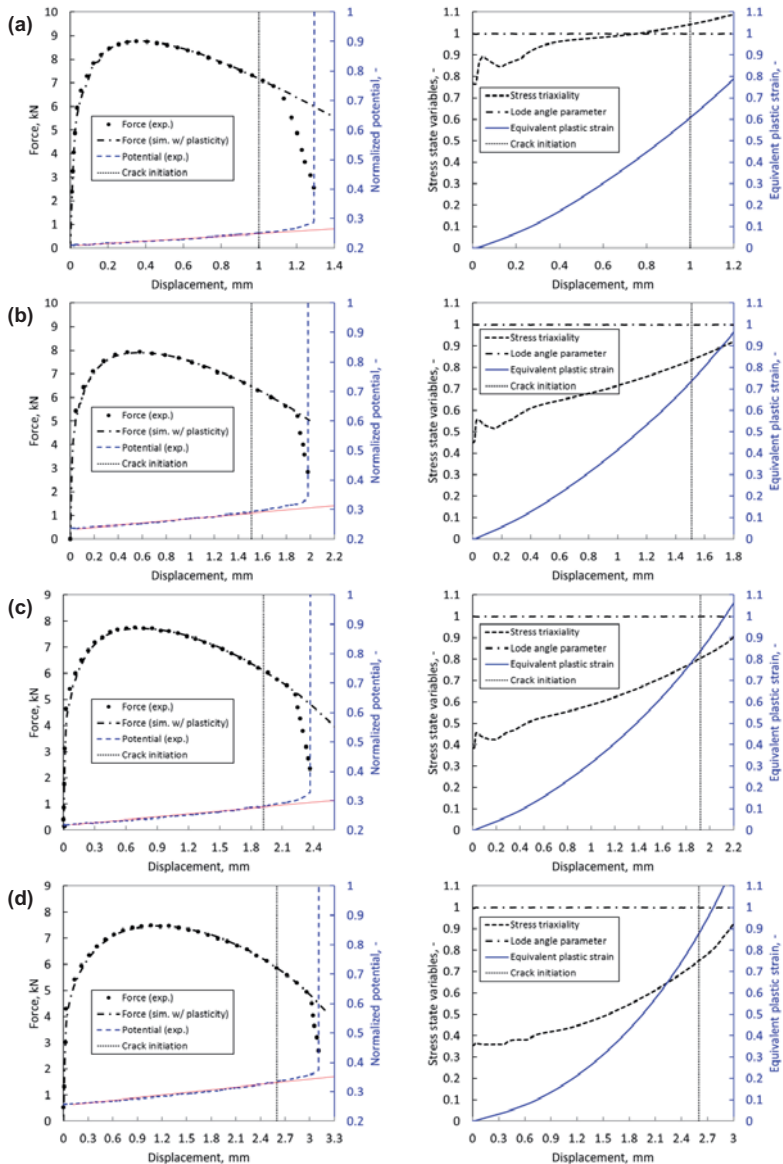


Fig. 6.22: Results of the NRB tests: experimental and numerical force–displacement curves with the measured electric potential (left column of the figure) and the history of the local variables, including stress triaxiality, Lode angle parameter and equivalent plastic strain of the critical element in simulation (right column of the figure); (a) to (d) are corresponding to four geometries of NRB tests, R2, R6, R12 and R42, respectively.

The histories of these three local variables for all NRB specimens are presented in the right column of Fig. 6.24. The stress triaxiality gradually increases during the deformation for each specimen, while the Lode angle parameter stays as one. In addition, the displacement to damage initiation is also indicated by the dotted line. The instant values of those variables at the damage initiation are all listed in Tab. 6.3. One can note that, with the smaller notched radius, the critical stress triaxiality gets higher.

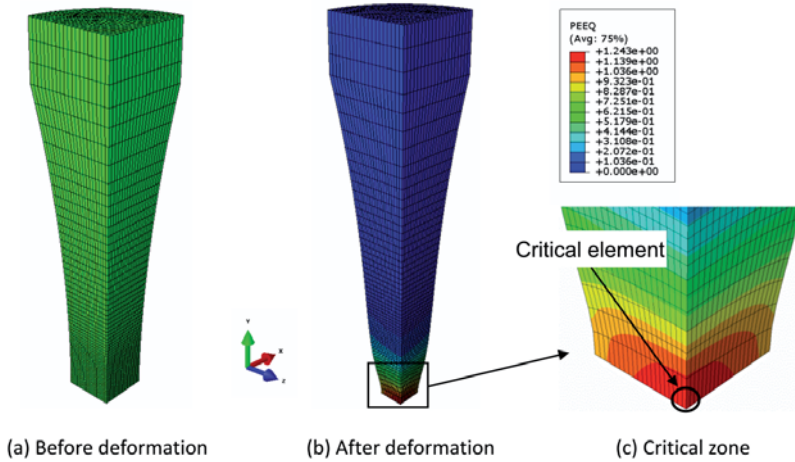


Fig. 6.23: Illustration about the deformation NRB test and the critical element where the local variables are extracted.

In analogue to the presented results for the NRB tests, the same procedures are performed for the SENB tests. Experimental and numerical force–CTOD curves for all tests are plotted in the left column of Fig. 6.24. For all four different specimen geometries, the divergence between the experimental and numerical results is less than 2.5 % in force before the damage initiation. In addition, the electric potential history is also plotted for the evaluation of the damage initiation instant and it is again indicated by the dotted line. Different from NRB tests, here the damage initiation takes place in a very early stage of deformation, especially for pre-cracked samples, which is rooted to the design and loading of the samples. However, what is in common with NRB tests is that soon after the damage initiation takes place, the force predicted by the elastoplastic FE simulation with Mises plasticity deviates from the experimental result.

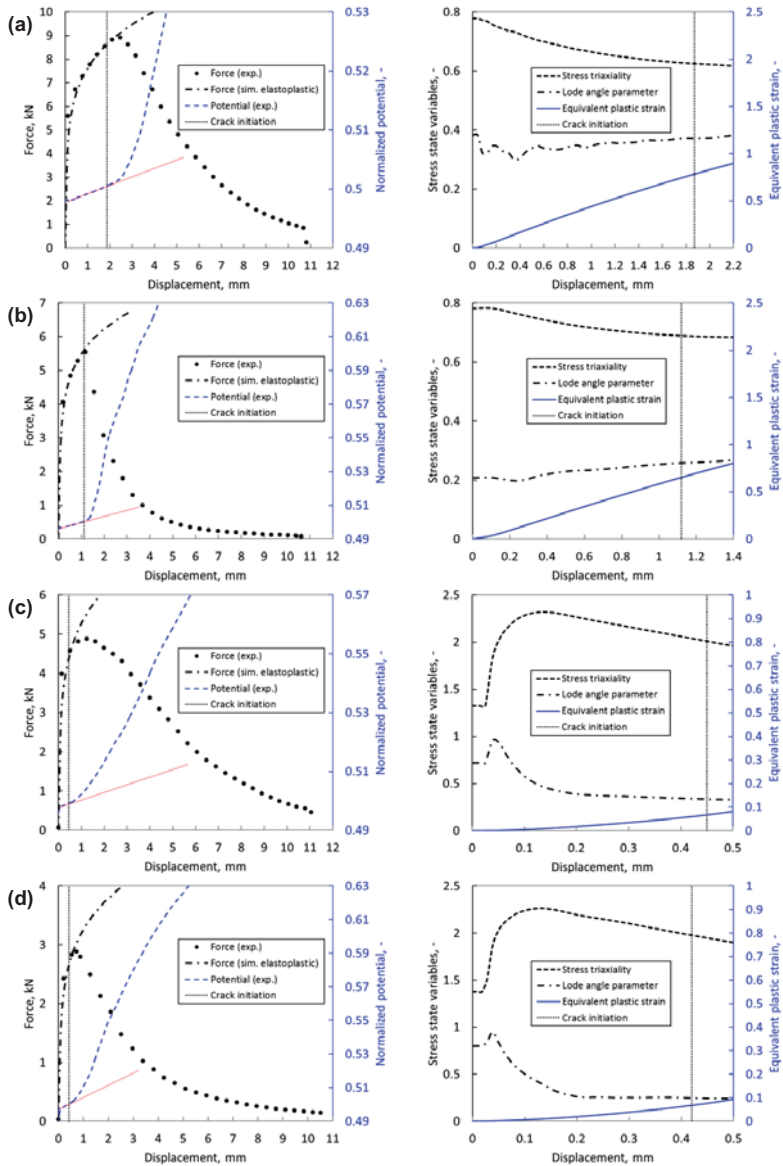


Fig. 6.24: Results of the SENB tests: experimental and numerical force–displacement curves with the measured electric potential (left column of the figure) and the history of the local variables, including stress triaxiality, Lode angle parameter and equivalent plastic strain of the critical element in simulation (right column of the figure); (a) to (d) are corresponding to four geometries of SENB tests from a to d.

This common feature also validates the evaluation of damage initiation, since the damage initiation describes a microscale phenomenon, and with the amount of damage accumulation, the influence of it is reflected by the “softening” in terms of force compared to the perfect elastoplastic deformation.

As proven by the experimental observation of the fracture surface, the first crack appears right beneath the pre-crack or notch (in specimens without pre-crack) in the mid-plane of thickness direction. The element at the same location also features the highest PEEQ during the deformation as indicated in Fig. 6.25. Therefore, the local variables, stress triaxiality, Lode angle parameter and PEEQ are plotted as a function of CTOD in the right column of Fig. 6.24 for all SENB tests. Despite some uncertainty at the beginning of the deformation, the stress state variables show generally a steady trend. Specimen (a) and (b), both without pre-cracks, feature moderate stress triaxiality, but their Lode angle parameters are varied by the implementation of side groove. Specimen (c) and (d) both reach a high stress triaxiality state over 2.0, due to the existence of the sharp fatigue pre-crack. The pre-determined damage initiation displacement is also indicated in the figure and the corresponding critical values are summarised in Tab. 6.3.

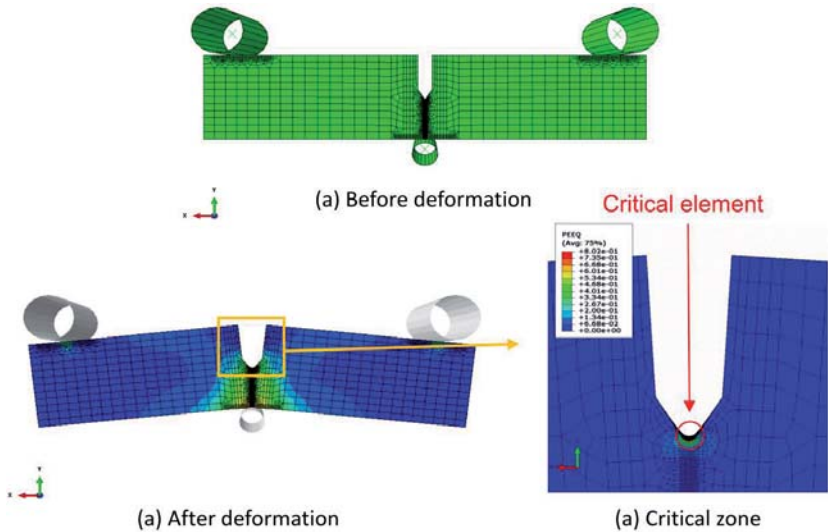


Fig. 6.25: The illustration of deformation for SENB test and the critical element where the local variables are extracted.

Tab. 6.3: All local variables corresponding to damage initiation for steel S355J2+N.

Specimen name	Displacement to damage, mm	Equivalent plastic strain, -	Stress triaxiality, -	Lode angle parameter, -
NRB-R2	1.0	0.607	1.045	1
NRB-R6	1.52	0.764	0.846	1
NRB-R12	1.92	0.836	0.802	1
NRB-R42	2.6	0.892	0.756	1
SENB-a	1.87	0.806	0.681	0.347
SENB-b	1.12	0.677	0.732	0.259
SENB-c	0.45	0.068	2.013	0.322
SENB-d	0.42	0.069	2.046	0.237

With all extracted local variables from critical element of both NRB and SENB tests at the damage initiation instant, the DIL is fitted by a nonlinear least squares method with trust-region algorithm in Matlab. The DIL function for steel S355J2+N with calibrated  $C_1$ - $C_4$  is given below:

$$\bar{\varepsilon}_1^p = [2.46e^{-1.35\eta} - 2.86e^{-1.95\eta}]\bar{\theta}^2 + 2.86e^{-1.95\eta} \quad \text{Eq. 6.3}$$

The fitted DIL together with the experimental data points are illustrated in Fig. 6.26 (a). As a symmetric DIL is adopted in the study, only the positive Lode angle parameter half is shown. To quantitatively evaluate the fitting quality, the residuals of the experimental data point from the fitted DIL are computed and visualised in Fig. 6.26 (b). Three relatively large residuals are resulting from specimen NRB-R12, SENB-a and SENB-b. The absolute value is about 0.02 for three cases, and the maximum relative error is less than 3% generated by sample SENB-b. Overall, the target equation shows satisfactory predictive capability within the studied range of stress states. To better analyse the influence of both stress triaxiality and Lode angle parameter on the damage initiation strain, a contour plot of the damage initiation strain in the space of stress triaxiality and Lode angle parameters is shown in Fig. 6.26 (c). As large strain gradient is observed across the change of the stress triaxiality from 0.4 to 2.2, the damage initiation is strongly influenced by hydrostatic pressure for steel S355J2+N. On the contrary, the strain gradient shows relatively minor changes for Lode angle parameter from zero to one, but the influence of Lode angle becomes relatively more obvious with the increase of stress triaxiality.

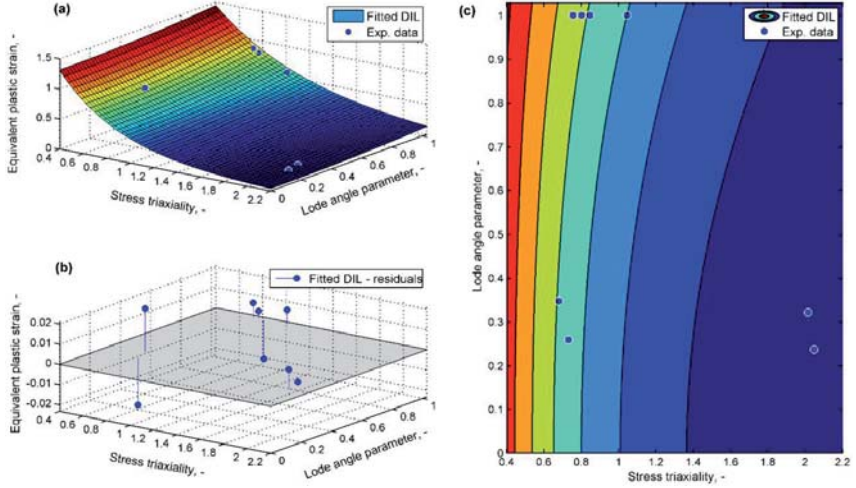


Fig. 6.26: Fitting of damage initiation locus (DIL) for steel S355J2+N: (a) experimental data points and fitted DIL in the space of equivalent plastic strain, stress triaxiality and Lode angle parameter, (b) residuals of the experimental data points from the fitted DIL, (c) equivalent plastic strain contour in the space of stress triaxiality and Lode angle parameter.

### 6.3.2.3 Calibration of the damage evolution law

After the DIL is determined, only the parameters  $G_f$  and  $D_{cr}$  remain for calibration. For this purpose, an iterative study was performed in order to find a set of parameters that delivers a sufficient agreement between experimental and numerical force vs. displacement curves for both NRB and SENB tests. In the current configuration of MBW model, these two damage evolution parameters are considered as constant under various stress states, as dependency of damage on stress state is considered in the description of damage initiation. However, note that although these two parameters are constant, the damage evolution rate is not a constant for various stress states, because  $\sigma_{y0}$  that characterises the yield stress at the onset of damage is different according to the definition of DIL. When damage initiates in the late stage of plastic deformation, its evolution naturally processes a faster rate than early damage initiation. Moreover, the combination of  $G_f$  and  $D_{cr}$  cannot be unique due to their possible interaction. For calibration,  $D_{cr}$  is assumed to be one, i.e. the material point could undergo a gradual stiffness degradation till it becomes zero. Under the constant assumption of these two parameters, only one sample, NRB-R2 is used for the iterative fitting of parameter  $G_f$ . For this

purpose, simulations with damage initiation and evolution are run with various values of  $G_f$  and finally  $G_f = 7$  yields the best fitting of force–displacement response to the experimental one, as shown in Fig. 6.27.

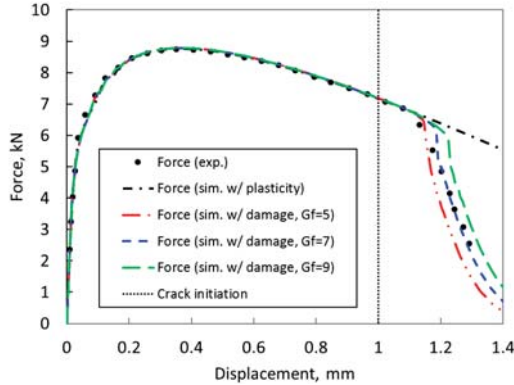


Fig. 6.27: Material parameter calibration of  $G_f$  with different values on NBR sample R2.

### 6.3.3 Validation and discussion

As  $G_f$  and  $D_{cr}$  are assumed to be constant, they only provide the basic characteristic of the damage evolution process of the material. Therefore, the use of the set of parameters calibrated only on sample NRB-R2 in other geometries to simulate the complete force–displacement or force–CTOD response serves as a verification procedure of not only these two damage evolution parameters, but also the damage initiation parameters, because the final damage evolution rate under different stress states is also decided by  $\sigma_{y0}$ , which is defined by the calibrated DIL. For this purpose, the completely calibrated MBW model with damage initiation and evolution parameters are applied to all the rest of specimens and their force–displacement/CTOD curves are presented in Fig. 6.28 (a) – (g) together with the experimental results.

Despite a deviation less than 10% observed in sample SENB-c, good agreements of the experiments and simulations are achieved. These results finally verify that the calibrated damage initiation and evolution parameters are suitable to describe the cold formability of steel S355J2+N.

## 6.4 Summary of the calibrated material parameters

In Tab. 6.4, all the material parameters, including the parameters for reference flow curves are listed for both steels DP600 and S355J2+N.

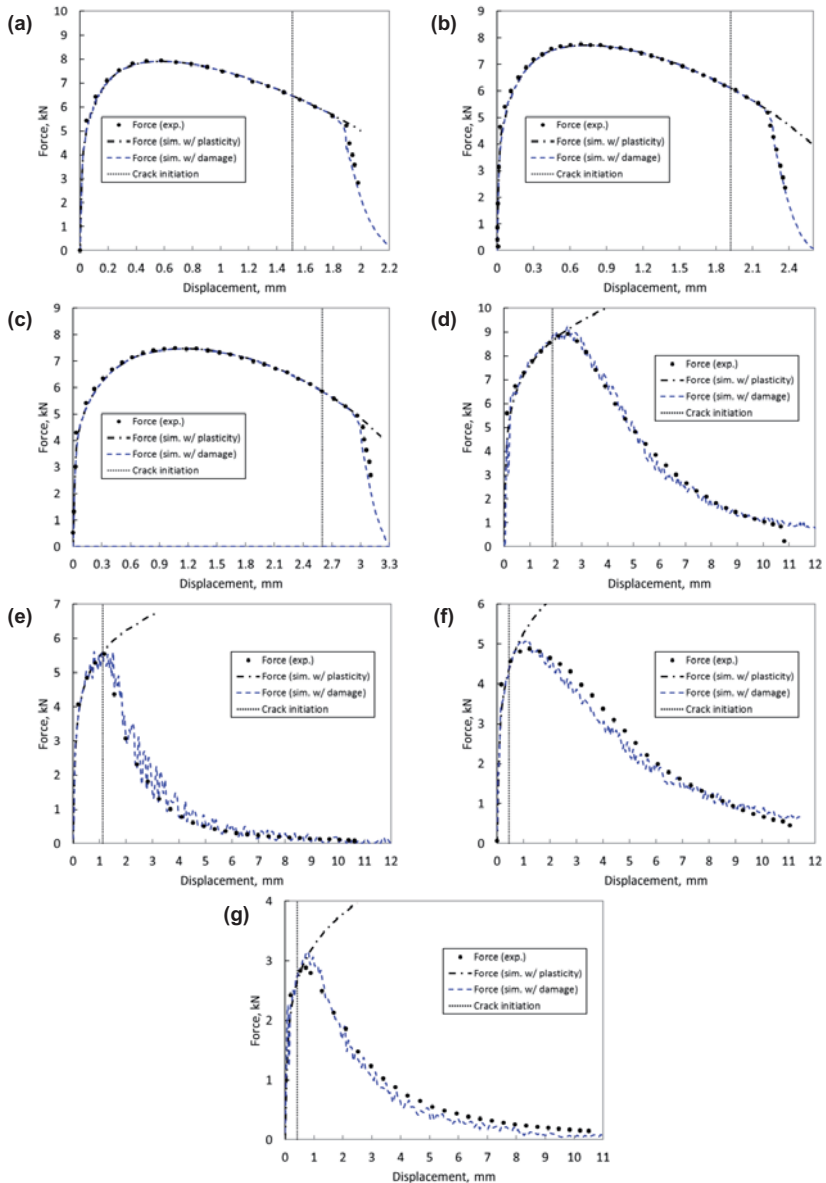


Fig. 6.28: Validation results for the NRB and SENB tests: force–displacement curves from experiment and damage mechanics simulations with the MBW model after parameter calibration; (a) to (c) are corresponding to four NRB tests, R6, R12 and R42, and (d) to (g) are corresponding to four SENB tests, a to d, respectively.



Tab. 6.4: Summary of all the material parameters in the MBW model for DP600 and S355J2+N.

Materials	Plasticity material parameters						Damage material parameters					
	Ref. flow curve		Stress-state correction				Damage initiation				Damage	
	$A$	$n$	$c_{\theta}^t$	$c_{\theta}^c$	$c_{\theta}^s$	$m$	$C_1$	$C_2$	$C_3$	$C_4$	$G_f$	$D_{cr}$
DP600	1201	0.198	0.93	1.0	0.97	5	0.43	1.14	0.12	0.98	300	0.1
S355J2+N	866.1	0.157	1.0	1.0	1.0	0	2.46	1.35	2.86	1.95	7	1.0

For the plasticity description of these two materials, the DP steel sheet owns higher yield strength and work hardening rate than the HSLA steel plate. The stress state dependent yielding and hardening is not obvious in the S355J2+N, so J2/Mises plasticity is used, whereas in the DP600 steel, the J3 correction by Lode angle effect is introduced. However, the correction based on the J3 effect is relatively minor.

For the damage part of these two steels, the difference is obvious. The 2D DILs are calculated under the plane stress assumption for a straightforward comparison. According to Eq. 3.12, the Lode angle parameter can be replaced by the stress triaxiality under plane stress assumption. Therefore, the DIL in the 3D space of  $(\bar{\epsilon}, \eta, \bar{\theta})$  is converted to the space of  $(\bar{\epsilon}, \eta)$  and they are plotted in Fig. 6.29. Under plane stress assumption, another space,  $(\epsilon_1, \epsilon_2)$  is often used for FLD characterisation. It is also adopted here to demonstrate the difference of the damage initiation between two steel grades. The 2D damage initiation curves can be equivalently transferred to the space of  $(\epsilon_1, \epsilon_2)$  according to Eq. A.19. The detailed derivation is given in the Appendix. After the transformation, the results are shown in Fig. 6.30 for both steels.

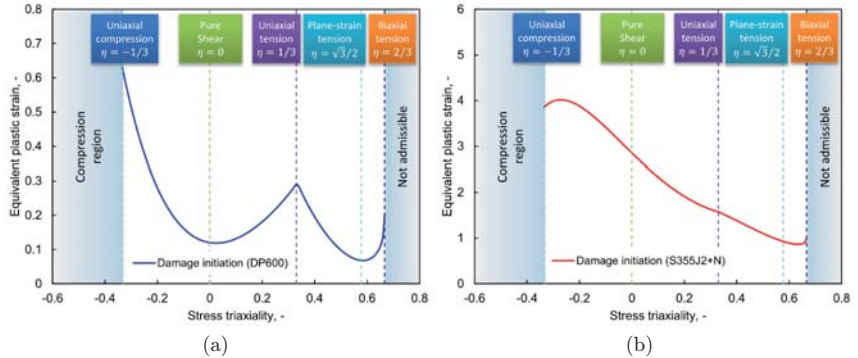


Fig. 6.29: The 2D damage initiation curves in the space of  $(\bar{\epsilon}, \eta)$  under the plane stress assumption for DP600 (a) and S355J2+N (b).

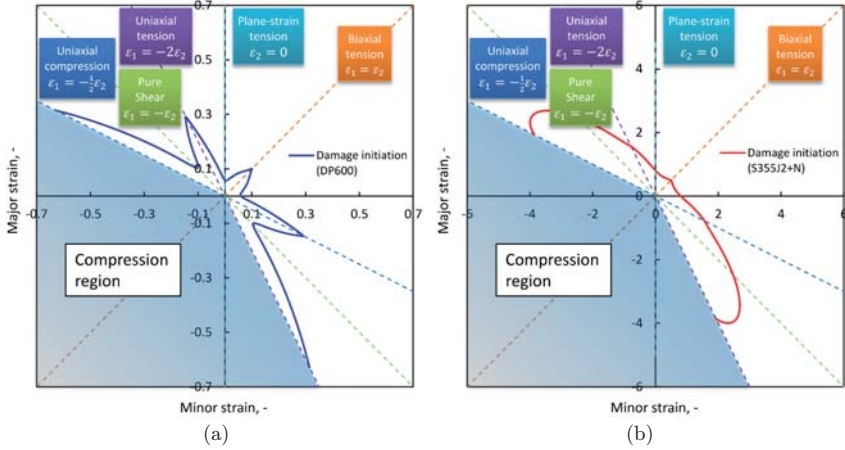


Fig. 6.30: The 2D damage initiation curves in the space of  $(\epsilon_1, \epsilon_2)$  under the plane stress assumption for DP600 (a) and S355J2+N (b).

From the comparison of the damage initiation between two steels in two spaces, it can be shown that the damage initiation strains over all stress states of the DP600 steel are considerably smaller than the S355J2+N steel. This also indicates that damage starts to play a role in the early stage of the plastic deformation for the DP steel, but it comes at a very late stage for the HSLA steel. The reason for it is closely related to the material microstructure and its resulting deformation and damage mechanisms of both steels. The DP600 steel comprised of ferrite and martensite owns a higher level of difference in terms of the deformation response of the two phases compared to the ferrite-perlite microstructure of the S355J2+N steel. The high difference results in a more incompatible deformation pattern which leads to the formation of damage in terms of debonding between the soft and hard phases or cracking in the hard phase at early state of plastic deformation. It is also shown that the DIL for DP600 is strongly dependent on both stress triaxiality and Lode angle, while the DIL for S355J2+N shows minor dependency on Lode angle. It is noted that in both spaces, only the stress states with one non-negative principal stress are employed. This limit is resulted from the fact that, for practical reasons, sheet can only be deformed by tensile forces and consequently one of the principal stresses must be positive or zero for the limit case [159].

At the uniaxial compression stress conduction or generally negative stress triaxiality conditions, the DILs are quite high, especially for S355J2+N. The existence of a cut-off value, at which ductile fracture will not happen in the negative stress triaxiality is still an on-going research

topic, as the experimental setup to realise the local fracture at this region is still a challenging task [160]. For the modelling of ductile fracture, different cut-off values or no cut-off value are incorporated in the models based on the formulation [161]. In the current implemented model, there is no existence of cut-off value. However the high strains at the negative stress triaxiality region indicates that ductile fracture is very unlikely to happen in practice. It is also noted that, the DILs at negative stress triaxiality are predicted by the model. As shown in Fig. 6.31, the stress triaxiality of experimental data points for the calibration of the DIL is in the range of (0, 0.8) for DP600 and (0.6, 2.2) for S355J2+N. Therefore, a more trustworthy DIL can be expected with some experimental data points at the negative stress triaxiality.

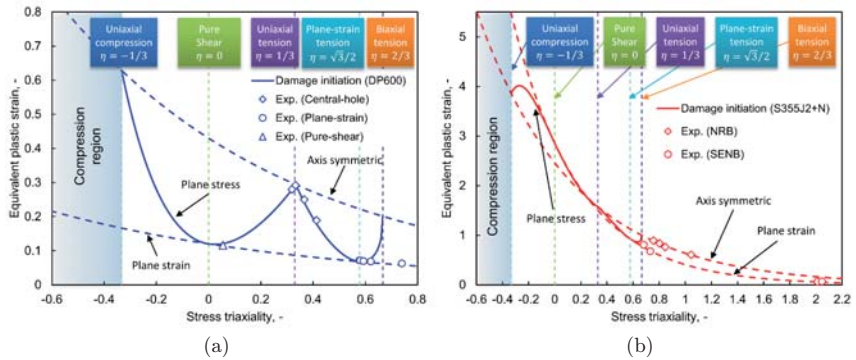


Fig. 6.31: The 2D damage initiation curves in the space of  $(\bar{\epsilon}, \eta)$  under the plane stress, axis symmetric and plane strain conditions and the experimental data points for the calibration of DIL for DP600 (a) and S355J2+N (b).

For a more quantitative discussion, the stress states region from uniaxial tension to biaxial tensions are chosen, as this region is most relevant to forming processes and the experimental data points are located within or close to this region. To show the different relation of plastic localisation, damage and fracture between two steels, the onset of necking, damage initiation, damage evolution and fracture are plotted in Fig. 6.32 under the assumption of plane stress condition and proportional loading. The DP600 steel shows a higher necking strains compared to the S355J2+N steel owing to its better strain hardening behaviour. As discussed before, damage is initiated at an early phase of plastic deformation for the DP600 steel and it also intersects with necking at high stress triaxiality region. However, it is subjected to substantial damage evolution till fracture due to the high fracture dissipation energy  $G_f$ , while the damage for S355J2+N gets non-negligible at a late deformation stage and quickly it leads to fracture.

It is also noted that the critical damage parameter for two steels are different. The critical value for DP600 is much smaller than the default value of one. It is related to the sudden fracture of the experiments and the fitting of the exact fracture point requires the sudden drop of the load carrying capability. On the contrary, the S355J2+N features a gradual fracture propagation, so the sudden drop is not required. Despite the rather small critical damage variable, the DP600 steel still undergoes more plastic deformation than the S355J2+N steel after damage initiation, as shown in Fig. 6.32.

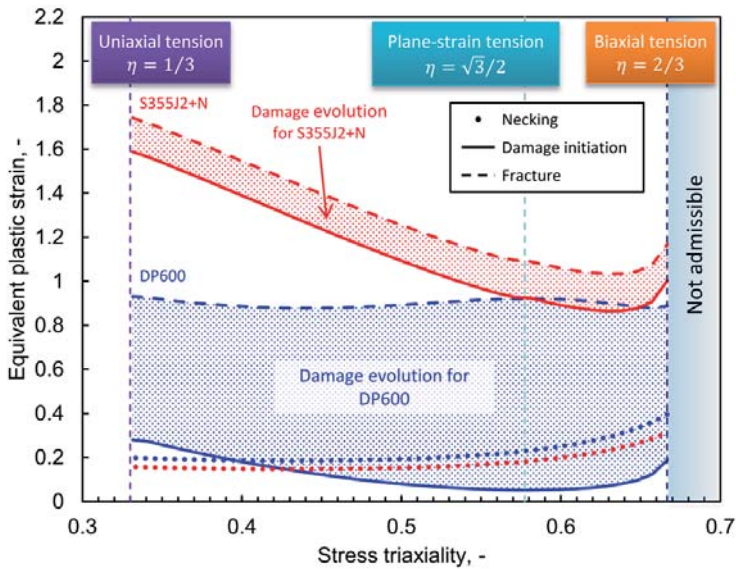


Fig. 6.32: Comparison of the 2D onset of necking, damage initiation and damage evolution to fracture in the space of  $(\epsilon_p, \eta)$  under the plane stress assumption between DP600 and S355J2+N.

Coping with the very different relation between plastic localisation, damage and fracture, the proposed model is used for both steels in a hybrid way and achieves good results for both materials. Therefore, it is concluded that the model is flexible enough to be used for various relation patterns between plasticity, damage and fracture.

Based on the local damage initiation strain and failure strain from Fig. 6.32, it is quite straightforward to conclude that the S355J2+N possesses a much better damage or fracture resistance than the DP600 steel. However, the experimental tensile properties show that they have similar fracture strains, as listed in Tab. 6.5. Taking the difference of the necking between

two steels into account, it is suggesting that the damage initiation and fracture strains are influenced by the strain localisation and the global performance of a component is contributed by the conjunct effect of strain localisation, damage initiation and evolution. It is noted that the exact values of the fracture strain are not comparable due to the different geometries for the tensile test and the fracture strain is dependent on the specimen geometry. Therefore, for a better understanding and illustration of the relation between strain localisation, damage initiation and fracture for these two steels, a virtual tensile experiment is designed.

The geometry of the virtual tensile test is shown in Fig. 6.33 (a). The test is performed under quasi-static condition in conjunction with the proposed damage model. As shown in Fig. 6.33 (b), the highlighted volume is used to measure the global strain and observe deformation.

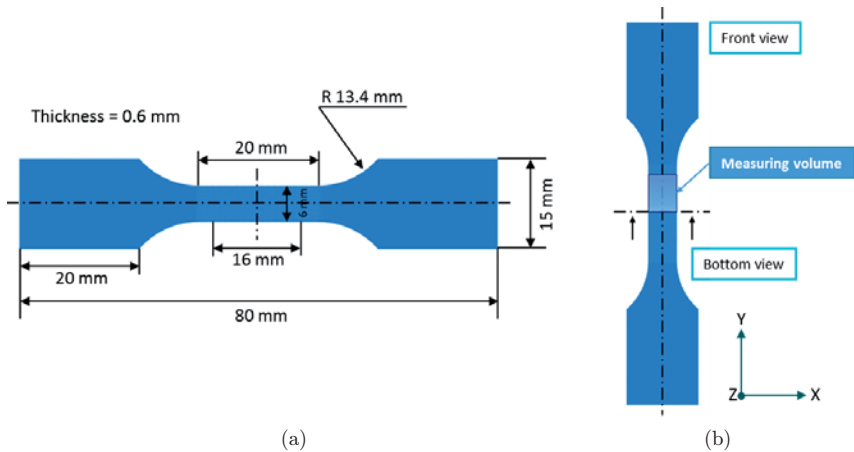


Fig. 6.33: A virtual tensile test; (a) the dimensions of the test specimen, (b) the illustration of the measuring and observing area and perspectives.

During the whole deformation history, three instants are chosen for analysis: maximum force, damage initiation and final fracture. Two perspective, the front view and bottom view, as indicated in Fig. 6.33 (b), are used to visualise the deformation. The deformation instants in both perspectives are shown in Fig. 6.34 for two steels. The grey frame is corresponding to the initial phase before any deformation. The deformation scale in the front view gives an indication of the global strain of the specimen. The DP600 shows a higher strain at the instant of maximum force, which is consistent with the higher uniform strain measured from tensile experiment, as listed in Tab. 6.5. On the contrary to the very different local strains for damage initiation and fracture in Fig. 6.32, very similar global strains for damage initiation and fracture

are observed and the values at damage initiation are listed in Tab. 6.5. However, very different deformation patterns are evident between these two steels at the damage initiation instant. Based on the front view, it is clear that the S355J2+N shows a very pronounced diffuse necking as well as localised necking shown as shear bands, while the necking for DP600 is very minor. For a better visualisation of the localised necking, the bottom view is zoomed in and shown in Fig. 6.35. In this perspective, the uniform deformation gives an indication of the global strain. Therefore, the higher uniform deformation corresponds to the higher the global strain. At the instant of damage initiation, the S355J2+N shows large strain localisation in terms of both diffuse and localised necking. Based on this analysis, it is trivial to conclude that the early and pronounced strain localisation of the S355J2+N gives arise to the high strains of damage initiation and fracture,

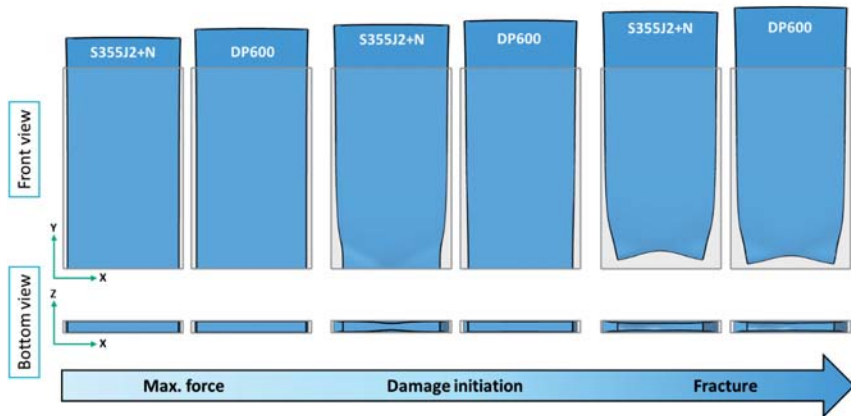


Fig. 6.34: Comparison of the deformation at different stages in the observing volume for two steels, S355J2+N and DP600 in front and bottom views.

The extent of strain localisation is quantified by the reduction of area of the cross section in the middle of the specimen and maximum reduction of the thickness. The area reduction corresponds to the overall effect by diffuse and localised necking, while the maximum thickness reduction describes the extent of localised necking. These two measures at the instant of damage initiation are listed in Tab. 6.5. Compared to the area reduction ratio, the maximum thickness reduction ratio shows a significant increase from DP600 to S355J2+N. Consequently it also gives arise to the increase of the local strain of the S355J2+N, as shown in Tab. 6.5.

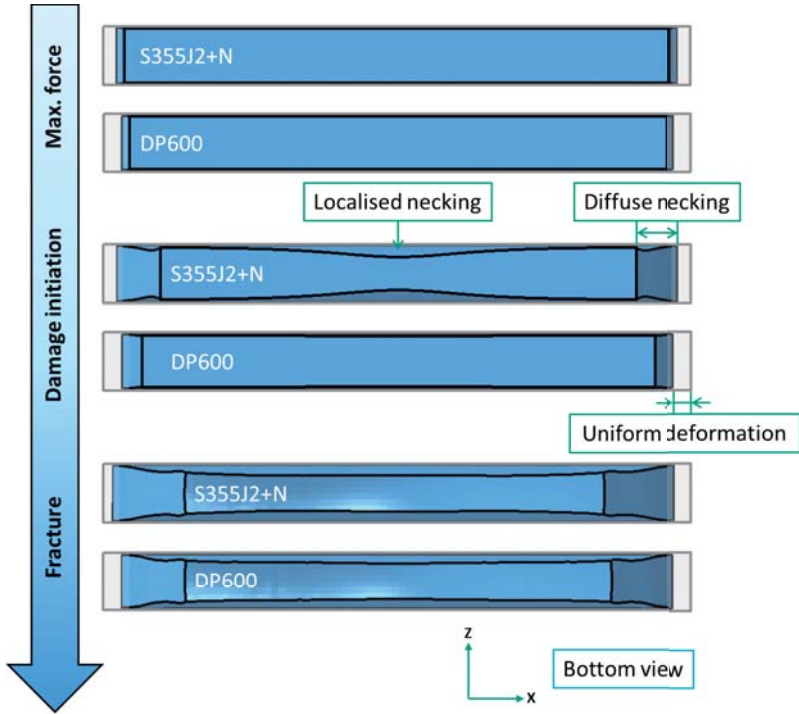


Fig. 6.35: Comparison of the deformation at different stages in the observing volume for two steels, S355J2+N and DP600 in bottom view.

Tab. 6.5: Comparison of the tensile properties from smooth tensile tests and the characteristics at the damage initiation instant from the virtual tensile test between S355J2+N and DP600.

Materials	Experimental measurement				Virtual experiment measurement @ damage initiation			
	Yield strength $R_{p0.2}$	Tensile strength $R_m$	Uniform elongation $A_u$	Fracture elongation $A_{80}$	Global strain	Local strain	Reduction of area	Max. thickness reduction
S355J2+N	398 MPa	549 MPa	14.4%	27.6%	24.1%	88.4%	35%	44%
DP600	390 MPa	704 MPa	16.5 %	25.4 %	25.3%	30.3%	21%	13%

To conclude the relation between plastic localisation, damage initiation and fracture of these two steels, the deformation history is represented in a schematic drawing (Fig. 6.36). Assuming only the in-plane deformation, the DP600 shows a higher uniform deformation strain than the S355J2+N. The damage, in terms of microvoids and/or microcracks, initiates at a much lower

local strain due to its microstructure configuration than the S355J2+N. However, owing to its excellent strain hardening behaviour, a similar global strain at damage initiation to the S355J2+N steel is reached. At this point, the strain localisation for S355J2+N is very pronounced and the damage is concentrated in the localisation region. The DP600, however, owns a more homogeneous deformation and the damage is also more uniformly distributed. Subsequently, different fracture pattern can be observed. The high-level strain localisation and the corresponding concentrated damage results in a gradual fracture mode and the homogenous deformation and uniform distribution of damage causes a sudden fracture.

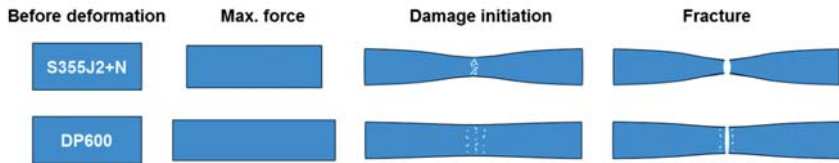


Fig. 6.36: Schematic representation of the relation pattern between plastic localisation, damage and fracture during the deformation for both S355J2+N and DP600.



# Chapter 7

## Model application

### 7.1 Nakajima test of steel sheet DP600

#### 7.1.1 Motivation of the prediction of forming limits

With the steel metal industry development in the recent years, especially various high strength steel grades, the material failure response under large plastic strain deformation shows a diverse pattern compared to the conventional highly ductile steels. Two decisive factors influencing the failure of materials are the damage accumulation and metal instability. Due to the different damage mechanisms of steels, the general material failure pattern can be categorised into three classes, damage-decisive failure, instability-decisive failure and damage-instability concurrent failure. The failure of the conventional highly ductile steel is considered as typical instability-decisive failure. However, for the newly developed high strength steels, in which damage plays a significant role during the plastic deformation, the failure pattern is mainly damage-decisive or damage-instability concurrent [12].

The FLD introduced by Keeler [162] and Goodwin [163] is often used in sheet forming industry for optimising forming process and exploring the material potential [164]. Such diagrams indicate both of the principal strains  $\epsilon_1$  and  $\epsilon_2$  at *necking* and *fracture* in the plane-stress state for different strain paths [164]. The curves indicating the instant of necking and fracture are referred to as forming limit curve to necking (FLC<sub>n</sub>) and forming limit curve to fracture (FLC<sub>f</sub>), respectively. As a safe operation regime is desired from these diagrams for the guidance of the metal forming processes, the more conservative one is often adopted and referred to as forming limit curve (FLC).

The FLD is normally obtained by experimental method, e.g. Nakajima tests. To avoid the complicated, time-consuming and expensive experimental approach of measuring the limiting strains in experiments, numerous theoretical models have been proposed to predict FLD on the basis of instability theory [2; 3; 164; 165]. They are quite applicable to conventional highly ductile materials such as mild steels, single-phase ferritic steels, and 5000 and 6000 series aluminium alloys, whereas it is, on the contrary, challenged by the application of AHSS, where damage is either decisive to the failure or non-negligible for the description of the plastic deformation and localisation. Therefore, various ductile fracture criteria are used to characterise the formability of these materials. They are mostly uncoupled approaches and good prediction of the  $FLC_f$  can be expected for the damage-decisive materials, i.e. the materials are fractured prior to necking. However, for the damage-instability concurrent material, the predictive capability of both types of models is limited. In this type of materials, complicated scenarios are anticipated, e.g. the failure is instability decisive under uniaxial and plane strain tension but it becomes damage decisive under biaxial tension. It is simply related to the interaction between plastic localisation and damage evolution. In such cases, the instability models need to be combined with coupled damage model to be able to fully predict both  $FLC_n$  and  $FLC_f$ . To develop a generalised damage model accounting for instability and damage as well as their interaction, the hybrid damage plasticity model is combined with an instability-based model. Attributed to its hybrid nature, the hybrid damage plasticity model can be easily switched between the uncoupled fracture model and the coupled damage model. Based on the formulation of the model, two criteria are given as guideline for forming process: the forming limit for defect-free condition and the forming limit indicating the final fracture. The first one is given by the damage initiation criterion while the latter one is defined once the accumulated damage becomes critical to trigger the final fracture. By integrating the instability model, the forming limit at necking can also be predicted considering the interaction with damage and fracture.

### 7.1.2 Experimental data and analysis

The Nakajima test is performed to characterise the formability of DP600. After the tests with ten different geometries of the blanks, both analysis methods, visual method and position-dependent method, are employed in this study to present the forming limits of DP600 steel.

The local in-plane strains measured from Nakajima tests at two instants, necking and final fracture are both plotted in Fig. 7.1. The position-dependent method recommended by the

standard is employed for the data evaluation for necking and the visual method is used for the evaluation of both necking and fracture. Compared to the result of the virtual method, the trends of the two FLCs are similar, but the result of the position-dependent method is, to a certain extent, lower than the result of visual method. As three parallel tests are performed for each geometry configuration, the scatter of the FLCs at both necking and fracture is indicated by the error bar. Generally the measurement is quite robust in the regime of plane-strain state, and the scatter gets more pronounced towards the uniaxial tension and the equibiaxial tension stress state.

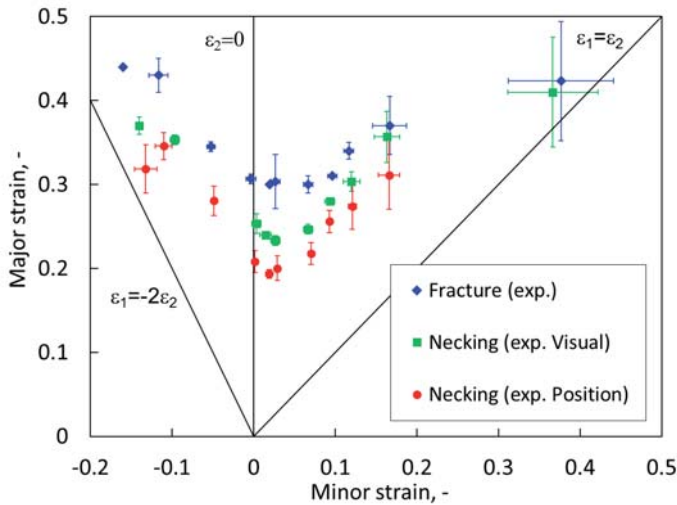


Fig. 7.1: The experimentally measured FLCs both at necking and final fracture. For the FLC at necking, two analysis methods, visual method and position-dependent method are used to characterise the forming limit.

### 7.1.3 Prediction of the FLC at necking

#### 7.1.3.1 Theoretical models for metal instability prediction

For the prediction of the forming limit on the left side of the FLD, the localised necking criterion postulated by Hill [2] is often considered. It is assumed that a narrow band is developed and the strain along the band direction becomes zero at the instant of localised necking. Mathematically, it is defined by

$$\frac{d\sigma_1}{d\varepsilon_1} = \sigma_1 \cdot (1 + \beta) \quad \text{Eq. 7.1}$$

where  $\sigma_1$  and  $\varepsilon_1$  are, respectively, the major principal stress and strain;  $\beta$  is defined as the ratio between the major and minor principal strain rate,  $\beta \equiv \frac{\dot{\varepsilon}_2}{\dot{\varepsilon}_1} = \text{const}$ . For the positive minor strain region in FLD, the diffuse necking criterion postulated by Swift [3] is widely used. It is assumed that the diffuse neck is formed when the load reaches maximum in both principal directions:

$$\frac{d\sigma_1}{d\varepsilon_1} = \sigma_1; \quad \frac{d\sigma_2}{d\varepsilon_2} = \sigma_2 \quad \text{Eq. 7.2}$$

Despite the wide application, it is generally considered that the Hill–Swift criterion, in particular the Swift diffuse necking criterion, underestimates the material formability. In the metal forming processes, the critical phase is not the occurrence of diffuse necking, but the localised necking, i.e. the plastic deformation is still allowed to a certain extent after the maximum force is reached. Hora et al. [165] found that when the maximum forming force is reached, the deformation states are gradually transformed to the plane-strain tension stress state. The additional tensile stress is introduced by the change of the state, and will disappear when plane-strain state is reached, i.e. the stress  $\sigma_{11}$  is not only a function of strain hardening but also the strain ratio  $\beta$ . By including this factor, Hora formulated the modified maximum force criterion (MMFC) defined by

$$\frac{\partial\sigma_1}{\partial\varepsilon_1} + \frac{\partial\sigma_1}{\partial\beta} \cdot \frac{\partial\beta}{\partial\varepsilon_1} = \sigma_1 \quad \text{Eq. 7.3}$$

Under the assumption of Mises yield criterion, associated flow rule, rigid plasticity and the proportional loading condition, the Hill–Swift necking criterion and MMFC are both numerically formulated in Matlab in cooperation with isotropic hardening law.

#### 7.1.3.2 Results based on the coupled MMFC with MBW model

The prediction of the FLC by MBW model at the instant of damage initiation is plotted in Fig. 7.2 (a). The damage initiation forming limit gives a quite conservative result, as it is corresponding to the forming limit at the occurrence of damage in mesoscale, such as the nucleation of voids or the formation of microcracks. It is concluded that the forming process under this limit is completely defect-free.

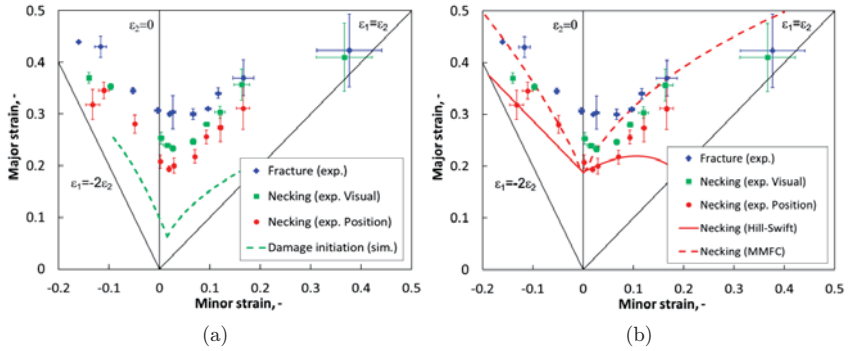


Fig. 7.2: (a) The FLCs measured by experiments at the instants of necking and fracture and the FLCs predicted by MBW model at the damage initiation and the final fracture; (b) Comparison of the FLCs predicted by the Hill–Swift necking criterion and the MMFC with the experimental FLC at necking.

In Fig. 7.2 (b), the predicted FLCs by Hill–Swift necking criterion and the MMFC in cooperation with the flow curve estimated by Holloman equation are both plotted. It is natural that the two predicted FLCs are the same under the plane-strain tension condition and they both agree well with the experimental measurement. As aforementioned, the Hill–Swift criterion underestimates the forming limit of the material, in particular on the positive minor strain side when the strain path is close to the equibiaxial tension. The result of the MMFC enhances the predicted forming limit by including the strain path change. It shows a better fit to the experiment, especially on the negative minor strain side. On the positive minor strain side, it slightly overestimates the forming limit of the material considering the scatter of the experiments.

To investigate the influence of the flow curve and the damage effect, in addition to the Hollomon equation, another four equations, Voce, Swift–Voce, Swift and Bergstrom, are employed for the extrapolation of the flow curve. All of these equations achieve good quality of fitting till the UTS, but they differ very much when the plastic strain gets large, as shown in Fig. 7.3. Both the Hill–Swift necking criterion and MMFC are run with these five different curves and the predicted FLCs are presented in Fig. 7.4. It is obvious that for either criterion the predicted FLC is shifted up if the hardening of the material is strong, and vice versa. The sensitivity of the Hill–Swift necking criterion to the flow curve is high. Except for a very strong flow curve estimated by Bergström equation, the rest all underestimate the formability of the

material. The MMFC, however, shows less sensitive behaviour than the Hill–Swift criterion. It is also noted that in the transition region from the plane-strain tension to the equibiaxial tension, the result of Swift–Voce equation shows a very good agreement with the experimental FLC, while the prediction of it in the regime from the uniaxial tension to the plane-strain tension, including the plane-strain tension is not as good as the result of Hollomon equation. This phenomenon simply proves that the hardening of the material is influenced by damage and it is not identical under any stress states. Therefore, to achieve an overall good prediction of the FLC, the inclusion of the damage effect is required and the damage effect is stress state dependent.

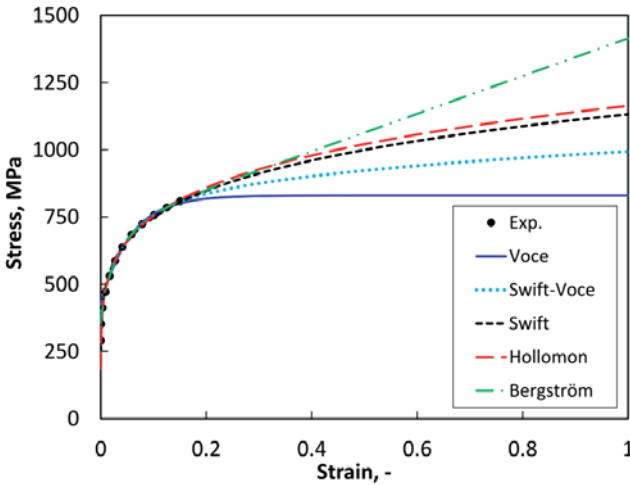


Fig. 7.3. The extrapolated flow curves from the true stress–strain curve from uniaxial tensile test based on different equations, Voce, Swift–Voce, Swift, Hollomon and Bergstroem.

In Fig. 7.5, the prediction of FLC at necking given by the coupled MMFC and MBW model is presented together with the experimental results and the predictions by Hill–Swift and MMFC without consideration of the damage. Compared to the prediction by the MMFC in conjunction with the original Hollomon flow curve, the FLC is generally lower and, more importantly, a consistently good agreement of the FLC at necking across the whole FLC from uniaxial tension to equibiaxial tension is achieved. It is recalled that in the MBW damage model, the flow behaviour is reduced from its original stress–strain curve based on the uniaxial tensile test by two parts: the stress-state-dependent yielding and the damage degradation. For DP600 steel, the yielding difference is not pronounced. As the damage initiation is quite early indicated in

Fig. 7.1 (a), the reduction or improvement of the FLC prediction is mainly contributed by the incorporation of the damage degradation and its effect on the material strength. The consistency of the good agreement under different stress states is resulted from the stress-state dependent damage initiation definition as well as its implicit effect on the subsequent damage evolution. It is noted that all the parameters used in the prediction are calibrated from the previous chapter and the code is programmed in Matlab following the numerical algorithm illustrated in Chapter 3 for the MBW damage model and the implementation methodology presented by Aretz [166] for the Hill–Swift criterion and MMFC.

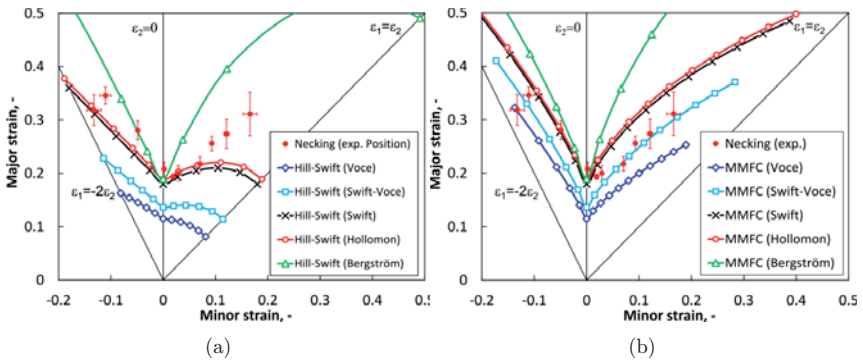


Fig. 7.4. (a) Comparison of the FLC predicted by the Hill–Swift necking criterion in cooperation with various formulations of the flow curve extrapolated from the result of tensile test; (b) Comparison of the FLC predicted by the MMFC in cooperation with various formulations of the flow curves.

## 7.1.4 Prediction of the FLC at ductile fracture

### 7.1.4.1 FE model

In the finite element simulation of Nakajima test, only a quarter of the experimental setup is modelled due to the symmetry as shown in Fig. 7.6 (a). The corresponding model setup and the mesh are shown in Fig. 7.6 (b). In the model, the drawing die, blank holder and the punch are considered as rigid bodies, and for the 1/4 of the specimen the 3D 8-node brick element with reduced integration (C3D8R) is employed. The surface-to-surface contact is employed between all the contact areas. The friction coefficient between specimen and drawing die and blank holder is assumed as 0.3, whereas it is 0.01 between specimen and punch. As the experiments, a constant velocity is applied on the punch and the die is fixed in all freedoms.

The blank holder is also fixed in all freedoms but the vertical displacement in order to respond the clamping force applied on it. The FE model is run in the environment of Abaqus /Explicit with the material subroutine VUMAT of the MBW model.

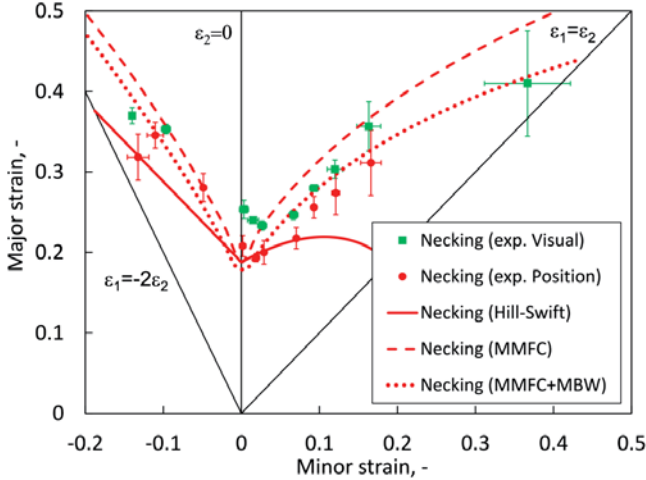


Fig. 7.5. Comparison of the FLC predicted by the Hill–Swift necking criterion and MMFC in cooperation with the original Hollomon flow curve extrapolated from the result of tensile test and predicted by the MMFC in cooperation with the MBW damage model with the experimental result.

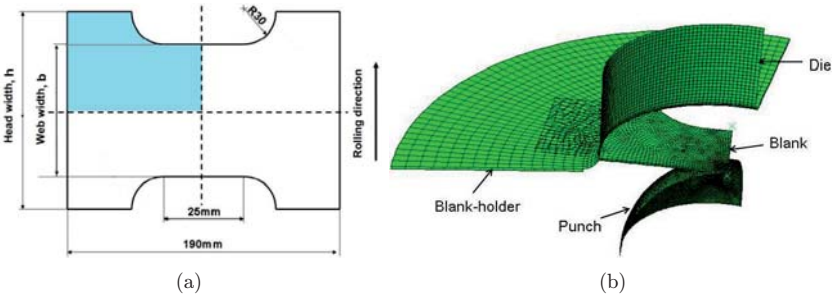


Fig. 7.6. (a) Drawing and dimensions of the Nakajima test specimens and the coloured area is referred to as the quarter of the blank which is modelled in simulations, (b) Mesh of the FE model for Nakajima test after applying reflection symmetry twice.

The detailed mesh configuration and size distribution are depicted in Fig. 7.7. The previous mesh strategy is applied here. Generally, the blank is partitioned to three zones, the critical



zone, transitional zone and non-critical zone. The critical zone basically covers the main part of plastic deformation of the blank and the element size of the critical zone is predefined, as all the plasticity and damage parameters calibrated in section 6.2 are mesh related.

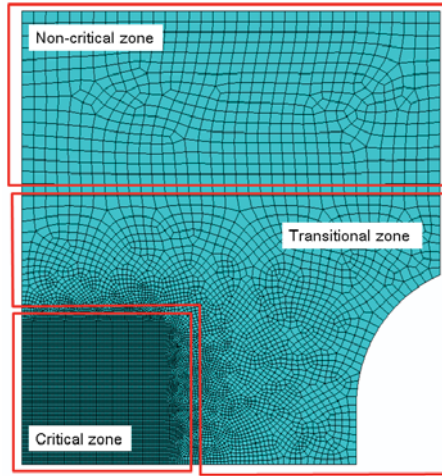


Fig. 7.7. The mesh of the blank with web width of 140 mm for the Nakajima test simulation.

As the Nakajima simulation deals with complicated contact definition and multistep forming, the Abaqus/Explicit is preferred. However, to use Abaqus/Explicit for a quasi-static condition could result in considerably expensive numerical effort, in particular, when the model contains large number of elements. Two methods are used in the study to reduce the computational expense, time scaling and mass scaling.

For the time scaling, firstly, the frequency extraction procedure in Abaqus/Standard is performed to determine the time period required to obtain a proper quasi-static response. Once the lowest natural frequency is known, the approximation lower bound on step time duration is determined. The frequency analysis shows that the blank has a fundamental frequency of 178.29 Hz in the model with web width 20 mm and 211 Hz in 160 mm, corresponding to a period of 0.005609 s and 0.004739 s, respectively. Therefore, the step time of 0.01 s is used in the simulation step which is larger enough than the time period 0.005609 s for the lowest mode. Mass scaling is also often used in Abaqus/Explicit for computational efficiency in quasi-static analyses. Mass scaling for quasi-static analysis is usually performed on the entire model. However, when different parts of a model have different stiffness and mass properties, it may be useful to scale only selected parts of the model or to scale each of the parts independently.

As the mass scaling increases, the solution time decreases. The quality of the results also decreases because dynamic effects become more prominent, but there is usually some level of scaling that improves the solution time without sacrificing the quality of the results. For a proper mass scaling factor, it is usually determined by restricting the kinetic energy ratio in the total internal energy during the deformation history [139].

For the Nakajima simulations, the blank is selected as an element set to be scaled. Four fixed values of scale factor, such as 5, 15, 20 and 30 are used in the damage mechanics simulation throughout the entire deformation history. As recommended in Ref. [139], the largest scale factor which still can be acceptable shall not result in more than 10% of the kinetic energy over internal energy ratio. In the Nakajima simulations with all different web widths, a scale factor of 20 is finally selected for the mass scaling without scarifying the result quality.

#### 7.1.4.2 Simulation results based on the MBW model

With the MBW damage model applied to the Nakajima test, one can visualise the different stages of the deformation history. As depicted in Fig. 7.8, three critical stages of the deformations are indicated, the damage initiation, the fracture onset and the fracture propagation. The damage initiation is corresponding to the moment when the damage variable is becoming non-zero, and the onset of the fracture is triggered when the critical amount of damage accumulation is reached for the first time in the specimen on an element or integration point. Ultimately, the fracture propagates till the complete loss of the load carrying capability of the specimen, i.e. the moment when the force drops to zero in the force–displacement curve of the test. The element deletion technique is used for the simulation of the crack formation and propagation. It is noted that for the DP600 sheet material the last two stages, fracture onset and propagation to complete loss of load carrying capability, are extremely close (in the order of 0.1 s) in experiments and simulations. Therefore, it is practical to identify them as one event and assume the sudden drop of the force as the fracture point.

In Fig. 7.9, punch force vs. stroke curves for the Nakajima tests are presented in order to compare experimental and numerical results. Three repeated identical experiments were conducted for each web width and they all showed quite consistent mechanical behaviour. Therefore, for the comparison of the other geometries, only one experimental force–displacement curve is taken. In order to keep the figure understandable, only test with web width of 40 mm, 100 mm and 160 mm are presented. Comparing the experiments and the numerical results by MBW damage model, a very good overall agreement of the

force–displacement is reached. From the simulations, two important stages of the deformation aforementioned, damage initiation and fracture point are indicated on the force–displacement curve. The damage initiation stage implies that damage degradation starts to effect on the stress–strain behaviour of the material, and the following deformation is not defect-free. This information can only be provided by simulations, but not verified by the experiments. On the other hand, the fracture point, corresponding to the moment for the complete loss of load carrying capacity, is well predicted by the MBW damage model for all the geometries.

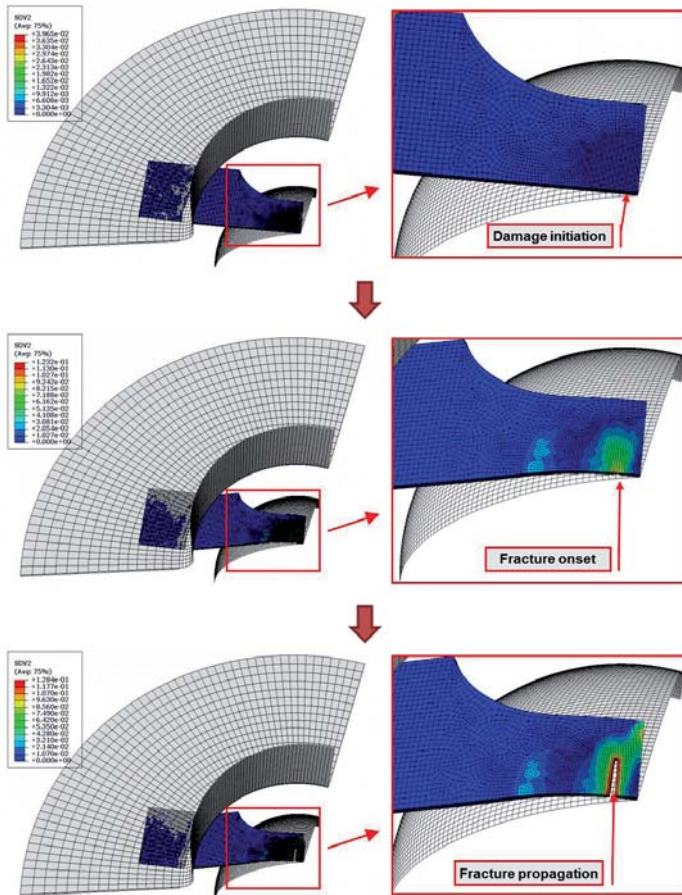


Fig. 7.8. Three critical stages of the deformation history of the Nakajima test, i.e. the damage initiation, the onset of the fracture and the final fracture; illustrated by the simulation with MBW damage model with web width of 40 mm.

The specimen morphologies at the final fracture moment are shown in Fig. 7.9. The final fracture is initiated very close the sample centre and propagates perpendicular to the loading direction, which agrees with the experimental observation. The deviation of the fracture position from the specimen centre results from the friction between the specimen and punch. Ideally, the final fracture appears at the exact sample centre if frictionless condition is assumed between the sample and punch. However, as it is rather difficult to get complete frictionless in the experiments, the small amount of deviation of the final fracture from the centre is also confirmed in the experiments.

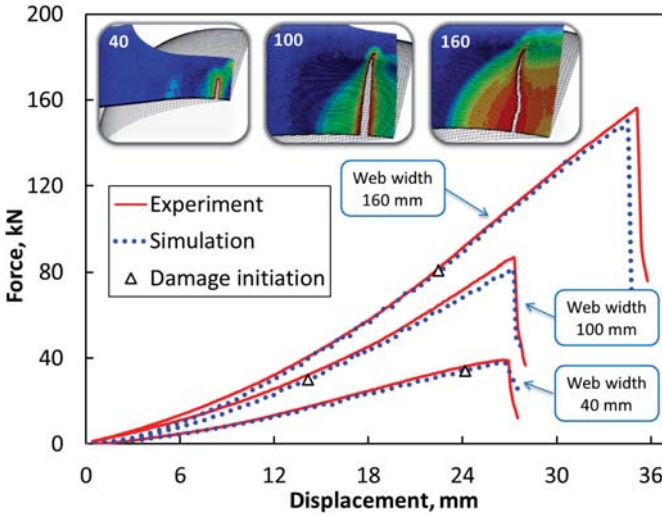


Fig. 7.9. Comparison of the load vs. punch displacement curves of the Nakajima test with web width of 40 mm, 100 mm and 160 mm between experiments and the simulations with MBW damage model; The predicted the fracture path at the fracture point of the selected tests by simulations are also shown.

The ability of predicting the final fracture point serves as one important criterion to verify the model applicability and validate the accuracy of the calculation of both local and global variables. For a more quantitative comparison between experiments and simulations, the punch stroke at the instant of final fracture from experiments and simulations are presented in Fig. 7.10 for all tested geometries. Since three tests were performed in parallel for each geometrical configuration, average values are given as experimental results, and the error bar indicates the range from minimum to maximum values. The specimen with web width of 20 mm shows the

largest relative fracture displacement to the average experimental result,  $\sim 13\%$ , which results in about 7% error considering the experimental scatter. However, for most of the geometries, the predicted fracture punch displacement is within the scatter of the experimental result or gives a less than 5% error compared to the experimental result with scatter.

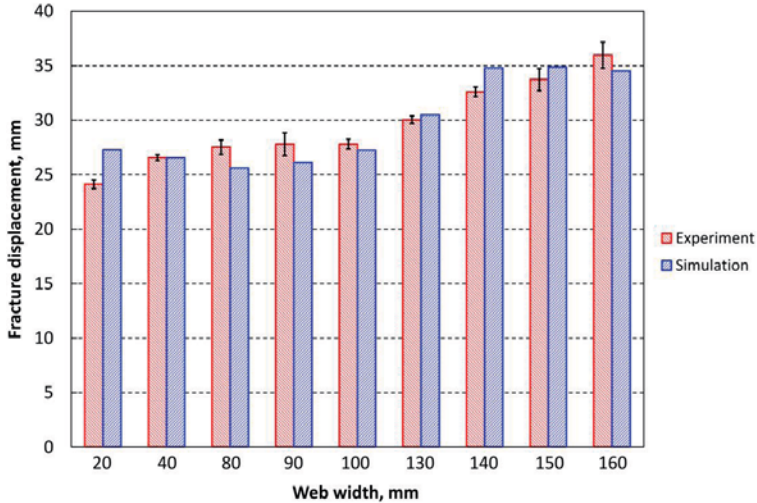


Fig. 7.10: Comparison of the fracture displacement between the experiments and simulations of all the Nakajima tests.

Zooming in the focus to the local variables, e.g. the forming limit, can be also evaluated, at the stage of damage initiation as well as the onset of fracture. According to the experimental analysis procedure, the FLC extracted from simulations at the onset of fracture can also be directly compared to the experimental FLC at the fracture. It is noted that in the simulation, the pair of the logarithmic strains are extracted at the instant when the first element reaches the critical value of the damage,  $D_{cr}$ . The comparison of the FLC at fracture between experiments and simulations is shown in Fig. 7.11. Overall, a good agreement is achieved, except for a small range of underestimation close to the equibiaxial tension state. One reason for this is tracked back to the experimental program as well as the analysis technique. Note that the FLCs measured from experiments are not covering the complete strain paths from uniaxial to equibiaxial tension. A certain range of forming limits is not given in the vicinity of equibiaxial tension condition. The uncertainty of the analysis technique in conjunction with the missed experimental data produces a certain scatter on the right side of the FLD. In general,

from these results it can be concluded that the MBW model is a suitable approach to characterise the cold formability of steel DP600.

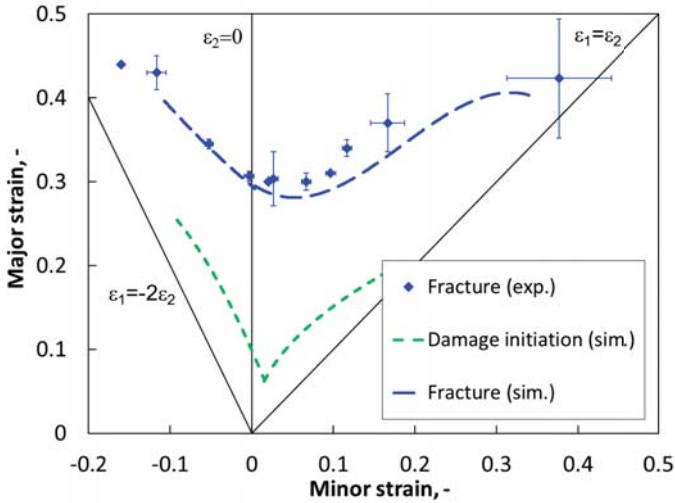


Fig. 7.11. The FLCs measured by experiments at the instant of fracture and the FLCs predicted by MBW model at the damage initiation and the final fracture.

## 7.2 Bending test of heavy plate S355J2+N

### 7.2.1 Motivation of the simulation of the bending test

For the safety assessment of structures and components in mechanical and civil engineering, mainly the strength and toughness properties of the selected construction materials are of interest [167; 168]. In order to foster more economic and sustainable lightweight design, new methods are currently developed that shall allow for improved exploitation of mechanical property profiles [169; 170]. Furthermore, the steel industry has developed a variety of high strength steels with excellent toughness properties [171]. Since the superior mechanical properties are achieved by applying tailored thermos-mechanical processes during and after hot rolling, the alloying concepts can be retained on a comparably cheap level, resulting in excellent weld ability of such HSLA steels [172; 173].

However, since the modern steels allow for new structural design options, also the processing properties of these materials are nowadays in the focus of steel producers. In particular, a sufficient cold formability of HSLA steel plates is more and more often required in order to

create complex component geometries out of flat products without additional welding steps. Typical examples are the “yellow goods”, such as mobile cranes, bulldozers, scrapers, and graders. In order to build up this type of machines, significant requirements on the cold formability of materials, or more precisely on the bendability, can be defined. Consequently, techniques to experimentally characterise the bendability of HSLA steels were developed in terms of a bending test, and characteristic values were defined allowing checking whether the requirements on the bendability are met.

The bending tests are performed in order to define the critical ratio between punch diameter  $r$  and sample thickness  $t$  which allows achieving a bending angle of  $90^\circ$  without appearance of surface cracks. Obviously, extensive experimental efforts are required in order to determine the critical  $r/t$  ratio, since for every test a new punch of different punch radius is required, and in addition also the two support bearings have to be moved horizontally in order to adjust the distance between them. The target of this study is to numerically characterise the bendability of the heavy plate S355J2+N steel, and derive the corresponding critical  $r/t$  ratio with the calibrated material parameters in previous chapter.

## 7.2.2 FE model

### 7.2.2.1 Geometry

The investigations were performed on samples with a length of 400 mm, a width of 150 mm and a thickness of 15 mm. The corresponding FE model was then constructed with symmetry in the width direction, as shown in Fig. 7.12.

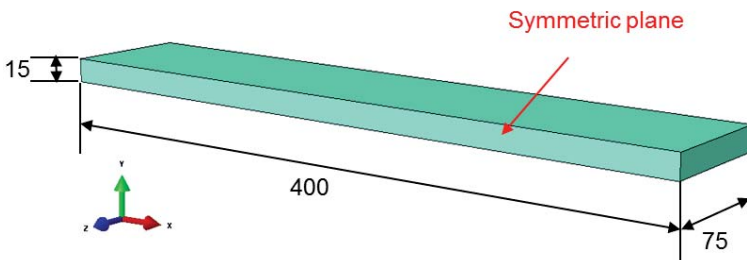


Fig. 7.12: Geometrical model for the simulation of bending tests; all units are in mm.

The  $r/t$  ratios are chosen as 0.2, 0.5, 0.8, 1.0, 1.2 and 1.5. The selection of these  $r/t$ -ratios was based on the available punch radii of the laboratory where the experiments were conducted. Before the simulations were carried out, the load line displacement of the punch required to

bend the sample to an angle of  $90^\circ$  was calculated analytically. Likewise, the simulations could be performed such that the required punch displacement is applied, and the punch moves back to its original position. All the geometrical details required to perform the simulations are summarised in Tab. 7.1, and Fig. 7.13 shows the geometrical set-up considered in the simulations.

Tab. 7.1: Geometrical details for all six simulations of bending tests.

$r/t$ , -	$t$ , mm	$r$ , mm	$d$ , mm	$3t+d$ , mm	Required load line displacement, mm
0.2	15	3	6	51	60.20
0.5	15	7.5	15	60	62.83
0.8	15	12	24	69	65.46
1.0	15	15	30	75	67.22
1.2	15	18	36	81	68.98
1.5	15	22.5	45	90	71.61

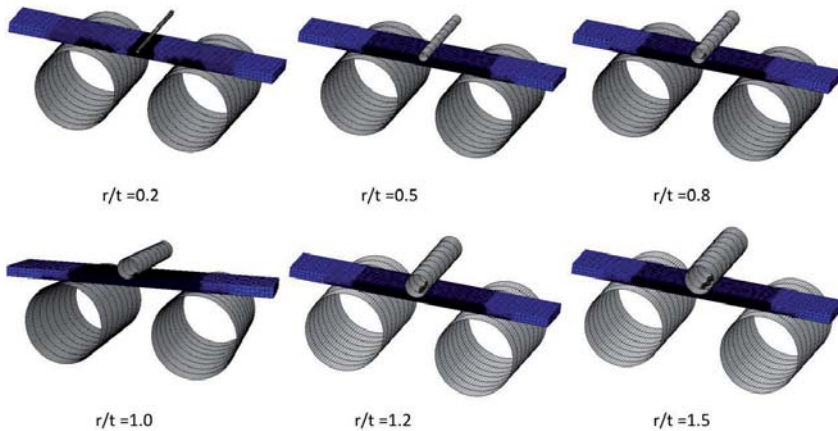


Fig. 7.13: Geometrical setup of the bending tests with six different  $r/t$  ratios.

#### 7.2.2.2 Enmeshment of the model

With the same approach in the simulation of SENB test in section 6.3.1, the vicinity of critical area, the middle of the plate, is meshed in very fine due to sensitivity to damage initiation. The other parts needs a fine mesh size are contact surfaces between the plate and three pins. This enmeshment of plate is illustrated shown in Fig. 7.14. The primary mesh sizes in different zones of the plate are given in Tab. 7.2.



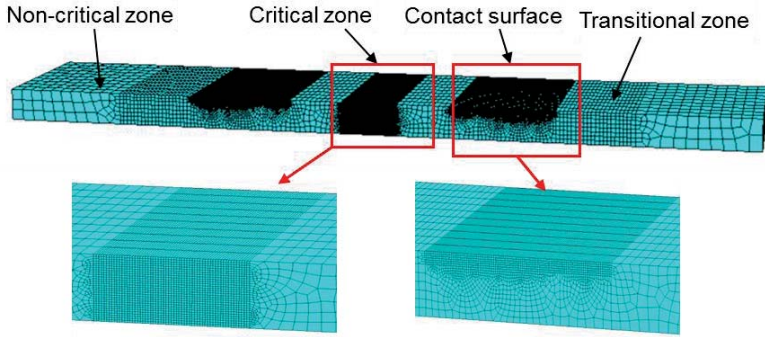


Fig. 7.14: Enmeshment of the steel plate in cold forming test model.

Tab. 7.2: Mesh size in different zones of the steel plate in the model.

Zone of plate	Non-critical	Transitional	Critical	Contact surface
Mesh size, mm	0.5×0.5×0.75	0.1×0.1×(0.1~0.5)	0.1×0.1×0.75	0.1×0.1×0.75

### 7.2.2.3 Boundary conditions and other settings of the model

The simulation is carried out by Abaqus in the mode of explicit consisting of two steps, initial step and main executing step. In the execution, the plate is considered deformable, while barriers and hammer are simply assumed as analytical rigid bodies. All boundary conditions are illustrated below in Fig. 8.9:

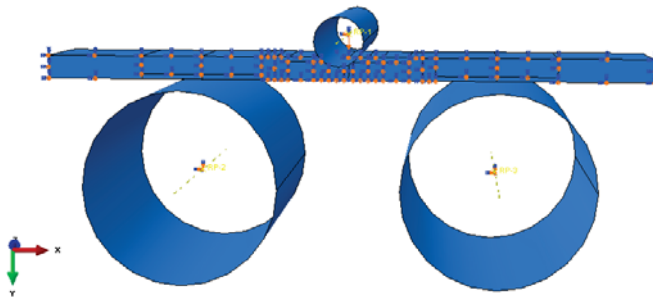


Fig. 7.15: Boundary conditions for executions in simulation.

Due to the simplification of the material property of the three pins, the boundary condition is constrained to a single reference point. All the boundary conditions lie in the category of displacement restriction. Simply the two barriers above are restricted in all directions to move, whereas the hammer on the top is fixed in both x and z directions, but movable in y direction

to deform the plate. The specific displacement is calculated to meet the requirement that after the hammer is back to the initial place, the plate remains bended at approximately  $90^\circ$ . For the plate, according to the symmetrical boundary condition the corresponding plane is restricted to move in the symmetrical direction, which is the z direction in this case. At the zones of contiguity among the pins and plate, surface to surface contact interactions are applied with the consideration of friction. The friction coefficient is assumed to be 0.1.

### 7.2.3 Results and discussion

With the calibrated material parameters of the MBW model for steel S355J2+N, numerical simulations were carried out in order to derive the critical  $r/t$  ratio. The corresponding experiments were conducted in the Heavy Plate Unit of ThyssenKrupp Steel Europe AG. Since neither forces nor displacements could be measured in these tests, the accuracy of the simulations can only be evaluated for the critical  $r/t$  ratio.

In the simulations, damage initiation has to be expected at the centre of the bottom side of the sample. This is because i) the applied bending moment is the largest in mid-length position where the punch applies the force; ii) the tensile stresses appear on the bottom side of the sample; iii) the most severe state of stress is found in mid-width position where the Lode angle parameter is zero. Therefore, for all six numerical models, the element in this critical position was evaluated. The loading paths of the critical elements in six models are shown in Fig. 7.16.

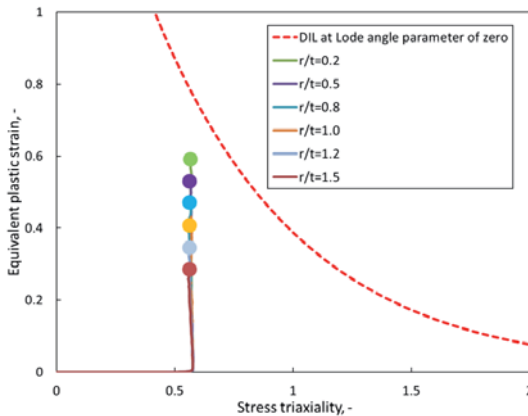


Fig. 7.16: Loading paths of the elements in the most critical position of the sample, together with the damage initiation strains as extracted from the DIL for a Lode angle parameter of zero.

The equivalent plastic strain is given as a function of the stress triaxiality (since the Lode angle parameter stays on a constant value of zero, a 2D approach is sufficient to express the loading paths). Obviously, the loading paths of the six simulations nearly coincide. Moreover, the stress triaxialities stay almost at a constant value of approximately 0.58 as soon as the elements begin to exhibit plastic deformations. The main difference between the six simulations is that with decreasing  $r/t$  ratio, the applied equivalent plastic strain increases at the bending angle of  $90^\circ$ . To check if the six designed bending configurations are safe or not, the previously calibrated DIL at Lode angle parameter of zero is also plotted in the same figure. Obviously, the applied equivalent plastic strain does not reach the critical equivalent plastic strain even for the most critical  $r/t$  ratio under investigation ( $r/t=0.2$ ), so that it can be concluded that the critical  $r/t$  ratio of steel S355J2+N is lower than 0.2. As presented in Fig. 7.17, the experimental investigations validate this conclusion. Since the material under investigation offers an impressive bendability, it was impossible to experimentally determine the critical  $r/t$  ratio due to the restrictions on the available punch radii.

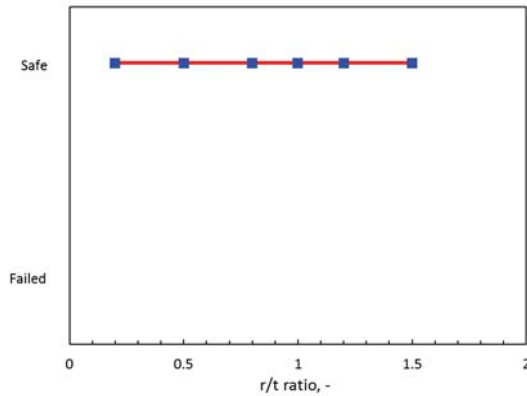


Fig. 7.17: Evaluation of simulation results and corresponding experiments.

One of the most interesting findings of the presented study is that the loading path stays approximately the same for all  $r/t$  ratios. From this it can be concluded that only the damage initiation strain at a Lode angle parameter of zero and a stress triaxiality of 0.58 has to be known in order to evaluate the material bendability and this stress state is exactly corresponding to the plane-strain tension condition. Consequently, a laboratory scale plane-strain tension test would provide enough information to evaluate the bendability of heavy

plates in the three-point bending test. Based on these findings, a new approach has been developed which allows evaluating the bendability of HSLA steel. It consists of the following steps:

- Step 1: Determination of the flow curve of material by a tensile test, including its mathematical description and the extrapolation to large strain.
- Step 2: Tensile test on the flat grooved plane-strain sample and identification of damage initiation using the DCPD method.
- Step 3: Numerical simulation of the test conducted under step 2 in order to determine the damage initiation strain. For this purpose, the central element of the sample is evaluated at the damage initiation displacement as determined in step 2. Noteworthy, these simulations are carried out in only elastoplastic mode without consideration of damage.
- Step 4: Numerical elastoplastic simulations of bending tests for different  $r/t$  ratios. The applied displacements must be sufficient to bend the sample to an angle of  $90^\circ$ .
- Step 5: Post-processing of the simulations in order to check when the critical strain in the element at the centre of the bottom side of the sample. In case it is reached before a bending angle of  $90^\circ$  is set, then the critical  $r/t$  ratio is already undergone.

This method only requires two experiments which can be easily performed in a universal tensile testing machine. Moreover, a couple of numerical simulations have to be performed, but no damage model has to be applied in these computations. Therefore, the presented approach will significantly reduce the efforts to determine the critical  $r/t$  ratio for the bendability analysis of heavy plates.

### 7.3 Conclusions

From the two application examples, the predictive capability of the hybrid damage plasticity model is well justified for both sheet metals and heavy plates. Despite the good precision of prediction, the model brings a large number of material parameters. To be able to use the model, extensive amount of effort is required to calibrate the material parameters. This is severely hindering the application of it to a general or industrial scale. Another main disadvantage is that the model has a phenomenological character, as there is no material information involved. This also limits the application of the model to consider material microstructure in order to optimise the material for improved mechanical behaviour.

---

The solution to this problem is basically two folds: i) reducing the number of material parameters of the phenomenological model by new formulations and, ii) predicting the phenomenological material parameters by a microstructure-informed model on the microscale. Therefore, these two aspects are addressed in the following two chapters, respectively. In Chapter 8, a simpler formulation of damage model is proposed and validated. In Chapter 9, an upscaling method from microscale to macroscale is proposed for determination of the material parameters of the phenomenological model and bringing the material character in the model for material design.



# Chapter 8

## Model improvement to reduce the number of material parameters

### 8.1 Introduction

The chapter addresses the problem of the complexity of the previously introduced hybrid plasticity model and proposes a reformulation of the model with alternative approaches to reduce the number of the material parameters, however keep similar level of accuracy of the model prediction. The development focuses on the coupled approach. The uncoupled approach features some attractive characteristics, such as simple formulation and implementation, easy calibration, and even small number of material parameters for some formulations. They also tend to determine more accurately the dependency of ductile fracture on stress states in terms of stress triaxiality and Lode angle. However, they miss the softening effect caused by damage for materials in which damage is pronounced during large plastic deformation. This will lead relatively poor predictive capability for the investigated sheet metal DP600. Therefore, the Lemaitre damage model, as one of the most popular continuum damage mechanics models, is considered as the starting point for the study. It offers a straightforward representation of the effect of damage on the material behaviour and also solves the problem with few material parameters. The conventional Lemaitre damage model incorporates the softening effect caused by damage in the stress-strain response, whereas the predictive capability of the model in the low stress triaxiality and Lode angle regime is rather limited. To improve the predicative capability of the Lemaitre damage model in more general stress states but still remain the low material parameter number, the effect of Lode angle on damage accumulation is

phenomenologically introduced to the model. Therefore, the model is referred to as a phenomenologically Lode effect added (PLA) Lemaitre damage model.

In this study, the development of the modified Lemaitre (PLA Lemaitre) damage model in the application of the modelling of ductile fracture of the steel sheet DP600 is presented. The constitutive equations of the conventional Lemaitre damage model and the PLA Lemaitre damage model are given. To demonstrate the necessity of incorporating the damage effect to stress-strain response, interrupted tests are performed to examine the damage evolution history. The detailed experimental program and the procedure for the material parameter calibration are presented in detail. The model is further validated with more experiments and the quantitative evaluation of the model is also provided.

## 8.2 Constitutive equations

The starting point of the Lemaitre damage model is the definition of damage interval state variable  $D$ , which influences the plasticity behaviour of the material and results the growth of interval voids and microcracks. Due to the effect of damage, the effective stress tensor  $\tilde{\boldsymbol{\sigma}}$  and effective stress deviator  $\tilde{\mathbf{s}}$  can be expressed as

$$\tilde{\boldsymbol{\sigma}} = \frac{\boldsymbol{\sigma}}{1 - D} \quad \text{Eq. 8.1}$$

$$\tilde{\mathbf{s}} = \frac{\mathbf{s}}{1 - D} \quad \text{Eq. 8.2}$$

where  $\boldsymbol{\sigma}$  and  $\mathbf{s}$  are the stress tensor and stress deviator for the damaged material. In terms of stress deviator,  $\mathbf{s}$ , and the hydrostatic pressure,  $p \equiv 1/3 \text{tr}[\boldsymbol{\sigma}]$ , the damage elasticity law is applied as following:

$$\mathbf{s} = (1 - D)2G\boldsymbol{\varepsilon}_d^e; \quad p = (1 - D)K\varepsilon_v^e \quad \text{Eq. 8.3}$$

where  $G$  and  $K$  are, respectively, the shear modulus and bulk modulus of the material;  $\boldsymbol{\varepsilon}_d^e$  and  $\varepsilon_v^e \equiv \text{tr}[\boldsymbol{\varepsilon}^e]$  are the elastic strain deviator components and the elastic volumetric strain. Therefore, considering that the damage variable  $D$  is only effective during plastic deformation, the corresponding yield function and the associated flow rule is defined by

$$\Phi = \frac{\bar{\sigma}}{1 - D} - \sigma_y(\bar{\varepsilon}^p) \quad \text{Eq. 8.4}$$



$$\dot{\boldsymbol{\varepsilon}}^p = \dot{\gamma} \frac{\partial \Phi}{\partial \boldsymbol{\sigma}} = \dot{\gamma} \frac{\mathbf{N}}{1-D} \quad \text{Eq. 8.5}$$

where  $\bar{\sigma}$  is the equivalent stress,  $\bar{\varepsilon}^p$  is the equivalent plastic strain and  $\sigma_y(\bar{\varepsilon}^p)$  is the flow curve of the undamaged material;  $\dot{\boldsymbol{\varepsilon}}^p$  represents the plastic strain rate and  $\dot{\gamma}$  is the plastic multiplier, which is subjected to the so-called Kuhn-Tucker conditions for the loading and unloading as

$$\dot{\gamma} \geq 0, \quad \Phi \leq 0, \quad \dot{\gamma} \Phi = 0 \quad \text{Eq. 8.6}$$

$\mathbf{N}$  is the plastic flow direction tensor given by

$$\mathbf{N} = \frac{\partial \Phi}{\partial \boldsymbol{\sigma}} = \frac{3}{2} \frac{\mathbf{s}}{\bar{\sigma}} \quad \text{Eq. 8.7}$$

In conventional Lemaitre damage model, the increment of damage variable  $\dot{D}$  is developed from the thermodynamic theory and accumulated mainly based on equivalent plastic strain rate  $\dot{\gamma}$  and the damage strain release rate  $Y$

$$\dot{D} = \dot{\gamma} \frac{1}{1-D} \left( \frac{-Y}{r} \right)^s \quad \text{Eq. 8.8}$$

where  $r$  and  $S$  are the material parameters, and  $Y$  is defined by

$$-Y = \frac{\bar{\sigma}}{2E(1-D)^2} \left[ \frac{2}{3}(1-\nu) + 3(1-2\nu) \left( \frac{p}{\bar{\sigma}} \right) \right] \quad \text{Eq. 8.9}$$

in which  $E$  and  $\nu$  are, respectively, the Young's modulus and Poisson ratio of the undamaged material.

From the above equation, the term  $p/\bar{\sigma}$ , referred to as stress triaxiality, is used in the definition of damage strain release rate  $Y$ , which introduces the influence of stress triaxiality to damage in the model. However, for another essential factor, the Lode parameter is not considered in this conventional Lemaitre model, which leads to inaccurate prediction in complex stress states. In order to remediate this shortage, we propose an addition of a Lode parameter sensitivity function, initially used in the Xue–Wierzbicki [69] damage model to Eq. (8), to include the effect of Lode parameter. The Lode parameter sensitivity function is defined by

$$\mu_\theta(\theta) = \chi + (1-\chi) \left( \frac{|\theta|}{\pi/6} \right)^k \quad \text{Eq. 8.10}$$

where  $\chi$  is non-negative material constant and  $k$  is a shape parameter of the Lode parameter sensitivity function. With this equation, Eq. 8.8 is rewritten as

$$\dot{D} = \frac{\dot{\gamma}}{\mu_{\theta}(\theta)} \frac{1}{1-D} \left(\frac{-Y}{r}\right)^s \quad \text{Eq. 8.11}$$

in which a phenomenological Lode effect is simply added to the original Lemaitre damage model. The model is, therefore, referred to as the phenomenologically Lode angle effect added (PLA) Lemaitre damage model. In addition, the ductile fracture is assumed to occur, when the damage is accumulated to a critical value,  $D_{cr}$ . The model is implemented into Abaqus/Explicit by a user defined subroutine, VUMAT.

### 8.3 Experimental and numerical procedures

A series of flat notched dog-bone specimens with various notch radii are designed for achieving the different stress states. The basic geometry of the notched dog-bone specimen is based on the standard smooth specimen geometry in EN 10002-1. Upon that, radii of 80mm, 20mm, 10mm, 5mm and 2mm are attached to gain the different stress triaxialities and Lode angles in the central cross-section of the specimen. The sketch of specimen geometry is shown in Fig. 8.1.

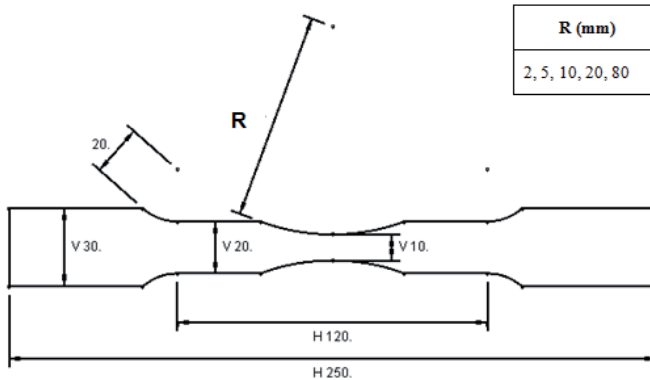


Fig. 8.1: Geometries and dimensions of the notched dog-bone tensile specimens.

In this design, the stress state of the specimen with notch radius 80mm is close to uniaxial tension. On the contrary, the stress state of the specimen with notch radius 2mm is similar to plane-strain tension. The stress states of the other three specimens with notch radii of 20mm, 10mm and 5mm are distributed between uniaxial tension and plane-strain tension. The gauge length of the specimen is 120mm and the cross-head speed is 0.2 mm/min. Before the

mechanical test, the specimen geometry is measured after the manufacture to guarantee the accuracy for the following FE model simulation. The measured featured dimensions are listed in Tab. 8.1.

Tab. 8.1: Measured geometries of the specimens after mechanical manufacture.

Sample serial	R80	R20	R10	R5	R2
Radius, mm	84	20	9.6	5	2
Min. cross-section, mm	10.02	10	9.98	10	10
Thickness, mm	1.5	1.5	1.5	1.5	1.5

The FE models are built in Abaqus/Explicit based on the measured geometries of tested specimens. As shown in Fig. 8.2, the model is developed in 1/8 size of the full specimen in order to reduce the total amount of elements and save the calculation time. Therefore, three symmetry boundary conditions are applied to the three symmetric planes of the model as indicated in Fig. 8.2 (c). The model is meshed by eight-node brick elements with reduced integration point (C3D8R) and each model is partitioned into critical zone, transitional zone and ineffective zone to mesh with different mesh sizes. The mesh size in critical zone is chosen as  $0.1 \text{ mm} \times 0.1 \text{ mm} \times 0.1 \text{ mm}$ . The height of the critical zone for each models is designed individually, to ensure that the contour of the PEEQ larger than 0.1 is always in the critical zone.

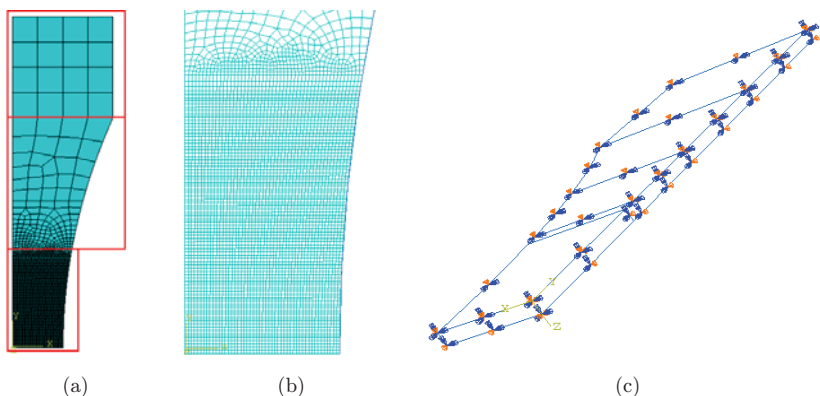


Fig. 8.2: Mesh and boundary conditions of the notched dog-bone specimen: (a) three partitioned mesh zones; (b) critical mesh zone; (c) boundary conditions set-up.

## 8.4 Results and discussion

### 8.4.1 Experimental investigation on the damage development during loading

Before the parameter calibration of the model, the development of damage during the plastic deformation is studied by interrupted experiments. The aim of the interrupted tests is to qualitatively correlate the damage development to the plastic deformation.

The notched dog-bone (NDB) specimen with notch radius of 5mm is used for the test in cooperation with the subsequent metallographic investigation. Four parallel NDB-R5 specimens are tested to the deformation stage (a), (b), (c) and (d), respectively. For better control of the characteristic of the stages, the testing sequence is reverse to the naming sequence. As shown in Fig. 8.3, specimen (d) is corresponding to the final fracture and it was the first one to be conducted. Stage (c) is intended to be 90% of the final fracture displacement obtained from the test at stage (d), and the stage is located between the final fracture and the maximum load. Accordingly, stage (b) is right at the maximum force, while stage (a) is corresponding to 60% of the fracture displacement. During each test, a video system is applied to recording the macroscopic deformation morphology of the front surface of the specimen. The corresponding picture at each stage of the deformation is shown in Fig. 8.3 and the four of them in a sequence with respect to time is describing the history of the deformation of the specimen. At the stage (a), although the deformation is naturally not homogeneous due to the nonlinearity of the specimen, obvious localised necking or shear band is not found. When the maximum load is reached at stage (b), a tiny tip of the localised necking/band is formed at the centre of the right side of the notch. Starting from this point, the plastic deformation is significantly concentrated to the centre line linking the two notches. An obvious band is formed at stage (c). It is noted that the localised necking/band is quite perpendicular to the loading, although it appears a certain angle tilted from the horizontal axis due to the misalignment of the camera. It can be also seen from the inclination of the specimen in the picture. The concentration of the deformation at localised band finally leads to the final fracture of the specimen at stage (d). It is a very sudden fracture occurrence and it is impossible to capture the initiation place of the fracture with the current camera under the crosshead speed of 0.2 mm/min, although it is already a very slow speed. The fracture path is completely in line with the centre line of the specimen linking the tips of the two notches.

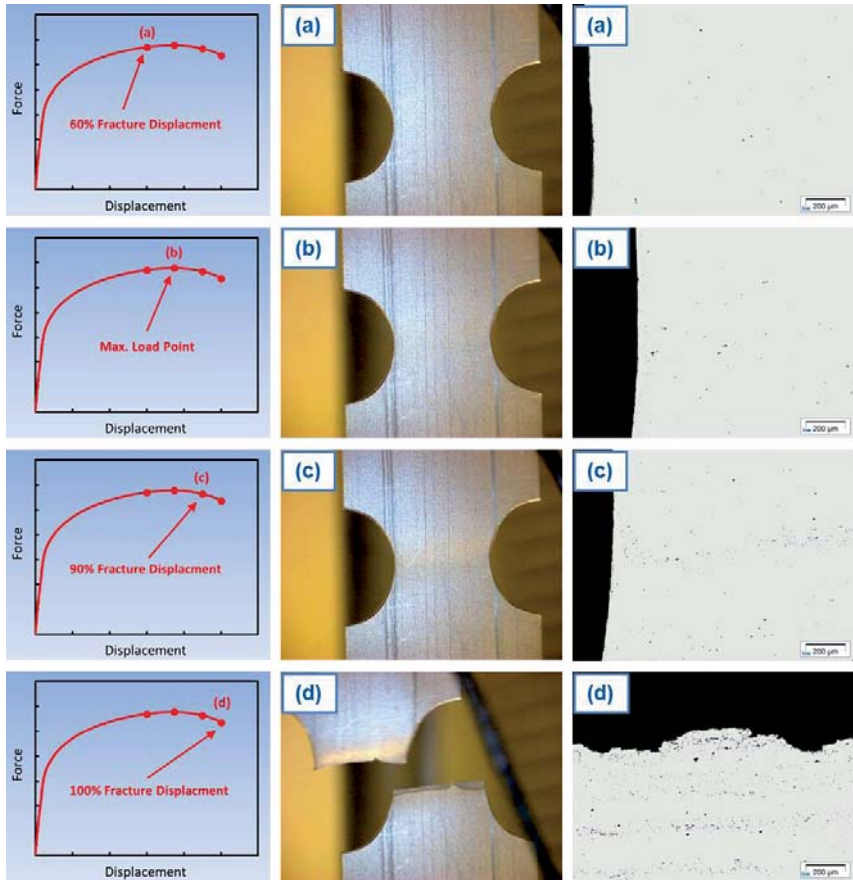


Fig. 8.3: Interrupted tests of the notched dog-bone tensile specimens with notch radius of 5 mm; three columns are corresponding to representation of the different interrupted points, the macroscopic deformation picture captured by a video system and the metallographs with 100 times magnification of the critical zone of the specimen at each interrupted point.

After the interrupted test, the zones with critical deformation are cut from the specimen and embedded in resin for LOM investigations. The four specimens at different deformation stages are polished to the middle thickness plane for the consistency of the comparison. For a qualitative comparison of the damage development at different stages, 100 times magnification is used. The metallographs for the four deformation stages are shown in Fig. 8.3. In the current investigation, damage is simply related to the void volume fraction. At the stage (a), voids are

rarely observed in the critical deformation zone, and the observed voids are uniformly distributed in the observing window. At the stage (b), more voids are observed and they tend to distribute near the centre line of the specimen, especially at the notch tip location, which is connected to the observation of initiation of the localised band from the video system. An extensively increased void volume fraction can be found at the stage (c) and they are densely located to the centre line of the specimen. In addition, they are not only distributed at the notch tip but also the centre of the specimen. The concentration of voids is an outcome of the formation of the entire localised band through the specimen width, but they are not uniformly distributed along the band line. From the studied specimen, the concentration at the centre slightly overtakes the notch tip. The concentration spot of damage/voids can be considered as a hint of the final fracture initiation location. At the stage (d), significantly large amount of voids are observed at the centre of the fractured specimen. Most of the voids are located right beneath the fracture surface and large cluster of voids are also visible at this region. Several void bands parallel to the fracture surface but away from it are also observed.

To conclude: the amount of damage developed during the plastic deformation is not negligible, in particular after the maximum load is reached. For this reason, a coupled damage model is desired for the simulation of the DP600 steel sheet.

### 8.4.2 Parameter calibration

The damage parameter calibration is performed by an iterative procedure of evaluating the fitting goodness of the force–displacement response of the tests. Three steps are defined for this purpose:

- Calibration of the parameters from the conventional Lemaitre damage model,  $r$  and  $S$ .
- Calibration of the parameters from the Lode added function,  $\chi$  and  $k$ .
- Calibration of the critical damage parameter,  $D_{cr}$ .

The advantage of this programme is that the calibration steps are independent from each other. Therefore, no iterative procedure is required between steps, only within each step. As the Lode function,  $\mu_\theta(\theta)$  is assumed to be one under uniaxial/axisymmetric tension, i.e.  $\theta$  equals to  $\pi/6$ , the calibration of  $r$  and  $S$  is not influenced by the Lode function under such loadings. It is normally suggested  $S$  remains unity for steels in literature [83; 84], which leaves  $r$  as the only independent parameter. Once  $r$  and  $S$  are calibrated, the Lode function parameters,  $\chi$  and  $k$  can be calibrated iteratively under another loading condition when the Lode angle is not equal to  $\pi/6$ . At last, the calibration of  $D_{cr}$  is performed based on the common fitting quality of

the final fracture on the aforementioned two loading cases. Usually an average value of for the best fits for both cases is used. With this programme, only four independent parameters need to be calibrated and a clear parameter calibration strategy is defined. The details of the parameter calibration for DP600 steel sheet is shown in the following section.

For the first step, calibration of  $r$ , a smooth dog-bone tensile test is often recommended, as its stress state is uniaxial tension. However, it is noted that the stress state only stays uniaxial tension before necking appears. In addition, it also consumes extensive computational effort to run a simulation of it because a large number of fine elements is required to be distributed to the entire section of the homogenous part of the specimen. Instead, the tensile test of notched dog-bone specimen with a radius of 80 mm is used for the calibration. Although the Lode function is not completely unity, it is very close to one due to the wide notch. In Fig. 8.4, the influence of  $r$  is illustrated. In general, the force–displacement response is not very sensitive to  $r$ , as the prediction by the model with different  $r$  values only differs slightly. Considering the potential influence of the Lode function, the prediction with a slight overestimation ( $r = 38$ ) is adopted. As the actual value of the Lode parameter is smaller than unity, the slight estimation will be corrected when the Lode functions is applied.

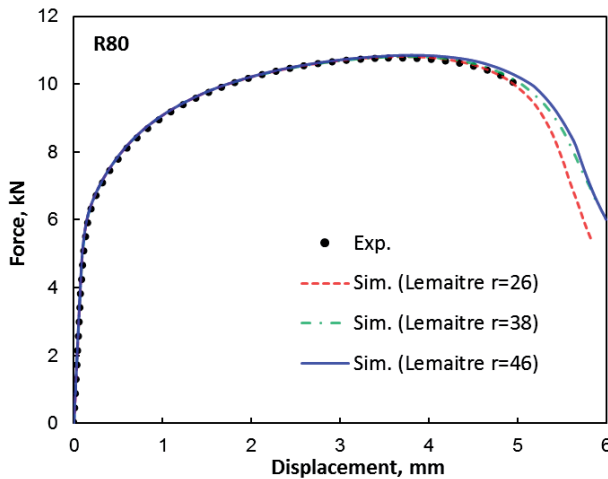


Fig. 8.4: Comparison the influence of parameter  $r$  in the conventional Lemaitre damage model,  $S$  is assumed to be one.

In the calibration step two, before the detailed calibration for DP600, a parametric study is performed to show the individual effect of each parameter for a better control during the

calibration procedure. In Fig. 8.5 (a), the effect of different  $\chi$  on the Lode function is shown in the principal strain space when  $k = 1$ . As pointed out by Xue [174],  $\chi$  is controlling the lower limit of the Lode function value under shear or plane-strain tension loading condition. When  $\chi$  is set as one, the Lode function is not effective for any kinds of loading conditions.

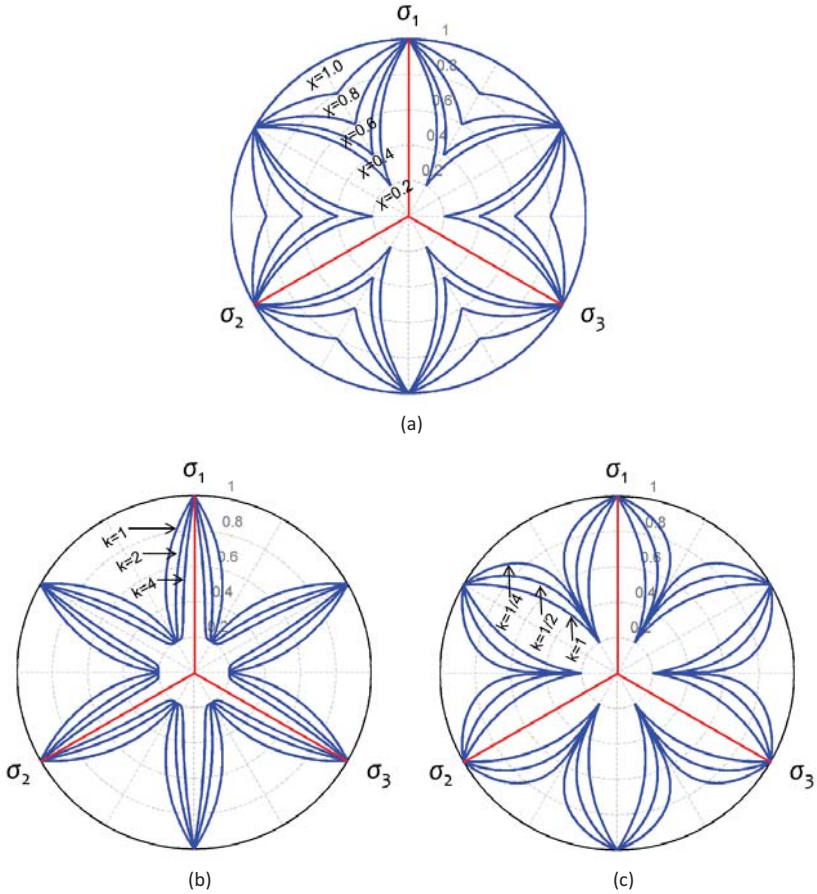


Fig. 8.5. (a) Effect of different  $\chi$  on the Lode function in the principal strain space under  $k = 1$ ; (b) Effect of different  $k$ , from a quarter to one, on the Lode function under  $\chi = 0.2$ ; (c) Effect of different  $k$ , from one to four, on the Lode function under  $\chi = 0.2$ .

In Fig. 8.5 (b) and (c), the effect of  $k$  on the Lode function is shown when  $\chi = 0.2$ . When  $k$  is set as one, a linear relation is defined of the Lode function with respect to the Lode angle, although it appears curved in the polar space of the principal strains. If  $k$  changes from one



to zero, as shown in Fig. 8.5 (b), the relation between Lode function and Lode angle is becoming highly nonlinear. The distribution of the Lode function is more concentrated to one and a sudden drop to the  $\chi$  value is expected when Lode angle becomes zero. On the contrary, if  $k$  varies from one to infinite, the opposite effect is observed on the Lode function, as shown in Fig. 8.5 (c). In general,  $\chi$  controls the lower limit of the Lode function and  $k$  contributes to the distribution of the Lode function in the Lode angle range.

The employed specimen for the calibration of  $\chi$  and  $k$  is the notched dog-bone specimen with a radius of 2 mm. The reason for using this specimen is that the stress state of the critical deformation zone of it is very close to the plane-strain tension. Under ideal plane-strain tension,  $\theta$  equals to zero, which leads to the Lode function value as parameter  $\chi$ . Although  $\theta$  is not completely zero and it is also not constant during the deformation for R2 specimen, the iterative calibration starts with only parameter  $\chi$ , assuming ideal plane-strain tension by setting  $k$  as 10. In Fig. 8.6 (a), the influence of parameter  $\chi$  on the force–displacement curve of R2 specimen is shown. With the currently applied values of  $\chi$ , 0.2, 0.4 and 0.6, none of them gives perfect result and a better  $\chi$  is in the range from 0.2 to 0.3. However, considering the magnification effect of the Lode function by assuming ideal plane-strain tension in the R2 specimen, the lower value of  $\chi$  is used. The underestimation of the force response is corrected by setting an appropriate  $k$  value. As shown in In Fig. 8.6 (b), different  $k$  values are applied to the simulation of R2 specimen under  $\chi = 0.2$ , and  $k = 4$  is finally employed.

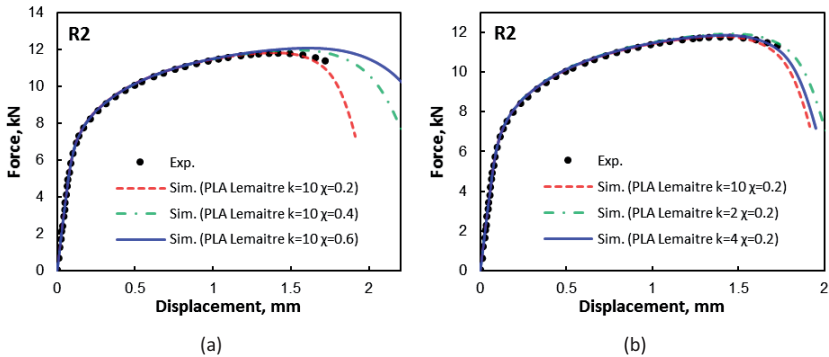


Fig. 8.6. (a) Comparison the influence of parameter  $\chi$  in PLA-Lemaitre damage model ( $k = 10$ ); (b) Comparison the influence of parameter  $k$  in PLA-Lemaitre damage model ( $\chi = 0.2$ ).

The last step is the calibration of  $D_{cr}$  based on the simulation results for both R80 and R2 specimens. With previously calibrated parameters, simulations with PLA Lemaitre damage

model are run for both specimens. For reference, simulations with original Lemaitre damage model and Mises plasticity are run as well. The results are shown in Fig. 8.7. For R80 specimen, compared to the result of Mises plasticity model, the Lemaitre damage model as well as the PLA Lemaitre damage model is in a good agreement with the experiment. For R2 specimen, both the Mises plasticity and original Lemaitre damage model overestimate the experimental force to a large extent after the maximum force is reached, while the PLA Lemaitre damage model show a good agreement with the experiment. By balancing the prediction on the final fracture of two specimens, a constant  $D_{cr}$  as 0.2 is applied to the PLA Lemaitre damage model for the control of element deletion to simulate the fracture. A good prediction on the fracture displacement is achieved for both specimens with this value, as shown in Fig. 8.7.

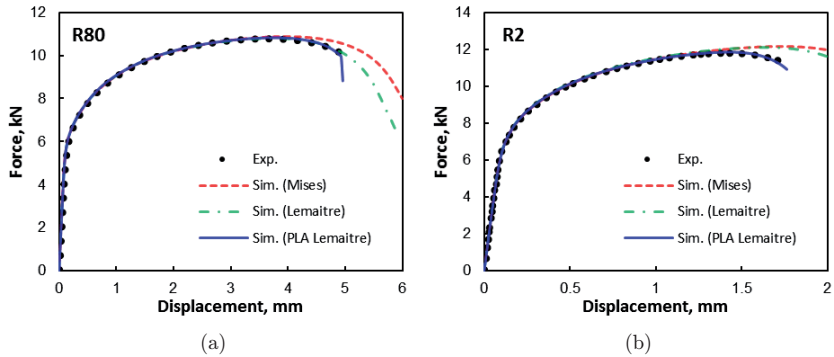


Fig. 8.7: Comparison of the experimental force–displacement curves and the numerical predictions by Mises plasticity model, Lemaitre damage model and PLA Lemaitre damage model for notched dog-bone specimens with radii of (a) 80 mm and (b) 2 mm.

All the calibrated parameters are listed in Tab. 8.2. In total there are five parameters, two from the original Lemaitre damage model, two for the added Lode function and one for the element deletion. As  $S$  is usually considered as unity for most of the steels in the original Lemaitre damage model, only four parameters are independent.

Tab. 8.2: Parameters of the PLA Lemaitre damage model for DP600 steel sheet.

Lemaitre Parameters		Lode Parameters		Element Deletion
$r$	$S$	$\chi$	$k$	$D_{cr}$
38.0	1.0	0.2	4.0	0.2

### 8.4.3 Validation of the model and discussion

To examine the predictive capability of the model, the rest geometries of the notched dog-bone specimens are simulated with the calibrated set of parameters to compare the force–displacement curves with the experimental ones, as shown in Fig. 8.8. In these results, the Mises plasticity model overestimates the force–displacement responses for all geometries, in particular after the maximum force as it is not considering the damage development. However, it is a good marker to compare the performance of other two models. The Lemaitre damage model without considering the Lode effect improves the prediction, but the softening effect is still not sufficient. PLA Lemaitre damage model with the Lode enhancement gives a good prediction for all three specimens in terms of the force–displacement response as well as the final ductile fracture.

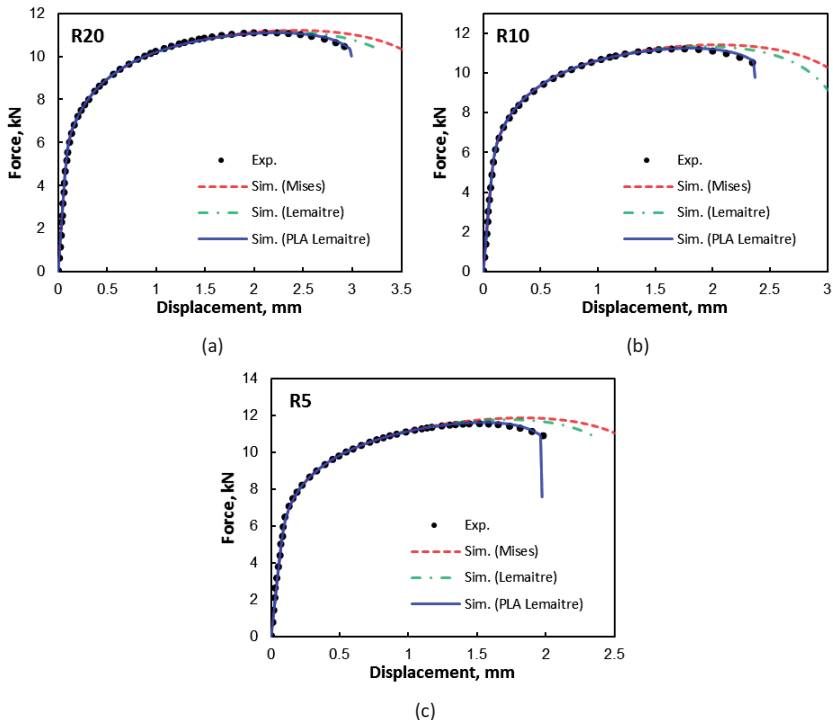


Fig. 8.8: Comparison of the experimental force–displacement curves and the numerical predictions by Mises model, Lemaitre damage model and PLA Lemaitre damage model of notched dog-bone specimens with radii of (a) 20 mm, (b) 10 mm and (c) 5 mm.

For the original Lemaitre damage model, a good result for large notch radius is obtained according to the similar stress state to the uniaxial/axisymmetric tension. With the decrease of the notch radius, the stress state changes toward plane-strain tension. By overlooking the effect of Lode angle, Lemaitre damage model is not capable of providing a consistently accurate prediction under different stress states from uniaxial tension to plane-strain tension. The PLA Lemaitre damage model, with adding the Lode effect on damage accumulation, realises the overall best predictive capability, which proves that the Lode angle is as important as the hydrostatic pressure to the description of the damage accumulation.

The response of the force–displacement curve is a result of the formulation of the damage accumulation. For a better understanding of the difference of the two damage models, the damage contour of the five specimens with Lemaitre (left for each geometry) and PLA Lemaitre damage model (right for each geometry) are shown in Fig. 8.9. The moment for the contours is taken at a displacement slight ahead to the final fracture. For the same geometry, both models are taken exactly at the same global displacement for accurate comparison. It is obviously noted that with the consideration of the Lode effect, the damage accumulation rate of PLA Lemaitre damage model is much faster than the original Lemaitre damage model. This is also corresponding to the faster drop of the global force response at the same displacement. In particular for the R2 specimen, the introduction of the Lode effect also changes the location of the maximum damage variable. In Fig. 8.9 (e), the maximum damage spot is located at the area between the centre and the edge of the specimen for PLA Lemaitre damage model, while it is at the exact edge of the notch for the original Lemaitre model.

The evidence of the fracture initiation spot is not supplied by the experiment, and the difference of the fracture initiation location prediction between two models is basically resulted from the model formulation. For a detailed analysis, a local study on the relevant elements of the R2 specimen is performed. Three locations/elements are considered, the centre element, the critical element and the edge element, as indicated in Fig. 8.10 (a). The stress states of the three elements are analysed first in terms of stress triaxiality and Lode parameter. In Fig. 8.10 (a), the red solid lines represent the history of the stress triaxiality of the three elements while the blue dashed lines correspond to the Lode parameter. The centre element and the critical element show similar stress states, and they are very close to the ideal plane-strain tension before the severe localisation that changes the local stress state substantially. On the other hand, the edge element is subjected to a loading close to uniaxial tension.

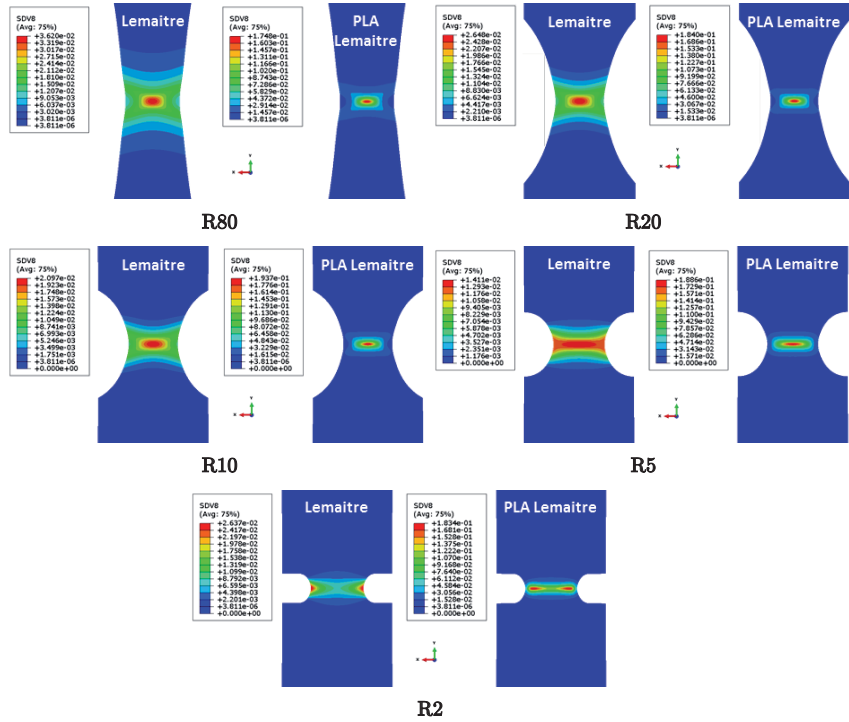


Fig. 8.9: Comparison of local damage variable distribution of notched dog-bone specimens with five different radii between Lemaitre damage model results and PLA Lemaitre damage model results at vicinity of the fracture displacement.

The damage accumulation is related to, on the one hand, the local stress state, and on the other hand, the local plastic deformation. In Fig. 8.10 (b), the equivalent plastic strain contour is also shown for the R2 specimen at the last increment before element deletion. The maximum local plastic deformation is concentrated to the edge element, different from the maximum damage accumulation location. It is commonly accepted that the area that undergoes the largest degree of plastic deformation initiates the fracture. The experimental support on this assumption for a wide range of stress states also remains unclear, which could be a potential further investigation topic. However, theoretically this divergence is possible and can be explained considering both the stress and strain contribution to the damage accumulation. In Fig. 8.10 (b), the relation between the equivalent plastic strain and damage variable is also shown. Despite the more plastic deformation of the edge element, the damage accumulation on

it is still far lower than the critical element due to the stress state difference, especially the Lode parameter. As the critical element owns higher stress triaxiality and lower Lode parameter, both of these, in particular the Lode parameter, contribute a faster damage evolution according to Eq. 8.11.

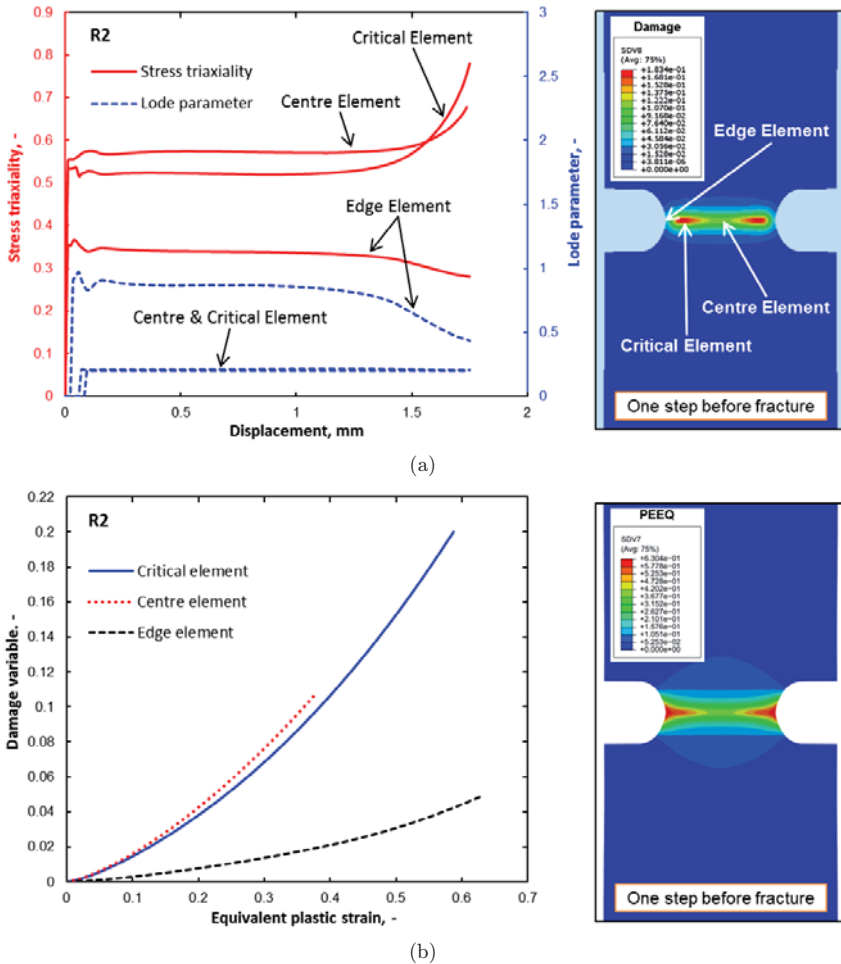


Fig. 8.10: (a) The history of local values, stress triaxiality and Lode parameter, at three different locations (centre, critical and edge element) of R2 specimen; (b) The development of damage vs. the equivalent plastic strain at three different locations (centre, critical and edge element) of R2 specimen.

Comparing the critical element and centre element, the damage accumulation rate of the centre element is slightly higher than the critical element because the centre element is closer to the plane-strain tension. However, the final accumulated damage of centre element is lower than critical element as it undergoes significantly less plastic deformation compared to the critical element. Therefore, the damage accumulation in the PLA Lemaitre damage model is an integrated result of the local stress state including stress triaxiality and more importantly the Lode angle and the plastic deformation. In the original Lemaitre damage model, the effect of the plastic deformation is dominant to the damage accumulation, but the stress state is not obvious without the consideration of Lode effect under the current parameter set.

In general, the stress state from the designed specimens ranges from the uniaxial tension to plane-strain tension. However, due to the nonlinear geometry and localisation, the stress state does not keep constant during the deformation. In Fig. 8.11, the history of the stress state of the critical element (defined as the element that owns the highest damage accumulation) for five geometries is shown. It is noted that the stress triaxiality tends to get much higher than 0.578 with the plastic deformation, while Lode parameter is decreasing to zero. With the higher stress triaxiality, the local stress state goes beyond the conventional plane-strain tension, but more generalised case.

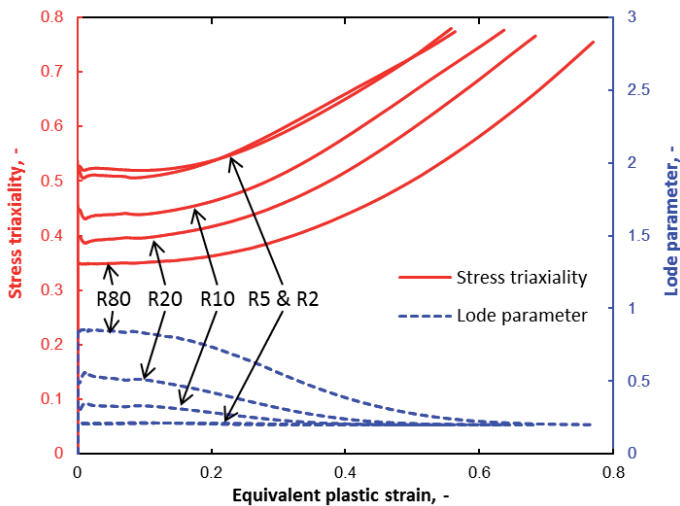


Fig. 8.11: The history of the local stress state variables, stress triaxiality and Lode parameter, at the critical elements of the notched dog-bone specimens with five different radii.

In the typical uncoupled approach, the fracture strain is considered as the fracture indicator with a weighted function involving the stress state. Due to the nonlinear behaviour of the stress state history, it is usually averaged during the whole process. In the PLA Lemaître damage model, a single damage parameter, critical damage accumulation  $D_{cr}$  is used for the prediction of fracture for all stress states, as the stress state influence on the damage evolution is already included. In Fig. 8.12 (a), the effective stress–strain curves and the damage accumulation responses of the critical elements in the five geometries are shown. It is note that the damage accumulation rate and the effective stress are very different from each other. Therefore, the stress state dependency of the fracture strain is a nature outcome as plotted in Fig. 8.12 (b). The five failure strains are obtained at the moment when  $D_{cr}$  is reached, and a typical damage curve which is normally adopted for the uncoupled approach can be fitted based on them.

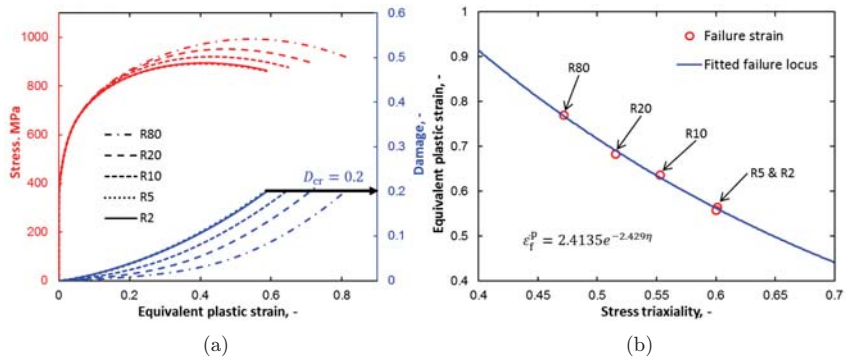


Fig. 8.12: (a) The effective stress–strain curves and the damage accumulation responses of the critical elements of the notched dog-bone specimens with five different radii; (b) The damage curve fitting based on the failure strains from the five geometries.

## 8.5 Conclusions

The study presents the development of a modified Lemaître damage model, PLA-Lemaître damage model. Several conclusions can be drawn from it:

- From the investigation of interrupted tests with damage quantification by light optical microscopy, it is proved for the current DP steel, that damage starts to develop to a non-negligible extent at the maximum load and the further localisation of the plastic deformation significantly accelerate the rate of damage evolution. Therefore, the softening effect introduced by the damage is a necessary factor for the description of



the plastic flow behaviour of the steel. The final fracture is a consequence of the interaction between the plastic localisation and damage evolution. The significance of damage development can be also proved by the large number of voids and coalesced voids right beneath the fracture surface.

- A new damage model, Phenomenologically Lode effect Added (PLA) Lemaitre damage model, is proposed. By adding the Lode effect function to conventional Lemaitre damage model, accurate predictions on both force–displacement curves and fracture displacements of DP600 under various stress states are achieved by PLA Lemaitre damage model. The Lode angle effect is therefore proved to be very important as well as stress triaxiality for the numerical simulation of damage accumulation.
- In the model, only four independent parameters are necessary to be calibrated for individual material. Additionally, the material parameter calibration strategy is rather straightforward. Only two commonly used notched dog-bone specimens are required to conduct the material parameter calibration. Due to the interaction of the Lode effect controlling parameters on the damage evolution rate, an iterative procedure is necessary for the determination of these two parameters. The rest parameters are directly determined.
- A study of the damage accumulation from a local viewpoint shows that the inclusion of the Lode effect on the Lemaitre damage model also influences the crack initiation location for the specimens whose stress states are in the vicinity of plane-strain tension. The direct proof of this observation is not accessible with the current setup of the experiments. Further improvements of the investigation are suggested and planned. Finally the coupled approach can also be interpreted in the space of fracture strain and stress states, which is normally employed in the uncoupled approach. A typical damage curve is obtained based on the failure strains of the designed five geometries ranging from the uniaxial tension stress state to plane-strain tension. It is a nature outcome of the formulation of the model with consideration of stress triaxiality and Lode angle on the damage accumulation. The model satisfies the global force–displacement response with the inclusion of damage effect and also validates the stress state dependency of ductile fracture observed in the uncoupled approach.



# Chapter 9

## Including a mechanism description by multiscale modelling

### 9.1 General ideas

Recent experimental and numerical studies show that both stress triaxiality and Lode angle have effect on the failure strain [52; 54; 55; 60; 64; 65; 175-177]. These experimental and numerical investigations mainly focus on the macroscopic crack initiation observed by naked eyes or DIC. However, for the application of dual-phase steels, damage has become such a pronounced phenomenon that large amount of damage in terms of voids for example are accumulated in the material before crack and fracture [12]. Therefore, to address the importance of the damage initiation and evolution rather than fracture, the hybrid approach to describe the plasticity and damage behaviour of such materials is proposed, and in the model a microstructural-level based DIL with the dependency of both stress triaxiality and Lode angle is also observed and calibrated from experiments. Despite the good precision of predictive capability, the model brings a large number of material parameters. The effort to calibrate these parameters is severely hindering the application of it to a general or industrial scale. Another main disadvantage is that the model has a phenomenological character, as there is no material information involved. This also limits the application of the model to consider material microstructure in order to optimize the material for improved mechanical behaviour. For this reason, a micro to macro scaling approach that brings the microstructural information in the phenomenological macroscopic model is required.

The microstructure based modelling incorporating with RVE technique is applied to the area of study [7; 116-120; 123-127; 132]. The focus of these studies varies from demonstrating

different damage mechanisms or revealing the dominant damage mechanism to predicting the failure strain under uniaxial tensile condition and the modes or patterns of failure under different loading conditions. However, they are so far mainly qualitative. In addition, the difference between damage and fracture is not clearly defined and distinguished in these studies. For the conventional highly ductile materials, the differentiation of these two terms makes minor impact on analysing the failure of materials or structural integrity, because the final fracture of these materials are mainly driven by extensive strain localisation rather than damage. Damage normally occurs in a quite late phase of deformation prior to the final fracture. However, it is not the case for the newly developed steels, in particular the high strength steels, where damage introduces non-negligible impacts on the strength and formability and finally triggers the final fracture [12]. Therefore, in the hybrid damage mechanics model, a clear criterion of damage initiation is introduced. It is normally a strain-based criterion depending on stress triaxiality and Lode angle.

The damage initiation strain is corresponding to the onset of damage, i.e. the material degradation from a microscopic level. Beyond this point, the material is no longer defect-free and there is damage that starts to accumulate inside the structure, which is detrimental to the safety and integrity of component in application. For the forming of the high strength steels, e.g. DP steel, the determination of the damage initiation strain is more relevant, as it gives an indication of the forming limit. In this context, to predict the damage initiation is more beneficial than fracture to explore the material properties in manufacturing components.

The key purpose of this section, therefore, is to quantitatively evaluate the damage initiation under different stress states and reveal the underlying mechanism of the dependency of damage initiation on stress states from a microstructural level. A 2D real microstructure micrograph of the DP600 steel is used to generate the RVE. The plastic strain localisation theory by Sun et al. [123] is applied to the simulation without any other damage models or imperfections and the damage initiation under different stress states is considered as the nature outcome of the localisation of the plastic strain due to the microstructural-level deformation incompatibility. Three typical stress state scenarios for sheet metal forming are considered in this study, uniaxial tension, plane-strain tension and equibiaxial tension. The quantitative results obtained from the RVE simulation are compared to the experimentally calibrated DIL.

## 9.2 Experimental study on the damage initiation

To observe the damage mechanisms of the DP600 steel, fractured central-hole and plane-strain specimens corresponding to uniaxial tension and plane-strain tension stress state, respectively, are prepared and subjected to the SEM analysis. The specimens are cut along the loading direction throughout the thickness and they are then polished to the thickness plane where severe plastic deformation occurred. The micrographs captured on the through-thickness cross-section of both specimens are presented in Fig. 9.1. By zooming in to the local area just beneath the fracture surface, large amount of voids are observed. Most of those voids are already enlarged and the damage initiation for them is difficult to be recognised. There are also some small voids which are just initiated. Two types of patterns of the initiation of these voids are classified. One prominent one is that for both loading cases there are voids generated at the ferrite–martensite interface between the martensite islands which are close to each other or around the interface of the ferrite and martensite phase boundaries (indicated by red circles in Fig. 9.1). Secondly, small fraction of martensite cracking is also observed in both cases, as shown by the green rectangles in Fig. 9.1. Generally, this observation is in line with the conclusion of Ahmad et al. and the result obtained by Avramovic-Cingara et al. [17] for their DP600 steel with uniformly distributed martensite islands.

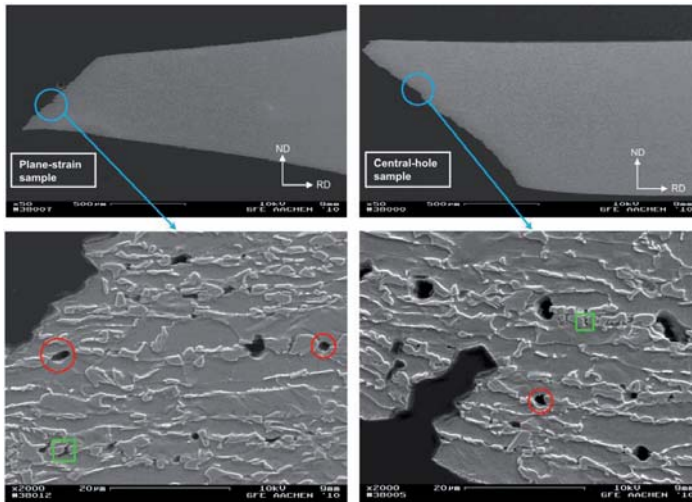


Fig. 9.1: Micrographs by SEM analysis of the through-thickness cross-section of fractured plane-strain specimen and central-hole specimen.

For the experimental characterisation of damage initiation, the instant is captured by DCPD method. The characteristic length of the damage initiation is normally in the order of dozens of microns. This length scale is of importance when the RVE size is considered to correlate the prediction of damage initiation by RVE simulation to the experimentally measured damage initiation by DCPD. The detailed calibration procedure and the 3D calibrated DIL for the DP600 steel sheet using the method is presented in section 6.2.1.3. The DIL is re-presented in Fig. 9.2 (a) for the ease of reading.

Under the plane stress condition, by combining Eq. 3.12 and Eq. 6.2, the 3D DIL can be expressed in the space of equivalent plastic strain and stress triaxiality, as shown in Fig. 9.2 (b). As the plane-stress condition is often assumed in the sheet metal society and the RVE model is 2D, the upscaling investigation in the thesis is focused on the 2D DIL in the space of equivalent plastic strain and stress triaxiality under the plane-stress assumption.

## 9.3 Numerical procedures for RVE simulation

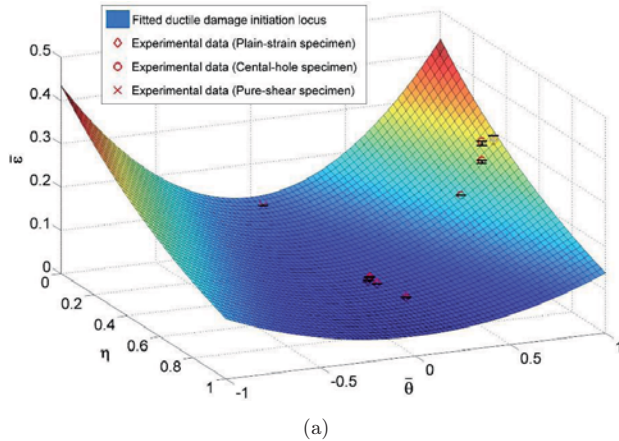
### 9.3.1 RVE construction and data evaluation

For the construction of RVE, the original EBSD micrograph in Fig. 4.1 is cut into a  $25\ \mu\text{m} \times 25\ \mu\text{m}$  square, as shown in Fig. 9.3. The size of the RVE is pre-determined by the characteristic length of the damage initiation detected by DCPD method, which often displays the length about 25 microns. Then the micrograph is automatically segmented into two different phases using a photo processing software. By adjusting the colour tolerance in the software, two phases can be differentiated and a monochrome image is generated, in which martensite phase ends up with black and ferrite phase ends up with white, as shown in Fig. 9.3. In this model, only two phases are considered to be present and perfect bonding is assumed between the two phases.

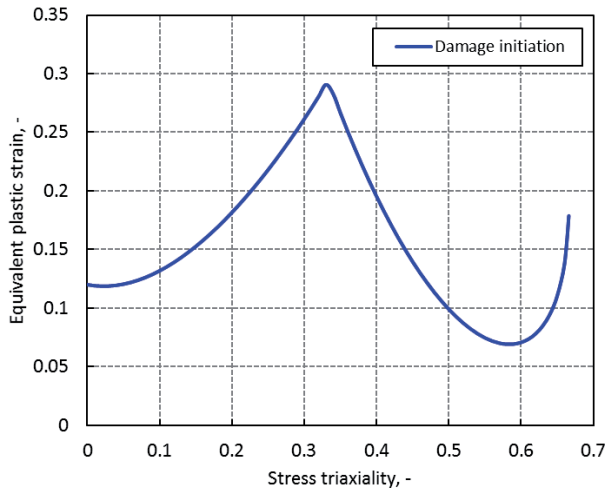
In order to study the influence of mesh size and element shape on the RVE simulation, three different types of mesh are applied. The corresponding mesh specifications and morphologies are shown in Fig. 9.4.

The first mesh is generated by an in-house software, which can directly transform the micrograph into a mapped mesh of a tessellation, which is comprised of regular, square elements. The element size for this mesh is  $0.2\ \mu\text{m} \times 0.2\ \mu\text{m}$ . Using this method, the phase boundaries of ferrite and martensite have stepped shapes. Obviously, the accuracy of the

discretisation of the microstructure increases with increasing of element number. This mesh is called type-1 mesh hereinafter.



(a)



(b)

Fig. 9.2: The calibrated ductile DIL by the DCPD method; (a) 3D locus in the space of equivalent plastic strain, stress triaxiality and Lode angle parameter, (b) 2D locus in the space of equivalent plastic strain and stress triaxiality under the plane stress condition.

The motivation of the second mesh is to alter the element size as well as the shape of the phase boundary. Lines defining the boundaries between the two phases in the monochrome graph are

extracted by the photo processing software. Subsequently the boundary-line image is converted from raster to vector form. The vectorised lines are then imported to Abaqus, which can generate a 2D mesh with quadrangular elements. The element size of this type of mesh is homogeneous with average value of about  $0.1 \mu\text{m}$ . One important feature of this mesh is that the phase boundary is completely smooth and this mesh is called type-2 mesh hereinafter.

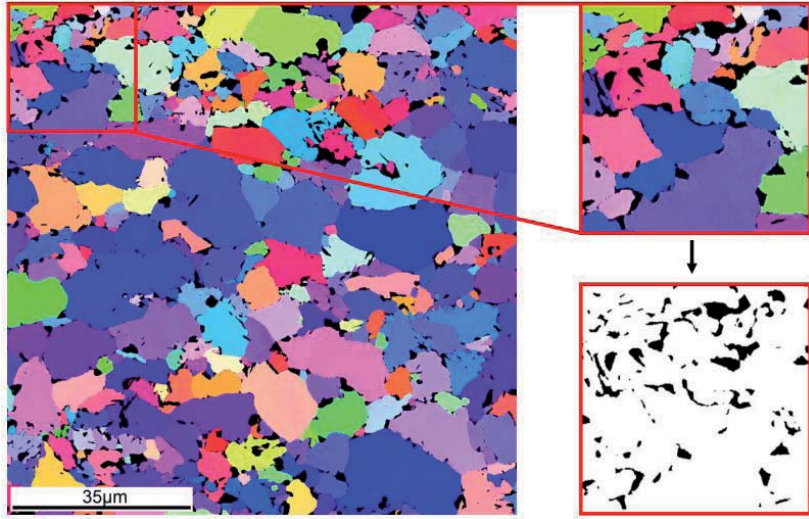


Fig. 9.3: Converting of original EBSD micrograph into a monochrome micrograph with the size of  $25 \mu\text{m} \times 25 \mu\text{m}$  for the RVE construction.

The third mesh is targeted to be a balanced one in terms of the description of the phase boundary, element size and the computation time. The mesh consists of both coarse elements and fine elements. Zones near the phase boundaries of ferrite and martensite are meshed with finer elements to maintain the morphology precisely and other parts are meshed with coarse elements for the optimisation of the computation time. The size of course element is about  $0.5 \mu\text{m} \times 0.5 \mu\text{m}$  while that of fine element is about  $0.1 \mu\text{m} \times 0.1 \mu\text{m}$ . The phase boundary is partially smooth with some stepped shape at some regions. This mesh is called type-3 mesh hereinafter. Since the sheet material is mostly subjected to in-plane loading, the stress state is often considered to be plane stress. Therefore, in this study, for all three different types of mesh, four-node continuum plane stress element with reduced integration point (CPS4R) is used.



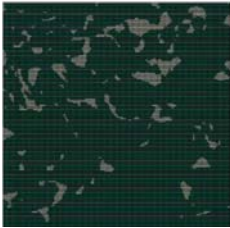
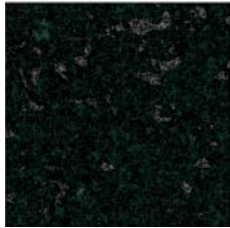
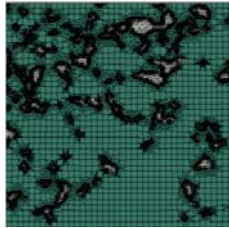

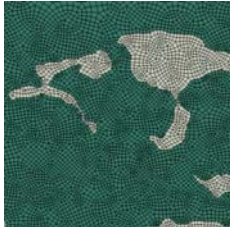
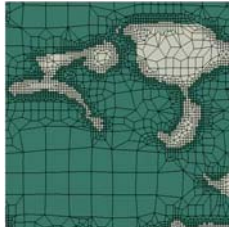
Mesh type	1	2	3
Mesh method	In-house software	Abaqus	OOF2
Overall morphology			
Local morphology			
Element type	CPS4R	CPS4R	CPS4R
Element size	0.2 $\mu\text{m}$	$\sim 0.1\mu\text{m}$	Course mesh: $\sim 0.5\mu\text{m}$ Fine mesh: $\sim 0.1\mu\text{m}$
Characteristics	Regular, square elements, stepped shapes boundary	Irregular elements, smooth boundary	Finer meshes at phase boundaries

Fig. 9.4: Summary of the morphology and characteristics of the three different types of mesh of the RVE.

The commercial finite element code Abaqus/Standard is used in the analyses. The goal of the study is to investigate the dependency of damage initiation on the stress states by the plastic strain localisation theory. Therefore, three stress state scenarios which are often met in loadings for sheet metal, uniaxial tension, plane-strain tension and equibiaxial tension, are considered and applied to the RVE. The boundary conditions are generally displacement controlled. Note that since the RVE is based on real microstructure and the mesh is also irregular except for type-1, the periodic boundary conditions are generally not appropriate. Therefore, the homogenous boundary condition used by Sun et al. [21] is applied in this study. In general, for all three stress states, the nodes along the left edge are constrained in the x direction, but free in the y direction. Correspondingly, nodes on the bottom edge are restricted to move in the y direction but free in the x direction. For uniaxial tension loading, all the nodes along the right

edge are given the same displacement in the x direction while they can freely move in the y direction during the tensile loading. For plane strain tensile loading, all the nodes along the right edge are given the same displacement in the x direction while nodes along the top edge are restricted to move in the y direction but freely move in the x direction. For equibiaxial tensile loading, in addition to the displacement on the nodes along right edge, all the nodes along the top edge are given the same displacement (equal to the displacement applied on the right edge) in the y direction.

For the quantitative evaluation of the RVE simulation, the overall stress and strain of the RVE is calculated. The equations for the calculation of stress and strain of the RVE under uniaxial tension is shown in Ref. [123; 124]. Here a way to calculate the stress and strain of the RVE for general cases under plane stress assumption is shown. The sum of the force in the x direction of all the nodes along the right edge is denoted by  $F_1$ , and the average displacement in the x direction of all the nodes along the right edge is denoted by  $U_1$ . Correspondingly,  $F_2$  and  $U_2$  are indicating the force and displacement for the nodes along the top edge in the y direction, respectively. The history of the force and displacement for two edges are obtained from the RVE simulation. Accordingly, the engineering stress and strain for both normal directions are calculated by:

$$\sigma_{\text{eng}(1,2)} = \frac{F_{(1,2)}}{A_{0(1,2)}} \quad \text{Eq. 9.1}$$

$$\varepsilon_{\text{eng}(1,2)} = \frac{\Delta l}{l_0} = \frac{U_{(1,2)}}{l_{0(1,2)}} \quad \text{Eq. 9.2}$$

where  $A_{0(1,2)}$  represents the cross section area of the x direction and y direction, and  $l_{0(1,2)}$  indicates the length of the RVE in the x and y direction. Therefore, the true stress and strain can be calculated:

$$\sigma_{(1,2)} = \sigma_{\text{eng}(1,2)}(1 + \varepsilon_{\text{eng}(1,2)}) \quad \text{Eq. 9.3}$$

$$\varepsilon_{(1,2)} = \ln(1 + \varepsilon_{\text{eng}(1,2)}) \quad \text{Eq. 9.4}$$

By treating the RVE as an aggregate, the Mises equivalent stress is used to represent the effective stress of the RVE. Because there are only normal stresses applied, the effective stress and strain are defined by:

$$\bar{\sigma} = \sqrt{\sigma_1^2 + \sigma_2^2 - \sigma_1\sigma_2} \quad \text{Eq. 9.5}$$

$$\bar{\varepsilon} = \sqrt{\frac{4}{3}(\varepsilon_1^2 + \varepsilon_2^2 + \varepsilon_1\varepsilon_2)} \quad \text{Eq. 9.6}$$

For the detailed derivation, the readers are referred to Appendix A.

### 9.3.2 Flow curve calibration

Due to the different plastic properties and strain-hardening behaviour, flow curves of both phases in DP steel need to be calculated separately. In this study, the numerically estimated flow curve for each phase is used. The numerical flow curves are approximated by an empirical model, part of which is based on the dislocation theory while the Peierl's stress is based on the local chemical composition [123]. This approach has been employed frequently in the RVE simulation of multi-phase steels, in particular DP steels [178]. Recently, Sun et al. [7; 116-122; 125-127] used the synchrotron-based high-energy X-ray diffraction to measure and simulate the flow curve for ferrite phase. However, the flow curve for martensite phase still relies on literature or numerical estimation. The estimation equation is defined as:

$$\sigma_y = \sigma_p + \sigma_{pc} + a \cdot M \cdot G \cdot \sqrt{b} \cdot \sqrt{\frac{1 - \exp(-M \cdot k_r \cdot \varepsilon)}{k_r \cdot L_d}} \quad \text{Eq. 9.7}$$

with:

$\sigma_y$ : yield stress;

$\sigma_p$ : Peierl's stress;

$\sigma_{pc}$ : additional strengthening due to precipitations and carbon in solution;

$a$ : constant;

$M$ : Taylor factor;

$G$ : shear modulus;

$b$ : burger's vector;

$L_d$ : dislocation mean free path;

$k_r$ : recovery rate.

The Peierl' s stress  $\sigma_p$ , which depends on the chemical composition of the solid solution, can be calculated by the following equation:

$$\begin{aligned} \sigma_p = & 77 + 80 \cdot (\%Mn) + 750 \cdot (\%P) + 60 \cdot (\%Si) + 80 \cdot (\%Cu) + 45 \cdot (\%Ni) \\ & + 60 \cdot (\%Cr) + 11 \cdot (\%Mo) + 5000 \cdot N_{ss} \end{aligned} \quad \text{Eq. 9.8}$$

Besides, carbon partitioning, which has significant influence on the value of yield stress and strain-hardening behaviour, is estimated on the basis of mass balance and phase fraction. The carbon content in martensite phase is measured by electron probe micro-analyser (EPMA). In this study, both flow curves for ferrite and martensite are calculated according to the equations above and the free parameters are inversely fitted to get the best agreement of the true stress-strain curve between experiment and the RVE simulation, as recommended by Rodriguez et al. [123]. The flow curves of the DP600 experimentally measured and calculated by RVE simulation are presented in Fig. 9.5. All the material parameters for both phases are given in Tab. 9.1.

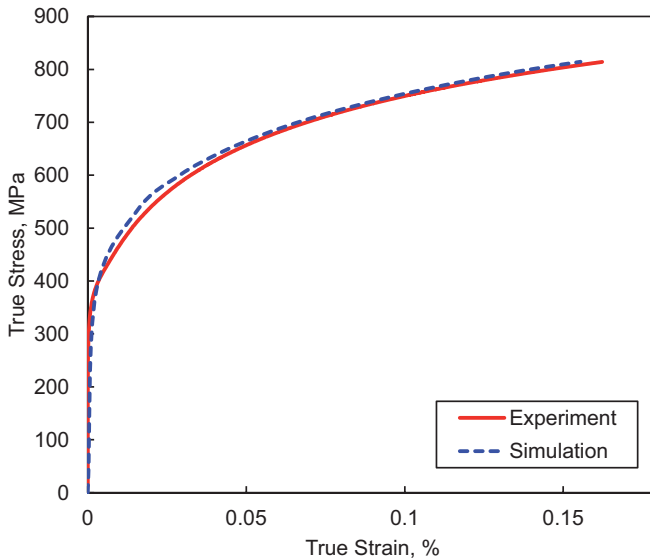


Fig. 9.5: Comparison of the true stress strain curve between experimental result by uniaxial tensile test and the simulation result based on RVE simulation.

Tab. 9.1: Material parameters for the estimation of the flow curve for ferrite and martensite phase.

Phase	Fraction	%C	$\sigma_p$	$\sigma_{pc}$	$a$	$M$	$b$	$G$	$k_r$	$L_d$
Ferrite	90%	0.072	236.789	144.667	0.550	3.0	$2.5 \cdot 10^{-10}$	80000	0.800	$1.0 \cdot 10^{-5}$
Martensite	10%	0.479	236.789	1370.135	0.330	3.0	$2.5 \cdot 10^{-10}$	80000	41.000	$3.8 \cdot 10^{-8}$

## 9.4 Results and discussion

### 9.4.1 RVE simulation under uniaxial tension loading condition

The RVE models with three types of mesh are run under the uniaxial tension loading condition in Abaqus/Standard. The engineering stress–strain curve is accordingly calculated for three types of mesh and plotted in Fig. 9.6 together with the experimental one. Since the experimental results show a certain range of uncertainty after the UTS, the uncertainty range is shown in Fig. 9.6 as a semi-transparent band. The prediction on UTS and the failure strain based on different types of mesh are well fitted to the experiment ones, except that the failure strain predicted by RVE with type-2 mesh is slightly smaller than the experimental observation. However, the UTS prediction is quite accurate for all three different types of mesh. The difference after the UTS is originated from the propagation of the localisation band in different mesh types, which will be discussed next.

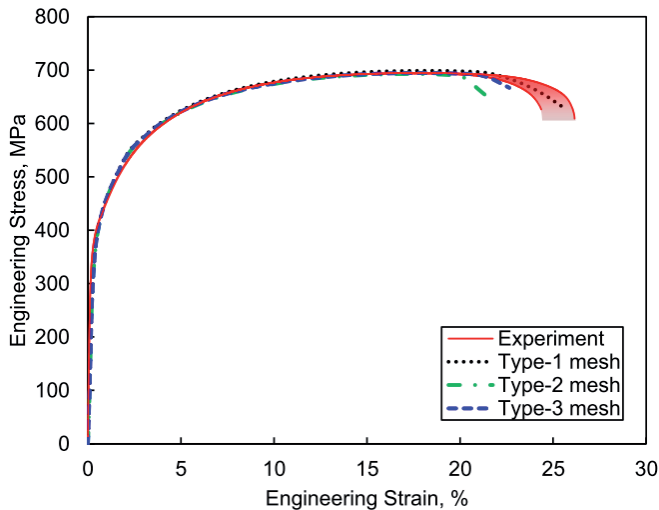


Fig. 9.6: Comparison of the engineering stress–strain curve under uniaxial tensile loading condition between experiment and the RVE simulation based on three different types of mesh.

Based on the uncertainty of the softening and the early damage effect in this type of steels, in this study, the stage at UTS is considered as a critical moment during the plastic deformation. In the microstructural scale, it is regarded as the sign of damage initiation. Therefore, the PEEQ deformation contour at UTS for three RVEs is shown in Fig. 9.7.

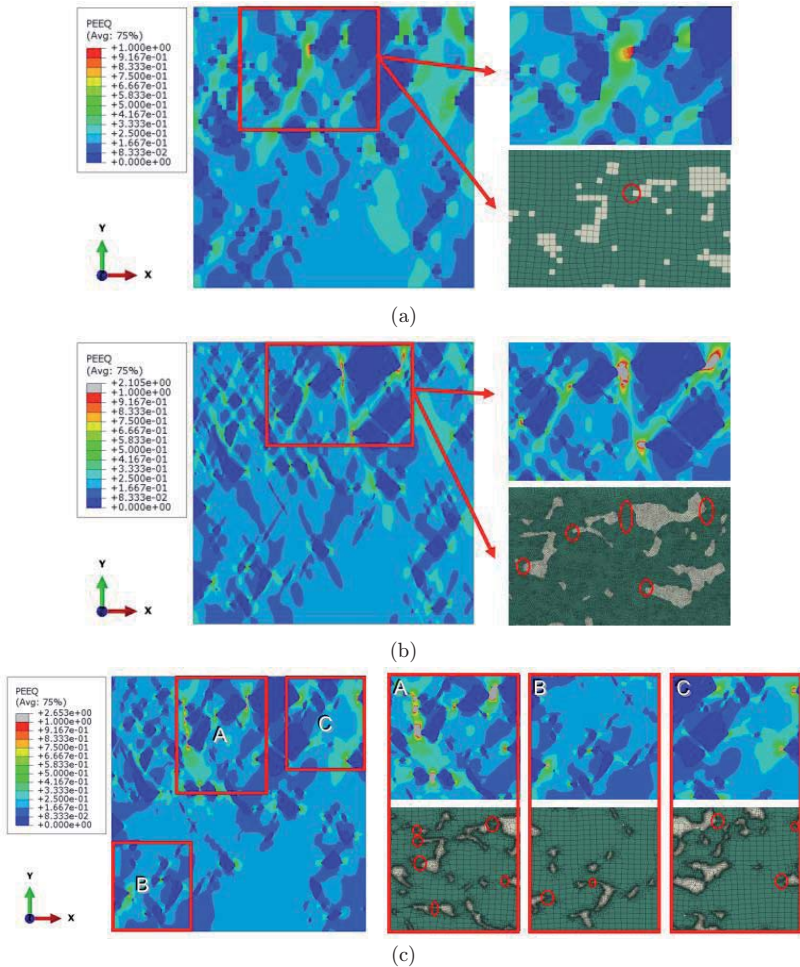


Fig. 9.7: Equivalent plastic strain (PEEQ) contour of the deformation at the maximum load under uniaxial tensile loading condition for different types of mesh: (a) type-1 mesh, (b) type-2 mesh, (c) type-3 mesh.

In the global view of the PEEQ contour of the RVEs, a large amount of shear bands triggered by plastic strain localisation is present at this stage of deformation for all three models. Quantitatively, the model with type-1 mesh shows lowest maximum PEEQ (about one), while the maximum PEEQ for the other two models have reached two. It is also shown that there are multiple spots of severe localisation (PEEQ large than one) in models with type-2 and type-

3 mesh. The difference is simply caused by the element size and the numerical description of the phase boundary. With finer elements and smooth phase boundary, the local PEEQ gradient is higher, although the global stress–strain curve remains unaffected.

From a local viewpoint, three models show some consistent locations for the plastic strain localisation, which are indicated by the red rectangular in Fig. 9.7 (a) and (b) and by the rectangular A in Fig. 9.7 (c). By comparing the local PEEQ contour and the deformation contour with material label (white indicating martensite and green ferrite), one can conclude that the severe localised deformation is situated at the ferrite–martensite phase boundary between the fragmented martensite islands, as revealed from the SEM analysis in Fig. 9.1. In addition, another favourable position to trigger the plastic strain localisation is at the interface of ferrite and martensite, where the martensite islands feature a relatively sharp edge. This is observed in the RVE model with mesh type-2, as shown in Fig. 9.7 (b), as well as the RVE model with type-3, as shown in Fig. 9.7 (c), not only in rectangular A, but also B and C. These spots of severe plastic strain localisation are very likely to develop voids initiated at the interface of ferrite and martensite. The second type of damage initiation can only be captured with fine element size discretisation and the smooth phase boundary, such as mesh type-2 and type-3. In general, the dominant damage mechanism found out from the numerical study is the interface debonding caused by the severe plastic strain localisation. This also agrees with the experimental observation shown in Fig. 9.1, and the literature for dual-phase steel with low or medium volume fraction of martensite [178]. As shown in Fig. 9.8, the plastic strain localisation area just crosses a martensite grain. This indicates that besides ferrite–martensite interface decohesion damage mechanism, martensite cracking could also occur in the weak parts of martensite grains caused by the plastic strain localisation in the ferrite phase.

After the damage initiation, the plastic strain localisation further develops to form finally a localisation band through-out the entire RVE. The PEEQ contour at this moment of three different models under uniaxial loading is shown in Fig. 9.9. Different patterns of localisation band are observed for different RVE models: the band for type-1 mesh is parallel to  $y$ -axis while that of type-2 and type-3 mesh is inclined to the  $y$ -axis. The different behaviour of the propagation of the localisation is also corresponding to the difference observed in the engineering stress–strain response. Basically it is interpreted that in the latter two types of mesh, the localisation propagates as the pattern of shear bands and this requires less energy to dissipate than forming a vertical localisation band for model with type-1 mesh.

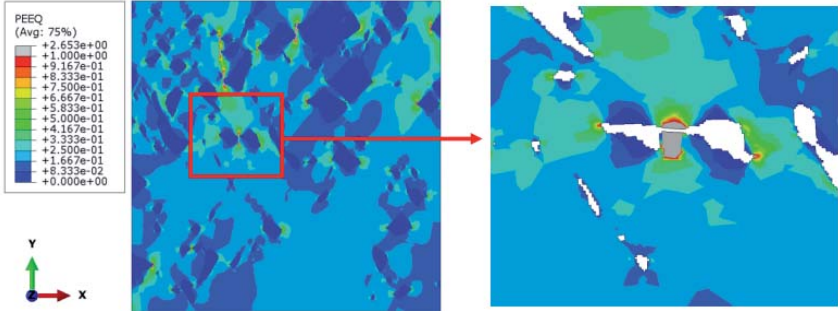


Fig. 9.8: The severe plastic stain localisation at the interface of the ferrite and martensite crossing the martensite island which could potentially trigger the martensite crack (white colour: martensite phase, the rest colour: ferrite phase).

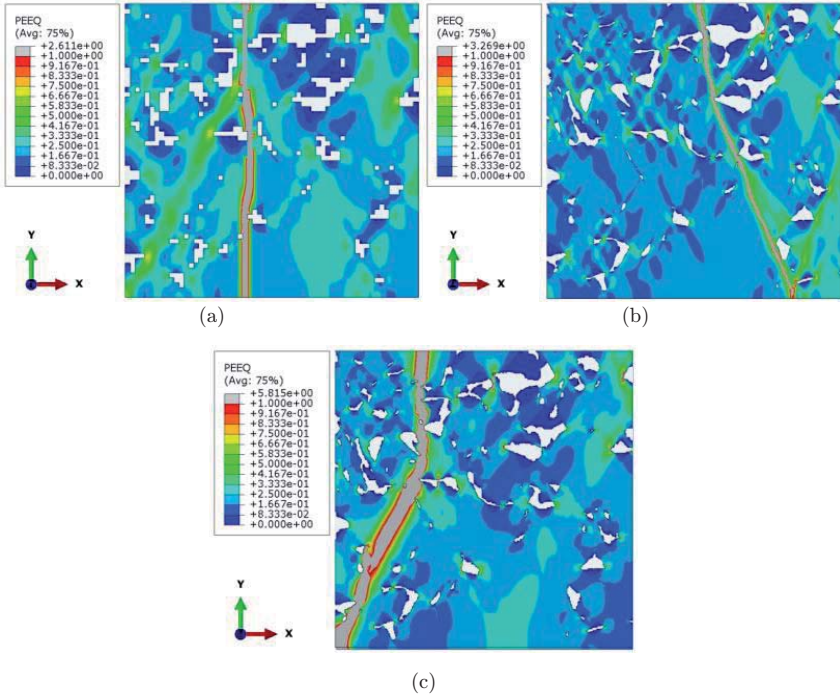


Fig. 9.9: PEEQ contour of the deformation at the moment when throughout localisation is formed under uniaxial tensile loading condition for different types of mesh: (a) type-1 mesh, (b) type-2 mesh, (c) type-3 mesh.



To achieve a balance between the computational expense and the prediction quality in terms of both stress–strain curve and the local variables, type-3 mesh is considered as the optimal RVE model and it is the specified type for the further study under other loading conditions.

#### 9.4.2 Prediction of damage initiation under different stress states

The RVE with type-3 mesh is further loaded under the loading conditions of plane-strain tension and equibiaxial tension to investigate the influence of the stress states on damage initiation and failure pattern of the RVE. During the deformation, the force and displacement of the right and top edges in the RVE are recorded and the effective stress and stain are accordingly calculated.

To upscale the damage initiation from micro to macro, the damage initiation strain is required from the RVE simulation. Although the upscaling is across two levels, one shall note that the length scale of the damage initiation is kept the same. It is crucial to be able to avoid the size effect during the upscaling. In the microscale, the maximum force criterion (MFC) is used to characterise the onset of damage. The assumption for such an upscaling is that the damage initiation in macroscale is corresponding to the localisation of the plastic strain due to the microstructural-level deformation incompatibility in a microscale for the DP steel. Basically during the deformation, once the maximum effective stress is reached for the RVE, it is considered as the damage initiation of the material and the corresponding effective stain is regarded as the strain to damage initiation.

To reveal the influence of the stress states on the damage initiation, PEEQ contour for both plane-strain tension and equibiaxial tension loadings at the maximum effective stress is shown in Fig. 9.10.

In the global view of the deformation of the RVE, different from the formation of large amount of shear bands under the uniaxial tension loading condition, the localisation spots under plane-strain tension are few and they propagate vertically while the localisation spots under equibiaxial tension are well distributed in the RVE and they propagate freely depending on the microstructure morphology. In the indicated area in the red rectangular, the deformation is viewed in detail to correspond to the material label as well. It is noted that, the most severe plastic strain localisation occurs at the similar location to the uniaxial tension loading condition. It is also worth noting that damage initiation still occurs at the interface of the ferrite and martensite phases either in the middle of two martensite islands close to each other or the martensite island with a sharp edge. The propagation modes for both cases are quite different

and they are shown in Fig. 9.11. The localisation pattern for plane-strain tension features approximately vertical band across the entire RVE, and for equibiaxial tension, two localisation bands are developed, one vertical and one horizontal.

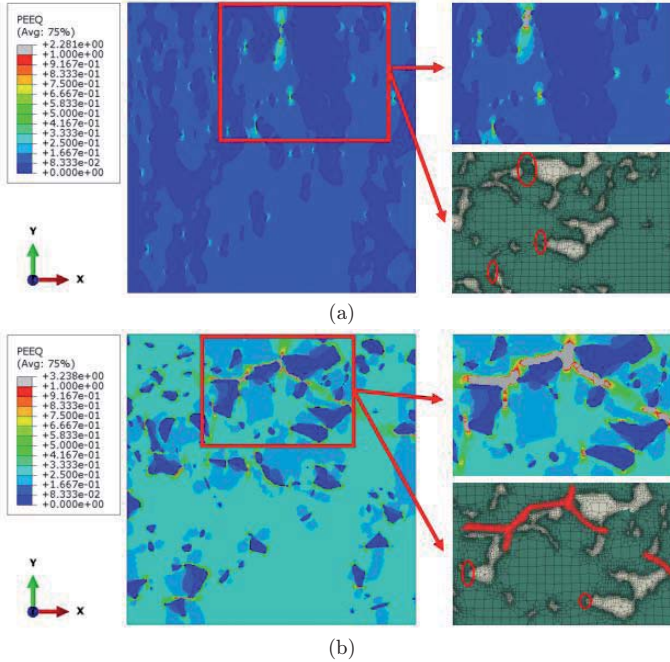


Fig. 9.10: PEEQ contour of the deformation at the maximum load under: (a) plane-strain tension, (b) equibiaxial tension loading condition.

For three typical stress states, uniaxial tension, plane-strain tension and equibiaxial tension, the effective stress and strain during the entire deformation of the RVE is calculated and plotted in Fig. 9.12 together with the experimentally measured flow curve.

Although no damage criteria are attached to the micromechanics model, the stress for all cases shows a maximum and decreases due to the plastic strain localisation arising from the incompatible deformation between the ferrite and martensite phases. On these curves, square markers are used to indicate the maximum stresses. The predicted maximum stresses for three different loading conditions are significantly different from each other. Equibiaxial tension has the highest maximum stress and highest strain to damage initiation while plane-strain tension features the lowest maximum stress and the lowest strain to damage initiation.

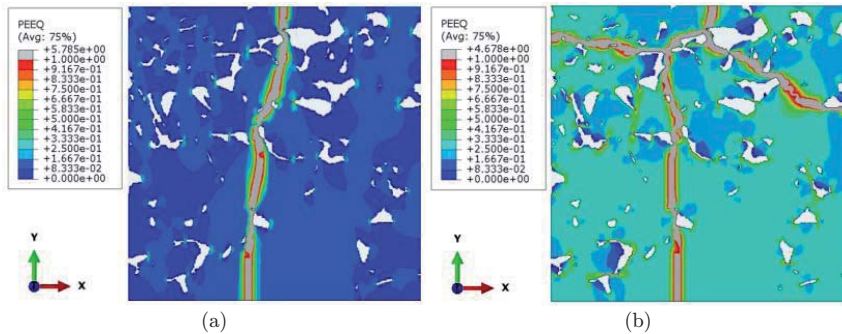


Fig. 9.11: PEEQ contour of the deformation at the moment when throughout necking is formed under: (a) plain-strain tension, (b) equibiaxial tension loading condition.

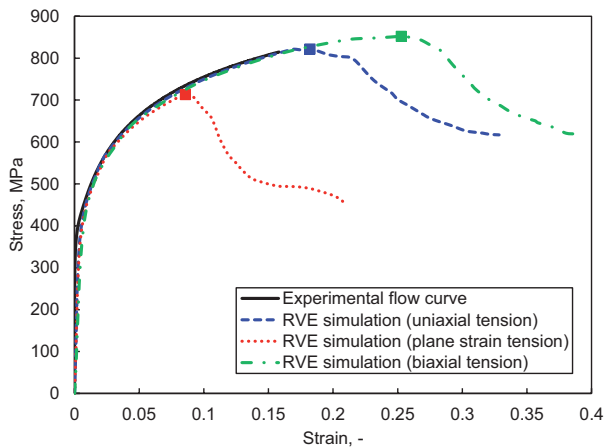


Fig. 9.12: Comparison of the effective stress–strain curve calculated from RVE simulation with type-3 mesh for three different loading conditions with the experimentally measure flow curve.

In Fig. 9.13, the predicted strains to damage initiation by the RVE simulation are plotted against the stress triaxiality and compared to the experimentally measured DIL under the plane stress condition. Considering the uncertainty in the experimental measurement and the surface fitting for the DIL, a fairly good agreement is achieved between the experimental result and the numerical prediction by RVE simulation. From this quantitative analysis, the DIL predicted by the RVE simulation clearly shows the dependency on stress state. It is noted that its dependency is shown not only on stress triaxiality, but also on the Lode angle, because of the increase of the damage initiation stain under equibiaxial tension loading. More importantly,

it also provides a physical understanding of the dependency in a microstructural level. It is proved that the dependency arises from plastic strain localisation due to the microstructure heterogeneity nature.

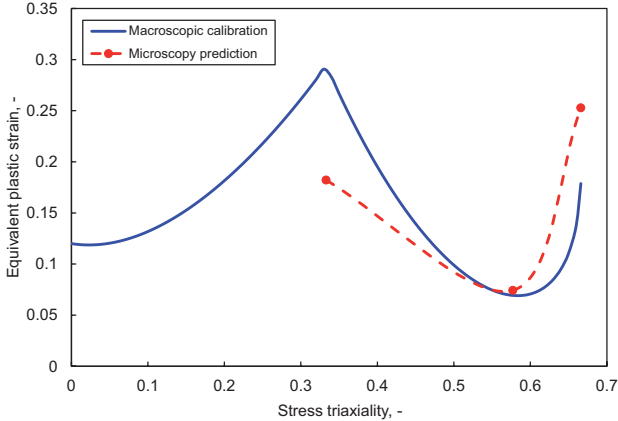


Fig. 9.13: Comparison of experimentally calibrated DIL and the predicted results of RVE under three different loading conditions, uniaxial tension, plane-strain tension and equibiaxial tension.

## 9.5 Conclusions

The aim of this section is to quantitatively evaluate the damage initiation under different stress states and reveal the underlying mechanism of the damage initiation dependency on stress states from a microstructural level. FE model based on real microstructure of the DP600 steel sheet is employed and different types of mesh are investigated. The plastic strain localisation theory is applied to the simulation without any other damage models or imperfections and the damage initiation under different stress states is considered as the nature outcome of the localisation of the plastic strain due to the microstructural-level deformation incompatibility. Three typical stress state scenarios common for sheet metal forming are considered, uniaxial tension, plane-strain tension and equibiaxial tension. The quantitative evaluation of the damage initiation for three stress states obtained from the RVE simulation is compared to the experimentally calibrated DIL. The following conclusions can be drawn:

- Under different loading conditions, uniaxial tension, plane-strain tension and equibiaxial tension, the damage initiation prefers to occur at the interface of the ferrite and martensite phases either in the middle of two martensite islands close to each other or the martensite

island with a sharp edge. It agrees with the experimental observation from SEM analysis on the through-thickness cross-section of fractured plane-strain and central-hole specimens of the DP600 steel, as well as the literature for dual-phase steel with low or medium volume fraction of martensite [17]. It is concluded that the damage initiation arises from the severe plastic strain localisation at the interface of ferrite and martensite caused by the incompatible deformation behaviour of these two phases.

- A practical method to evaluate the damage initiation quantitatively is developed based on the real microstructure using the plastic strain localisation theory. From the evaluation, the damage initiation clearly shows a dependency on stress states in a microstructural level. The predicted DIL shows dependency on the stress triaxiality and Lode angle, and a fairly good agreement is also achieved compared to the experimentally measured DIL. This result provides a physical insight of the ductile damage initiation from a material microstructural perspective. The damage initiation dependency on stress states arises from the plastic strain localisation due to the incompatible deformation behaviour from the microstructure heterogeneity nature. This result can also facilitate the material parameter calibration procedure in a macroscopic modelling level to avoid the effort on exhausting experiments with various geometries to create different stress states.
- The influences of the element size and the numerical discretisation of the phase boundary on the RVE simulation are investigated. Three types of mesh are therefore generated, coarse mesh with regular brick elements that create stepped interface, fine mesh with irregular quadrilateral elements that create smooth interface, and combined fine and coarse mesh with fine elements for the description of the interface and coarse elements for the rest. It is found that with fine element size and smooth interface discretisation, the damage initiation is characterised more precisely, although the difference on the stress–strain curve is not pronounced, in particular before the maximum of the stress.



# Chapter 10

## Conclusions and future studies

### 10.1 Concluding remarks

The aim of the present thesis is to develop a model for accurate ductile fracture prediction of modern high strength steel sheets and heavy plates. The main conclusions are drawn in the following:

- The terms of damage and fracture are clearly distinguished. The damage initiation is corresponding to a microscopic event when the microstructure develops an irreversible degradation on a given length scale. Fracture describes macroscopic behaviour that can be defined as occurring when a component or system stops complying with its service requirements. The onset of damage and the subsequent damage evolution have been identified as the key factors in the application of the modern high strength steels. To reflect the differences and relations between damage and fracture, a generalised hybrid damage mechanics model is formulated in this study, which consists of three constituents: i) a plasticity model to characterise the material behaviour before the damage initiation; ii) a phenomenological criterion to indicate the damage initiation, and iii) a dissipation-energy-based damage evolution law to quantitatively represent the microstructure degradation and reflect its effect on material strength properties.
- A complete programme that covers material parameter calibration and methodology for the use of the model is developed in the thesis. By using the experimental-numerical approach, a practical, reliable and systematic material parameter calibration procedure with comprehensive experiments designed for both steel sheets and heavy plates is defined. For the critical identification of the instant and location of the first microcrack appearance, methodology incorporating a non-destructive testing method is introduced.

- The model has been successfully applied to two high strength steel grades, a dual phase (DP) steel sheet (DP600) and a high strength low alloy (HSLA) steel plates (S355J2+N). The damage initiation loci (DIL) for both steels show the dependency on stress triaxiality and Lode angle. The comparison of them shows the damage starts to play a non-negligible role at a much earlier deformation stage in the DP steel than in the HSLA structural steel. However, the DP steel undergoes considerably more plastic deformation than the HSLA steel after damage initiation, which indicates that the DP steel owns a higher damage tolerance than the HSLA steel. Although two steels show very different relation patterns between plasticity, damage and fracture, good results on the forming limit prediction for DP600 and bendability prediction for S355J2+N are achieved. The predictive capability and the flexibility of the model owing to its general and hybrid character is demonstrated for applications with various relation patterns between damage and fracture.
- In order to reduce the number of material parameters, a modified Lemaitre damage model is proposed by phenomenologically adding the Lode effect function to the conventional Lemaitre damage model. With only four independent material parameters, accurate predictions on both force–displacement curves and fracture displacements of DP600 under various stress states are achieved. The Lode angle effect is therefore proved to be also critical for the numerical simulation of damage accumulation.
- Multiscale modelling approach to link the microstructure to the phenomenological material parameters is employed for saving the effort on parameter calibration and for material design. A method to quantitatively upscale the damage initiation from micro to macro is developed based on the material microstructure using the plastic strain localisation theory. It is shown that the damage initiation arises from the severe plastic strain localisation at the interface of ferrite and martensite caused by the incompatible deformation behaviour of these two phases. The predicted damage initiation also shows dependency on the stress triaxiality and Lode angle, and a fairly good agreement is also achieved compared to the experiments. It is revealed that the damage initiation dependency on stress states is a nature reflection of the different plastic strain localisation behaviour under various stress states due to the incompatible deformation from the microstructure-level heterogeneity.



## 10.2 Future studies

Satisfactory experiences on the use of the model in the damage/fracture prediction for steel sheets and heavy plates are presented in the thesis. Solutions for tackling the intrinsic drawbacks of the model are also provided. Nevertheless, there are still rooms for further improvement of the model and future studies to incorporate more practical applications.

- **Finite strain formulation.** For the reason of simplicity and practicability, the small strain formulism is adopted in the thesis. For large strain deformation, e.g. significant strain localisation, the finite strain formulism is preferred.
- **Mesh size dependency.** It is well known that the mesh size dependency is a non-negligible effect for simulations with large non-linear deformation or high deformation gradients, which could result from either the material or the geometry side. The effect is even more pronounced when the softening effect is incorporated into the formulation of the model. Some preliminary solution by the mesh regularisation is provided in the thesis. However, it still requires to keep the mesh size constant in a certain level to achieve the best performance of the numerical prediction, which significantly restricts the application of the model to the component scale. Alternative mesh regularisations that could allow a wider range of the mesh sizes are to be investigated for a simple and fast transferability of the model to large scale applications. Ultimately, a more generalised and fundamental approach to reduce the mesh dependency is applying the non-local formulation to the proposed damage model.
- **Damage evolution law.** Although a good overall prediction of the fracture displacements is achieved by the current damage evolution law, a certain over-estimation is obtained in the flat-grooved specimen for the DP600 steel sheet. It can be traced to the function of the damage evolution law with respect to only the equivalent plastic strain rate. A more general damage evolution law with dependency on the stress states will add more flexibility to the model.
- **Temperature and strain rate influence.** In the present thesis, the model development and the application examples are under the conditions of room temperature and quasi-static loadings. However, high strain rate and high temperature change due to the adiabatic heating have significant influence on both the plasticity, damage and fracture behaviour of materials. There are various empirical models for the description of these influences on the plasticity part and they are straightforward to be integrated to the

model. However, what is overlooked in these models is the evolution of these influences with the strain hardening. Therefore, an *evolving* model that describes the instantaneous influences of the strain rate and temperature on the plasticity behaviour over the accumulated strain is required.

- **Complex loading path.** The investigated loading in the thesis is also restricted to only monotonic loading. For sheet metal forming, however, the loading is not always monotonic, and sometimes complex loading path is necessary. To cope with the damage/fracture prediction in these types of loading, combined kinematic hardening and isotropic hardening is preferred for the plasticity model part, and the damage evolution concept also needs to be adapted for the consideration of the effective damage during the complex loading path.
- **Cleavage fracture.** To prevent catastrophic failures caused by the cleavage fracture of structural steels remains the prior principle for assessment of structural and material integrity. For this reason, the extension of the model to include the prediction of cleavage fracture is necessary.
- **Anisotropy.** In the present thesis, isotropic plastic yielding and hardening are assumed for material deformation behaviour. Although a non-quadratic yield function that distinguishes the yielding under different stress states is adopted, the plasticity model remains isotropic. A generalisation of the model in an anisotropic framework to account for both anisotropic plasticity and damage/fracture could lead the model to more applications of steels.
- **Experimental damage qualification method.** The DCPD method applied in the thesis only gives a qualitative indication of the damage initiation, but there are still several factors that also substantially influence the electric resistance, such as severe plastic deformation and strain localisation, are not accounted for in the current method. A more careful look at the method is required and more quantitative work shall be planned for further development. Only with very fine resolution of the potential signal the change of the electric resistance caused by damage can be quantitatively identified and the other factors can be sorted out. For this, electro-mechanical simulations are required.
- **Microstructure property relationship.** With the development of integrated computational materials engineering (ICME), the investigations on the material

---

microstructure and property relationship have been significantly enriched. One prosperous trend is to incorporate the dominant microstructural features, which are commonly identified as phase fraction, grain size distribution, texture, inclusions, precipitates, etc. and their respective deformation or failure mechanisms to the model and estimate the macroscopic material properties. The successful up and down-scaling are the fundamental milestones for the material design. A preliminary study on the multiscale simulation has been performed at the end of the thesis, and the damage initiation locus is linked to the phase-level inhomogeneity. However, the coupling of the entire failure process, including the damage evolution and final fracture with more microstructural features remains open. Further experimental and numerical investigations are expected to close this gap. On the other hand, the resolution of the material structure also needs to be further enhanced by incorporating the grain-level inhomogeneous features (grain size distribution, texture, etc.) or even beyond.



## Appendix

### Transformation between the space of $(\bar{\varepsilon}, \eta)$ and $(\varepsilon_1, \varepsilon_2)$ under the plane stress condition

According to the definition of Mises equivalent stress in Eq. 3.6, it can be written in the principal stress space as follows:

$$\bar{\sigma} = \sqrt{\frac{1}{2}[(\sigma_1 - \sigma_2)^2 + (\sigma_2 - \sigma_3)^2 + (\sigma_3 - \sigma_1)^2]} \quad \text{Eq. A.1}$$

Under the assumption of plane stress, we assume  $\sigma_3 = 0$ .

$$\bar{\sigma} = \sqrt{\sigma_1^2 + \sigma_2^2 - \sigma_1\sigma_2} \quad \text{Eq. A.2}$$

Associated with the Mises equivalent stress, the equivalent strain is defined by:

$$\bar{\varepsilon} = \int \sqrt{\frac{2}{3} \dot{\varepsilon}_{ij} \dot{\varepsilon}_{ij}} dt \quad \text{Eq. A.3}$$

where  $\dot{\varepsilon}_{ij}$  is the strain rate tensor. The equivalent strain rate must be integrated over time. Assuming that the strain rate remains constant during deformation, the equivalent strain can be calculated by:

$$\bar{\varepsilon} = \sqrt{\frac{2}{3} \varepsilon_{ij} \varepsilon_{ij}} = \sqrt{\frac{2}{3} \left[ \varepsilon_{11}^2 + \varepsilon_{22}^2 + \varepsilon_{33}^2 + \frac{1}{2} (\varepsilon_{12}^2 + \varepsilon_{23}^2 + \varepsilon_{31}^2) \right]} \quad \text{Eq. A.4}$$

In the principal strain space, there is no shear deformation:

$$\varepsilon_{12} = \varepsilon_{23} = \varepsilon_{31} = 0 \quad \text{Eq. A.5}$$

Assuming the metal incompressibility, one can obtain:

$$\varepsilon_1 + \varepsilon_2 + \varepsilon_3 = 0 \quad \text{Eq. A.6}$$

Finally, the equivalent strain is expressed in terms of the principal strains:

$$\bar{\varepsilon} = \sqrt{\frac{4}{3} (\varepsilon_1^2 + \varepsilon_2^2 + \varepsilon_1 \varepsilon_2)} \quad \text{Eq. A.7}$$

For the ease of the expression, the stress ratio  $\alpha$  and the strain ratio  $\beta$  are defined:

$$\alpha = \frac{\sigma_2}{\sigma_1}; \quad \beta = \frac{\dot{\varepsilon}_2}{\dot{\varepsilon}_1} \quad \text{Eq. A.8}$$

Combining Eq. A.2, Eq. A.7, and Eq. A.8, it is readily to obtain

$$\bar{\sigma} = \sigma_1 \sqrt{\alpha^2 - \alpha + 1} \quad \text{Eq. A.9}$$

and

$$\bar{\varepsilon} = \varepsilon_1 \sqrt{\frac{4}{3}(\beta^2 + \beta + 1)} \quad \text{Eq. A.10}$$

By applying the associated flow rule,

$$\dot{\boldsymbol{\varepsilon}}^p = \dot{\gamma} \frac{\partial \Phi}{\partial \boldsymbol{\sigma}} = \dot{\gamma} \frac{\partial \bar{\sigma}}{\partial \boldsymbol{\sigma}} \quad \text{Eq. A.11}$$

The relation between  $\beta$  and  $\alpha$  is obtained

$$\beta = \frac{\dot{\varepsilon}_2}{\dot{\varepsilon}_1} = \frac{\partial \bar{\sigma} / \partial \sigma_2}{\partial \bar{\sigma} / \partial \sigma_1} = \frac{2\alpha - 1}{2 - \alpha} \quad \text{Eq. A.12}$$

It can be also written as

$$\alpha = \frac{2\beta + 1}{2 + \beta} \quad \text{Eq. A.13}$$

As the stress triaxiality is the ratio of the mean stress over the equivalent stress, under the plane stress condition, the mean stress is written as

$$\sigma_m = \frac{\sigma_1 + \sigma_2 + \sigma_3}{3} = \frac{1 + \alpha}{3} \sigma_1 \quad \text{Eq. A.14}$$

Accordingly the stress triaxiality is defined by

$$\eta = \frac{1 + \alpha}{3\sqrt{\alpha^2 - \alpha + 1}} \quad \text{Eq. A.15}$$

Inserting Eq. A.13 to Eq. A.15, the relation between  $\eta$  and  $\beta$  is obtained

$$\eta = \frac{1 + \beta}{\sqrt{3(\beta^2 + \beta + 1)}} \quad \text{Eq. A.16}$$

By solving  $\beta$  from Eq. A.16, it is obtained

$$\beta = \begin{cases} \frac{(-3\eta^2 + 2) + \sqrt{-27\eta^4 + 12\eta^2}}{6\eta^2 - 2}, & \eta < 0 \\ \frac{(-3\eta^2 + 2) - \sqrt{-27\eta^4 + 12\eta^2}}{6\eta^2 - 2}, & \eta \geq 0 \end{cases} \quad \text{Eq. A.17}$$

It is noted that under the plane stress assumption, the range of  $\eta$  is  $[-2/3, 2/3]$ .

Concluding from the derivation above, the transformation equations from the  $(\varepsilon_1, \varepsilon_2)$  space to  $(\bar{\varepsilon}, \eta)$  space under plane stress condition are

$$\begin{pmatrix} \beta = \frac{\varepsilon_2}{\varepsilon_1} \\ \eta = \frac{1 + \beta}{\sqrt{3(\beta^2 + \beta + 1)}} \\ \bar{\varepsilon} = \varepsilon_1 \sqrt{\frac{4}{3}(\beta^2 + \beta + 1)} \end{pmatrix} \quad \text{Eq. A.18}$$

and the equations from the  $(\bar{\varepsilon}, \eta)$  space to  $(\varepsilon_1, \varepsilon_2)$  space are

$$\begin{pmatrix} \beta = \begin{cases} \frac{(-3\eta^2 + 2) + \sqrt{-27\eta^4 + 12\eta^2}}{6\eta^2 - 2}, & \eta < 0 \\ \frac{(-3\eta^2 + 2) - \sqrt{-27\eta^4 + 12\eta^2}}{6\eta^2 - 2}, & \eta \geq 0 \end{cases} \\ \varepsilon_1 = \frac{\bar{\varepsilon}}{\sqrt{\frac{4}{3}(\beta^2 + \beta + 1)}} \\ \varepsilon_2 = \beta \varepsilon_1 \end{pmatrix} \quad \text{Eq. A.19}$$





# Literature

- [1] Chung K., Kim H., Lee C. (2014): Forming limit criterion for ductile anisotropic sheets as a material property and its deformation path insensitivity. Part I: Deformation path insensitive formula based on theoretical models. *International Journal of Plasticity*, 58:3-34.
- [2] Hill R. (1952): On discontinuous plastic states, with special reference to localized necking in thin sheets. *Journal of the Mechanics and Physics of Solids*, 1(1):19-30.
- [3] Swift H.W. (1952): Plastic instability under plane stress. *Journal of the Mechanics and Physics of Solids*, 1(1):1-18.
- [4] Marciniak Z., Kuczynski K. (1967): Limit strains in the processes of stretch forming sheet metal. *International Journal of Mechanical Sciences*, 9(9):609-612.
- [5] Storen S., Rice J.R. (1975): Localized necking in thin sheets. *Journal of the Mechanics and Physics of Solids*, 23(6):421-441.
- [6] Hora P., Tong L., Berisha B. (2013): Modified maximum force criterion, a model for the theoretical prediction of forming limit curves. *International Journal of Material Forming*, 6(2):267-279.
- [7] Uthaisangsuk V., Muenstermann S., Prahl U., Bleck W., Schmitz H.P., Pretorius T. (2011): A study of microcrack formation in multiphase steel using representative volume element and damage mechanics. *Computational Materials Science*, 50(4):1225-1232.
- [8] Garrison W.M., Moody N.R. (1987): Ductile fracture. *Journal of Physics and Chemistry of Solids*, 48(11):1035-1074.
- [9] Pineau A. (2006): Development of the local approach to fracture over the past 25 years: Theory and applications. *International Journal of Fracture*, 138(1-4):139-166.

- 
- [10] Anderson T.L. (2005): Fracture mechanics: Fundamentals and applications, Boca Raton, FL, Taylor & Francis.
- [11] Hubo R., Hocke A., Haunus F., Schuetz W. (2010): Stahentwicklung fuer maritime bauwerke. In: 25<sup>th</sup> Aachener Stahlkolloquium, Aachen, Germany, 2010.
- [12] Tasan C.C., Hoefnagels J.P.M., ten Horn C.H.L.J., Geers M.G.D. (2009): Experimental analysis of strain path dependent ductile damage mechanics and forming limits. *Mechanics of Materials*, 41(11):1264-1276.
- [13] Shen H.P., Lei T.C., Liu J.Z. (1986): Microscopic deformation-behavior of martensitic ferritic dual-phase steels. *Materials Science and Technology*, 2(1):28-33.
- [14] Kang J.D., Ososkov Y., Embury J.D., Wilkinson D.S. (2007): Digital image correlation studies for microscopic strain distribution and damage in dual phase steels. *Scripta Materialia*, 56(11):999-1002.
- [15] Ososkov Y., Wilkinson D.S., Jain M., Simpson T. (2007): In-situ measurement of local strain partitioning in a commercial dual-phase steel. *International Journal of Materials Research*, 98(8):664-673.
- [16] Ghadbeigi H., Pinna C., Celotto S., Yates J.R. (2010): Local plastic strain evolution in a high strength dual-phase steel. *Materials Science and Engineering a-Structural Materials Properties Microstructure and Processing*, 527(18-19):5026-5032.
- [17] Ahmad E., Manzoor T., Ali K.L., Akhter J.I. (2000): Effect of microvoid formation on the tensile properties of dual-phase steel. *Journal of Materials Engineering and Performance*, 9(3):306-310.
- [18] Maire E., Bouaziz O., Di Michiel M., Verdu C. (2008): Initiation and growth of damage in a dual-phase steel observed by x-ray microtomography. *Acta Materialia*, 56(18):4954-4964.
- [19] Kadkhodapour J., Butz A., Ziaei-Rad S., Schmauder S. (2011): A micro mechanical study on failure initiation of dual phase steels under tension using single crystal plasticity model. *International Journal of Plasticity*, 27(7):1103-1125.
- [20] Kadkhodapour J., Butz A., Rad S.Z. (2011): Mechanisms of void formation during tensile testing in a commercial, dual-phase steel. *Acta Materialia*, 59(7):2575-2588.
- [21] Avramovic-Cingara G., Ososkov Y., Jain M.K., Wilkinson D.S. (2009): Effect of martensite distribution on damage behaviour in dp600 dual phase steels. *Materials*

- Science and Engineering a-Structural Materials Properties Microstructure and Processing, 516(1-2):7-16.
- [22] Tomota Y., Tamura I. (1982): Mechanical-behavior of steels consisting of two ductile phases. Transactions of the Iron and Steel Institute of Japan, 22(9):665-677.
- [23] Korzekwa D.A., Lawson R.D., Matlock D.K., Krauss G. (1980): A consideration of models describing the strength and ductility of dual-phase steels. Scripta Metallurgica, 14(9):1023-1028.
- [24] Szewczyk A.F., Gurland J. (1982): A study of the deformation and fracture of a dual-phase steel. Metallurgical Transactions a-Physical Metallurgy and Materials Science, 13(10):1821-1826.
- [25] Suh D., Kwon D., Lee S., Kim N.J. (1997): Orientation dependence of microfracture behavior in a dual-phase high-strength low-alloy steel. Metallurgical and Materials Transactions A-Physical Metallurgy and Materials Science, 28(2):504-509.
- [26] Erdogan M. (2002): The effect of new ferrite content on the tensile fracture behaviour of dual phase steels. Journal of Materials Science, 37(17):3623-3630.
- [27] Calcagnotto M., Adachi Y., Ponge D., Raabe D. (2011): Deformation and fracture mechanisms in fine- and ultrafine-grained ferrite/martensite dual-phase steels and the effect of aging. Acta Materialia, 59(2):658-670.
- [28] Lemaitre J. (1985): A continuous damage mechanics model for ductile fracture. Journal of Engineering Materials and Technology-Transactions of the Asme, 107(1):83-89.
- [29] Bao Y., Wierzbicki T. (2004): A comparative study on various ductile crack formation criteria. Journal of Engineering Materials and Technology, 126(3):314-324.
- [30] Dunand M., Mohr D. (2010): Hybrid experimental-numerical analysis of basic ductile fracture experiments for sheet metals. International Journal of Solids and Structures, 47(9):1130-1143.
- [31] Ebnoether F., Mohr D. (2013): Predicting ductile fracture of low carbon steel sheets: Stress-based versus mixed stress/strain-based mohr-coulomb model. International Journal of Solids and Structures, 50(7-8):1055-1066.
- [32] Luo M., Dunand M., Mohr D. (2012): Experiments and modeling of anisotropic aluminum extrusions under multi-axial loading - part ii: Ductile fracture. International Journal of Plasticity, 32-33:36-58.

- 
- [33] Mohr D., Dunand M., Kim K.H. (2010): Evaluation of associated and non-associated quadratic plasticity models for advanced high strength steel sheets under multi-axial loading. *International Journal of Plasticity*, 26(7):939-956.
- [34] Beese A.M., Luo M., Li Y., Bai Y., Wierzbicki T. (2010): Partially coupled anisotropic fracture model for aluminum sheets. *Engineering Fracture Mechanics*, 77(7):1128-1152.
- [35] Lou Y.S., Huh H. (2013): Prediction of ductile fracture for advanced high strength steel with a new criterion: Experiments and simulation. *Journal of Materials Processing Technology*, 213(8):1284-1302.
- [36] Schlueter N., Grimpe F., Bleck W., Dahl W. (1996): Modelling of the damage in ductile steels. *Computational Materials Science*, 7(1-2):27-33.
- [37] Noon A., Kalwa C. Modeling of damage behavior of high strength pipeline steel. In: 18th European conference on fracture of materials, Dresden, Germany, 2010.
- [38] Muenstermann S., Langenberg P., Dahl W., Eisele U., Roos E. (2004): Der kurzrisseffekt bei der bruchmechanischen prüfung. *MP Materialprüfung*, 46(10):501-505.
- [39] Muenstermann S. (2006). Numerische beschreibung des duktilen versagensverhaltens von hochfesten baustählen unter berücksichtigung der mikrostruktur. Ph.D. Thesis, RWTH-Aachen University.
- [40] Dengel D., Harig H. (1980): Estimation of the fatigue limit by progressively-increasing load tests. *Fatigue of Engineering Materials and Structures*, 3(2):113-128.
- [41] Kucharczyk P., Rizos A., Muenstermann S., Bleck W. (2012): Estimation of the endurance fatigue limit for structural steel in load increasing tests at low temperature. *Fatigue & Fracture of Engineering Materials & Structures*, 35(7):628-637.
- [42] Tasan C.C. (2010). Micro-mechanical characterization of ductile damage in sheet metal. Ph.D. Thesis, Universiteitsdrukkerij TU Eindhoven.
- [43] Ramazani A. (2013). Microstructure based failure model of DP steels. Ph.D. Thesis, RWTH-Aachen University.
- [44] Maire E., Bordreuil C., About L., Boyer J.C. (2005): Damage initiation and growth in metals. Comparison between modelling and tomography experiments. *Journal of the Mechanics and Physics of Solids*, 53(11):2411-2434.
- [45] Besson J. (2009): Continuum models of ductile fracture: A review. *International Journal of Damage Mechanics*, 19(1):3-52.

- 
- [46] Atkins A.G. (1997): Fracture mechanics and metalforming: Damage mechanics and the local approach of yesterday and today. In: Rossmannith H.P. (ed.), Fracture research in retrospect - an anniversary volume in honour of george r. Irwin's 90th birthday. Taylor & Francis.
- [47] Faleskog J., Gao X.S., Shih C.F. (1998): Cell model for nonlinear fracture analysis - i. Micromechanics calibration. *International Journal of Fracture*, 89(4):355-373.
- [48] Gao X.S., Faleskog J., Shih C.F. (1998): Cell model for nonlinear fracture analysis - ii. Fracture-process calibration and verification. *International Journal of Fracture*, 89(4):375-398.
- [49] Prahl U., Bourgeois S., Pandorf T., Aboutayeb M., Debordes O., Weichert D. (2002): Damage parameter identification by a periodic homogenization approach. *Computational Materials Science*, 25(1-2):159-165.
- [50] Kim J. (2004): Modeling of void growth in ductile solids: Effects of stress triaxiality and initial porosity. *Engineering Fracture Mechanics*, 71(3):379-400.
- [51] Hancock J.W., Mackenzie A.C. (1976): Mechanisms of ductile failure in high-strength steels subjected to multi-axial stress states. *Journal of the Mechanics and Physics of Solids*, 24(2-3):147-160.
- [52] Hancock J.W., Brown D.K. (1983): On the role of strain and stress state in ductile failure. *Journal of the Mechanics and Physics of Solids*, 31(1):1-24.
- [53] Mirza M.S., Barton D.C., Church P. (1996): The effect of stress triaxiality and strain-rate on the fracture characteristics of ductile metals. *Journal of Materials Science*, 31(2):453-461.
- [54] Bao Y., Wierzbicki T. (2004): On fracture locus in the equivalent strain and stress triaxiality space. *International Journal of Mechanical Sciences*, 46(1):81-98.
- [55] Mackenzie A.C., Hancock J.W., Brown D.K. (1977): Influence of state of stress on ductile failure initiation in high-strength steels. *Engineering Fracture Mechanics*, 9(1):167-188.
- [56] Hancock J.W., Mackenzie A.C. (1976): On the mechanisms of ductile failure in high-strength steels subjected to multi-axial stress-states. *Journal of the Mechanics and Physics of Solids*, 24(2-3):147-160.

- 
- [57] Johnson G.R., Cook W.H. (1985): Fracture characteristics of 3 metals subjected to various strains, strain rates, temperatures and pressures. *Engineering Fracture Mechanics*, 21(1):31-48.
- [58] Bao Y.B., Wierzbicki T. (2004): On fracture locus in the equivalent strain and stress triaxiality space. *International Journal of Mechanical Sciences*, 46(1):81-98.
- [59] McClintock F.A. (1968): A criterion for ductile fracture by growth of holes. *Journal of Applied Mechanics*, 35(2):363-371.
- [60] Rice J.R., Tracey D.M. (1969): On ductile enlargement of voids in triaxial stress fields. *Journal of the Mechanics and Physics of Solids*, 17(3):201-217.
- [61] Cockcroft M.G., Latham D.J. (1968): Ductility and the workability of metals. *Journal Institute of Metals*, 96:33-39.
- [62] Wierzbicki T., Bao Y., Lee Y.-W., Bai Y. (2005): Calibration and evaluation of seven fracture models. *International Journal of Mechanical Sciences*, 47(4-5):719-743.
- [63] Oh S.I., Chen C.C., Kobayashi S. (1979): Ductile fracture in axisymmetric extrusion and drawing .2. Workability in extrusion and drawing. *Journal of Engineering for Industry-Transactions of the Asme*, 101(1):36-44.
- [64] Bai Y.L., Wierzbicki T. (2008): A new model of metal plasticity and fracture with pressure and lode dependence. *International Journal of Plasticity*, 24(6):1071-1096.
- [65] Barsoum I., Faleskog J. (2007): Rupture mechanisms in combined tension and shear—experiments. *International Journal of Solids and Structures*, 44(6):1768-1786.
- [66] Gao X., Zhang G., Roe C. (2009): A study on the effect of the stress state on ductile fracture. *International Journal of Damage Mechanics*, 19(1):75-94.
- [67] Mirone G., Corallo D. (2010): A local viewpoint for evaluating the influence of stress triaxiality and lode angle on ductile failure and hardening. *International Journal of Plasticity*, 26(3):348-371.
- [68] Bai Y.L., Wierzbicki T. (2010): Application of extended mohr-coulomb criterion to ductile fracture. *International Journal of Fracture*, 161(1):1-20.
- [69] Xue L. (2007): Damage accumulation and fracture initiation in uncracked ductile solids subject to triaxial loading. *International Journal of Solids and Structures*, 44(16):5163-5181.

- 
- [70] Gruben G., Hopperstad O.S., Børvik T. (2012): Evaluation of uncoupled ductile fracture criteria for the dual-phase steel docol 600dl. *International Journal of Mechanical Sciences*, 62:133–146.
- [71] Lou Y., Huh H., Lim S., Pack K. (2012): New ductile fracture criterion for prediction of fracture forming limit diagrams of sheet metals. *International Journal of Solids and Structures*, 49:3605–3615.
- [72] Lou Y., Huh H. (2013): Extension of a shear-controlled ductile fracture model considering the stress triaxiality and the lode parameter. *International Journal of Solids and Structures*, 50:447–455.
- [73] Lou Y., Yoon J.W., Huh H., Archie F. (2013): Modeling of shear ductile fracture considering a changeable cut-off value for stress triaxiality. *International Journal of Plasticity*.
- [74] Li H., Fu M.W., Lu J., Yang H. (2011): Ductile fracture: Experiments and computations. *International Journal of Plasticity*, 27(2):147-180.
- [75] Dunand M., Maertens A.P., Luo M., Mohr D. (2012): Experiments and modeling of anisotropic aluminum extrusions under multi-axial loading - part i: Plasticity. *International Journal of Plasticity*, 36:34-49.
- [76] Li Y., Wierzbicki T. (2010): Prediction of plane strain fracture of ahss sheets with post-initiation softening. *International Journal of Solids and Structures*, 47(17):2316-2327.
- [77] Luo M. (2012). Anisotropic ductile fracture of metal sheets: Experimental investigation and constitutive modeling. Ph.D. Thesis, Massachusetts Institute of Technology.
- [78] Kachanov L.M. (1958): Time of the rupture process under creep conditions. 8:26-31.
- [79] Lemaitre J. (1992): A course on damage mechanics, Berlin, Springer-Verlag.
- [80] Lubarda V.A., Krajcinovic D. (1995): Some fundamental issues in rate theory of damage-elastoplasticity. *International Journal of Plasticity*, 11(7):763-797.
- [81] Voyiadjis G.Z., Park T. (1999): The kinematics of damage for finite-strain elasto-plastic solids. *International Journal of Engineering Science*, 37(7):803-830.
- [82] Voyiadjis G.Z., Deliktas B. (2000): Multi-scale analysis of multiple damage mechanisms coupled with inelastic behavior of composite materials. *Mechanics Research Communications*, 27(3):295-300.
- [83] Teng X. (2008): Numerical prediction of slant fracture with continuum damage mechanics. *Engineering Fracture Mechanics*, 75(8):2020-2041.

- 
- [84] de Souza Neto E.A. (2002): A fast, one-equation integration algorithm for the lemaître ductile damage model. *Communications in Numerical Methods in Engineering*, 18(8):541-554.
- [85] Kachanov L.M. (1999): Rupture time under creep conditions. *International Journal of Fracture*, 97(1-4):xi-xviii.
- [86] Brunig M., Chyra O., Albrecht D., Driemeier L., Alves M. (2008): A ductile damage criterion at various stress triaxialities. *International Journal of Plasticity*, 24(10):1731-1755.
- [87] Chow C.L., Yang X.J., Chu E. (2001): Effect of principal damage plane rotation on anisotropic damage plastic model. *International Journal of Damage Mechanics*, 10(1):43-55.
- [88] Chow C.L., Jie M., Hu S.J. (2003): Forming limit analysis of sheet metals based on a generalized deformation theory. *Journal of Engineering Materials and Technology*, 125(3):260-265.
- [89] Chow C.L., Yang X.J. (2004): A generalized mixed isotropic-kinematic hardening plastic model coupled with anisotropic damage for sheet metal forming. *International Journal of Damage Mechanics*, 13(1):81-101.
- [90] Chow C.L., Jie M. (2009): Anisotropic damage-coupled sheet metal forming limit analysis. *International Journal of Damage Mechanics*, 18(4):371-392.
- [91] Niazi M.S., Wisselink H.H., Meinders T., Huetink J. (2012): Failure predictions for dp steel cross-die test using anisotropic damage. *International Journal of Damage Mechanics*, 21(5):713-754.
- [92] Niazi M.S., Wisselink H.H., Meinders V.T., van den Boogaard A.H. (2013): Material-induced anisotropic damage in dp600. *International Journal of Damage Mechanics*, 22(7):1039-1070.
- [93] Mashayekhi M., Ziaeirad S., Parvizian J., Niklewicz J., Hadavinia H. (2007): Ductile crack growth based on damage criterion: Experimental and numerical studies. *Mechanics of Materials*, 39(7):623-636.
- [94] Gurson A.L. (1977): Continuum theory of ductile rupture by void nucleation and growth: Part I—yield criteria and flow rules for porous ductile media. *Journal of Engineering Materials and Technology-Transactions of the Asme*, 99(1):2-15.



- 
- [95] Tvergaard V. (1981): Influence of voids on shear band instabilities under plane-strain conditions. *International Journal of Fracture*, 17(4):389-407.
- [96] Tvergaard V. (1982): On localization in ductile materials containing spherical voids. *International Journal of Fracture*, 18(4):237-252.
- [97] Tvergaard V., Needleman A. (1984): Analysis of the cup-cone fracture in a round tensile bar. *Acta Metallurgica*, 32(1):157-169.
- [98] Gologanu M., Leblond J.B., Devaux J. (1993): Approximate models for ductile metals containing nonspherical voids - case of axisymmetrical prolate ellipsoidal cavities. *Journal of the Mechanics and Physics of Solids*, 41(11):1723-1754.
- [99] Gologanu M., Leblond J.B., Devaux J. (1994): Approximate models for ductile metals containing nonspherical voids - case of axisymmetrical oblate ellipsoidal cavities. *Journal of Engineering Materials and Technology-Transactions of the ASME*, 116(3):290-297.
- [100] Gologanu M., Leblond J.B., Perrin G., Devaux J. (1997): Recent extensions of Gurson's model for porous ductile metals. In, *Continuum micromechanics*. New York, Springer-Verlag.
- [101] Castaneda P.P., Zaidman M. (1994): Constitutive models for porous materials with evolving microstructure. *Journal of the Mechanics and Physics of Solids*, 42(9):1459-1497.
- [102] Kailasam M., Castaneda P.P. (1998): A general constitutive theory for linear and nonlinear particulate media with microstructure evolution. *Journal of the Mechanics and Physics of Solids*, 46(3):427-465.
- [103] Xue L. (2008): Constitutive modeling of void shearing effect in ductile fracture of porous materials. *Engineering Fracture Mechanics*, 75(11):3343-3366.
- [104] Nahshon K., Hutchinson J.W. (2008): Modification of the gurson model for shear failure. *European Journal of Mechanics a-Solids*, 27(1):1-17.
- [105] Nielsen K.L., Tvergaard V. (2009): Effect of a shear modified gurson model on damage development in a FSW tensile specimen. *International Journal of Solids and Structures*, 46(3-4):587-601.
- [106] Nielsen K.L., Tvergaard V. (2010): Ductile shear failure or plug failure of spot welds modelled by modified Gurson model. *Engineering Fracture Mechanics*, 77(7):1031-1047.
- [107] West O., Lian J., Muenstermann S., Bleck W. (2012): Numerical determination of the damage parameters of a dual-phase sheet steel. *ISIJ International*, 52(4):743-752.

- 
- [108] Bonora N., Gentile D., Pironi A., Newaz G. (2005): Ductile damage evolution under triaxial state of stress: Theory and experiments. *International Journal of Plasticity*, 21(5):981-1007.
- [109] Dunand M., Mohr D. (2011): On the predictive capabilities of the shear modified gurson and the modified mohr-coulomb fracture models over a wide range of stress triaxialities and lode angles. *Journal of the Mechanics and Physics of Solids*, 59(7):1374-1394.
- [110] Muenstermann S., Uthaisangsk V., Prah U., Bleck W. (2007): Experimental and numerical failure criteria for sheet metal forming. *Steel Research International*, 78(10-11):762-770.
- [111] Thoennesen F. (2009). Mikrostrukturbasierte Zaehigkeitsvorhersagen am Beispiel von Pipelinestaehlen. RWTH-Aachen University.
- [112] Ishikawa N., Parks D.M., Socrate S., Kurihara M. (2000): Micromechanical modeling of ferrite-pearlite steels using finite element unit cell models. *ISIJ International*, 40(11):1170-1179.
- [113] Al-Abbasi F. (2003): Micromechanical modeling of dual phase steels. *International Journal of Mechanical Sciences*, 45(9):1449-1465.
- [114] Al-Abbasi F.M., Nemes J.A. (2008): Predicting the ductile failure of dp-steels using micromechanical modeling of cells. *International Journal of Damage Mechanics*, 17(5):447-472.
- [115] Yu Q.M., Hou N.X., Yue Z.F. (2010): Finite element analysis of void growth behavior in nickel-based single crystal superalloys. *Computational Materials Science*, 48(3):597-608.
- [116] Uthaisangsk V., Prah U., Bleck W. (2011): Modelling of damage and failure in multiphase high strength DP and TRIP steels. *Engineering Fracture Mechanics*, 78(3):469-486.
- [117] Vajragupta N., Uthaisangsk V., Schmaling B., Muenstermann S., Hartmaier A., Bleck W. (2012): A micromechanical damage simulation of dual phase steels using XFEM. *Computational Materials Science*, 54:271-279.
- [118] Uthaisangsk V., Prah U., Bleck W. (2009): Stretch-flangeability characterisation of multiphase steel using a microstructure based failure modelling. *Computational Materials Science*, 45(3):617-623.

- 
- [119] Uthaisangsuk V., Prah U., Bleck W. (2009): Characterisation of formability behaviour of multiphase steels by micromechanical modelling. *International Journal of Fracture*, 157(1-2):55-69.
- [120] Uthaisangsuk V., Prah U., Bleck W. (2008): Micromechanical modelling of damage behaviour of multiphase steels. *Computational Materials Science*, 43(1):27-35.
- [121] Ramazani A., Mukherjee K., Prah U., Bleck W. (2012): Modelling the effect of microstructural banding on the flow curve behaviour of dual-phase (DP) steels. *Computational Materials Science*, 52(1):46-54.
- [122] Ramazani A., Schwedt A., Aretz A., Prah U., Bleck W. (2013): Characterization and modelling of failure initiation in dp steel. *Computational Materials Science*, 75:35-44.
- [123] Sun X., Choi K.S., Liu W.N., Khaleel M.A. (2009): Predicting failure modes and ductility of dual phase steels using plastic strain localization. *International Journal of Plasticity*, 25(10):1888-1909.
- [124] Sun X., Choi K.S., Soulami A., Liu W.N., Khaleel M.A. (2009): On key factors influencing ductile fractures of dual phase (DP) steels. *Materials Science and Engineering a-Structural Materials Properties Microstructure and Processing*, 526(1-2):140-149.
- [125] Paul S.K. (2013): Effect of material inhomogeneity on the cyclic plastic deformation behavior at the microstructural level: Micromechanics-based modeling of dual-phase steel. *Modelling and Simulation in Materials Science and Engineering*, 21(5).
- [126] Paul S.K. (2012): Micromechanics based modeling of dual phase steels: Prediction of ductility and failure modes. *Computational Materials Science*, 56:34-42.
- [127] Paul S.K., Kumar A. (2012): Micromechanics based modeling to predict flow behavior and plastic strain localization of dual phase steels. *Computational Materials Science*, 63:66-74.
- [128] Nygard M., Gudmundson P. (2002): Three-dimensional periodic voronoi grain models and micromechanical fe-simulations of a two-phase steel. *Computational Materials Science*, 24(4):513-519.
- [129] Nygard M., Gudmundson P. (2002): Micromechanical modeling of ferritic/pearlitic steels. *Materials Science and Engineering a-Structural Materials Properties Microstructure and Processing*, 325(1-2):435-443.

- 
- [130] Zhao Y.W., Tryon R. (2004): Automatic 3-d simulation and micro-stress distribution of polycrystalline metallic materials. *Computer Methods in Applied Mechanics and Engineering*, 193(36-38):3919-3934.
- [131] Uthaisangsuk V. (2009). Microstructure based formability modelling of multiphase steels. Ph.D. Thesis, RWTH-Aachen University.
- [132] Choi K.S., Liu W.N., Sun X., Khaleel M.A. (2009): Influence of martensite mechanical properties on failure mode and ductility of dual-phase steels. *Metallurgical and Materials Transactions A-Physical Metallurgy and Materials Science*, 40A(4):796-809.
- [133] Choi K.S., Soulami A., Liu W.N., Sun X., Khaleel M.A. (2010): Influence of various material design parameters on deformation behaviors of trip steels. *Computational Materials Science*, 50(2):720-730.
- [134] Choi K.S., Liu W.N., Sun X., Khaleel M.A. (2009): Micro structure-based constitutive modeling of TRIP steel: Prediction of ductility and failure modes under different loading conditions. *Acta Materialia*, 57(8):2592-2604.
- [135] Lemaitre J. (1984): How to use damage mechanics. *Nuclear Engineering and Design*, 80(2):233-245.
- [136] Landron C., Bouaziz O., Maire E., Adrien J. (2010): Characterization and modeling of void nucleation by interface decohesion in dual phase steels. *Scripta Materialia*, 63(10):973-976.
- [137] Bouchard P.O., Bourgeon L., Fayolle S., Mocellin K. (2011): An enhanced Lemaitre model formulation for materials processing damage computation. *International Journal of Material Forming*, 4(3):299-315.
- [138] Borvik T., Hopperstad O.S., Berstad T., Langseth M. (2001): A computational model of viscoplasticity and ductile damage for impact and penetration. *European Journal of Mechanics a-Solids*, 20(5):685-712.
- [139] ABAQUS User's manual (Version 6.12) (2012). Hibbit, Karlsson and Sorensen Inc.
- [140] Hillerborg A., Mod er M., Petersson P.-E. (1976): Analysis of crack formation and crack growth in concrete by means of fracture mechanics and finite elements. *Cement and Concrete Research*, 6(6):773-781.
- [141] Anand L., Aslan O., Chester S.A. (2012): A large-deformation gradient theory for elastic-plastic materials: Strain softening and regularization of shear bands. *International Journal of Plasticity*, 30-31:116-143.

- [142] Brunet M., Morestin F., Walter H. (2004): Damage identification for anisotropic sheet-metals using a non-local damage model. *International Journal of Damage Mechanics*, 13(1):35-57.
- [143] Andrade F.X.C., de Sa J.M.A.C., Pires F.M.A. (2011): Ductile damage nonlocal model of integral-type at finite strains: Formulation and numerical issues. *International Journal of Damage Mechanics*, 20(4):515-557.
- [144] de Souza Neto E.A., Peric D., Owen D.R.J. *Computational methods for plasticity: Theory and applications* (2008). JohnWiley & Sons Ltd.
- [145] Racherla V., Bassani J.L. (2007): Strain burst phenomena in the necking of a sheet that deforms by non-associated plastic flow. *Modelling and Simulation in Materials Science and Engineering*, 15(1):S297-S311.
- [146] Hershey A.V. (1954): Plasticity of isotropic aggregate of anisotropic facecentered cubic crystals. *Journal of Applied Mechanics*, 21:241-249.
- [147] Hosford W.F. (1972): A generalized isotropic yield criterion. *Journal of Applied Mechanics*, 39(2):607-609.
- [148] Cazacu O. (2004): A criterion for description of anisotropy and yield differential effects in pressure-insensitive metals. *International Journal of Plasticity*, 20(11):2027-2045.
- [149] Cazacu O., Plunkett B., Barlat F. (2006): Orthotropic yield criterion for hexagonal closed packed metals. *International Journal of Plasticity*, 22(7):1171-1194.
- [150] Barlat F., Brem J.C., Yoon J.W., Chung K., Dick R.E., Lege D.J., Pourgoghrat F., Choi S.H., Chu E. (2003): Plane stress yield function for aluminum alloy sheets-Part I: Theory. *International Journal of Plasticity*, 19(9):1297-1319.
- [151] Hu W.L., Wang Z.R. (2005): Multiple-factor dependence of the yielding behavior to isotropic ductile materials. *Computational Materials Science*, 32(1):31-46.
- [152] EN 10025. Hot rolled products of structural steels, European Committee for Standardization, Brussels, Belgium, 2004.
- [153] EN 10002-1. Metallic materials – tensile testing, Part 1: Method of test at ambient temperature, European Committee for Standardization, Brussels, Belgium, 2001.
- [154] Bao Y. (2004): Dependence of fracture ductility on thickness. *Thin-Walled Structures*, 42(8):1211-1230.
- [155] Bleck W. (2012): *Materials characterisation*, textbook for RWTH students, Department of Ferrous Metallurgy, RWTH Aachen University.

- 
- [156] Ma N. (2013). Prediction of springback for ultra high strength steel sheets. Ph.D. Thesis, RWTH-Aachen University.
- [157] EN ISO 7438. Metallic materials – bend test, European Committee for Standardization, Brussels, Belgium, 2005.
- [158] Mirone G. (2004): A new model for the elastoplastic characterization and the stress–strain determination on the necking section of a tensile specimen. *International Journal of Solids and Structures*, 41(13):3545-3564.
- [159] Marciniak Z., Duncan J.L., Hu S.J. (2002): *Mechanics of sheet metal forming*, Woburn, United States, Butterworth-Heinemann.
- [160] Bai Y.L., Wierzbicki T. (2015): A comparative study of three groups of ductile fracture loci in the 3d space. *Engineering Fracture Mechanics*, 135:147-167.
- [161] Bao Y., Wierzbicki T. (2005): On the cut-off value of negative triaxiality for fracture. *Engineering Fracture Mechanics*, 72(7):1049-1069.
- [162] Keeler S.P. (1969): A valuable aid for evaluation sheet forming. *Sheet Metal Industries*, 45:633-640.
- [163] Goodwin G.M. (1968): Application of strain analysis to sheet metal forming problems. *La Metallurgica*, 60:767-771.
- [164] Bleck W., Deng Z., Papamantellos K., Gusek C.O. (1998): A comparative study of the forming-limit diagram models for sheet steels. *Journal of Materials Processing Technology*, 83(1):223-230.
- [165] Hora P., Tong L., Reissner J. A prediction method for ductile sheet metal failure. In: Lee J.K., Kinzel G.L., Wagoner R.H. (eds) *NUMISHEET 1996*, Dearborn, 1996. pp 252-256
- [166] Aretz H. (2007): Numerical analysis of diffuse and localized necking in orthotropic sheet metals. *International Journal of Plasticity*, 23(5):798-840.
- [167] EN 1993. Design of steel structures, European Committee for Standardization, Brussels, Belgium., 2005.
- [168] Ouchi C. (2001): Development of steel plates by intensive use of tmcp and direct quenching processes. *ISIJ International*, 41(6):542-553.
- [169] Liu B., Liu X.J., Zhang H. (2009): Strain-based design criteria of pipelines. *Journal of Loss Prevention in the Process Industries*, 22(6):884-888.

- [170] Muenstermann S., Schruff C., Lian J., Dobereiner B., Brinnel V., Wu B. (2013): Predicting lower bound damage curves for high-strength low-alloy steels. *Fatigue & Fracture of Engineering Materials & Structures*, 36(8):779-794.
- [171] Lai G.Y., Wood W.E., Clark R.A., Zackay V.F., Parker E.R. (1974): Effect of austenitizing temperature on microstructure and mechanical-properties of as-quenched 4340 steel. *Metallurgical Transactions*, 5(7):1663-1670.
- [172] Hulka K., Heisterkamp F. (1998): Development trends in HSLA steels for welded constructions. *Proceedings of the International Conference on Microalloying in Steels*, 284-2:343-350.
- [173] Czyryca E.J., Link R.E., Wong R.J., Aylor D.A., Montemarano T.W., Gudas J.P. (1990): Development and certification of HSLA-100 steel for naval ship construction. *Naval Engineers Journal*, 102(3):63-82.
- [174] Xue L. (2008): A unified expression for low cycle fatigue and extremely low cycle fatigue and its implication for monotonic loading. *International Journal of Fatigue*, 30(10-11):1691-1698.
- [175] Zhang K.S., Bai J.B., Francois D. (2001): Numerical analysis of the influence of the lode parameter on void growth. *International Journal of Solids and Structures*, 38(32-33):5847-5856.
- [176] Gao X., Kim J. (2006): Modeling of ductile fracture: Significance of void coalescence. *International Journal of Solids and Structures*, 43(20):6277-6293.
- [177] Barsoum I., Faleskog J. (2011): Micromechanical analysis on the influence of the lode parameter on void growth and coalescence. *International Journal of Solids and Structures*, 48(6):925-938.
- [178] Rodriguez R., Gutierrez I. (2003): Unified formulation to predict the tensile curves of steels with different microstructures. In: Chandra T., Torralba J.M., Sakai T. (eds), *Thermec'2003*, pts 1-5, Materials science forum. Zurich-Uetikon, Trans Tech Publications Ltd, pp. 4525-4530.